Alma Mater Studiorum – Università di Bologna

DOTTORATO DI RICERCA IN

Ingegneria Civile, Ambientale e dei Materiali

Ciclo XXVIII

Settore Concorsuale di afferenza: 09/D1

Settore Scientifico disciplinare: ING-IND 22

A COMPREHENSIVE STUDY OF FLY ASH BASED GEOPOLYMERS ACTIVATED AT ROOM TEMPERATURE

Presentata da: **Maria Elia Natali**

Coordinatore Dottorato

Prof. Alberto Lamberti

Relatore

Prof. Maria Chiara Bignozzi

Correlatori

Prof. Cecilia Monticelli

Prof. Stefania Manzi

Esame finale anno 2016

To what comes next

ABSTRACT

This research presents the overall results obtained by investigating the performances of fly ash based geopolymers activated at room temperature. Several characterization tests have been perfomed, starting from a deep understanding of the raw materials, in view of finding alternative solutions to the use of traditional hydraulic binders or ceramic materials via alkali-activation. Different types of geopolymer samples (i.e., pastes, mortars and reinforced mortars) have been formulated by varying the nominal Na_2O/SiO_2 molar ratio in the activating solutions (and in a specific case the curing conditions) and their chemical, physical, mechanical and microstructural performances have been evaluated comparing the results obtained by using different types of precursors and by a traditional cement-based binder. Specific attention has ben focused on durability issues such as high temperature applications and corrosion resistance of the embedded rebars in geopolymer mortars exposed to aggressive environments. Alkali-activation has been found to represent a valid approach in developing performant cement-free products but step forward are needed in order to optimize the solution chemistry and enhance physical and mechanical properties starting from a deep understand at nanoscale of the geopolymerization reaction mechanisms.

ACKNOWLEDGEMENTS

I am very grateful to my supervisor Prof. Maria Chiara Bignozzi for her continuous technical guidance, motivation, human support and brilliant suggestions during the entire period of my research work in Bologna. I would like to thank also Prof. Stefania Manzi, Prof. Elisa Franzoni and the entire Material Engineering research group at DICAM.

Thanks to Prof. Cecilia Monticelli, and all her group at the University of Ferrara, for providing a fundamental support for my research and being a vision for professionality and scientific relevance.

I'd like to thank Prof. Claire White and Prof. Antoine Morandeau for their guidance and constant support during my foreign research period at Princeton University, which has been a turning point and a highly productive and inspiring moment for my research and my life.

I am thankful to all my Department colleagues at the University of Bologna (Enrico, Gabriela, Lorenza, Giulia, Parsa) for providing a joyful working atmosphere and sharing ideas and funny moments and to Dr. Roberto Gaiba for helping me in solving analytical problems and being my scientific mentor.

I want to thank my parents for their motivation and continuous support, even in hard moments. Finally, special thanks to all my friends, the one who have always been there, since the moment I started, and to all the new I met during those three intense years of changings. You all are the reason and motivation for this important achievement and I'm sure you'll be also for what comes next. A new step.

Sincerely, Thanks.

CONTENTS

LIST OF TABLES

LIST OF FIGURES

1 INTRODUCTION

The increasing need in enhancing sustainable and zero-energy consuming technologies in the field of construction materials by promoting a partial/total substitution of Ordinary Portland Cement (OPC), has led to a strong focus on the development of low-CO_2 emission binder systems. In these terms, various studies have highlighted alkali-activated materials (AAM) as a potential competitive alternative to OPC. This class of inorganic amorphous materials derives from the alkali-activation of aluminosilicate powders with suitable amorphous content. Many aluminosilicate precursors are suitable for activation and when the raw material has a high content of SiO_2 + Al_2O_3 (generally > 80 wt. %) and a low CaO content, like class F fly ash (FA), the final product is referred to as geopolymer [1,2]. The chance to use by-products as precursors, along with a room or slightly higher curing temperature, makes geopolymers low-polluting products and, consequently, promising green building materials.

The aim of this thesis was therefore to evaluate a sustainable alternative to commonly used building materials, particularly OPC, by promoting their total substitution, at same technological conditions, with by-products. More specifically, this research focuses on fly ash based geopolymers activated at room temperature and on the evaluation of their potentialities for the use in the civil sector.

The first part of the research was focused on a deep understand of the precursors, in order to assess their properties, variability and suitability for the alkali-activation process. Then, different formulations have been tested to elucidate how specific parameters could influence the final properties of the obtained paste and mortar materials. Particular attention

was directed on long-term performances and durability issues such as resistance to high temperature, carbonation, chloride penetration and corrosion, while a traditional OPC binder was used as reference.

The existing literature and state of the art related to geopolymer precursors and properties is reviewed in Chapter 2. This thesis focuses on fly ash based geopolymers and therefore this Chapter has been tailored towards this geopolymer sub-class. However, other aluminosilicate sources, such as metakaolin and slag, and the relevant geopolymers, are also discussed along with the introduction of new types of precursors derived from waste streams such as coal gangue and red mud. The conceptual models for the geopolymerization process, the main properties and applications of geopolymers together with their limitations are also reported.

In Chapter 3 the source materials employed, the samples preparation and characterization methods used through this thesis are outlined, including a short description of the mathematical basis for the main techniques used.

Chapter 4 is focused on the results obtained by the characterization of the precursors. Five different types of fly ash have been chosen as representative of the variability of this by-product and extensively analyzed through a series of characterization techniques, which pointed out their chemical composition, particle size distribution, morphology and mineralogical phase composition, highlighting both the crystalline and amorphous components.

Chapter 5 elucidates the main physical and microstructural results of geopolymer pastes derived from the alkali-activation of two different types of fly ash, providing also evidences for the different behaviour reported. This Chapter also reports the results obtained for samples obtained by different curing conditions, in order to evaluate the influence of curing on the final performances.

Chapter 6 specifically focuses on the use of one selected type of fly ash for the production of geopolymer mortars and presents their results in terms of physical, microstructural and mechanical performances in unreinforced and reinforced systems exposed to aggressive environments, including a corrosion behavior evaluation of the embedded rebars.

Chapter 7 then provides the concluding remarks. In this Chapter, the main results from each investigative Chapter are reiterated to provide an overall picture of what this thesis has achieved in regards of furthering the understanding of geopolymers.

References are finally reported in Chapter 8.

The novelty of this research is the proposed integrated approach involving the optimization of the alkali-activation process at room temperature and its exploitation in terms of products potentially market ready thus providing an alternative to those based on hydraulic lime and/or Ordinary Portland Cement. Some of the here reported results have been published as journal papers, which are all associated with developing a deep understanding geopolymer technology.

The research project was developed at the Department of Civil, Chemical, Environmental and Materials Engineering (DICAM) of the University of Bologna in collaboration with the Corrosion and Metallurgy Study Center "Aldo Daccò" of the University of Ferrara, the Curtin University of Perth, Western Australia and, for a period of six months, at the Department of Civil and Environmental Engineering (CEE) of the Princeton University, NJ, USA.

2 LITERATURE REVIEW

In this Chapter an overview of the existing literature on geopolymers technology, the chemical aspects, the raw materials and activators including the applications, durability and sustainability issues is reported, with the aim of highlighting the questions that will be answered along the thesis in the context of fly ash based geopolymers activated at room temperature.

2.1 History of geopolymer technology

Geopolymers are a relatively new class of inorganic amorphous materials derived from the activation of solid amorphous aluminosilicate sources by means of alkaline solutions at ambient or slightly elevated temperatures (< 100 °C). The consolidate product exhibits engineering performances equivalent, or even superior in specific cases, to OPC [1,2]. Geopolymers represent a subset of a broader group of inorganic binders, called alkali-activated materials (AAMs), derived from the reaction of an amorphous solid aluminosilicate-rich powder with an alkaline salt, such as sodium hydroxide and sodium silicate. Specifically, geopolymers represent the sub-class which is characterized, in terms of chemical composition, by the highest amount of silica and alumina ($SiO_2 + Al_2O_3 > 80$ wt.%), while AAMs can refer to precursors based on both aluminosilicate and Ca-containing amorphous/crystalline phases. The specifics of this classification are graphically synthetically reported in Figure. 2.1 [3] and help to elucidate the terminology and definitions of “geopolymers”, which have become more diverse and often conflicting during time. The term “geopolymer” was first introduced in the late 1970s by Davidovits,

a French researcher who created this name to describe aluminosilicate inorganic polymeric cements [4]. However similar materials have been around for far longer than this.

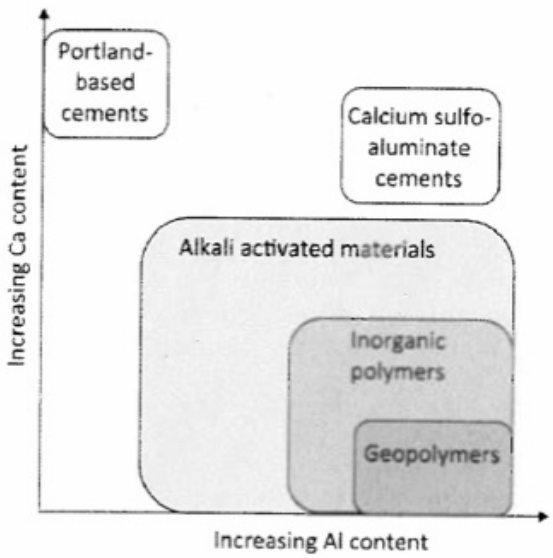

Figure. 2.1 Classification of different subsets of AAMs, with comparison to OPC and calcium sulfoaluminate binder chemistry [3].

The first use of alkaline solutions as a component for cementitious materials dates back to 1930s, when the German Kühl studied the behaviour of a mixture composed of industrial waste, cement and potassium hydroxide (KOH) [5]. In 1940 Purdon [6] conducted the first laboratory tests on cement-free binders obtained by the activation of blast furnace slag through sodium hydroxide (NaOH) [7]. In 1950s, Glukhovsky, an Ukrainian scientist, focused his attention on durability issues of materials used in ancient Rome and Egypt, made mainly of natural rocks, emphasizing the differences with the low durability of traditional Portland cement. The main hydration products of OPC are calcium silicate hydrate (C-S-H) and Portlandite, while in the case of natural rocks, zeolitic compounds containing alkali are formed. The latter gel composition is characterized by a high durability [8]. On the basis of these studies, Glukhovsky developed the so called “soil silicate concretes” or “soil cements” proposing, in imitation of the microstructural characteristics at the base of the natural rocks, the activation of alkaline raw materials containing silica and alumina, such as clays, feldspars, volcanic ashes and various kind of suitable industrial wastes which were available in the area around Kiev, Ukraine [9,10]. Numerous artifacts including small buildings, railroad ties, roads, pipes, channels for drainage and irrigation, prefabricated elements have been

produced using this technology in Ukraine at that time. Later studies carried out on samples taken from these facilities, have shown a high durability and a very compact structure characterizing these materials [11]. Blast furnace slag geopolymers were then first trialed in some concrete applications in Soviet Union and numerous structures, railroad ties, roads, pipes, channels for drainage and irrigation have been constructed in the following years even though this technology was not completely developed at the industrial scale. Afterwards, a turning point in the history of geopolymers is represented by the research of the French author Davidovits who patented in 1979 a binder obtained by the alkaline activation of metakaolin first coining the term "geopolymer". According to the author the term adopted was the key to the success of this "new" material: the prefix "geo" implies that the material mimic natural rocks while the suffix "polymers" describes the chemical reactions which occurs during hardening [6]. Davidovits research started as a result of some fires that broke out in France between 1970 - 73 and which involved organic based plastics. The purpose was to find alternative materials to organic matrices for compounds resistant to high temperatures and to acid attacks. The first applications of geopolymers were flame retardant coatings in cruise ships, matrix for carbon fibers composite, thermal protection of wooden structures, adhesives for high temperature applications, monolithic refractories and other niche applications [10]. In 1983 Davidovits patented the "Pyrament" [6], a binder which composition is 80 wt.% OPC and the remaining 20 wt.% a geopolymeric source and which is able to reach a compressive strength of 20 MPa in just 4 - 6 hours. Due to its characteristics, "Pyrament" is ideal for infrastructure and flooring fast repair and it was widely used during the Gulf War for damaged tracks restoration. After that, another geopolymer patent is the "E-Crete^{TM}", filed by the Australian Zeobond in 2007 [12]. It is an alkali-activated binder based on fly ash and blast furnace slag, which is mostly used for infrastructure applications, pavements and buildings (Figure. 2.2).

Some of the basic steps and the most interesting studies on the development of alkali-activated materials and geopolymers are reported in Table. 2.1. The interest around this topic grew extensively over the last few decades, with a large number of publications revealing the suitability of these binders as cement alternatives in the field of construction materials [13,14]. Currently, the main research in the field of geopolymers is held in Australia, New Zeland and Europe but a growing interest is developing at global level due to the huge potential of these new materials to lower CO_2 emissions in the

construction industry, due to the use of by-products as raw materials and in the use of low process temperature, so being environmentally-friendly and more sustainable.

Figure. 2.2 Thomastown Recreation Centre, Thomastown, Australia, E-Crete™ technology used [15].

Author	Year	Significance
Feret	1939	Slag used for cement
Purdon	1940	Alkali-slag combination
Glukhovsky	1959	Theoretical basis and development of alkaline cements
Glukhovsky	1965	First called "alkaline cements"
Davidovits	1979	"Geopolymer" term
Malinowski	1979	Ancient aqueducts characterized
Forss	1983	F-cement (slag-alkali-superplasticizer)
Langron, Roy	1984	Ancient building materials characterized
Davidovits, Sawyer	1985	Patent of "Pyrament" cement
Krivenko	1986	DSc thesis, R_2O–RO–SiO_2–H_2O
Malolepsy, Petri	1986	Activation of synthetic melilite slags
Malek et al.	1986	Slag cement-low level radioactive wastes forms
Davidovits	1987	Ancient and modern concretes compared
Deja, Malolepsy	1989	Resistance to chlorides shown
Kaushal et al.	1989	Adiabatic cured nuclear wastes forms from alkaline mixtures
Roy, Langton	1989	Ancient concretes analogs
Majundar et al.	1989	C12A7– slag activation
Talling, Brandstetr	1989	Alkali-activated slag
Wu et al.	1990	Activation of slag cement
Roy et al.	1991	Rapid setting alkali-activated cements
Roy, Silsbee	1992	Alkali-activated cements: an overview
Palomo, Glasser	1992	"Chemically Bonded Ceramics" with metakaolin
Roy, Malek	1993	Slag cement
Glukhovsky	1994	Ancient, modern and future concretes
Krivenko	1994	Alkaline cements
Wang, Scrivener	1995	Slag and alkali-activated microstructure

Table. 2.1 Bibliographic history of some important events about alkali-activated binders [8].

2.2 Geopolymer chemistry

Geopolymers are characterized by silicon and aluminum tetrahedral structures linked together by oxygen atoms. To describe the three-dimensional geopolymeric structures, a new terminology was proposed by Davidovits during an IUPAC Symposium in 1976 [16]. The geopolymer structures includes three classes of inorganic polymers that, depending on the silica/alumina ratio, are based on three different monomeric units (Figure. 2.3) [4]:

- poly(sialate) (PS) with [-Si-O-Al-O-] as the repeating unit, with $SiO_2/Al_2O_3 = 2$;
- poly(sialate-siloxo) (PSS) with [-Si-O-Al-O-Si-O-] as the repeating unit, with $SiO_2/ Al_2O_3 = 4$;
- poly(sialate-disiloxo) (PSDS) with [-Si-O-AI-O-Si-O-Si-O-] as the repeating unit, with $SiO_2/Al_2O_3 = 6$ as repeating unit.

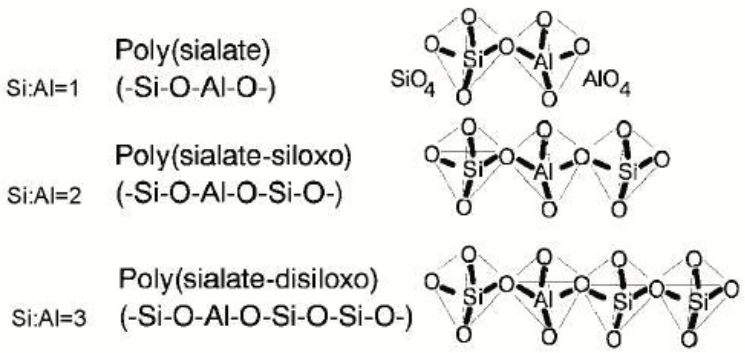

Figure. 2.3 Types of polysialate units [4].

Sialate is an abbreviation for silicon-oxo-aluminate. The sialate network consists of SiO_4 and AlO_4 thetrahedra linked alternately by sharing all the oxygens. Positive ions (Na^+, Ca^{++}, K^+...) must be present in the framework cavities to balance the negative charge of Al_3^+ in IV-fold coordination. Poly-sialates have this empirical formula:

$$Mn[-(SiO_2)_z - AlO_2]n \cdot wH_2O$$

where: *M* is a cation such as potassium, sodium or calcium, *n* is the degree of polymerization and *z* is 1, 2 or 3 depending on the type of sialate structure formed. Poly-

sialates are chain- and ring-polymers with Si_4^+ and Al_3^+ in IV-fold coordination with oxygen and range from amorphous to semi-crystalline [16].

For the synthesis of geopolymers three main components are required: raw material, inactive filler and geopolymer liquor (Figure. 2.4) [17]:

- raw materials include natural aluminosilicate materials or aluminosilicate wastes such as industrial slag, coal ashes and others. The main role in the geopolymerization process is to provide the source of Si and Al ions. Although geopolymers are traditionally produced through alkali-activation of naturally occurring aluminosilicates, the results of several studies published in the last years have shown that industrial residues with high silicon and aluminum contents may be considered as suitable source materials for the production of inorganic polymers. This represents the main advantage offered by geopolymer technology;

- the inactive filler is added to increase the amount of Al_3^+ ions. One of the most utilized inactive filler is kaolin or metakaolin (obtained from kaolin calcinations). This filler is required when the Al dissolution rate of the raw material is not sufficient to promote the production of the geopolymer gel. The inactive filler reduces the reactivity of the mixture by increasing the reaction time between the raw material and the alkali activator, promoting the gel formation and than improving mechanical strength and decreasing the porosity and permeability of the resulting geopolymer;

- the geopolymer liquor is an alkaline solution obtained by mixing an alkali metal hydroxide solution with a sodium silicate solution (waterglass). The geopolymer liquor is required to dissolve the raw materials and it plays also the additional role of activator, binder, dispersant and plasticizer.

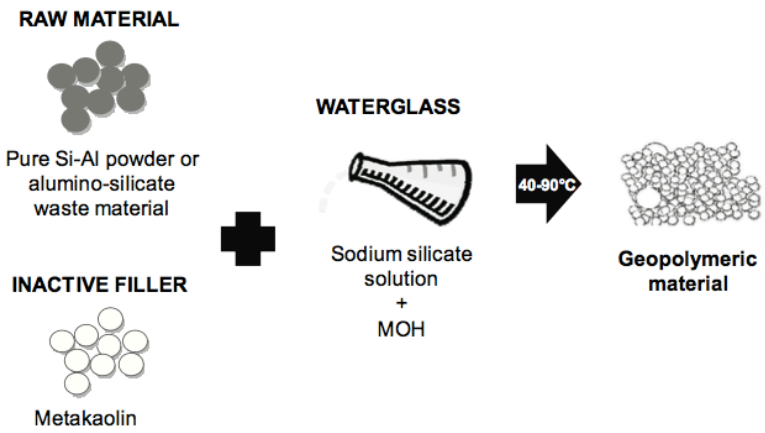

Figure. 2.4 Main components used to produce geopolymeric materials [17].

2.3 The chemical process

There have been several models proposed over the years regarding the geopolymerization process. One of the most used and highly simplified is proposed by Duxson et al. [18] and displayed in Figure. 2.5. In this reaction the aluminosilicate precursor dissolves in a highly alkaline solution releasing aluminate and silicate monomers, which undergo condensation reactions to move the system towards equilibrium releasing water. Then, the supersatured aluminosilicate solution undergoes gelation forming the initial geopolymeric gel (named *gel 1*). This gel tends to reorganize its structure with time to form a more cross-linked gel (named *gel 2*). Depending on the conditions, part of this gel undergoes nucleation and crystalline precipitates, zeolitic in nature, form along with the amorphous gel. This conceptual model has been described as highly simplified primarily due to the fact that geopolymerisation is here described as a linear reaction process. However, realistically these processes will occur simultaneously, with dissolution of the aluminosilicate source occurring simultaneously with repolymerisation of silicate and aluminate species. The second main limitation regards the implied simplicity of the precursor materials, which is not the case especially when by-products, such as fly ash, are used.

A more realistic model has been proposed by Provis and van Deventer [19] and is reported in Figure. 2.6. This model better replicates the complex nature of geopolymerisation through depiction of the various silicate and aluminosilicate species that can form, together with the tendency for monomeric species to add to the polymerized aluminosilicate gel. Provis and van Deventer [19] used this conceptual

model as the basis for a reaction kinetic model of geopolymerisation. The output from the model was directly compared with energy dispersive X-ray diffraction measurements and alternating current impedance spectroscopy, proving that the model adequately replicates the observations measured experimentally.

Both the conceptual models have advanced the overall understanding of geopolymerisation, especially regarding the dominant mechanisms responsible for this process. Nevertheless, they must be expanded to incorporate the more subtle processes contributing to the reaction's complexity [20].

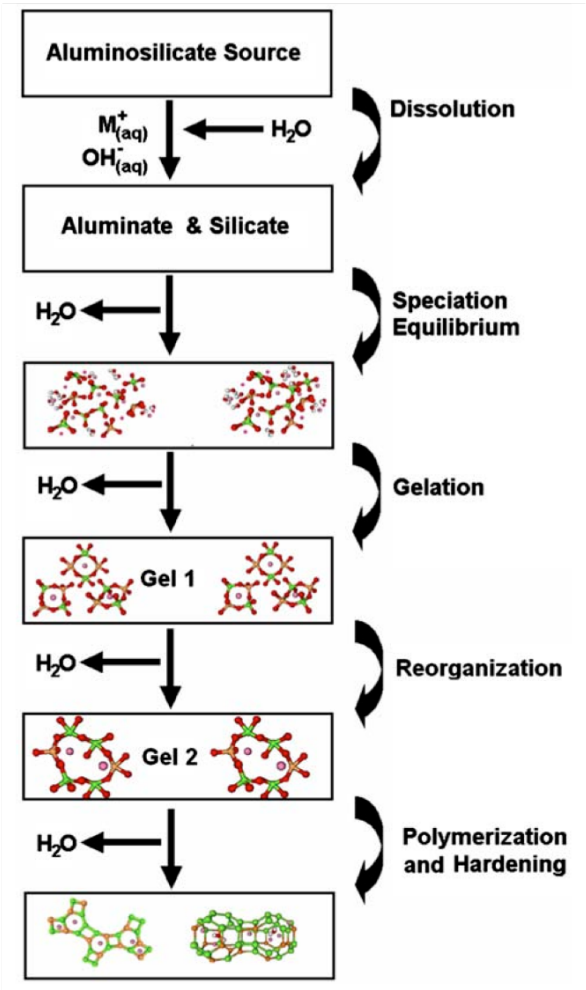

Figure. 2.5 Conceptual model of the geopolymerisation reaction, as reported by Duxson et al. [18].

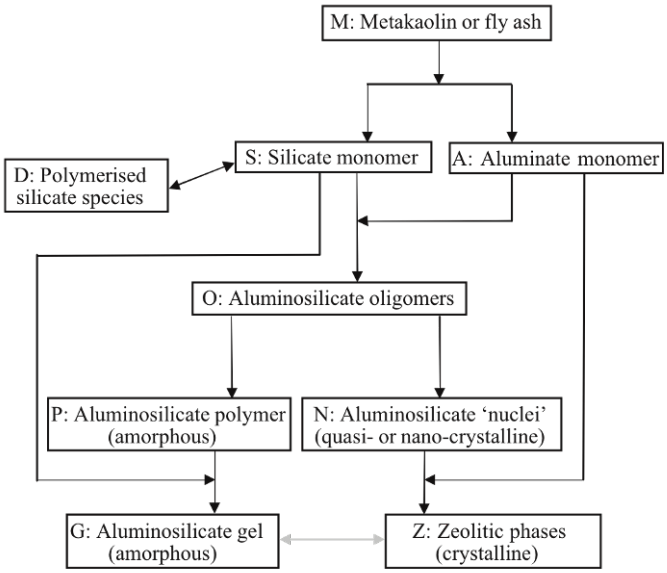

Figure. 2.6 Conceptual model of geopolymerisation, as reported by Provis and van Deventer [19] showing the sequence of events occurring during this complex reaction process.

2.4 Precursors

Starting raw material, also mentioned as geopolymerization precursor, plays an important role in the formation of geopolymer and in the development of a variety of different properties, as different gels can form during reaction depending on the precursor intrinsic characteristics. Theoretically, any material composed of amorphous silica and alumina can be alkali-activated and materials rich in Al (clays like kaolin) and/or rich in Si (like FA, slag and rice husk) have been used so far [21]. Of course, the chance to use by-products of industrial processes as precursors, such as FA or slags, has recently become a priority according to the pressing need to implement sustainable and zero-energy consuming technologies in field of building materials. On the other hand, the high variability in composition, even for material derived from a single plant, for non-process-controlled by-products represents a challenge in their use as precursors, as composition controls reactivity and solubility in an alkaline solution [22-28]. For that reason, metakaolin has been used as a model system for a long time, as the use of this precursor has the advantage to provide a pure and more readily characterized starting material, derby enhancing the microstructural understanding of the final product [29].

The following Subchapters will provide information about the characteristics of the most frequently used geopolymer precursor and their production, with particular focus on

fly ash.

2.4.1 Metakaolin

Metakaolin is a dehydroxylated form of the clay mineral kaolinite, which forms a highly reactive and amorphous aluminosilicate after calcining under carefully conditions. Its particles are extremely small with an average particle size of 3 μm and its color is white (Figure. 2.7). Kaolinite is an hydrate aluminium disilicate, the most common constituent of kaolin which composition is highly suitable for geopolymerization (i.e., SiO_2 = 46.54 wt.%, Al_2O_3 = 39.5 wt.%, H_2O = 13.96 wt.%, major oxides [30]). Stones that are rich in kaolinite are known as China clay or kaolin, traditionally used in the manufacture of porcelain. Kaolinite dehydroxylation temperature depends on its specific structural layer stacking order, purity and crystallinity: disordered kaolinite dehydroxylates between 530 and 570 °C, ordered kaolinite between 570 and 630 °C. Dehydroxylated disordered kaolinite shows higher pozzolanic activity than ordered [31]. The dehydroxylation of kaolin to metakaolin is an endothermic process due to the large amount of energy required to remove the chemically bonded hydroxyl ions. Above the temperature range of dehydroxylation, kaolinite transforms into metakaolin, a complex amorphous structure that retains some long-range order due to layer stacking [32]. Much of the aluminum of the octahedral layer becomes tetrahedrally and pentahedrally coordinated [33]. In essence, metakaolin consists of alternating buckled silicate and aluminate layers, with the silicon in IV-coordination and the aluminum in a mixture of IV-, V- and VI-coordination. The key to the reactivity of metakaolin, as compared to kaolinite, is the strain in the bonding network induced by the thermal dehydroxylation.

In order to produce a pozzolan, nearly complete dehydroxylation must be reached without overheating to avoid sintering. This produces an amorphous, highly pozzolanic state, whereas overheating forms a dead burnt, nonreactive refractory, containing mullite [34]. Reported optimum activation temperatures vary between 550 and 850 °C for varying durations, however the range 650 - 750 °C is most commonly quoted [35]. In comparison with other clay minerals kaolinite shows a broad temperature interval between dehydroxylation and recrystallization, much favoring the formation of metakaolin and the use of thermally activated kaolin clays as pozzolans. Also, because the octahedral layer is directly exposed to the interlayer (in comparison to for instance T-

O-T clay minerals such as smectites), structural disorder is attained more easily upon heating.

The reaction between alkalis and metakaolin at slightly elevated temperatures depends in the exact reaction conditions and may form a variety of zeolites. The first detailed scientific study on the alkali-activation of metakaolin was published in 1992 by Palomo et al. [36] and research has intensified since that time as this system was adopted as a model for some chemical aspects of more complex systems (as the case of fly ash).

The main drawbacks of metakaolin based geopolymers for large-scale applications include the use of a natural raw material and the high temperature needed for its dehydroxylation, characteristics that clearly reduce their environmental sustainability. Moreover, metakaolin is characterized by a very high surface area and a plate-like particle shape, meaning a high water demand in the mix. This turns in problems related to the drying shrinkage and cracking as the excess of water, which is not chemically bonded in the case of geopolymers, leaves the hardened product. Additionally, the use of an excess of solution may lead to the formation of efflorescences, which are pronounced for metakaolin-based geopolymers compared to other precursors.

a) b)

Figure. 2.7 A kaolin querry in China (a); metakaolin powder (b) [37].

2.4.2 Ground granulated blast-furnace slag

Ground granulated blast-furnace slag (GGBFS) is obtained by quenching molten iron slag (a by-product of iron and steel-making) from a blast furnace in water or steam, to produce a glassy, granular product that is then dried and ground into a fine powder (average particle size about 20 μm) (Figure. 2.8).

The chemical composition of a slag varies considerably depending on the composition of the raw materials in the iron production process and between specific furnaces and ores. Silicate and aluminate impurities from the ore and coke are combined in the blast furnace with a flux, which lowers the viscosity of the slag. In the case of pig iron production, the flux consists mostly of a mixture of limestone and forsterite or in some cases, dolomite [37]. In the blast furnace the slag floats on top of the iron and is decanted for separation. Slow cooling of slag melts result in an unreactive crystalline material consisting of an assemblage of Ca-Al-Mg silicates. To obtain a good slag reactivity or hydraulicity, the slag melt needs to be rapidly cooled or quenched below 800 °C in order to prevent the crystallization of merwinite and melilite. To cool and fragment the slag, a granulation process can be applied in which molten slag is subjected to jet streams of water or air under pressure. Alternatively, in the pelletization process the liquid slag is partially cooled with water and subsequently projected into the air by a rotating drum [37]. In order to obtain a suitable reactivity, the obtained fragments are ground to reach the same fineness as Portland cement.

The main components of blast-furnace slag are CaO (30-50 wt.%), SiO_2 (28 - 38 wt.%), Al_2O_3 (8 - 24 wt.%), and MgO (1 - 18 wt.%). In general increasing the CaO content of the slag results in raised slag basicity and in an increase in compressive strength. The MgO and Al_2O_3 content show the same trend up to respectively 10 - 12 wt.% and 14 wt.%, beyond which no further improvement can be obtained. Several compositional ratios, or so-called hydraulic indices, have been used to correlate slag composition with hydraulic activity, the latter being mostly expressed as the binder compressive strength.

The glass content of slags suitable for blending with Portland cement typically varies between 90 - 100 wt.% and depends on the cooling method and the temperature at which cooling is initiated. The glassy structure of the quenched glass largely depends on the proportions of network-forming elements such as Si and Al over network-modifiers such as Ca, Mg and to a lesser extent Al. Increased amounts of network-modifiers lead to higher degrees of network depolymerization and reactivity [37].

Common crystalline constituents of blast-furnace slags are merwinite and melilite. Other minor components, which can form during progressive crystallization, are belite, monticellite, rankinite, wollastonite and forsterite. Minor amounts of reduced sulphur are

commonly encountered as oldhamite [37].

In the context of geopolymer synthesis from slag glasses, the key glass network forming cations are Al^{3+} and Si^{4+} while the divalent Ca^{2+} and Mg^{2+} act as network modifiers along with alkalis present. The high variability of the precursor, as previously mentioned, results in different reactivity in alkali-activated materials, which has been described in the work of Shi et al. [5] and in the nature of the formed hydrated slag phases [38-40]. However, much remains to be discovered regarding the specific network structure of the phases present in each type of slag as well as the influence of these phases on the progress of the alkali-activation reactions.

a) b)

Figure. 2.8 A GGBFS plant in China (a); GGBFS powder (b) [41].

2.4.3 Fly ash

Fly ash is a by-product from burning pulverized coal in electric power generating plants. During combustion, mineral impurities in the coal (clay, feldspar, quartz, and shale) fuse in suspension and float out of the combustion chamber with the exhaust gases. As the fused material rises, it cools and solidifies into spherical glassy particles called fly ash (Figure. 2.9). Fly ash is collected from the exhaust gases by electrostatic precipitators or bag filters. The fine powder does resemble Portland cement but it is chemically different. The major consequence of the rapid cooling is that few minerals have time to crystallize, and that mainly amorphous, quenched glass remains. Nevertheless, some refractory phases in the pulverized coal do not melt entirely, and remain crystalline. In consequence, fly ash is an heterogeneous material. SiO_2, Al_2O_3, Fe_2O_3 and occasionally

CaO are the main chemical components present in fly ashes. The mineralogy of fly ashes is very diverse. The main phases encountered are a glass phase, together with quartz, mullite and the iron oxides hematite, magnetite and/or maghemite.

Two classes of fly ash are defined by ASTM C618 [42]: Class C and Class F. Class C are often high-calcium fly ashes with carbon content less than 2 wt.%; whereas, Class F are generally low-calcium fly ashes with carbon contents less than 5 wt.% but sometimes as high as 10%. In general, Class C ashes are produced from burning sub-bituminous or lignite coals and Class F ashes bituminous or anthracite coals. Performance properties between Class C and F ashes vary depending on the chemical and physical properties of the ash. Many Class C ashes, when exposed to water, react and become hard just like cement, but not Class F ashes. Most, if not all, Class F ashes will only react with the by-products formed when cement reacts with water. Even though the worldwide production of class C/F FA is actually increasing and anticipated to reach approximately 2000 million tons in 2020, only 45% is valorized for different purposes including as a supplementary cementitious material (SCM), while the remaining 55% is disposed of in landfills [43].

This work focuses on class F fly ash. The use of class F FA as an aluminosilicate precursor for geopolymerization has been studied extensively over the last few decades, with a large number of publications revealing the suitability of these binders as cement alternatives in the field of construction materials [13,14]. It has been shown that the intrinsic characteristics of the FA, particularly particle size distribution, morphology, amorphous fraction and oxide composition [22-28,44], the mix design, including type and dosage of activators [45,46], and reaction conditions (i.e., temperature, humidity, curing regime and duration) [47,48] can influence the final properties of the geopolymer product. Moreover, certain formulations of FA based geopolymers have good thermal stability upon firing at 800 - 1200 °C [49], are resistant to acid attack and the alkali-silica reaction (ASR) [50] and assist in preventing corrosion of steel reinforcement [51,52]. In addition to the use of FA based geopolymer binders in the construction sector, FA represents a promising material for a range of other applications such as soil amelioration, ceramics, catalysts, and in zeolite synthesis [53-55].

a) b)

Figure. 2.9 A Basin electric coal power station cooperative in USA (a); fly ash powder (b) [56].

2.4.3.1 Fly ash for geopolymerization: atomic structure characterization methods

Given the broad range of promising applications for FA, it is important to have a detailed understanding of the chemistry, physical attributes and associated variability in properties for this underutilized industrial by-product. The composition and properties of FA are linked to the physical and chemical properties of the coal rank combined with the attributes of the combustion process [53,54]. Furthermore, it is well accepted that chemical variability may also be found in FA sourced from the same coal power plant [22,26].

For the use of industry by-products in geopolymers, particle size distribution, chemical composition and crystalline structures/glassy phases of the precursor material are key factors that must be understood, as this information controls the precursor reactivity and solubility in an alkaline solution [22-28]. Particle size distribution, morphology and chemical composition, which are relatively easy to detect via traditional characterization methods (i.e., laser granulometry, optical microscopy, scanning electron microscopy-energy dispersive X-ray spectroscopy (SEM-EDS), inductively coupled plasma-optical emission spectrometry (ICP-OES), X-ray fluorescence (XRF)) reveals in most cases similar properties for different FA sources, even though these different sources are seen to result in geopolymer products with vastly different performance characteristics [25,27]. Conversely, characterization and quantification of glassy phases and their relevant modification after geopolymerization, which is challenging due to the disordered nature of these phases at the atomic length scale, can lead to determination of crucial differences in the atomic structures. Magic-angle-spinning nuclear magnetic

resonance (MAS NMR) performed on FA usually reveals resonances between - 80 and - 108 ppm [28], which are associated to the glassy phases and poorly ordered crystalline structure, however this technique is mostly used to monitor the structural reorganization of the gel after geopolymerization. In fact, peak identification remains somewhat controversial in the literature, where a single resonance can be attributed to crystalline or disordered phases (albeit with possible differences in the full-width half-maximum of these peaks), and chemical shifts are influenced by the multiple possibilities that exist for bonding environments involving non-bridging oxygens [57]. Other limitations include the presence of overlapped peaks, where deconvolution is carried out using the assumption of Gaussian line shapes together with the minimum possible number of components (Gaussians) for an accurate description of the given spectrum [57].

Other quantitative methods used in the literature are devitrification [25,58] and the Arjuan's dissolution method [28,59]. The first consists of performing thermal treatment on the FA over a range of temperatures and residence times followed by analysis of the crystalline materials which formed during thermal treatment using X-ray diffractometry (XRD). Although this technique detects differences in terms of glass separation (i.e., the formation of glassy SiO_2 or $Al_6Si_2O_{13}$) [25], the crystallization temperature of some phases may coincide with the formation of small amounts of other phases so that an unambiguous separation is not obtainable. The dissolution method consists of dissolving glassy phases in 1% HF acid (wt.%) and subtracting the residual mass from the initial [28,59], which clearly does not allow for identification of any qualitative information on the dissolved glassy composition. Other investigations include a synergy of XRD, SEM-EDS and multispectral image analysis (MISA) [23,24], where individual images are mathematically linked to form a multispectral image suitable for detection and quantification of the individual phases. Even though the results from this method show promise in the detection of the various glassy components and are consistent with Rietveld quantitative X-ray diffraction analysis [60], they are based on a series of analytical assumptions and user-defined constraints, which can have an influence on the resulting images. Reciprocal space analysis (using X-ray or neutron scattering data) and subsequent Rietveld refinement [60] are excellent methods for identification and quantification of the crystalline phases in FA, and, through the use of XRF in combination with Rietveld analysis, quantitative information on the amorphous fraction in the FA can be obtained together with the average chemical composition of this

amorphous component. However, the main limitation of these methods is the fact that they do not reveal any information on the local atomic structure of the amorphous component, since amorphous structural information is manifested as a relatively featureless diffuse peak in reciprocal space data [61].

2.4.3.2 Atomic structural characterization of amorphous phases in fly ash: the PDF technique

The aforementioned methods give a comprehensive quantitative/qualitative description of crystalline structure and microstructure of FA, however, the major limitation of these methods is the lack of information on the local atomic structure of the amorphous phases. This information is crucial as it is largely responsible for the reactivity of the FA during the alkali-activation reaction, and therefore contributes to the physical properties of the resulting geopolymer binder. On the other hand, X-ray and neutron total scattering and subsequent pair distribution function (PDF) analysis is ideally suited for analyzing amorphous and nanocrystalline materials, since diffuse scattering arising from disordered phases gives rise to distinct atom-atom correlations in real space [62]. Analyses carried out using the PDF technique include the study of synthetic calcium-silicate-hydrate (C-S-H) gels in conventional cement [63,64], and the analysis of the carbonation reaction in this gel [65]. The latter investigation (carbonation of C-S-H gel) revealed how the use of real space scattering data (PDFs) enabled for a more accurate determination of the various phases (crystalline and disordered) that are present throughout the carbonation reaction [65].

Previous investigations have centered on using PDF analysis to study the local atomic structure of metakaolin and metakaolin based geopolymers, since this aluminosilicate precursor is often used as a model system for class F fly ash [66-71]. PDF data on metakaolin-based geopolymers have been obtained using X-ray and neutron PDF analysis, including *in situ* experiments on the geopolymerization reaction over an extended time period (up to 128 days) [69]. These investigations have revealed the role free silica in the activator plays in the geopolymerization reaction (in silicate-activated metakaolin pastes), including the influence on reaction kinetics and the resulting sodium aluminosilicate (N-A-S-H) gel. Silica promotes metakaolin dissolution at early stages of the reaction but is seen to reduce the rate of reaction at later stages compared to hydroxide-activated metakaolin pastes, likely due to the enhanced precipitation of the gel

on the partially reacted particles, thus limiting further dissolution of the metakaolin particles [69]. PDF analyses of alkali-activated metakaolin-GGBFS and GGBFS pastes have highlighted the role of calcium in the evolution of nanostructure during the alkali-activation reaction. Specifically, for GGBFS based pastes more significant changes were observed in the local atomic structure of hydroxide-activated systems compared to silicate-activated over the initial 10 hours of formation [72]. An overview of the research centering on the nanostructural characterization of metakaolin based geopolymers and alkali-activated GGBFS pastes using synchrotron beam-line techniques is reported by Provis et al. [62], while Meral et al. [68] analyzed a range of supplementary cementitious materials using PDF analysis including silica fume, class F FA and metakaolin. In the aforementioned paper only one type of class F FA was analyzed by X-ray PDF analysis and, prior to measurement, the sample was processed to isolate the glassy phase by density difference of the constituents [73].

The evidence in the need of a specific analysis in this field for this type of precursor led to specific analyses which results will be collected in the following Subchapters and reported in a scientific paper [74].

2.4.4 Other precursors

Research performed on geopolymers so far has been primarily using the aforementioned precursors, including mixtures of slag-FA, FA-metakaolin, slag-metakaolin, etc. [21] but recent studied have greatly widened the sources and types of precursors which can be used. Among them it is possible to find [75]:

- silico-manganese (SiMn) slag: a discharge from the smelting of silicomanganese, lower in calcium content compared to GGBFS and containing a significant amount (> 10 wt.%) of manganese within the glassy phase;
- coal gangue: mineral waste discharged during coal excavation and washing mainly consisting in kaolin, quartz and feldspar;
- red mug: waste generated during alumina extraction of bauxite ores mainly consisting of SiO_2, Al_2O_3 and Fe_2O_3 as well as mineral phases of quartz, zeolites containing sodium and calcium, clays, hematite and others;

- mine tailings: which remain after vanadium extraction from the coal and consist of quartz, feldspar, zeolites and sodium silicate;
- catalyst residues: an agglomeration of zeolite crystals held together by an aluminosilicate matrix including amorphous silica and clays;
- coal bottom ash: by-product of coal combustion, which is collected at the bottom of furnaces that burn coal for the generation of steam, the production of electric power or both. Grain size in this case is coarser, spanning from fine sand to gravel;
- rice husk ash: waste generated through burning rice husk for the generation of electricity. The main component is silica (> 90 - 95 wt.%) in amorphous/partially crystalline phases with residual carbon as impurity and other trace elements such as K and Ca;
- palm oil fuel ash: by-product of the palm oil industry;
- waste glass: from consumer utilization and industrial process;
- waste ceramics: by demolition of masonry buildings and by-product of porcelain
- paper sludge ash: residual waste stream produced from pulp production and paper mill operation which combustion can generate an ash with high reactive aluminosilicate components with good pozzolanic properties;
- sludges resulting from water treatment: mainly composed of smectite clays such as montmorillonite;
- natural minerals: such as albite, volcanic ashes, pumice-type ashes, natural pozzolans.

2.5 Alkaline activators

To initiate the geopolymerization reaction a chemical activator and a high pH is needed in order to dissolve a certain quantity of silicon and aluminum and to hydrolyze the surfaces of the particles of the raw materials. Various different types of solutions have been used as activators in geopolymer synthesis, alone or in combination, such as NaOH, KOH, Na_2SiO_3, $Ca(OH)_2$, and others.

In general, geopolymers are obtained through the use of an alkaline medium, however, they differ in terms of the raw materials, the types and concentrations of the activators, the kinetics of the reactions, the chemical reactions and, primarily, in terms of

the structural arrangement of the chains that make up the matrix (N-A-S-H has a three-dimensional structure and C-A-S-H has a linear structure) [76]. Depending on the precursor materials and the alkaline activators used, both N-A-S-H and C-A-S-H gels can be present in the same alkali-activated matrix [44,77].

The most used alkali activators are a mixture of sodium or potassium hydroxide (NaOH, KOH) with sodium waterglass ($n SiO_2Na_2O$) or potassium waterglass ($n SiO_2K_2O$). The alkali activators play a crucial role in the polymerization reaction, behaving more swiftly when soluble silica is present, leading to a reaction product with more Si and higher mechanical strength [21]. Among activators, sodium based solutions are the less expensive but the potassium based ones display more favourable phase behaviour and rheology. Alternative activating solutions include carbonates, aluminates and even water, but none of these have seen a widespread use in the synthesis of aluminosilicate geopolymers up to date.

In the following Subchapters sodium hydroxide and sodium silicate, which were used as activating solutions in this work, are described. The combination between those two activators have been reported as effective in literature, with waterglass enhancing the polymerization process of the ionic species present in the system [45]. Nevertheless, it was also emphasized that an activating solution made of NaOH + waterglass must be optimized in terms of defining not only the SiO_2/Na_2O ratio but also the total amount of Na_2O and SiO_2 in the solution, respecting the thresholds of $Na_2O > 7$ wt.% and $SiO_2 > 1$ wt.%, above or below which mechanical strength development is delayed. The equilibrium between NaOH and waterglass in the solution in fact maintains the system with a high pH and a high level of soluble Si^{4+} in the process [45].

2.5.1 Sodium hydroxide

Sodium hydroxide (NaOH), commercially known as caustic soda, is a strong mineral base, solid at ambient temperatures in the form of drops or pellets (Figure. 2.10), which is also extremely hygroscopic and deliquescent. NaOH is highly soluble in water (1090 g/l) and its dissolution develops a significant amount of heat. Because of its strong basicity it is highly corrosive. NaOH is the most commonly used hydroxide in geopolymer synthesis, being both the cheapest and the most widely available of the alkali hydroxides.

In the geopolymerization process, NaOH is used in aqueous solution with a molar concentration which can vary between 5 and 15 M [78,79]. A work conducted by Rattanasak et al. [79] demonstrated the ability of sodium hydroxide to leach the particles of fly ash. The raw materials used in the aforementioned study were volcanic ashes with the following chemical composition: SiO_2 = 39.5 wt.%, Al_2O_3 = 19.5 wt.%, Fe_2O_3 = 14.1 wt.% and CaO = 17.3 wt.%, while alkaline activators used were sodium silicate and sodium hydroxide in different molar concentrations (5, 10, 15M). In this paper it was highlighted that the leaching effect was increased with increasing the molar concentration of NaOH, leading to the formation of geopolymer gel around the ash particles (Figure. 2.11). In addition, the geopolymer products with higher NaOH concentration showed higher compressive strength.

The study led to the conclusion that a higher amount of sodium hydroxide in contact with the precursor promotes the release of silica and alumina monomers with consequent improving of the geopolymerization process and increasing of mechanical performance. In a study by Ryu et al. [14] fly ash based geopolymers were activated by using different molar concentration of NaOH (6, 9, 12 M) highlighting an increase in compressive strength with the increase of activator concentration. Similar results were also obtained by Wang et al. [80], which attribute the effect to a higher degree of particle dissolution and consequent higher monomer condensation.

a) b)

Figure. 2.10 NaOH pellets (a); NaOH flakes (b).

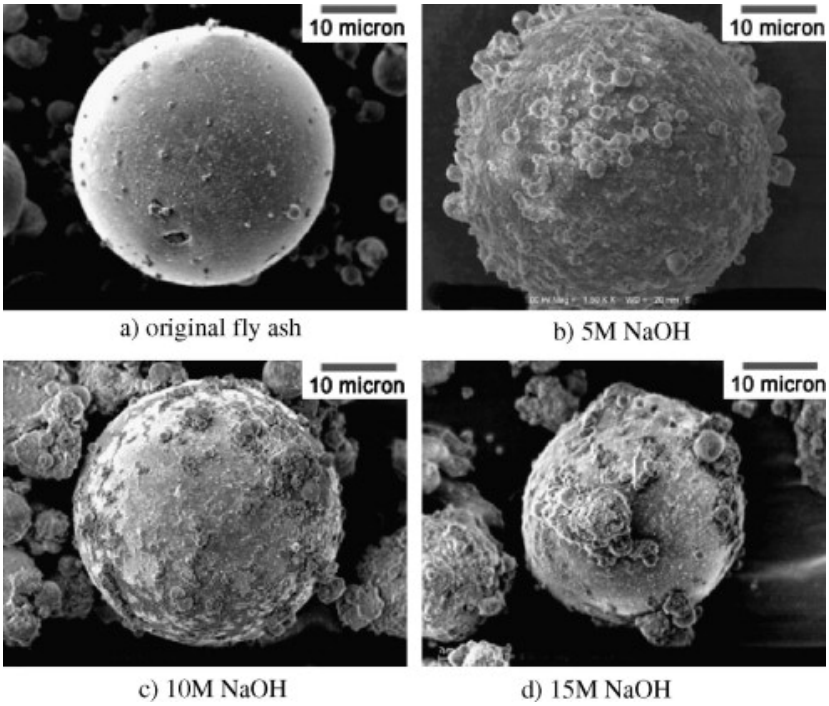

Figure. 2.11 SEM micrographs of fly ash particle in contact with different NaOH molar concentrations after 10 min [79].

2.5.2 Sodium silicate

Sodium silicate is the common name for compounds with the formula $Na_2(SiO_2)_nO$. A well-known member of this series is sodium metasilicate, Na_2SiO_3. In the liquid state (also called "soluble glass" or waterglass) is transparent and viscous and it is also available in solid form. In industry, the various grades of sodium silicate are characterized by their SiO_2:Na_2O weight ratio, which can vary between 2:1 and 3.75:1. Grades with this ratio below 2.85:1 are termed alkaline. Those with a higher SiO_2:Na_2O ratio are described as neutral. Sodium silicate is generally used in cements, passive fire protection, textile and lumber processing, refractories, and automobiles.

The use of sodium silicate as activator for geopolymers has been extensively reported and synthetized in a paper by Rashad et al. [81]. In general, it has been noticed that increasing the sodium concentration leads to an increase in the compressive and flexural strength of the samples but, on the other hand, may also cause some defects on some properties of geopolymer system, above all on shrinkage. Rashad et al. [81] activated slags with commercial liquid sodium silicate (silica modulus (SiO_2/Na_2O) of 1.7) with concentrations of 3.5%, 5.5%, 6.5% and 10.5% of Na_2O, by slag weight. They noted an increase in compressive strength and a reduction of the apparent porosity and un-hydrated

particles while increasing the activator amount (Figure. 2.12). Neto et al. [82] activated slag mortars with sodium silicate at concentrations of 2.5%, 3.5% and 4.5% of Na_2O, by weight. They reported that an increase in activator amount caused an increase in the degree of hydration, which led to an increase in gel volume and accordingly, a reduction in porosity. Allahverdi et al. [83] activated slag pastes with alkaline activator at concentrations ranging from 1% to 6% of Na_2O, by weight. They found an increase in the workability and compressive strength with increasing Na_2O concentration but also the increase of drying and autogenous shrinkage. Chi [84] activated slag concretes with liquid sodium silicate at concentrations of 4%, 5% and 6% of Na_2O, by weight. The results showed an increase in the compressive strength and splitting tensile strength with increasing activator concentration. Acevedo-Martinez et al. [85] reported that the compressive strength of alkali-activated slag mortars activated with waterglass at different concentrations of 4%, 6% and 10% of Na_2O increased with increasing Na_2O concentration. Yang et al. [86] reported that the higher the Na_2O to source material ratio, the better the compressive strength development at long-term age. Cincotto et al. [87] reported that the porosity decreased with increasing Na_2O concentration but autogenous shrinkage was more evident.

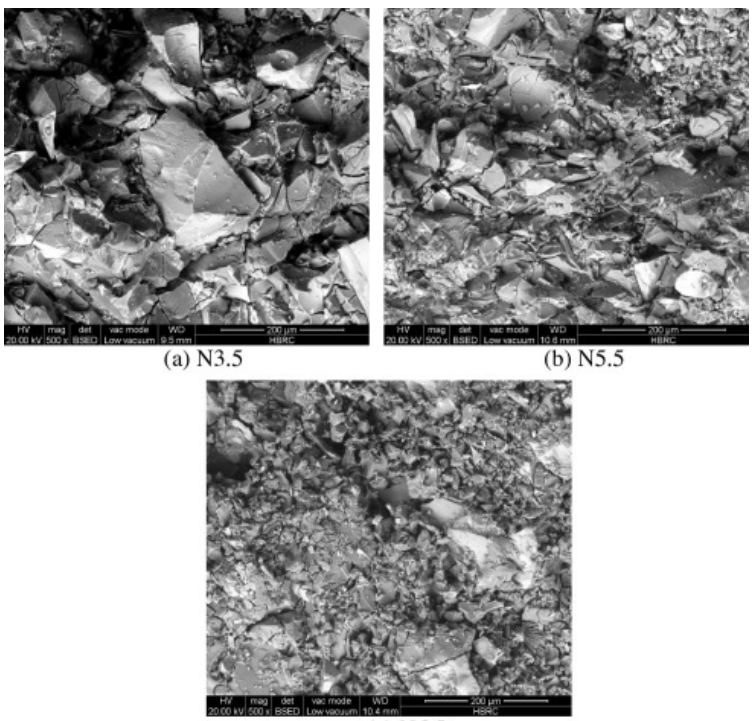

Figure. 2.12 SEM micrographs of fracture of Na_2O = 3.5% (a), Na_2O = 5.5 (b) and Na_2O = 6.5 (c) pastes after 28 days of hydration [81].

2.6 Additives and fillers

Additives and fillers are commonly used in geopolymers in order to optimize the functionality, improve the mechanical performance and avoid the dimensional shrinkage due to elimination of the not chemically bonded water. Additives and fillers can be chosen to optimize specific thermo-mechanical properties and/or chemical-physical properties, depending on their shape and on their chemical nature. Shape is of fundamental importance in relation to the mechanical behaviour of the material and particularly fiber-reinforced composites allow improving the general performances of the material. The most often used filler is silica sand containing quartz while, among fibers, the most widespread are glass and carbon fibers. The choice of the additive nature (metal, ceramic, plastic, in the form of powder, grains, short/long fibers, fabrics, etc.) allows optimizing specific physical or mechanical properties, depending on the application. One of the most important characteristics for additives and fillers is that they must be inert and thermally compatible with the geopolymer matrix, in order to avoid any heat stress during the process. Geopolymer technology allows the production of a wide range of composite materials for high-tech applications in various industrial sectors, such as civil engineering, industrial waste treatment, automotive industry and aerospace, foundries, plastics industries, etc. [10,88].

2.7 Process parameters

Many parameters can affect the final properties of geopolymers, among which the most important are: the reactivity of the precursors [22,26], the alkali concentrations and the molar ratios chosen for the activation [44-46], the curing temperature and conditions [89-92]. A high variability in results has been found by changing one or more of these parameters, thus specific experiments are needed to give indications on how they contribute in modifying the microstructure.

In this work the main process parameters chosen were the Na_2O/SiO_2 molar ratio in the formulations and the curing, which was at ambient temperature and laboratory conditions (T = 25 °C, R.H. = 35% or R.H. = 65%). Additional experiments were performed on sealed samples cured at ambient temperature (T = 25 °C) and in oven at 50 °C and 70 °C for the first 24 hours.

2.7.1 The role of Na_2O/SiO_2 molar ratio for fly ash based geopolymers

Several studies have been highlighting the Na_2O/SiO_2 molar ratio as one of the key factors affecting the properties of geopolymers [14,93-96]. In general, it has been outlined that a high Na_2O/SiO_2 molar ratio promotes high levels of geopolymerization. Similar findings have been demonstrated in the case of fly ash geopolymerization at elevated temperatures without the addition of sodium silicate solution [93] and for metakaolin geopolymerization at room temperature without addition of sodium hydroxide [95].

However, a work on the alkali-activation at room temperature of volcanic ashes [94] reports that compressive strength of geopolymers increases with the decreasing of Na_2O/SiO_2 molar ratio. Indeed, the chemical composition, the content and distribution of amorphous phases, the fineness of the precursor as well as the activating temperature are all key parameters in influencing the extent of the geopolymerisation process.

Soluble silicate concentration has been found to significantly alter the dissolution and precipitation characteristics of fly ash at pH 13.95 and 20 °C [96]. For low soluble silicate content ($Na_2O/SiO_2 > 8.4$) in the activating solutions, fly ash dissolution is inhibited by the formation of secondary precipitates on the fly ash particles surface, whereas for high amounts of soluble silicate ($Na_2O/SiO_2 < 3$) an evident dissolution of Al, Si and Ca atoms has been determined, followed by the subsequent precipitation of gel phases.

2.7.2 The curing process

Focusing on curing conditions and temperature, the majority of the works made on geopolymers have highlighted how sealed and high temperature cured samples result in more durable and higher mechanical strength products.

In a study conducted by Maria Izqueirdo et el. [89] it is evident that, whatever the FA composition is, geopolymerization in a sealed environment results in higher mechanical strength products with higher leaching resistance compared to an open air curing. It is also reported that, compared to a temperature controlled process, open air cured samples are subject to shrinkage, cracking and manifest greater porosity, thus being significantly vulnerable in terms of durability.

Wallah et al. [90] compared geopolymer mortars and concretes obtained by the activation of three different types of FA cured at room temperature and 60 °C for the first 24 hours. It was found that geopolymers cured at 60 °C for the first 24 hours do not show a substantial increase of compressive strength whereas an increase was found for room temperature samples. Moreover, mechanical resistance after 7 days of curing was found to be linked to the average temperature of the environment in which they were stored: samples maintained in warmer environments developed higher mechanical resistance than those cured in relatively colder environments. Shrinkage, in case of room temperature curing, was found to be up to 10 times superiors than in the case of curing at higher temperatures. In addition, mass loss due to acid attack for 60 °C cured samples was found to be 3% lower compared to the others.

In a study conducted by Atiş et al. [91] very high strength FA based geopolymer mortars were produced by heating samples for 24 hours after casting at 115 °C and Adam et al. [92] reached optimum values for FA based samples cured at 120 °C for 20 hours.

As such heat treatments could be considered a drawback in terms of feasibility for a new construction material, it is important to consider which are the real benefit it can produce, in improving physical and microstructural properties depending on the precursor type and relevant activation system and to optimize results in the case of room temperature (RT) activation.

Only a few studies have focused so far on RT activation [97,98] and also the effect of open and closed curing conditions on the properties of the final product has been scarcely studied [89]. The aim of this study was to firstly analyze the behaviour of not sealed fly ash geopolymer samples at RT reproducing the conditions often adopted at the construction sites. Additional experiments were also made in order to compare the results with sealed samples and oven cured samples (50 °C and 70 °C for the first 24 hours).

2.8 Applications

A key attribute of geopolymer technology is the robustness and versatility of the manufacturing process, which enable products to be tailor-made from a range of diverse aluminosilicate raw materials so that they can achieve specific properties for a given application at a competitive cost. Applications of particular interest up to date include low

or high strength concretes with good resistance to chloride penetration, fire and/or acid resistant coatings, and waste immobilization solutions for the chemical and nuclear industries [99].

Despite these key technological attributes, and environmental and cost savings compared to OPC, a large-scale production of geopolymer products is still not available. This is mostly probably due to the low profit margins and high financial risk involved with the introduction of a new technology in the construction industry, so that the majority of the works include scientific literature exploring the properties and potentialities of geopolymeric materials on the laboratory scale. However there is a growing understanding of the real world-scale capabilities of the technologies being developed through plant trials and commercial rollouts, most of which are naturally protected by confidentiality agreements [99].

The most important characteristics, which have been detected so far and which clearly show big potentialities for geopolymers, are synthetized in the work of Duxson et al. [99] as follows:

- high compressive strength gain;
- good abrasion resistance, particularly when mixed with fillers;
- rapid controllable setting and hardening;
- fire resistance (up to 1000 °C) and no emission of toxic fumes when heated;
- high level of resistance to a range of different acids and salt solutions;
- not subject to deleterious alkali-aggregate reactions;
- low shrinkage and low thermal conductivity;
- adhesion to fresh and old concrete substrates, steel, glass, ceramics;
- high surface definition that replicates mould patterns;
- inherent protection of steel reinforcing due to high residual pH and low chloride diffusion rates.

It is important to note that not all geopolymer products possess all of these properties, as there is no single formulation and recipes have to be tailored to achieve required specifications at a minimum cost. Particularly in the case of geopolymers, as already mentioned in this dissertation, an imperative key factor to tailor the final product to attain and optimize combinations of the above properties is the knowledge and understanding of

raw material reactivity and chemistry. Metakaolin has already been described as a "model system" for geopolymers, due to its pure structure, so some properties are best achieved by the use of this precursor compared to by-products. On the other hand the cost of this precursors compared to others limits the use for specific niche applications, even tough it may still represent a big advantage in specific contexts as high tech ceramics.

Geopolymers can also be used as matrices for composite materials and for high temperature applications, fireproof or refractory insulating walls or panels. In addition, when reinforced with carbon fibers, geopolymers, made in the form of flexible sheets, can represent a valid alternative for the repair of damaged concrete or masonry structures. Within the construction industry, the use of geopolymers has already been successfully tested on pipes for drainage, prefabricated facade, prefabricated beams and columns.

Davidovits [6] ranked the field of application of geopolymers according to the Si/Al ratio as shown in Table. 2.2. Low Si/Al ratio favors a very rigid three-dimensional lattice while higher ratios are characterized by a polymeric behaviour.

Si/Al	Applications
1	Masonry, ceramic, fire resistant elements
2	Cements and concrete
3	Aluminum foundry application, fiber reinforced elements
> 3	Geopolymers for industrial applications, adhesives
20 - 35	Reinforced composites

Table. 2.2 Possible applications of geopolymers based on their Si/Al ratio by Davidovits [6].

The commercial uptake of geopolymer technology therefore provides the opportunity to create value in a large number of disparate markets, from construction to aerospace, using essentially the same technology. These different markets have vastly different needs: some may utilize bulk amounts of coal ash to form a variety of value-added products, whereas others involve production of inexpensive ceramic-like materials from purer precursor materials [99]. This is not to say, however, that geopolymer technology is the most suitable or most competitive technology available for all of the applications noted above. Along with traditional OPC systems, other new or alternative cementing systems will continue to be utilized in the market where most applicable, and often in hybrid or blended products. In blended systems, knowledge of the chemistry and science of each component, as well as their interactions with each other, is vital [99].

Fly ash based geopolymerisation has only become the subject of intense research interest within the past decade, however there are currently a number of well-established academic and industrial research centers worldwide that are investing significantly in developments in this field. While development of products is not difficult to achieve on a laboratory scale simply by empirical mix formulation, the ability to understand and control the setting process and repeatability using variable material sources have always proven to be issues in large-scale production. These issues have been the primary industrial research focus, although the nature of the work is largely outside of the public domain [99].

Significant academic knowledge has also been generated in this vein, including extensive studies on developments of different characterization techniques, the effects of different chemical additives and/or contaminants, and the influence of curing conditions (humidity, time and temperature). Production of geopolymer concrete on a full manufacturing scale can now be achieved for high-strength ready-mix concrete, which represents the successful implementation of a technically very challenging product [99].

2.9 Durability

An area in which significant research has still to be conducted is the study of the durability of geopolymers. In fact, most previous studies have focused on the process of alkali-activation itself and on the physical-mechanical properties of geopolymers with less emphasis on the durability aspects. This is also due to the lack of standards and durability tests for this relatively new material class, for which standard durability test for OPC are actually used. More than any other technological aspect or engineering property, durability is the factor that overrides all other technological drivers in determining the success or failure of geopolymer technology in the construction industry. At this point in time, and given the relatively short history of geopolymer research, all that can be stated is that preliminary accelerated testing shows very promising results indeed, and that work is intensively ongoing. In this section the most recent relevant results in terms of durability, listed by Pacheco-Torgal et al. [50] and Provis et al. [75] are synthetically reported.

2.9.1 Acid attack

One of the main properties of geopolymers is their relatively high resistance to acid media such as nitric, sulphuric or hydrochloric acids, especially when compared to traditional Portland cement mortars or concrete. In this latter case the dissolution of $Ca(OH)_2$ and calcium sulfoaluminates leaves a very porous corroded surface. Conversely, the low CaO/SiO_2 ratio present in the (N,C)-A-S-H in geopolymer binders leaves a coherent layer that, even after decalcification, hinders the ingress of other aggressive media [75].

Corroded depth and mass loss are often used to characterize the acid induced degradation of cements and concretes [75]. Lloyd et al. [100] found that the corroded depth was a more sensitive measurement of the progress of attack on AAMs than change in mass, because acid attack on N-A-S-H gels leads to the formation of an apparently intact, but porous and low-strength, reaction product layer on the sample surface, rather than actual dissolution of the binder. The corroded depth and the vulnerability to acids were also shown to change depending on the formulation. For example, in Figure. 2.13 it is possible to see the appearance of the corroded layers on geopolymer samples containing different amounts (7% and 15%) of Na_2O in the formulation after 28 days exposure to pH 1.0 sulphuric acid [100].

Shi and Stegemann [101] found that the corroded depth of alkali-activated slag paste was about 1.3 mm, compared to 2.5 mm for Portland cement paste after 580 days of immersion in pH 3 nitric acid solutions, and its resistance to corrosion in HCl and H_2SO_4 was also higher than that of Portland cement paste [101]. However, the dealumination of N-A-S-H gel has been identified in HCl solution, along with the destruction of the zeolites formed in alkali-activated fly ash binders, independent of the type of activator used [102].

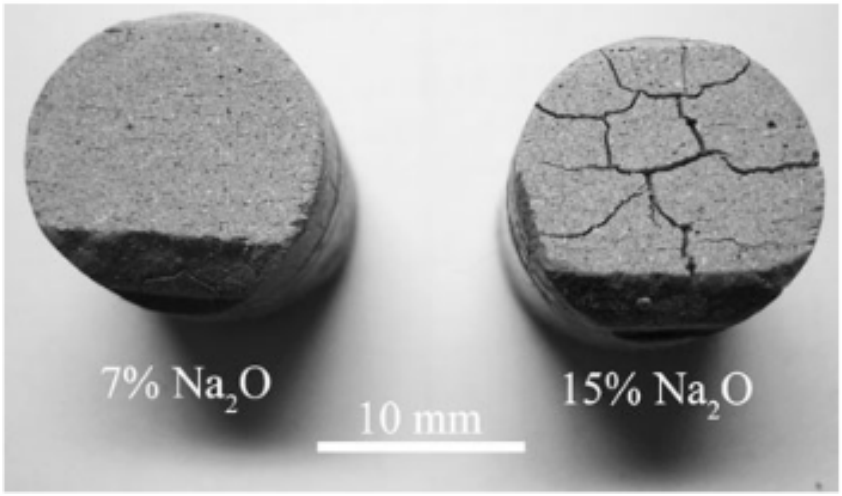

Figure. 2.13 The appearance of the corroded layers on geopolymer samples containing 7% Na_2O (left) and 15% Na_2O (right) after 28 days exposure to pH 1.0 sulphuric acid [100].

2.9.2 Sulfate attack

Even in the case of sulfate, due to differences in phase chemistry of the hydration products for geopolymers compared to OPC, the attack mechanisms are notably different. Deterioration of concrete is attributed to the expansive reactions of calcium-rich cement hydration products, with sulfates producing internal stress and a subsequent expansive disruption of the matrix. In the case of AAMs, their sulfate resistance has been shown to be superior to regular and even sulfate-resistant Portland cement. This aspect is because Na_2SO_4 can actually be used as an activator in favoring the structural evolution of the binding phases and densification of the system [5].

However, when AAMs containing any significant level of calcium are immersed in $MgSO_4$ solutions, significant loss of compressive strength occurs due to decalcification of the C-A-S-H, and gypsum and/or ettringite can be formed (Figure. 2.14) [103,104].

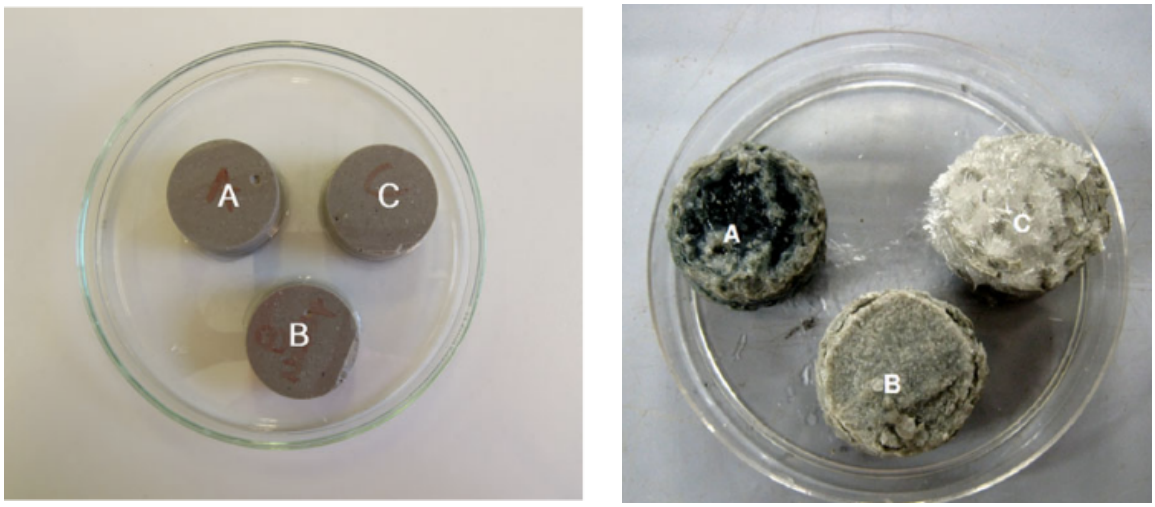

a) b)

Figure. 2.14 Physical conditions of geopolymer samples: A = w/b 0.40; B = w/b 0.50 and C = w/b 0.60, after immersion in Na_2SO_4 (a) and $MgSO_4$ (b) for 90 days [104].

2.9.3 Alkali-aggregate reaction

AAMs usually contain a very high content of alkalis, meaning that potential alkali-aggregate reactions (AAR) become a concern in infrastructure applications. Many researchers have confirmed that AAR does in fact happen in alkali-activated slag based materials [105,106], with significant amounts of AAR reaction product observable (Figure. 2.15). However the expansion was in almost all cases smaller than that of conventional Portland cement based materials tested in parallel. Even in this case, the calcium plays an essential role in the expansive nature of the reaction so when fly ash or metakaolin are used as precursors, the expansion of the specimens have been shown to decrease or become very small or negligible [50,75].

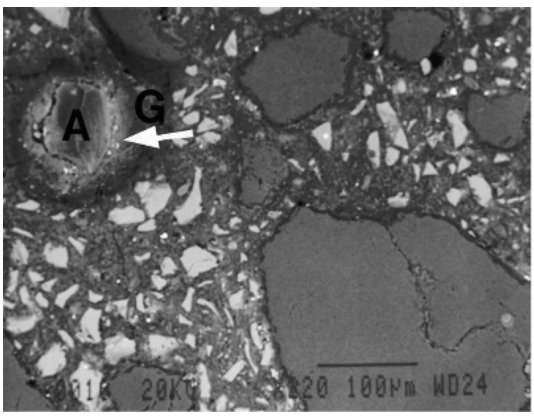

Figure. 2.15 Backscattered electron imaging of the interior region of AAS concrete with the reactive aggregates after 10 months from the start of experiment. A, Reactive aggregate; G, alkali ± silica gel [106].

2.9.4 Resistance to freeze-thaw

With respect to the behaviour of geopolymers to freeze-taw deterioration, the available results are contradictory, even though the majority of the works show positive results. Skvara [107] indicates a very high resistance for fly ash based samples activated by sodium silicate, even though after 150 cycles the strength values dropped to about 70% of the strength measured in unexposed samples held at ambient temperature for the same period of time. According to Yunsheng and Wei [108] alkali-activated fly ash can stand more than two times freeze-taw cycles compared to same compressive strength Portland cement samples and other positive results in this sense were reported also in the case of slag based samples [109]. On the contrary, Puertas et al. [110] observed a worst behaviour for fly ash based samples activated by NaOH compared to Portland cement-based samples when both materials are exposed to 50 freezing/thawing cycles. It is probable that the discrepancy is related to a difference in the microstructure of the two studied materials, as pore size and distribution have a significant influence in the resistance to frost.

2.9.5 Resistance to high temperature and to fire

As already mentioned, one of the main property of geopolymers is their high thermal resistance, even without any thermal pretreatment. In fact, traditional refractory materials needs elevated temperature to achieve their thermal resistance (from 1200 °C up to 1600 to 1700 °C) and, as in the case of high temperature resistance cements, even in the case they are no thermally pretreated, their main component is aluminous cement, which is a type of quick-hardening cement having a high alumina content and processed between 1550 °C and 1600 °C.

For applications between 1000 - 1200 °C, silica based geopolymers show good results, both in terms of cost and in terms of performances with the possibility to obtain medium/low fire resistant refractory structures at lower or comparable costs than those of Portland cement building structures, which decompose at temperature > 400 - 500 °C [111]. Geopolymers with high thermal resistance (up to 1600 to 1700 °C) can be identified in the alumino-phosphate type. These geopolymers however, unlike those described above, need to be processed at 300 - 400 °C before achieving their properties

and have as limitation that they are strongly acid, which precludes their use in basic environments. Substantially with an appropriate assessment of the advantages and disadvantages, geopolymers for refractory use may claim many points in medium/low temperature applications.

Numerous studies [49,112,113] have been conducted in the last years in the field of geopolymers based on fly ash exposed to high temperatures, in order to investigate their potential application in the field of refractory materials and/or fire resistant materials.

Bakharev [49] analyzed the thermal stability of geopolymers prepared using two types of class F fly ash (fly ash type 1, composition by weight: SiO_2 = 50.0%, Al_2O_3 = 33.0%, Fe_2O_3 = 12.0%, and CaO = 6.5%; fly ash type 2, composition by weight: SiO_2 = 61.4%, Al_2O_3 = 28.0%, Fe_2O_3 = 1.1% and CaO = 0.6%) activated with alkaline solutions containing sodium or potassium. The purpose of the work was to verify their use in the field of refractories. Samples were subjected to a temperature of 800 ° C, 1000 ° C and 1200 ° C. Results have shown significant differences depending on the activator type and on the type of fly ash used. Concerning the activator, higher thermal resistance was achieved by samples activated with potassium compared to sodium, which tend to develop shrinkage cracking and deterioration of strength connected to a dramatic increase of pore size after calcining. Regarding the precursor, samples prepared with fly ash type 1, which developed a good mechanical strength (35 - 45 MPa) before exposure to high temperature, registered a strong loss of strength after exposure to 800 °C while fly ash type 2 samples (having more crystalline phases and therefore being less reactive) developed low mechanical strength immediately after the activation (2 MPa), but improved their resistance (up to 5 - 16 MPa) once exposed to 800 °C. Moreover, geopolymer activated by sodium were initially amorphous, while once exposed to the temperature of 800 °C, the formation of nepheline ($NaAlSiO_4$) and jadeite ($NaAlSi_2O_6$) was registered. The presence of these crystalline phases is responsible for the increase in porosity and deterioration of the mechanical strength.

Moreover, the significant presence of iron oxide (Fe_2O_3) in fly ash causes a degradation of the properties which was also observed by Rickard et al. [112]. In his study, performed on geopolymers obtained from the activation of class F fly ash (wt.% composition: SiO_2 = 51.6%, Al_2O_3 = 4.23%, Fe_2O_3 = 2.15% and CaO = 1.75%) several characterizations were carried out (through the use of dilatometry, TGA, DTA, XRD and

SEM) concluding that geopolymers obtained from fly ash containing high percentages of iron oxide and crystalline phases of silica at temperatures higher than 500 °C have variables thermal properties. The quartz was found to have only a minor influence on the thermal expansion as quartz impurity was not found to interact with the geopolymer matrix upon heating to 900 °C and did not influence the post heating morphology or phase composition. On the contrary, the iron oxides present in the fly ash (which was amorphous or short-range ordered) directly affected the thermal properties of the geopolymer by influencing the thermal expansion, altering the phase composition, and changing the morphology after heating due to its oxidation and transformation in hematite resulting in a variable thermal expansion at high temperatures. The temperature and exothermic nature of the hematite phase change were observed to be influenced by silicon and aluminum substitutions in the iron oxides as well as the oxidization state of the iron [112].

The work conducted by Kong et al. [113] presented the results on the effect of elevated temperature on geopolymer paste, mortar and concrete made using class F fly ash as precursor (composition by weight: SiO_2 = 48.8%, Al_2O_3 = 27.0%, Fe_2O_3 = 10.2% and CaO = 6.2%). The geopolymers were synthesized with sodium silicate and potassium hydroxide solutions. Various experimental parameters have been examined by the authors such as specimen sizing, aggregate sizing, aggregate type and superplasticizer type. The study identified specimen size and aggregate size as the two main factors governing geopolymer behaviour at elevated temperatures (800 °C). As for the size, a significant temperature difference between the surface and core of the specimen cross-section was observed to induce thermal cracking. Therefore, thermal incompatibility arising from thermal gradient was observed to be the reason for the size effects. As for aggregates, smaller sized aggregates (< 10 mm) were observed to promote spalling and extensive cracking in the geopolymer concrete while geopolymer concretes containing larger aggregates (> 10 mm) were more stable in elevated temperatures. Strength loss in geopolymer concrete at elevated temperatures was attributed in this case to the thermal mismatch between the geopolymer matrix and the aggregates [113].

Metakaolin generally seems to act better than other precursors, probably due to the lower degree of reaction and incomplete polymerization of the latter precursor compared to the purer one and to the presence of impurities (i.e., iron content), which lower the

melting temperature of the material. Krivenko and Guziy [114] found good resistance to fire for alkali-activated binders, suggesting an use for high fire risk buildings. Those results were confirmed by Pernà et al. [115]. Temuujin et al. [78] used geopolymers as steel coatings founding they maintained integrity after firing while Zhao et al. [116] showed that no spalling were observed after firing on alkali-activated concrete compared to OPC.

2.9.6 Efflorescences

The formation of efflorescences in alkali-activated materials is a pretty common problem and seems to be due to an excess of alkali in the formulations. In fact due to the weak bond between the sodium ions (Na^+) and the aluminosilicate structure, sodium tends to leach and create efflorescences in the form of carbonates. This phenomenon occurs primarily on ambient temperature cured samples, while samples cured at elevated temperature doesn't show evident signs of salts. This was explained by Temuujin [117] as due to an insufficient geopolymerization, and so the presence of leachate sodium, for RT cured samples. The tendency towards efflorescence in geopolymers is also due to the open microstructure of some materials, which have a lower extent of reaction, partly due to the high alkali concentration in the pore solution [118]. Van Deventer et al. [119] recognized that geopolymers suffer from severe efflorescence, which is originated by the fact that alkaline and/or soluble silicates that are added during processing cannot be totally consumed during geopolymerisation.

Some attempts have been made to reduce efflorescences by using potassium hydroxide instead of sodium hydroxide in the activator [120,121], because potassium is more strongly bound to the aluminosilicate gel framework, and also because potassium carbonate crystals are usually less visually evident than their sodium counterparts. Recent works include the addition of alumina-rich admixture (as calcium aluminate) and hydrothermal curing at temperatures of 65 °C or higher [122]. Photographs of specimens tformulation by varying the total Na/Al molar ratio (from 0.61 to 1.23) are reported in Figure. 2.16 [122].

However these results constitute a step back in the development of alkali-activated binders due to the limitations for on-site concrete placement operations due to the use of

specific curing.

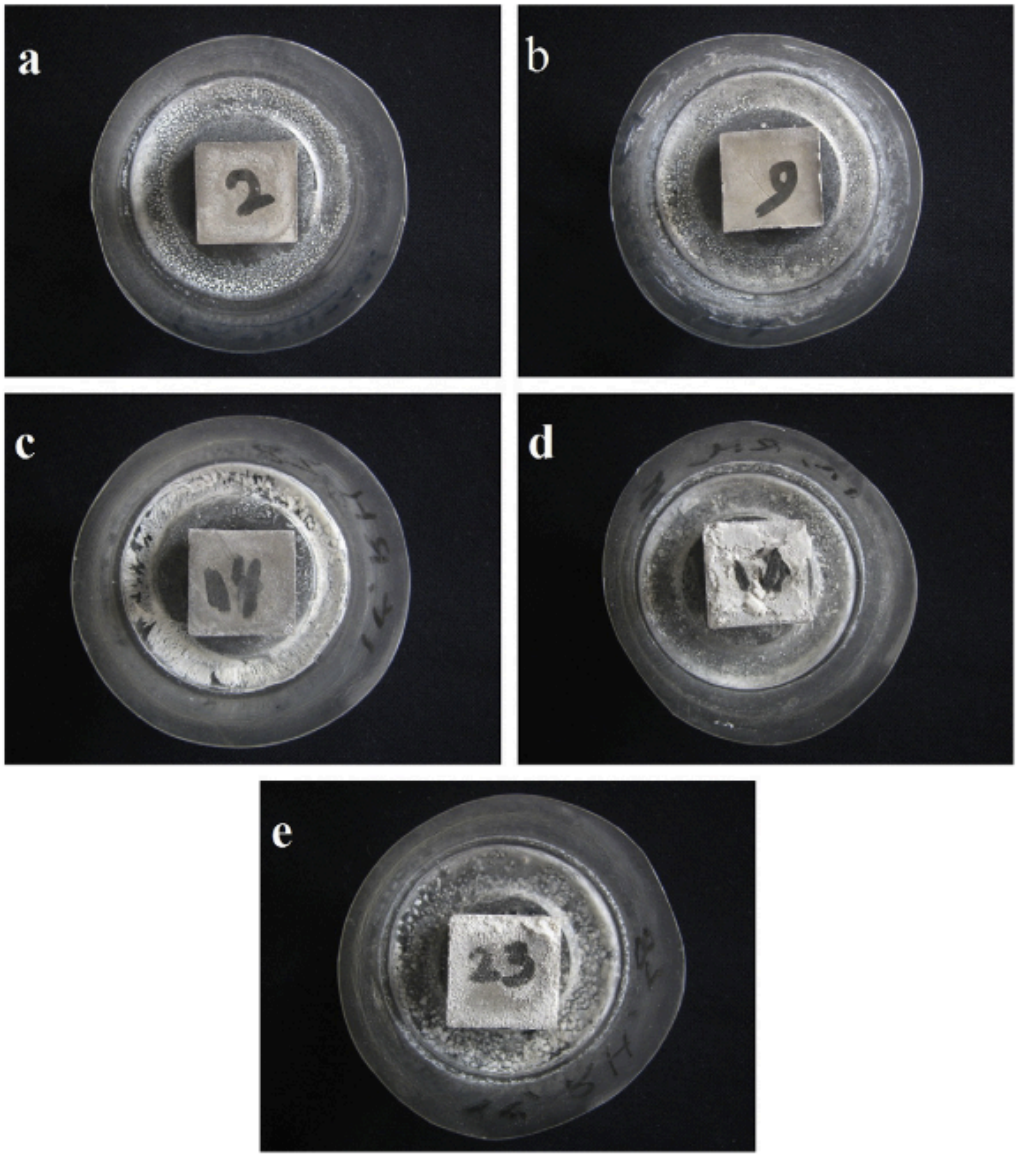

Figure. 2.16 Photographs of specimens tested qualitatively for their efflorescence extent, at the end of the test period (28 days), by varying the total Na/Al molar ratio: (a) = 0.61, (b) = 0.77 (c) = 0.97, (d) = 1.08, and (e) = 1.23. Efflorescence crystal deposits on the tops of the specimens and white rings surrounding the specimens correspond to leached alkali metal salts [122].

2.9.7 Carbonation

The carbonation of OPC mortar and concrete is a widely studied and reasonably well-understood phenomenon. Carbon dioxide from the atmosphere diffuses inside the material and dissolves in the pore water, forming carbonic acid. Carbonic acid may then

attack calcium-containing phases. Initially the calcium hydroxide (Ca(OH)), and then calcium silicate hydrates (C-S-H) and calcium aluminosilicate hydrates (C-A-S-H) are decalcified by reactions which extract their calcium to form calcium carbonate. $Ca(OH)_2$ in particular plays a buffering role by releasing hydroxide into the pore solution as the pH begins to decrease, but it will at some point become depleted and no longer able to maintain this buffering. This may lead, in the long-term, to a reduction in the alkalinity of the cementitious system accompanied by reduced mechanical performances and the corrosion of steel reinforcement due to depassivation [123].

Throughout CO_2 exposure of alkali-activated binders, the main reaction products are expected to be carbonates (in particular calcite and trona [124]) derived from the carbonation of alkaline pore solutions and C-A-S-H gels. Especially in the case of low-calcium precursors, carbonation involves the conversion of the alkali rich solution to carbonate or bicarbonate salts with little modification of the (C,N)-A-S-H gel [57]. This phenomenon can be influenced by the microstructure, which in its turn is influenced by the formulation (activator type, binder content, etc., as show in Figure. 2.17). The mechanisms of strength loss induced by carbonation of such materials still require further investigation.

Another factor, which is important to consider, is that carbonation is generally measured in Portland cement samples by accelerated methods that include relative humidity between 50 and 70% (high R.H. is a key determining factor for carbonation processes) and high CO_2 concentrations (1%) [125]. Those conditions, due to changes in alkali carbonate phase equilibria, have been shown to provide results which are unlikely to represent the behaviour of geopolymers under actual service conditions, so overestimating the real risk of carbonation. In fact, under natural CO_2 conditions, the excess alkalis present in the pore solution of an alkali-activated binder may potentially maintain the internal pH at a level that is sufficiently high to protect steel in a passive state [57,125]. Given that, the currently testing methods are excessively aggressive. However a relatively high degree of acceleration is required to make the slow natural carbonation processes observable on a laboratory time scale and further work has to be done in this field.

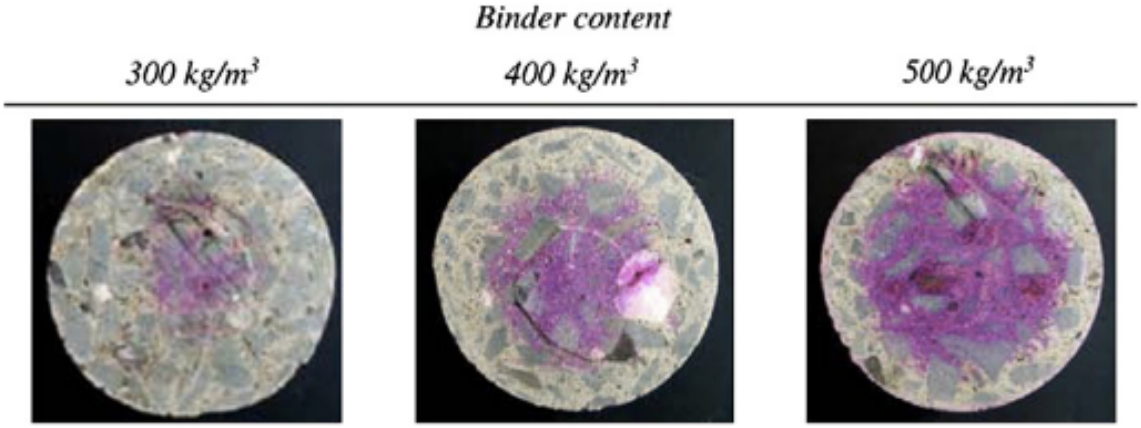

Figure. 2.17 Transverse sections of carbonated alkali-activated slag concretes after 1000 h of exposure to a 1% CO_2 environment, with the extent of carbonation revealed by a phenolphthalein indicator [123].

2.9.8 Chloride ingress and binding

Chloride ingress and binding in concrete are very important in defining the time taken to initiate corrosion of steel in reinforced concrete structures and elements [75]. Bernal et al. [98,126] studied the resistance of alkali-activated concretes to chloride permeability by rapid chloride permeability test (RCPT) and direct diffusion tests, and found that the correlations between the chloride diffusion coefficient resulting from the two methods were weak, which further reveals the limitations of the RCPT in analysis of alkali-activated concretes. It seems that the nature of the alkali-activated gel hydration products strongly influences chloride ionic transport [126], but a full description of these processes has not yet been published. In high-Ca alkali-activated systems, the C-A-S-H reduces porosity, while in low-Ca systems the N-A-S-H, which is more porous, appears to contribute significantly to higher chloride binding [98]. The pore solution chemistry becomes dominant for chloride penetration as for all the aforementioned durability aspects.

2.9.9 Corrosion of steel reinforcements

Reinforced concrete (RC) is the most commonly used construction material worldwide, but several problems can affect its matrix, in terms of durability and even sustainability. As far as durability is concerned, the main factors that cause deterioration of RC are mostly linked to corrosion of the reinforcements, with consequent fatal decrease in terms of construction service life, loading capacities and seismic resistance, so

that preventing corrosion is one of the most important goals to avoid RC deterioration. Normally, pH of the pore electrolyte in OPC is strongly alkaline due to the high alkalinity of calcium hydroxide (around 13 or even higher), aiding the formation of a passive film, which can prevent corrosion. This film can be damaged due to chloride attack [127-129] or due to carbonation, which causes a reduction of the pH of the pore electrolyte and undermines the stability of the passive film [130]. The binder plays a fundamental role in preventing or accelerating chloride penetration and concrete carbonation, because it affects the nature of the binder hydration products and the concrete porous microstructure. The steel corrosion occurs due to an electrochemical action, when metals of different nature are in electrical contact in the presence of water and oxygen. The process consists in the anodic dissolution of iron when the positively charged iron ions pass into the solution and the excess of negatively charged electrons goes to steel through the cathode, where they are absorbed by the electrolyte constituents to form hydroxyl ions. These in turn combine with the iron ions to form ferric hydroxide, which then converts to rust. The volume increase associated with the formation of the corrosion products leads to cracking and spalling of the concrete cover [50].

For alkali-activated binders the literature is small about their capability in preventing reinforced steel corrosion and results are sometimes even controversial. Some studies about chloride diffusion clearly show that alkali-activated binders are able to prevent the ingress of harmful elements that could start steel corrosion [51,131-137]. Early studies in the field of reinforced geopolymer samples show that, during 1-year exposure to a 95% R.H. atmosphere in the presence of 0 or 0.4% admixed chlorides, alkali-activated FA mortar (cured at 85 °C) and a RT cured mortar with an alkali-activated 70 FA/30 OPC binder mix afforded an excellent corrosion protection to the reinforcing bars. Protection was comparable to that obtained by traditional OPC mortar. On the contrary, with a 2% admixed chlorides, passive conditions were maintained for 200 days only in the mortar with the alkali-activated 70 FA/30 OPC binder mix, due to its lowest porosity [131]. After accelerated carbonation, FA mortars partially immersed in 0.2 M NaCl solutions afforded a higher corrosion protection to steel rebars than that afforded by traditional mortar exposed to the same aggressive environment [51,132]. The reason was attributed to the higher concentration of carbonate/bicarbonate ions in Na-containing pore electrolyte of FA mortars than in Ca-containing pore electrolyte of traditional OPC mortar. A high concentration of these ions is the consequence of the higher solubility of sodium

carbonate/bicarbonate salts in comparison to calcium salts. Therefore, an effective pH buffer forms in carbonated FA mortars capable to hinder local pH variations induced by electrochemical activity of the rebars, connected to corrosion. This hinders the formation of local galvanic cells and inhibits corrosion [51]. Roy et al. [133] compared chloride diffusion for OPC and alkali-activated binders reporting that geopolymers presented almost half of the diffusion values of the OPC binders. Saraswathy et al. [134] studied alkali-activated fly ash mixtures reporting a steel corrosion resistance similar to the one OPC binders. Miranda et al. [135] even demonstrated that alkali-activated fly ash binders have superior pH conditions than OPC binders. They reported that pH decreased with hydration reaction development, however an alkaline condition remained even after 5 years, since carbonation phenomenon had not take place. Aperador et al. [136] mentioned that alkali-activated slag concrete poor carbonation resistance is associated to a major cause for corrosion of steel reinforcement. Badal et al. [137] prepared reinforced geopolymer concretes using three fly ashes with different Ca content and subjected them to accelerated carbonation for a period of 450 days. The study indicates that geopolymer concretes prepared with fly ashes having reduced calcium content are more suitable for the production of durable concrete for structural applications under exposure to carbonating environments, as the properties of these materials seem to highly mitigate the risk of carbonation-induced reinforcement corrosion in concrete (see Figure. 2.18 and Figure. 2.19).

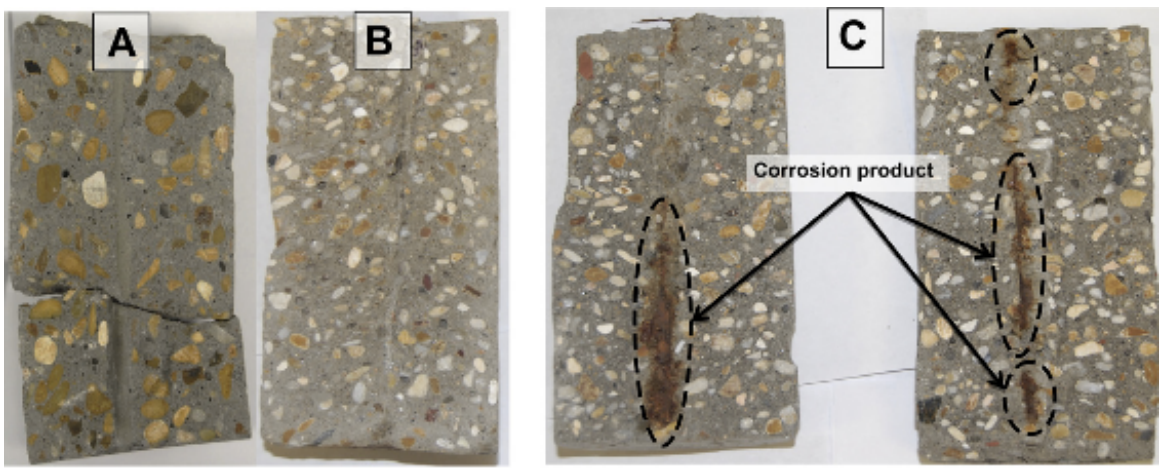

Figure. 2.18 Photographs of geopolymer concretes produced with increasing quantity of Ca in the fly ashes (A = 1.97 wt.%, B = 5 wt.%, C = 12.93 wt.%), showing the interface between the steel rebars and concrete [137].

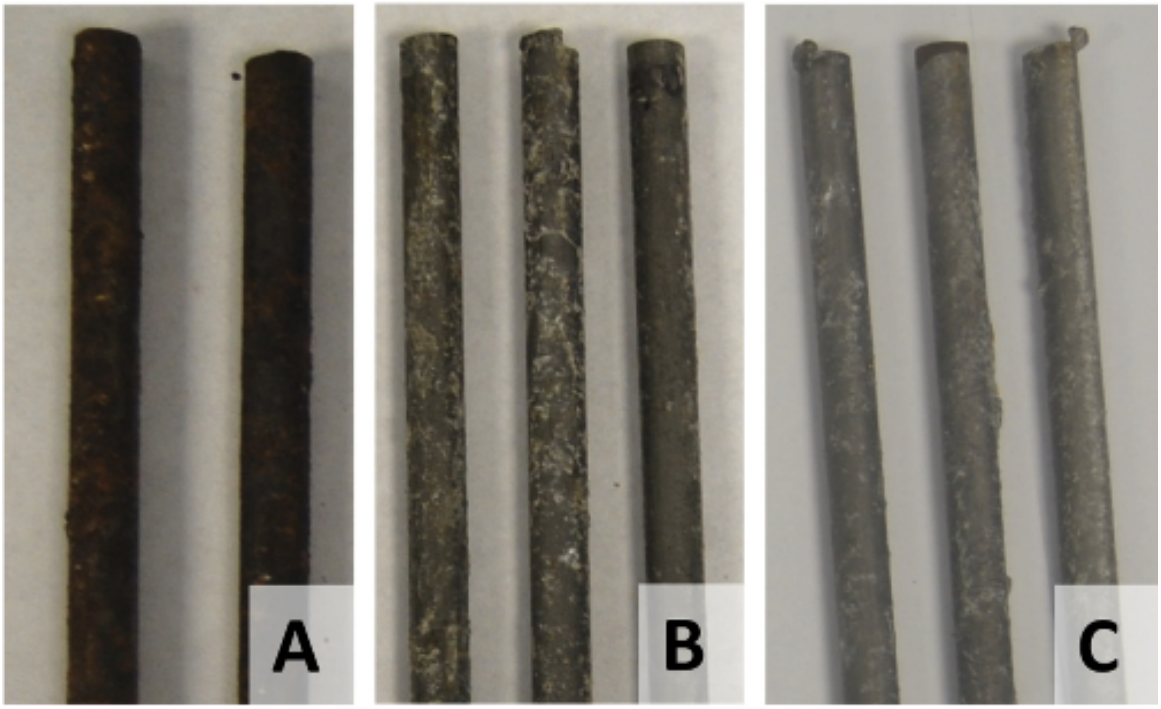

Figure. 2.19 Photographs of steel rebars removed from geopolymer concretes produced with high-Ca fly ash (A = 12.93 wt.%), and low-Ca fly ashes (B =1.97 wt.% and C = 5 wt.%), after 450 days of accelerated carbonation [137].

On the contrary, Bernal et al. [124] reported that the activation of GGBFS-metakaolin blends have low carbonation resistance. The same authors [123] found that alkali-activated slag concretes present some susceptibility to carbonation, which depends on the binder content. Lloyd et al. [118] show that geopolymer cement is prone to alkali leaching leading to a reduction in the pH, which is essential to prevent steel corrosion. They also mention that the presence of calcium is crucial for having durable steel-reinforced concrete, which is a setback for Si-Al geopolymers.

As already discussed, microstructure has a significant role in enhancing the penetration of aggressive agents, and so corrosion. For that reason, even the type of FA activator is expected to affect the corrosion behaviour of reinforcing bars. In fact, the addition of sodium silicate to sodium hydroxide in the binder activating solution was found to induce lower porosity and higher mechanical properties in geopolymers [14,29,44,94,138,139]. As a consequence, an improvement of the corrosion resistance of the embedded rebars was measured [140].

Further research about reinforced steel corrosion in alkali-activated materials is therefore highly needed, concerning alkalinity stability with curing time, as well as about

chloride diffusion and carbonation resistance.

2.10 Sustainability

With regard to traditional construction materials, the environmental impact of Ordinary Portland Cement, which is the most commonly used building material, results highly intensive, with a production of nearly one ton of CO_2 per ton of cement. 50% of its carbon dioxide emissions are caused by the processing of raw materials, 40% by the fuel consumption required to achieve the high processing temperatures (1450 °C) and the remaining 10% by the use of electricity and transportation [141]. Due to a worldwide increase in OPC demand, cement production could represent, in the close future, nearly 10% of total anthropogenic CO_2 emissions [142]. Similar considerations may also be applied to traditional ceramic materials (bricks and tiles), for which natural origin raw materials and high processing temperatures are used (between 1000 - 1300 °C).

From this point of view, the advantages offered by the geopolymer technology have already been discussed in the light of using by-products as raw materials and in the low processing temperatures. However, although these points represent a real benefit in terms of sustainability, few studies [142-145] have quantified the environmental impact and Life Cycle Assessment (LCA) - *cradle to grave* behaviour for geopolymers considering all the factors involved in this technology.

In a study by Turner et al. [143] a comprehensive analysis of carbon dioxide equivalent (CO_2-e) per unit of activity during the sourcing and manufacturing of raw materials, concrete production, and construction activities related to the production of 1 m^3 of concrete (strength class 40 MPa) in the Melbourne metropolitan area is reported.

Figure. 2.20 and Figure. 2.21 report the main factors considered in this analysis, while the contribution to CO_2-e from each of the activities, from sourcing raw materials to the manufacture and construction of 1 m^3 of concrete, is summarized in Figure. 2.22.

Portland cement is by far the most significant contributor to emissions, contributing by 76% of CO_2-e for OPC concrete. However, the alkali activators expend significant energy during manufacture and the contribution of the geopolymer binder (fly ash + sodium silicate + sodium hydroxide) is 201 kg CO_2-e/m^3 compared with OPC 269 kg

CO_2-e/m^3 (25.2%). The total emissions from the OPC and geopolymer concrete comparison mixes used in this report were estimated as 354 kg CO_2-e/m^3 and 320 kg CO_2-e/m^3 respectively, showing 10% difference [143].

This study placed a heavy emphasis upon transport as a contributor to the life cycle analysis and it was noted that the production of sodium hydroxide and sodium silicate was a major contributing factor to the carbon footprint as well as to cost. Moreover, a steam curing at 60 °C for 24 h is adopted for geopolymer concrete, which contribute for a 12.5% on their total emission. Thus, considering an ambient temperature curing for geopolymers, as in the case proposed in this research, the difference between the two technologies could be further reduced to 21%.

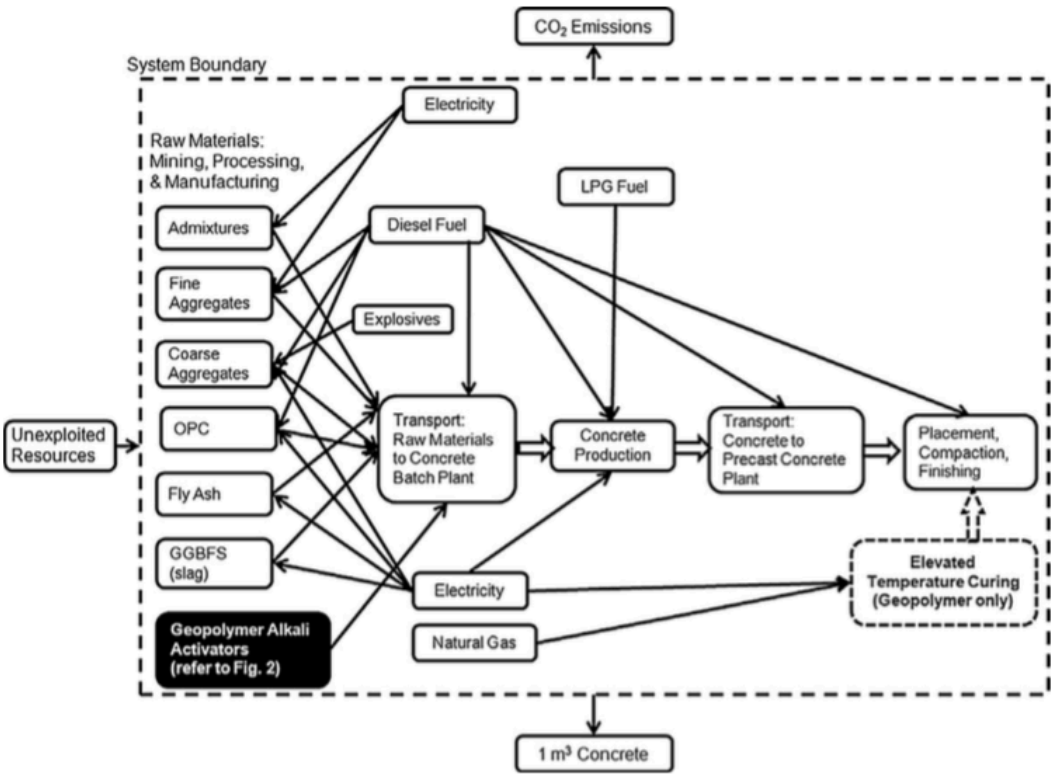

Figure. 2.20 CO_2 emissions system diagram for the production of 1 m^3 concrete [143].

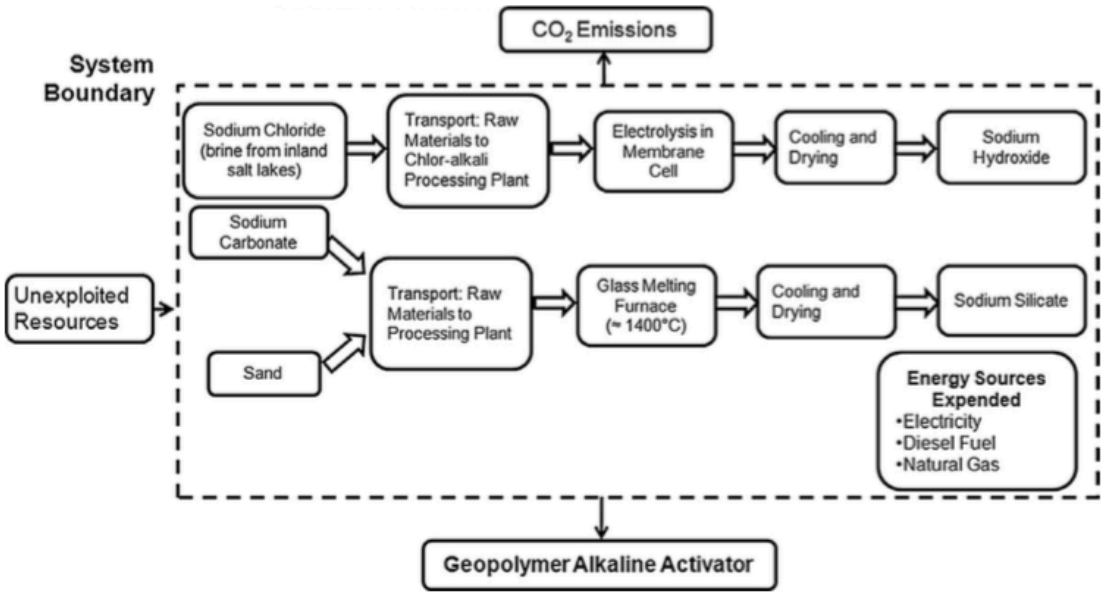

Figure. 2.21 CO_2 emissions system diagram for the production of alkali activators [143].

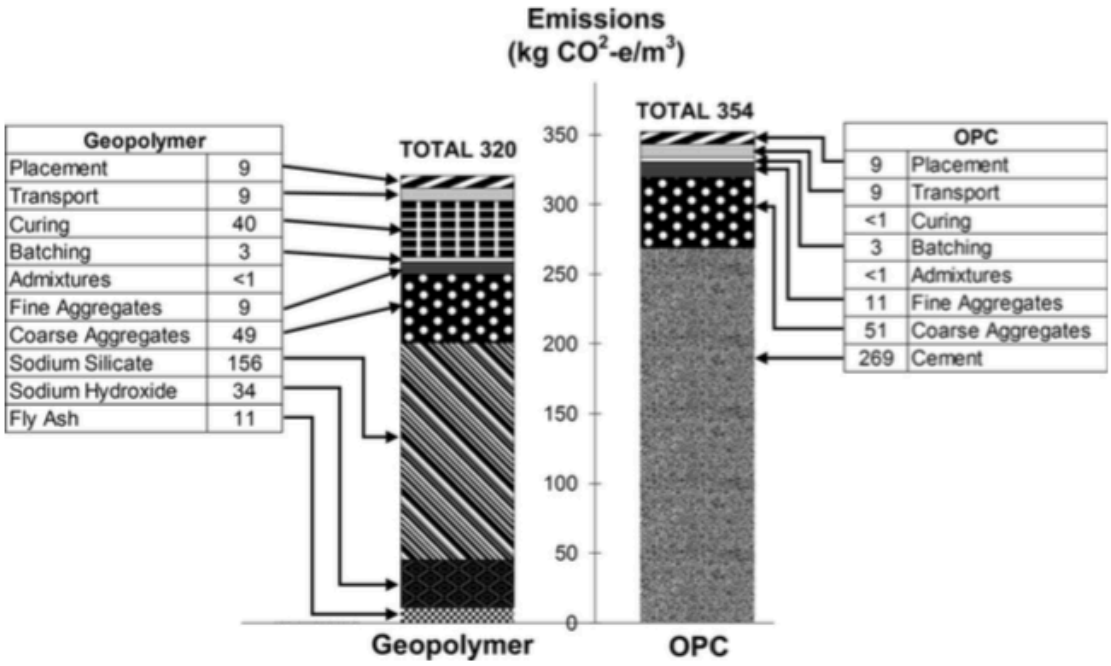

Figure. 2.22 Summary of CO_2-e for concrete mixtures with OPC and geopolymer binders, strength class 40 MPa [143].

On the other hand, the global cement requirement is projected to increase from the current 2540/year Mt to 4350 Mt/year by 2050 [144] and the worldwide production of fly ash and slags suitable for geopolymerization is currently insufficient. Heat et al. [144] report in fact that the current production of global fly ash from coal combustion is

approximately 500Mt/year with only 55% estimated to be suitable for the use in geopolymer binders. Same for slags, which production has been estimated to be approximately 242 Mt/year and only 82% of this production is estimated to be suitable for geopolymers. Thus, less than 20% of global cement requirement can currently be met by the use of fly ash and slag, which number is likely to decrease below 10% in view to moves from coal to more renewable forms of electricity production [144].

At this purpose, parallel to the use of these types of raw materials, a new research field is currently analyzing the LCA of other types of precursors (such as clays or materials derived from mineral waste streams [145]) to increase the amount of sustainable supplies for this technology.

3 MATERIALS AND METHODS

The source materials employed in the thesis and the samples preparation are outlined in this Chapter, including the characterization methods and a short description of the mathematical basis for the main used techniques.

Different types of samples were prepared depending on the tests performed and different formulations for paste and mortar samples activated at room temperature were investigated. Some experiments have also been performed on different curing conditions, in order to evaluate the influence of curing on the final performances. Reinforced samples were also cast in order to elucidate the corrosion resistance performances of geopolymer mortars compared to OPC.

The experimental techniques used for fly ash characterization include conventional X-ray and neutron diffraction and X-ray and neutron pair distribution function analysis, which are used to aid understanding the atomic structure of the investigated raw materials. As for geopolymers, physical-microstructural characteristics and mechanical properties of pastes and mortars obtained by room temperature activation are reported and discussed to verify their properties in view of their applications in the civil engineering field.

The novelty of this research is the proposed integrated approach involving the optimization of the alkali-activation process at room temperature and its exploitation in terms of products potentially market ready, thus providing an alternative to those based on hydraulic lime and/or Ordinary Portland Cement.

The behaviour of the investigated samples has also been evaluated in terms of durability in the case of reinforced samples. Electrochemical techniques such as the monitoring of corrosion potential and polarization resistance of reinforcements embedded in geopolymer mortar exposed to a chloride rich environment have been used at this purpose.

3.1 Materials

3.1.1 Fly ash

Five types of class F FA, according to ASTM C618 classification [42], sourced from different coal power stations around the world have been analyzed in this study. Italian FA (designated IFA) was sourced from Enel Produzione S.p.A. Torrevaldaliga Nord power station located in Italy (Civitavecchia, Rome) and provided by General Admixtures S.p.A. (Ponzano Veneto, Treviso). This fly ash complies with UNI EN 450-1 standard [146] and it is approved for use in the cement and concrete industry. Australian FA (designated AFA) was sourced from Collie power station in Western Australia, Australia. German FA (EFA-Füller® HP, here designated GFA) was sourced from Heyden power plant located in Petershagen (Germany). American FA (AMFA) was sourced by PSEG Mercer power station located in Hamilton, NJ (USA), while a high carbon-content FA (HCFA) was sourced by Headwater Resources Bryton Point power station located in Somerset, MA (USA). An overview of the principal oxide composition, for the investigated samples is reported in Table. 3.1 and Table. 3.2. The chemical composition of each fly ash was provided by the produces, as reported in their relevant material safety data shits (MSDS), exception for IFA and AFA, for which it was determined in laboratory by inductively coupled plasma optical emission spectrometry (ICP-OES) trough the use of an OPTIMA 3200 XL Perkin Elmer facility.

Geopolymer paste and mortar samples were mainly prepared using IFA as precursor, while some initial experiments where also performed on AFA based samples for comparison.

Type of FA	Components (wt.% as oxides)								
	SiO_2	Al_2O_3	Fe_2O_3	CaO	MgO	SO_3	Na_2O	K_2O	LOI
IFA	49.37	29.23	2.71	6.63	1.05	0.33	0.05	0.60	3.28
AFA	51.85	26.60	13.00	1.72	1.38	0.30	0.42	0.90	0.31
GFA	53.13	22.07	8.04	6.04	2.37	0.60	0.91	2.16	2.39
AMFA	41.43	21.64	12.66	3.24	0.99	0.30	0.38	1.78	3.09
HCFA	58.67	25.95	5.32	1.32	/	0.19	/	/	11.37

Table. 3.1 Principal oxides composition of FA and LOI (Loss On Ignition) [74].

Type of FA	Components (molar %)					
	Si	Al	Fe	Ca	Si/Al	Al_2O_3/SiO_2
IFA	53.11	37.06	2.19	7.64	1.43	0.35
AFA	54.68	33.06	10.32	1.94	1.65	0.30
GFA	57.96	28.38	6.60	7.06	2.04	0.24
AMFA	51.83	31.91	11.92	4.34	1.62	0.31
HCFA	61.97	31.31	4.23	1.49	1.92	0.26

Table. 3.2 Principal atoms (molar %) [74].

3.1.2 Alkali activators

The alkaline solutions selected for geopolymers activation were sodium hydroxide (NaOH in 8 M concentration) and sodium silicate (Na_2SiO_3).

Sodium hydroxide was supplied in pellets by Sigma Aldrich S.r.l. (Milan, Italy). The solution was obtained by dissolving pellets in distilled water (Figure. 3.1) in the correct proportions as to have a molar concentration equal to 8 M. In detail, being the molar mass of sodium hydroxide equal to 40 g/mol, in order to obtain a concentration equal to 8 M, it is necessary to dissolve 40x8 = 320 g of pellets in every liter of distilled water, according to the following formula:

$$Molar\ concentration\ (mol/l) = \frac{Concentration\ (g/l)}{Molar\ mass\ (g/mol)}$$

The 8 M NaOH composition is therefore: H_2O = 68.00 wt.% and NaOH = 32.00 wt.%. Sodium hydroxide is strongly caustic and corrosive, therefore, any skin contact must be avoided and protective equipment, like rubber gloves, safety clothing and eye protection, must be used when this chemical or its solutions are handled. Moreover, dissolution of sodium hydroxide is highly exothermic, and the resulting heat may cause heat burns or ignite flammables, that's why solutions were prepared and stored under a fume hood.

Sodium silicate solution was provided by Ingessil (Verona, Italy). The commercial product name of the specific product is "Reoflux B" and its composition is: SiO_2 = 29.01%, Na_2O = 14.71%, H_2O = 56.28%, by weight. It has a SiO_2/Na_2O = 1.99 and its density at 20 °C is = 1.5 ± 0.2 g/cm^3.

The activating solutions were mixed together and stirred in the due proportions 24 hours before casting. An additional stirring was made immediately before samples casing.

a) b)

Figure. 3.1 Sodium hydroxide solution preparation (a); mixed activator solutions ready for the use (b).

3.1.3 Cement

A common limestone Portland cement was used as reference to compare geopolymer performances. The commercial product used is "Tecnocem CEM II/A-LL 42.5 R" in compliance with EN 197-1 [147] produced by Italcementi (Figure. 3.2).

a) b)

Figure. 3.2 Limestone Portland cement powder (a); Tecnocem CEM II/A-LL 42.5 bag (b).

This product is able to achieve good mechanical strength values after 28 days of curing (42.5 MPa) and is currently one of the most widespread and used in the building sector.

3.1.4 Sand

Two types of sand were used in this investigation as fine aggregate:

- natural calcareous sand (d_{max} = 4 mm) provided by Consorzio Concave Bologna (Italy). The humidity condition of this sand has been checked before each casting in order to properly balance the amount of water to be added into the mix;
- natural sand with standardized grain size distribution according to EN 196-1 [148].

3.2 Samples preparation

Geopolymer pastes and mortar were prepared in this study with different procedures, depending on the characterization test performed.

As already mentioned, the focus of this research was on the use of IFA as precursor, but some initial analyses were performed also on AFA. This latter precursor has been in fact already extensively used in other works [78,112,117] and its behaviour was used as a reference for comparing the first results of IFA based geopolymers.

As for the case of geopolymer pastes (from now on simply called "geopolymers"), only IFA and AFA were used as precursors, and specific analyses regarding the performances of geopolymers depending on different curing conditions were further performed on IFA based samples. Mortars were prepared mainly using IFA as precursor, but some initial comparison have been made also using AFA.

As for the formulation, the main parameter chosen for fly ash activation was the Na_2O/SiO_2 molar ratio. The ratio of sodium hydroxide and sodium silicate solutions was adjusted in order to achieve molar ratios of Na_2O/SiO_2 ranging form 0.12 to 0.20, based on the total content of soda and silica present in the sample. Samples were named according to their precursor ash and activating solution Na_2O/SiO_2 molar ratio multiplied

by 100 (e.g., IFA16 refers to a sample obtained from Italian fly ash with Na_2O/SiO_2 molar ratio of 0.16). Some other nomenclature distinctions will be discussed in the specific Subchapters.

3.2.1 Geopolymers

3.2.1.1 IFA and AFA geopolymers

Geopolymers were prepared with constant fly ash content (FA = 69 wt.%) and a liquid/fly ash weight ratio (L/FA) of 0.45 by changing the relative amount of activators in order to obtain the predicted Na_2O/SiO_2 molar ratios of 0.12, 0.16, 0.18, 0.20. The mix design is reported in Table. 3.3. In the Table, the water content is the water contained in the alkaline solutions in percentage over all the constituents while L/FA = liquid/fly ash weight ratio, where L is calculated considering the total content of 8 M NaOH + Na-silicate solution.

The fly ash and the activating solution were mixed for 5 minutes by hand (in the case of small amounts, Figure. 3.3) or by a planetary mixer (in the case of big amounts). The slurry was then cast into cylindrical plastic molds (ϕ = 45 mm, h = 65 mm, Figure. 3.3 b-c) and prismatic metallic molds (40x40x160 mm^3), which were cured at T = 25 °C and R.H. = 65% for 24 hours. After de-moulding (Figure. 3.4), geopolymers were cured for a further 6 days at RT and slightly lower humidity (approximately 50%). Samples were tested after a week of curing.

Sample	FA wt.%	8 M NaOH wt.%	Na-silicate solution wt.%	Water [(a)] wt. %	L/FA [(b)] ratio	Molar ratio:	
						SiO_2/Al_2O_3	Na_2O/SiO_2
IFA12	69.0	5.2	25.9	18.1	0.45	3.48	0.12
IFA16	69.0	15.6	15.6	19.3	0.45	3.22	0.16
IFA18	69.0	20.7	10.5	20.0	0.45	3.10	0.18
IFA20	69.0	25.9	5.2	20.5	0.45	2.97	0.20
AFA12	69.0	5.2	25.9	18.1	0.45	4.00	0.12
AFA16	69.0	15.6	15.6	19.3	0.45	3.70	0.16
AFA18	69.0	20.7	10.5	20.0	0.45	3.55	0.18
AFA20	69.0	25.9	5.2	20.5	0.45	3.41	0.20

Table. 3.3 Mix design of the investigated geopolymer samples; [(a)] water content is the water contained in the alkaline solutions in percentage over all the constituents; [(b)] L/FA = liquid/fly ash weight ratio. L is calculated considering the total content of 8 M NaOH + Na-silicate solution [44].

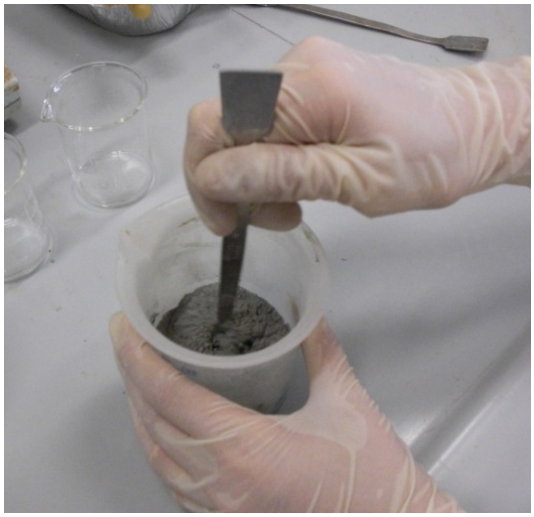

a)

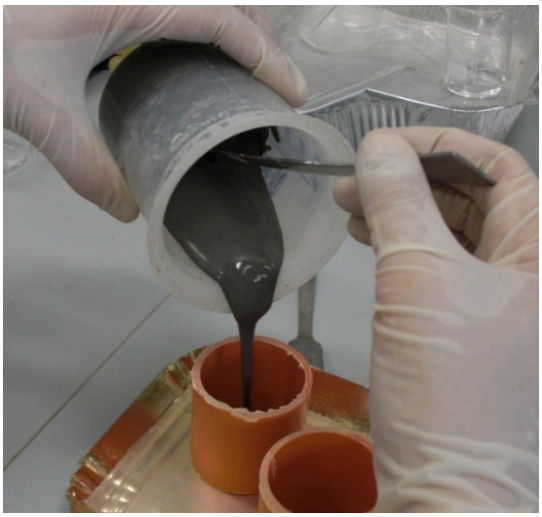

b)

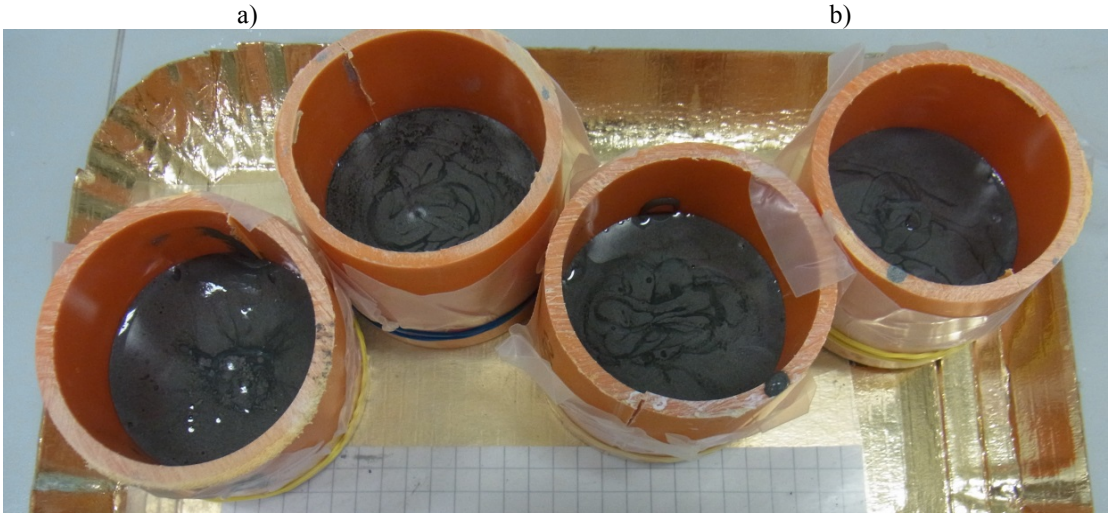

c)

Figure. 3.3 Geopolymer preparation (a) and casting (b,c).

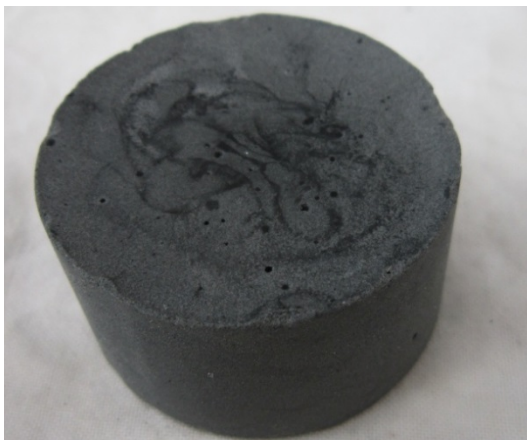

a)

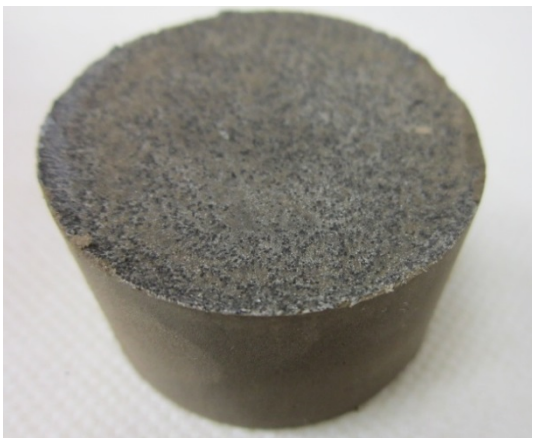

b)

Figure. 3.4 IFA sample after de-moulding (a); AFA sample after de-molding (b).

3.2.1.2 IFA sealed and oven cured samples

IFA sealed and oven cured samples were prepared with a constant amount of FA (69 wt.%) and alkali solutions (31 wt.%) by changing the relative amount of activators in order to obtain the predicted Na_2O/SiO_2 molar ratios of 0.12, 0.14, 0.16, 0.18, 0.20. The L/FA ratio was maintained equal to 0.45.

The slurries were prepared using a Hobart mixer and cast in cylindrical (ϕ = 50 mm, h = 50 mm) or cubical (50x50x50 mm^3) moulds (Figure. 3.5). After casting, samples were sealed in plastic bags and subjected to different curing conditions: room temperature (RT, 25 °C) or oven curing at 50 °C and 70 °C for the first 24 hours. Oven cured samples, which were completely hardened after 24 hours, were then demoulded and maintained sealed at RT for the remaining days while RT cured samples were demoulded after 7 days and maintained sealed for the remaining days. All the samples were tested after 28 days of curing.

In this case, samples were named according to their precursor, relevant Na_2O/SiO_2 molar ratio and curing condition for the first 24 hours (e.g., IFA20-RT corresponds to the formulation with Na_2O/SiO_2 = 0.20 which was cured at room temperature for the first 24 hours).

The mix design is reported in Table. 3.4 while the samples nomenclature is reported in Table. 3.5.

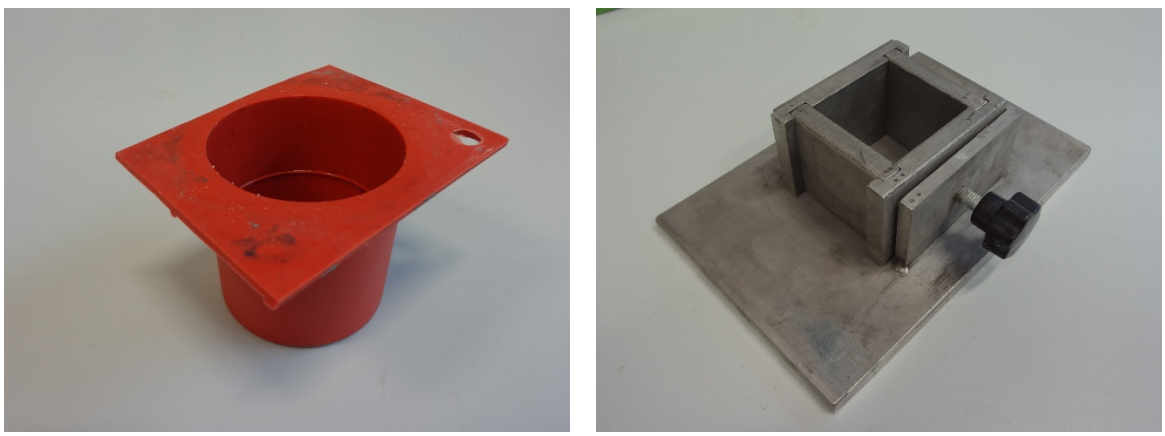

a) b)

Figure. 3.5 Cylindrical plastic mould (ϕ = 50 mm, h = 50 mm) (a); cubical steel mould (50x50x50 mm^3) (b).

Sample	FA wt.%	8 M NaOH wt.%	Na-silicate solution wt.%	Water wt.%	L/FA ratio	Molar ratios:	
						SiO_2/Al_2O_3	Na_2O/SiO_2
IFA12	69.0	5.2	25.9	18.1	0.45	3.48	0.12
IFA14	69.0	11.0	20.1	18.7	0.45	3.35	0.14
IFA16	69.0	15.6	15.6	19.3	0.45	3.22	0.16
IFA18	69.0	20.7	10.5	20.0	0.45	3.09	0.18
IFA20	69.0	25.9	5.2	20.5	0.45	2.96	0.20

Table. 3.4 Mix design of the investigated geopolymer samples [149].

Geopolymer type	Type of curing for the first 24 h		
	25 °C	50°C	70°C
IFA12	IFA12-RT	IFA12-50	IFA12-70
IFA14	IFA14-RT	IFA14-50	IFA14-70
IFA16	IFA16-RT	IFA16-50	IFA16-70
IFA18	IFA18-RT	IFA18-50	IFA18-70
IFA20	IFA20-RT	IFA20-50	IFA20-70

Table. 3.5 Nomenclature depending on curing conditions for the investigated samples [149].

3.2.2 Mortars

Three main types of geopolymer mortars (M1, M2, M3), characterized by the use of specific sand and curing conditions, were prepared in this investigation, as reported in Table. 3.6. For the case of M2 and M3 a cement-based mortar, named CEM, was prepared as well and used as reference.

All the specific formulations and casting procedures for each type of mortar are specified in the following Subchapters.

Mortar type	Binder type	Sand type	Curing conditions
M1	IFA - AFA	Standardized sand	T = 25 °C and R.H. > 65%
M2	IFA	Natural calcareous sand	T = 25 °C and R.H. = 35%
	CEM	Natural calcareous sand	T = 25 °C and R.H. = 35%
M3	IFA	Standardized sand	T = 25 °C and R.H. = 35%
	CEM	Standardized sand	T = 25 °C and R.H. > 95%

Table. 3.6 Investigated mortar samples.

3.2.2.1 Mortar type 1: IFA and AFA samples

Mortar type 1 (M1) IFA and AFA formulations were prepared with the aim to investigate the physical-mechanical properties on IFA and AFA based mortar samples.

Mortar samples were prepared using a Hobart mixer with a procedure similar to the one used for conventional cement mortar preparation (Figure. 3.6). Fly ash was added to the premixed alkaline solutions and mixed for 1 minute; then sand was added after 30 s. A small amount of extra water (1.6 wt.%) was added in Italian fly ash based mortars to reach the same workability as for Australian fly ash and the slurry was mixed for an additional minute. Finally, the mix was poured in metal moulds and vibrated for 1 min on a shaker table. After 1 day of curing at T = 25 °C and R.H. > 65%, prismatic specimens 40x40x160 mm^3 were demoulded and cured for a further 27 days (Figure. 3.6). As for the geopolymer pastes, the ratio of sodium hydroxide and sodium silicate solutions in the mortars was adjusted in order to achieve molar ratios of Na_2O/SiO_2 equal to 0.12, 0.16, 0.18 and 0.20 based on the total content of soda and silica present in the sample, but without considering silica content of sand. Mortar samples were named by adding the prefix M1 to the previously described acronym for pastes and their mix design is reported in Table. 3.7.

Sample	Sand wt.%	FA wt. %	8 M NaOH wt.%	Na-silicate solution wt.%	Additional water wt.%	L/FA	Na_2O/SiO_2
M1_IFA12	64.0	23.7	1.8	8.9	1.6	0.52	0.12
M1_IFA16	64.0	23.7	5.4	5.4	1.6	0.52	0.16
M1_IFA18	64.0	23.7	7.2	3.5	1.6	0.52	0.18
M1_IFA20	64.0	23.7	9.1	1.6	1.6	0.52	0.20
M1_AFA12	65.0	24.1	1.8	9.1	/	0.45	0.12
M1_AFA16	65.0	24.1	5.4	5.4	/	0.45	0.16
M1_AFA18	65.0	24.1	7.2	3.6	/	0.45	0.18
M1_AFA20	65.0	24.1	9.1	1.8	/	0.45	0.20

Table. 3.7 Mix design for the investigated IFA and AFA mortar samples [44].

a) b) c) d) e)

Figure. 3.6 Preparation (a,b), casting (c,d) and curing (e) of prismatic M1 mortar samples.

3.2.2.2 Mortar type 2: IFA and CEM samples

Mortar type 2 (M2) IFA and CEM formulations were prepared with the aim to investigate the corrosion protection afforded to the embedded rebars by RT cured

geopolymer mortars during partial immersion in 3.5% NaCl solution. The results were compared to those obtained in a traditional cement-based mortar. Results were interpreted in the light of microstructural, physical and mechanical properties of the prepared samples.

Three different geopolymer mortar mixes and a reference cement-based one were prepared. Their mix design is shown in Table. 3.8. Geopolymer mortars were activated by adjusting the relative amount of 8 M NaOH and sodium silicate solutions in order to achieve Na_2O/SiO_2 molar ratios of 0.12, 0.14 and 0.16. The liquid/binder weight ratio (L/B) was fixed at 0.52. The reference mortar (CEM) was prepared with the same sand/binder and L/B ratios adopted for geopolymer mortars.

Sample	Sand wt.%	FA wt.%	Cement wt.%	8M NaOH wt.%	Na-silicate solution wt.%	Water wt.%	L/B (a)	W/B (b)	Na_2O/SiO_2
M2_FA12	64.00	23.70	/	1.80	8.90	1.60	0.52	0.33	0.12
M2_FA14	64.00	23.70	/	3.80	6.90	1.60	0.52	0.34	0.14
M2_FA16	64.00	23.70	/	5.35	5.35	1.60	0.52	0.35	0.16
CEM	64.00	/	23.70	/	/	12.30	0.52	0.52	/

Table. 3.8 Mix design of the investigated IFA mortar samples and CEM; [(a)] L/B = liquid/binder ratio. L is calculated considering the total content of 8 M NaOH + sodium silicate solution + water; [(b)] W/B = water/binder ratio. W is calculated considering the water contained in the alkaline solutions + the added water [52].

The adopted mixing procedure was the same adopted for M1 (see Chapter 3.2.2.1) and different types of samples were cast, depending on the characterization test performed:

- microstructural and mechanical characterizations were performed on prismatic samples (40x40x160 mm^3), mechanically compacted and demoulded after 1 day curing at T = 25 °C and R.H. = 35%. The specimens were then kept at laboratory atmosphere (R.H. ≈ 35%) and tests were performed in due time. These exposure conditions aim at reproducing those often adopted at the construction sites;

- electrochemical tests and analyses and penetrated chloride content during partial immersion conditions in 3.5% NaCl solution were carried out on slabs with dimensions 200x250x50 mm^3. Three manually compacted slabs were prepared for

each formulation: two reinforced slabs with embedded steel bars (Figure. 3.7) and one unreinforced slab for chloride concentration analysis (Figure. 3.8). Each reinforced slab contained two sandblasted degreased ribbed carbon steel rods acting as working electrodes (W, ϕ = 10 mm), with ends masked with epoxy resin and isolated by thermo-shrinking adhesive tape to leave an exposed surface area of 7400 mm^2. In close proximity to these bars, two activated titanium wires and three symmetrically arranged stainless steel bars acted as reference (R) and counter (C) electrodes, respectively, during the electrochemical tests.

Slabs were cured in the moulds at T = 25 °C and R.H. = 35% for a week, then they were demoulded and cured at the laboratory atmosphere (R.H. ≈ 35%) for further 3 weeks, again to simulate practices often adopted in field applications. Finally, the lower side of each slab was ground so reducing the slab thickness by 2 mm, in order to avoid the skin effect and accelerate the ingress of chlorides. The ground side was finally exposed to the aqueous chloride solution, without slab pre-saturation (Figure. 3.9). Slab casting procedure and curing is shown in Figure. 3.10.

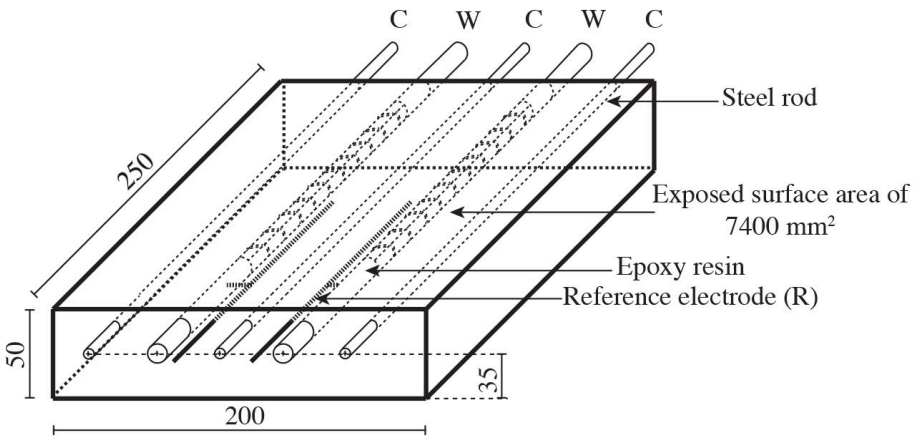

Figure. 3.7 Geometric scheme of the reinforced slabs (dimensions are expressed in mm): W = working electrodes, C = stainless steel counter electrodes, R = activated Ti reference electrodes [52].

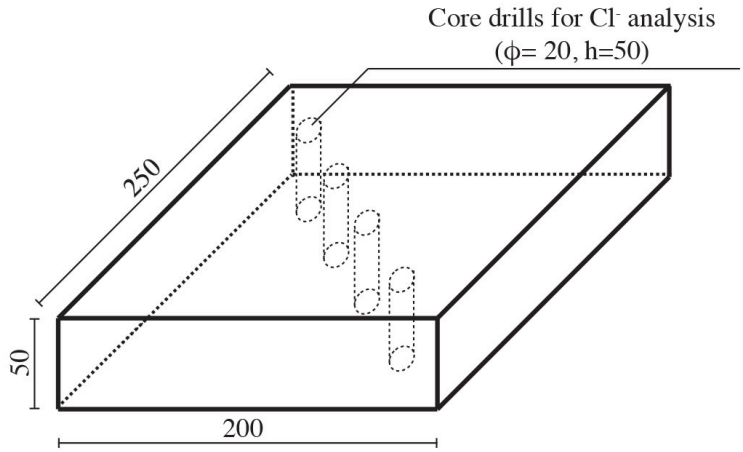

Figure. 3.8 Geometric scheme of the unreinforced slabs (dimensions are expressed in mm): core drills for Cl^- analysis are highlighted in dashed line [52].

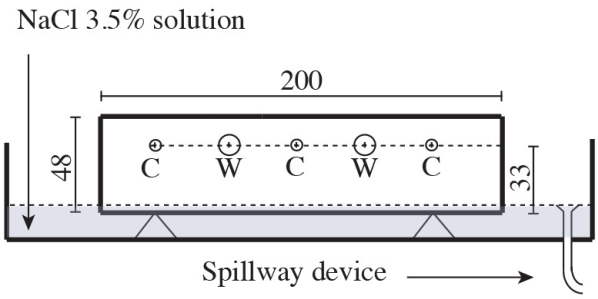

Figure. 3.9 Geometric section of the reinforced slab and set-up for tests under partial immersion conditions (dimensions are expressed in mm). The 3.5% NaCl solution head in contact with the specimen is 1 mm high [52].

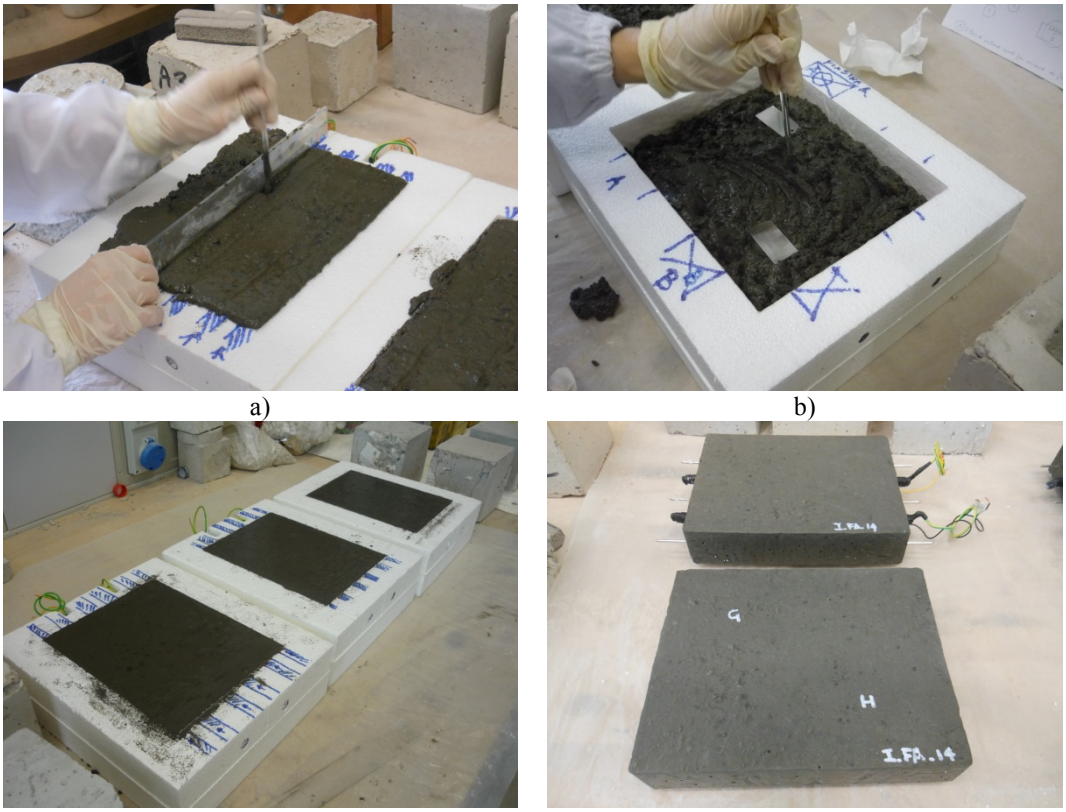

Figure. 3.10 Reinforced (a) and unreinforced (b) slab casting procedure; slabs curing before (c) and after (d) demoulding.

3.2.2.3 Mortar type 3: IFA and CEM samples

Mortar type 3 (M3) IFA and CEM formulations were prepared with the aim to investigate the corrosion protection afforded to the embedded rebars by RT cured geopolymer mortars during wet and dry (w/d) exposures to 0.1 M NaCl solution in comparison with CEM. Even in this case, an interpretation was made on the base of microstructural, physical and mechanical results.

For M3, same formulations as already described in the case of M2 mortar were prepared (see Table. 3.8) but standardized sand was used. A Hobart mixer was used for mortar samples preparation and same procedure described in the previous paragraphs was adopted for mixing. The slurries were cast in different types of moulds (cylinders, prisms or cubes), depending on the characterization test.

- mechanical and microstructural characterizations were performed on prismatic

samples (40x40x160 mm^3) which were mechanically compacted and demoulded after 1 day curing, then maintained at T = 25 °C and R.H. = 35% (geopolymers) and T = 25 °C and R.H. > 95% (CEM) till testing;

- chloride diffusion test was performed on cubes (100x100x100 mm^3) according to ASTM C1156 [151]. After 28 days of curing in the previous described conditions, cubes surfaces were scrubbed with a stiff nylon brush and rinsed with tap water, then allowed to air dry until no moisture could be removed from the surface. The cubes were then sealed with epoxy resin, exception for one surface, and pre-saturated by immersion in satured calcium hydroxide solution (CEM) and 0.1 M NaOH solution (geopolymers) for at least 24 hours. The 0.1 NaOH solution was chosen for geopolymers to expose them to a similar pH solution (12.7) compared to CEM, without compromising geopolymers microstructure by any calcium hydroxide precipitation. After saturation, cubes were removed from the two solutions, respectively, rinsed with tap water and immediately immersed in the exposure liquid (165 g/l NaCl) in a sealed container for the due exposure period (38 days). Cubes for chloride diffusion test are reported in Figure. 3.11;

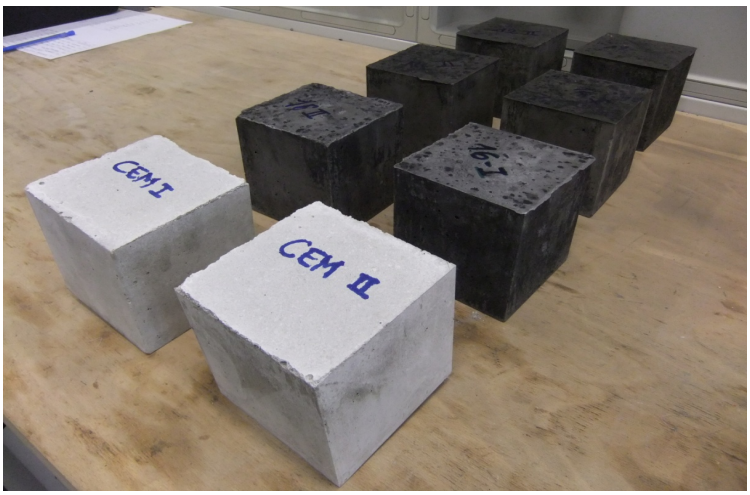

Figure. 3.11 M3 cubes for chloride diffusion test.

- electrochemical tests and chloride penetration measurements during w/d cycles in 0.1 M NaCl solution were performed on cylinders. Specifically, twelve cylinders (h = 100 mm, ϕ = 35 mm) were prepared for each type of mortar. Eight cylinders were prepared with embedded rebars (acting as working electrode, W) and reference electrode (R) for electrochemical test (Figure. 3.12) while four unreinforced cylinders were prepared for chloride penetration measurements

(Figure. 3.13). Rebars were ribbed carbon steel rods (sandblasted surface, ϕ = 10 mm) with both ends masked with epoxy resin to leave an exposed surface area of 1000 mm^2. A further thermoset band was applied to make the unexposed surface protection more long lasting. All the rebars were positioned along the longitudinal axis of the cylindrical samples, so that the mortar cover was about 15 mm thick. A quasi-reference low-impedance electrode constituted by an activated titanium wire was fixed to each reinforcing rod to facilitate electrochemical tests. Casting procedure is reported in Figure. 3.14 while Figure. 3.15 reports samples after demoulding.

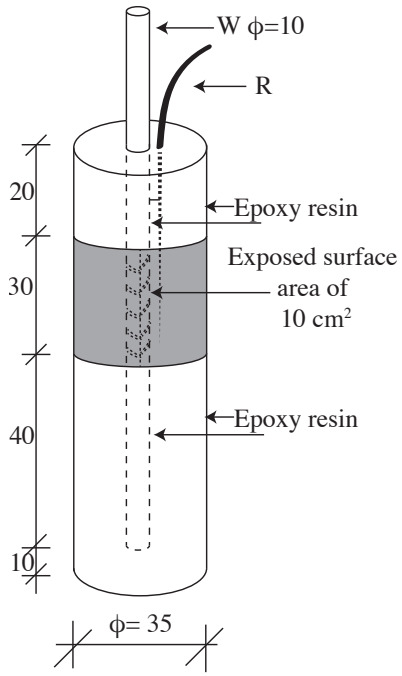

Figure. 3.12 Geometric framework of the reinforced cylinders (dimensions are expressed in mm): W = working electrode, R = activated Ti reference electrode [150].

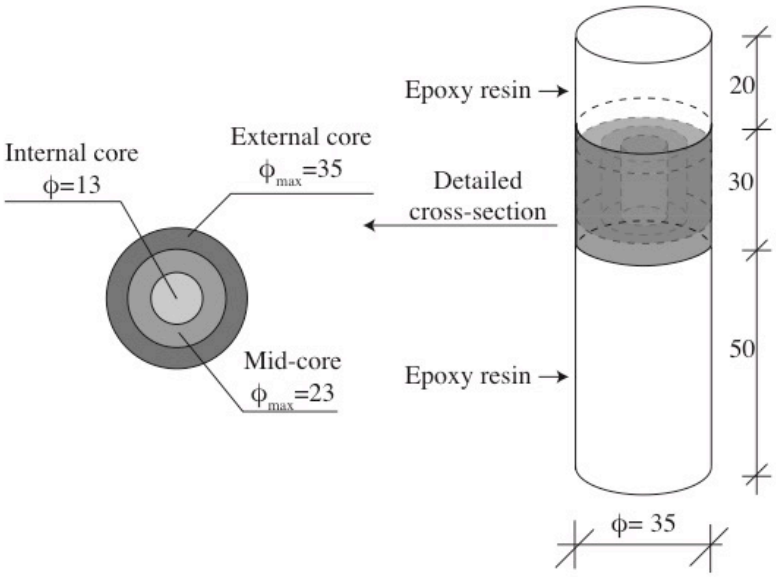

Figure. 3.13 Unreinforced cylinder with detailed cross-section for Cl^- analysis (dimensions are expressed in mm) [150].

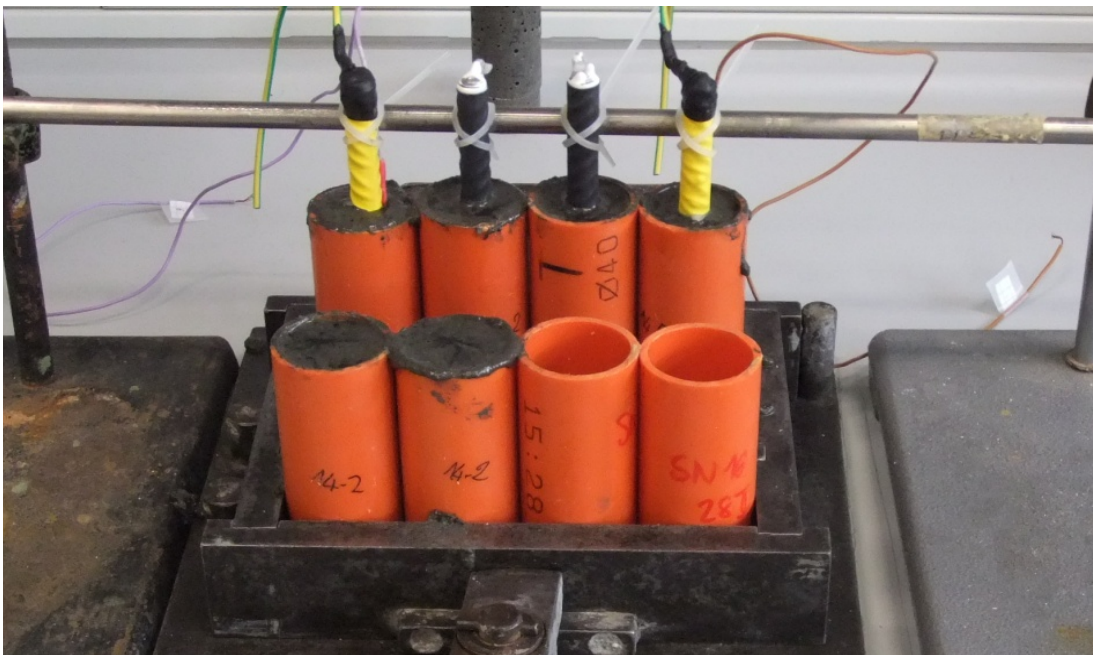

Figure. 3.14 M3 cylinders casting.

Figure. 3.15 M3 cylinders after demoulding.

All the samples, after pouring, were vibrated on a shaker table to reduce entrained air and cured at different conditions for 28 days. Geopolymer samples were cured at T = 25 °C and R.H. = 35% until testing, while CEM samples were cured at T = 25 °C and R.H. > 65% until testing.

After 28 days of curing, the top and bottom portions of all cylinders were screened by epoxy resin in order to drive penetrating chlorides to follow horizontal paths during w/d cycles. On samples for electrochemical tests the bare mortar surface was only around the un-screened rebar surface (as in Figure. 3.12 and Figure. 3.13).

3.3 Characterization methods

All the characterization methods used in this work are outlined in this Chapter, including a short description of the mathematical basis for the main techniques used. An overview of the performed test is reported in Table. 3.9.

Sample type		Characterization test
Fly ash	IFA and AFA	Particle size distribution Chemical composition Scanning Electron Microscopy Mineralogical phase analysis Quantitative Rietveld analysis
	IFA, AFA, AMFA, GFA, HCFA	X-ray and neutron PDF analysis
Geopolymers	IFA and AFA	Thermal treatment (800 °C) Weight loss after calcining Mineralogical phase analysis Scanning Electron Microscopy Thermogravimetrical analysis Pore size distribution Flexural and compressive strength
	IFA (sealed and oven cured samples)	Optical Microscope analysis Bulk density Water Absorption Dilatometric analysis Mineralogical phase analysis Pore size distribution pH
Mortar type 1 M1	IFA and AFA	Workability Water Absorption Flexural and compressive strength
Mortar type 2 M2	IFA	Bulk density Flexural and compressive strength Dynamic elastic modulus Water Absorption Capillary sorptivity Pore size distribution pH Optical Microscope analysis Scanning Electron Microscopy Total chloride content
	IFA (samples under partial immersion conditions)	Corrosion potential Polarization resistance Polarization curves (in leachate solution)
Mortar type 3 M3	IFA	Bulk density Flexural and compressive strength Dynamic elastic modulus Water Absorption Capillary sorptivity Pore size distribution pH Total chloride content (after w/d cycles) Apparent diffusion coefficient
	IFA (during w/d cycles)	Corrosion potential Polarization resistance

Table. 3.9 Test campaign on the studied samples.

3.3.1 Chemical, physical, microstructural and mechanical characterization

3.3.1.1 Particle size distribution

Particle size distribution was measured by a laser particle-size analyzer (Mastersizer 2000, Malvern Instruments, UK).

Laser diffraction is a widely used particle sizing technique for materials ranging from hundreds of nanometers up to several millimeters in size. The main reasons for its success are that it is a well-established rapid measurement (resulting generated in less than a minute), which gives an instant feedback and can easily measure large numbers of particles.

Laser diffraction measures particle size distributions by measuring the angular variation in intensity of light scattered as a laser beam passes through a dispersed particulate sample. Large particles scatter light at small angles relative to the laser beam and small particles scatter light at large angles [152]. The angular scattering intensity data is then analyzed to calculate the size of the particles responsible for creating the scattering pattern, using the Mie theory of light scattering and assuming a volume equivalent sphere model [153]. The particle size is reported as a volume equivalent sphere diameter.

Mie theory requires knowledge of the optical properties (refractive index and imaginary component) of both the sample being measured, along with the refractive index of the dispersant. Usually the optical properties of the dispersant are relatively easy to find from published data, and many modern instruments will have in-built databases that include common dispersants. For samples where the optical properties are not known, the user can either measure them or estimate them using an iterative approach based upon the goodness of fit between the modeled data and the actual data collected for the sample [152].

A simplified approach is to use the Fraunhofer approximation, which does not require knowledge of the optical properties of the sample. This can provide accurate results for large particles. However it should be used with caution whenever working with samples which might have particles below 50 μm or where the particles are relatively transparent [152].

3.3.1.2 Inductive Coupled Plasma-Optical Emission Spectrometry

The Inductive Coupled Plasma-Optical Emission Spectrometry (ICP-OES) analysis is an analytical technique used for the detection of chemical elements in a sample. It is a type of emission spectroscopy that uses the inductively coupled plasma to excite atoms and ions, which emit electromagnetic radiation at characteristic wavelengths. The intensity of this emission is indicative of the concentration of the investigated element within the sample. Argon gas is typically used to create the plasma.

In order to perform ICP-OES analysis, samples are to be fed into the instrument (Optima 3200 XL Perkin Emer) in a dissolved aqueous medium. Sample solutions should be clear (aqueous) and should not contain any suspended particles.

3.3.1.3 Optical Microscope analysis

Optical Microscope (OM) analysis was performed using an Olympus microscope SZX10 instrument on fresh fractured surfaces. At this purpose, planar sections were sliced from the main sample in order to obtain disks of about 1 cm thick (Figure. 3.16).

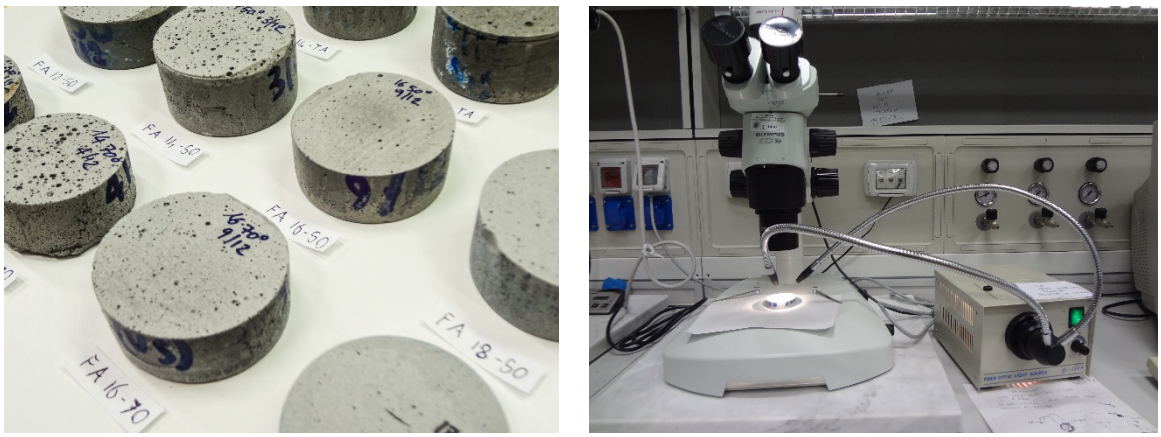

a) b)

Figure. 3.16 Samples for OM analysis (a); Olympus microscope SZX10 (b).

3.3.1.4 Scanning Electron Microscopy and Energy Dispersive X-ray Spectroscopy

Scanning Electron Microscopy (SEM) analysis was carried out by means of a Zeiss, Neon and MIRA Tescan field emission electron microscopes. Variable Pressure Scanning Electron Microscope (VP-SEM) Zeiss EP EVO 50 with secondary and back-scattered electrons detectors was also performed. The images from VP-SEM were collected in Variable Pressure mode (80 Pa). The accelerating voltage used for analyses was 20 keV.

The scanning electron microscope uses a focused beam of high-energy electrons to generate a variety of signals at the surface of solid specimens. The signals that derive from electron-sample interactions reveal information about the sample including external morphology (texture), chemical composition, and crystalline structure and orientation of materials making up the sample. In most applications, data are collected over a selected area of the surface of the sample, and a 2-dimensional image is generated that displays spatial variations in these properties. Areas ranging from approximately 1 cm to 5 microns in width can be imaged in a scanning mode using conventional SEM techniques (magnification ranging from 20x to approximately 30000x, spatial resolution of 50 to 100 nm). The SEM is also capable of performing analyses of selected point locations on the sample; this approach is especially useful in qualitatively or semi-quantitatively determining chemical compositions (using Energy Dispersive X-ray Spectroscopy, EDS), crystalline structure, and crystal orientations (using Electron Backscattered Diffraction, EBSD) [154].

Accelerated electrons in an SEM carry significant amounts of kinetic energy, and this energy is dissipated as a variety of signals produced by electron-sample interactions when the incident electrons are decelerated in the solid sample. It is the detection of specific signals which produces an image or a sample's elemental composition. These signals include secondary electrons (that produce SEM images), backscattered electrons (BSE), diffracted backscattered electrons (EBSD that are used to determine crystal structures and orientations of minerals), photons (characteristic X-rays that are used for elemental analysis and continuum X-rays), visible light (cathodoluminescence–CL), and heat [154]. The three signals which provide the greatest amount of information in SEM are the secondary electrons, backscattered electrons, and X-rays. Secondary electrons and backscattered electrons are commonly used for imaging samples. Secondary electrons are most valuable for showing morphology and topography on samples and emitted from the atoms occupying the top surface and produce a readily interpretable image of the surface. The contrast in the image is determined by the sample morphology. A high-resolution image can be obtained because of the small diameter of the primary electron beam [155]. Backscattered electrons are most valuable for illustrating contrasts in composition in multiphase samples (i.e., for rapid phase discrimination) and are primary beam electrons which are “reflected” from atoms in the solid. The contrast in the image produced is determined by the atomic number of the elements in the sample. The image will therefore

show the distribution of different chemical phases in the sample. Because these electrons are emitted from a depth in the sample, the resolution in the image is not as good as for secondary electrons [155]. X-ray generation is produced by inelastic collisions of the incident electrons with electrons in discrete orbitals (shells) of atoms in the sample. As the excited electrons return to lower energy states, they yield X-rays that are of a fixed wavelength (that is related to the difference in energy levels of electrons in different shells for a given element). Thus, characteristic X-rays are produced for each element in a mineral that is "excited" by the electron beam [154]. Detection and measurement of the energy permits elemental analysis (EDS). EDS can provide rapid qualitative, or with adequate standards, quantitative analysis of elemental composition with a sampling depth of 1-2 microns. X-rays may also be used to form maps or line profiles, showing the elemental distribution in a sample surface [155].

EDS systems are typically integrated into either a SEM instrument and include a sensitive X-ray detector, a liquid nitrogen dewar for cooling, and a software to collect and analyze energy spectra. The detector is mounted in the sample chamber of the main instrument at the end of a long arm, which is itself cooled by liquid nitrogen. The most common detectors are made of Si(Li) crystals that operate at low voltages to improve sensitivity, but recent advances in detector technology make available so-called "silicon drift detectors" that operate at higher count rates without liquid nitrogen cooling [154].

An EDS detector contains a crystal that absorbs the energy of incoming X-rays by ionization, yielding free electrons in the crystal that become conductive and produce an electrical charge bias. The X-ray absorption thus converts the energy of individual X-rays into electrical voltages of proportional size; the electrical pulses correspond to the characteristic X-rays of the element [154].

Together, these capabilities provide fundamental compositional information for a wide variety of materials.

3.3.1.5 Mineralogical phase analysis

Mineralogical phase analysis was conducted using a Bruker D8 Advance X-ray diffractometer operated at 40 kV and 40 mA using Cu-Kα radiation. The data for quantitative analysis was collected using a nominal 2θ step size of 0.01°, count time of

0.5 s and a 2θ range of 10 - 120°. Crystalline phases were identified using EVA version 3. Rietveld refinement was performed using Bruker AXS TOPAS version 4.2. A fluorite (CaF_2) internal standard (10 wt.%) was used to facilitate quantitative phase analysis including the abundance of the amorphous phase. The amorphous level was calculated from the difference between the sum of the analyzed weight fractions for all crystalline phases and 100% and may also include poorly ordered phase(s) and/or undetected phase(s) after Rietveld refinement.

Synchrotron X-ray total scattering data were collected at the 11-ID-B beamline at the Advanced Photon Source (APS), Argonne National Laboratory (ANL). Powder samples were loaded into polyimide capillaries and measured in transmission mode at ambient laboratory temperature using a Perkin Elmer amorphous silicon image plate detector [156] located at 172.8 mm from the sample. Data for an empty capillary and a Ni powder standard were also collected. A wavelength of 0.2114 Å was used (58.65 keV) and the measurement time was 20 min total with 0.1 s for each exposure. The program Fit2D [157] was used to calibrate the sample to detector distance and detector alignment using data from a CeO_2 powder standard. The normalized total scattering patterns, *S(Q),* and subsequent PDFs were produced using PDFgetX2 [158]. PDFs, *G(r)*, were calculated via a sine Fourier transformation of the total scattering data utilizing a Q_{max} of 23.5 $Å^{-1}$.The Ni dataset was fit in PDFgui [159] between 1 and 50 Å to obtain the instrument parameters, Q_{damp} and Q_{broad} (Q_{damp} of 0.037 $Å^{-1}$ and Q_{broad} of 0.030 $Å^{-1}$). The PDFs of the amorphous phases existing in the samples were obtained by subtracting contributes from the crystalline phases of quartz, mullite, and maghemite or magnetite by the use of PDFgui [159] and refinement of the scale factor, atomic displacement (u_i) and lattice parameters (*a*, *b* and *c*) over the *r*-range 0.01 - 49.99 Å [74].

Neutron data were collected at the Nanoscale-Ordered Materials Diffractometer (NOMAD) beamline located at the Spallation Neutron Source (SNS), Oak Ridge National Laboratory (ORNL). Powder samples were loaded into quartz capillaries and each data set was collected for 2 hours total run time, in 30 min segments, at ambient laboratory temperature. An empty capillary was also measured. To produce each total scattering function and associated PDF, the measured scattered intensities were normalized by scattering from a vanadium rod and subjected to a background subtraction from the empty capillary using the IDL software developed for the NOMAD instrument [160]. As was the

case for X-rays, the neutron PDFs were obtained via a sine Fourier transform of the total scattering function, *S(Q)*, using a Q_{max} of 28 Å^{-1} and Q_{min} of 0.5 Å^{-1}. The instrument parameters for NOMAD were Q_{damp} and Q_{broad} of 0.0176 Å^{-1} and 0.0192 Å^{-1}, respectively [74].

For both X-ray and neutron datasets the Fourier transform of the total scattering was obtained as follows:

$$G(r) = \frac{2}{\pi}\int_{Q=Q_{min}}^{Q=Q_{max}} Q[S(Q)-1]\sin(Qr)\,dQ$$

where Q is the momentum transfer defined as:

$$Q = \frac{4\pi \sin\theta}{\lambda}$$

Reciprocal space analysis was carried out on the X-ray and neutron data, where the crystalline phases were identified using Diffrac.EVA software version 3.1 together with the PDF-2/Release 2013 RDB database [74].

3.3.1.5.1 Diffraction theory

Diffraction is an experimental technique whereby incoming radiation (usually X-rays, neutrons or electrons) are diffracted or scattered from the atoms within the sample [161]. Analysis of the diffracted particles/rays/waves provides information regarding the atomic correlations of the material (atom-atom distances, angles and so on) and therefore allows for atomic structure elucidation [20]. In this study case, only powder diffraction method was used and thereby presented.

Powder diffraction from a crystalline sample gives rise to "Bragg peaks" from crystallographic planes within the material, which are indicative of atoms evenly arranged in a regular structure [161]. This repetitive structure can be uniquely described by its basic building block, the "unit cell". The mathematics behind this form of experimental analysis is based on Bragg scattering. Bragg's law is shown in the following equation:

$$n\lambda = 2dsin\theta$$

where λ is the wavelength of the incoming rays (particles), n is an integer

corresponding to the order of reflection, d is the spacing between planes and θ is the angle between the incident rays and the scattering planes [20]. Hence, by measuring the diffracted rays at angle θ and knowing the wavelength, λ, the spacing between crystallographic planes, d, can be elucidated [161]. A schematic representation of the Bragg's law is given in Figure. 3.17.

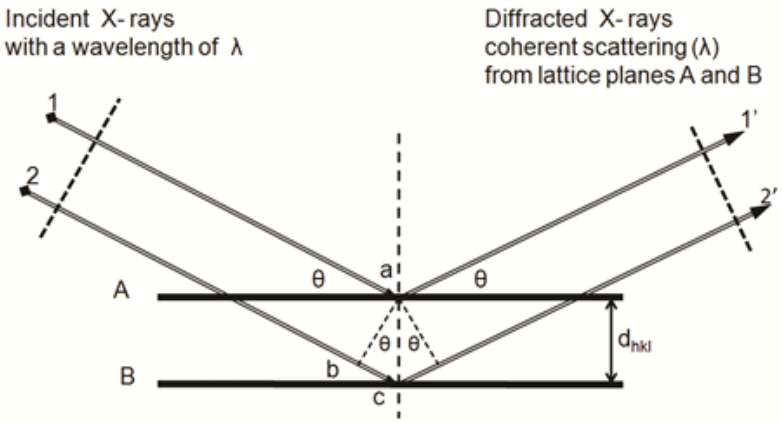

Figure. 3.17 Schematic representation of Bragg's Law: incoming parallel rays reflect from the crystallographic planes (horizontal lines) at an angle θ. Parallel lattice planes A and B showing the constructive interference of a front wave of parallel X-ray beam, 1 and 2 [161].

Synchrotron radiation enables faster acquisition of X-ray/neutron/electron diffraction datasets as compared with laboratory-based diffractometers due to the higher intensity of the incoming rays. This higher intensity, in combination with high-precision optics and detectors, also allows high-resolution powder patterns to be generated. Throughout this thesis the use of high-resolution diffraction has enabled accurate phase identification of samples on two synchrotron (X-ray and neutron) diffraction beamlines at different facilities [20].

The first beamline used to obtain high-resolution X-ray powder diffraction patterns was the 11-ID-B beamline at the Advanced Photon Source (APS), Argonne National Laboratory (ANL) while Nanoscale-Ordered Materials Diffractometer (NOMAD) beamline located at the Spallation Neutron Source (SNS), Oak Ridge National Laboratory (ORNL) was used to obtain high-resolution neutron power diffraction patterns. Those facilities will be described in the following Chapters.

3.3.1.5.2 Pair Distribution Function analysis

Conventional diffractometry is well suited to the structural analysis of crystalline

materials. However, any material that contains disorder, disrupting the crystallinity, will exhibit diffuse scattering. This form of scattering contains non-crystalline information (the amorphous contribution) about the material [162]. In a conventional diffraction pattern this form of scattering is present as broad humps or halos, which are typically removed along with the instrumental background in detailed structural analysis calculations.

Pair Distribution Function analysis takes into account this diffuse scattering through indirect analysis of the total scattering pattern, i.e., both Bragg and diffuse scattering [162]. After correcting for instrumental contributions the total scattering pattern is sine Fourier transformed, yielding the Pair Distribution Function (PDF). This function gives the probability of finding two atoms separated by the distance, *r*, as shown in the following equation:

$$G(r) = 4\pi r\rho_0(g(r) - 1)\ \frac{2}{\pi}\int_0^\infty Q[S(Q) - 1]\sin(Qr)\,dQ$$

In this equation *S(Q)* is the total scattering function, *G(r)* is the PDF and ρ_0 is the atomic number density in atoms/Å^3 [20].

The definition of the PDF given above is based on the assumption that all scattering measured is elastic, i.e., there is no energy loss or gain between the incident and outgoing waves/rays. X-ray and neutron powder diffraction data contain elastic and inelastic scattering, and coherent and incoherent scattering. The coherence of the scattering refers to whether there is a definite phase relationship between scattered waves allowing them to interfere constructively and destructively. For incoherent scattering there is no definite phase relationship between the scattered waves, and therefore they do not interfere. Since the structural information in the scattering comes about from interference between the scattered waves, only coherent scattering contains any structural information. Hence, the information contained in PDF analysis must come from elastically and coherently scattered rays [20].

The acquisition of high-resolution total scattering patterns has been carried out for both X-ray and neutron diffraction throughout this thesis.

High-resolution X-ray powder total scattering was carried out on 11-ID-B beamline at the Advanced Photon Source (APS), Argonne National Laboratory (ANL). At ANL, 11-ID-B is specifically dedicated to PDF measurements with area detectors. The instrument operates at high X-ray energies (58.66 keV, 86.7 keV) and is optimized for high throughput measurements and non-ambient/*in-situ* measurements. Typical configurations may involve a sample changer, cryostream, compact furnace/flow cell, compact pressure cells (< 15 GPa, under development), and single-crystal diffuse scattering (under development) [163].

Other facilities are also present at ANL like the 11-ID-C, D, etc. The 11-ID-C is used for scattering studies at extreme conditions. The high energy X-ray beam (115 keV) is highly penetrating and allows a wide coverage of reciprocal space over a small angular scattering range. This is particularly advantageous for experiments that require bulky sample environments (e.g., magnets, cryostats, levitator). The 11-ID-D provides laser-induced time-resolved (LITR) spectroscopic and scattering tools to probe electronic and structural changes along reaction pathways. These tools are used to probe complex hierarchical systems with potential applications in areas of energy conversion/storage such as solar cells, light emitting devices, molecular machines, or catalytic systems. Another sector is also present at ANL (Sector 8-ID), which is part of the APS X-ray Science Division and is equipped with two experiment enclosures: 8-ID-I is dedicated to the study of equilibrium fluctuations and fluctuations about the evolution to equilibrium condensed matter in the small-angle X-ray scattering (SAXS) geometry via X-ray photon correlation spectroscopy (XPCS) or X-ray intensity fluctuation spectroscopy (XIFS); 8-ID-E is dedicated to the study of ordering and kinetics at surfaces and interfaces via the technique of grazing incidence X-ray-scattering (GIXS) in both small-angle (GISAXS) and wide-angle (GIWAXS) regimes. 8-ID-E also hosts programs to measure equilibrium dynamics via XPCS at large wave vector transfers and at liquid surfaces [163].

Figure. 3.18 reports a schematic beamline layout for the 11-ID experiment enclosures.

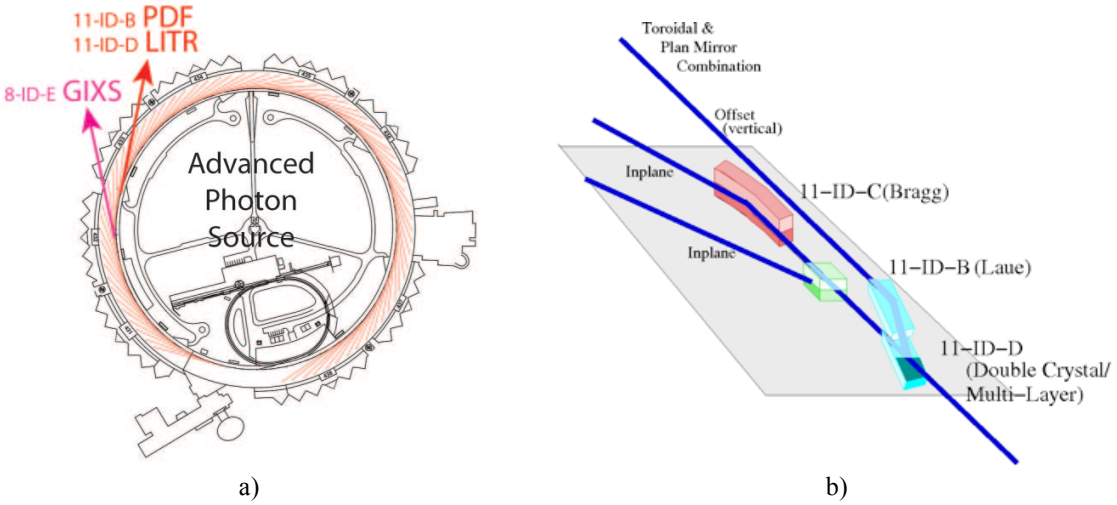

a) b)

Figure. 3.18 Schematic ANL plan (a); schematic layout of the 11-ID beamline (b) [163].

High-resolution neutron powder total scattering was carried out on the Nanoscale-Ordered Materials Diffractometer (NOMAD) beamline located at the Spallation Neutron Source (SNS), Oak Ridge National Laboratory (ORNL). NOMAD is a high-flux, medium-resolution diffractometer that uses a large bandwidth of neutron energies and extensive detector coverage to carry out structural determinations of local order in crystalline and amorphous materials. It enables studies of a large variety of samples ranging from liquids, solutions, glasses, polymers, and nanocrystalline materials to long-range-ordered crystals. The enhanced neutron flux at SNS, coupled with the advanced neutron optics and detector features of NOMAD, allows for unprecedented access to high-resolution pair distribution functions, small-contrast isotope substitution experiments, small sample sizes, and parametric studies [164]. Schematic arrangements for the NOMAD instrument are reported in Figure. 3.19 and Figure. 3.20.

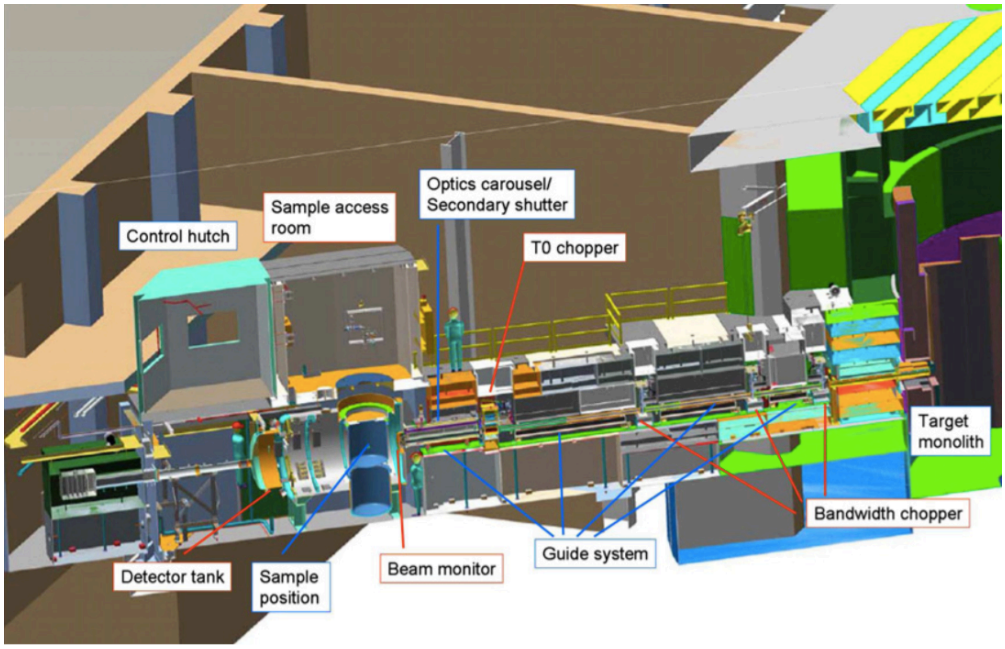

Figure. 3.19 Cut-away overview of the NOMAD beam layout. A person standing on the top of the shielding gives an idea of the scale. The distance from the moderator inside the target monolith to the sample position is 19.5 m [160].

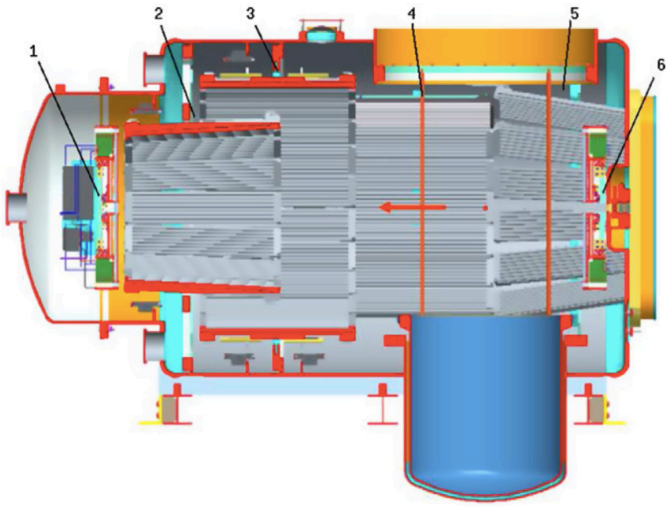

Figure. 3.20 Schematic view of the detector arrangement around the sample position. The neutron direction is indicated with an arrow, the sample position with a dot. 1 = current installed set of detectors, 2-5 = other detector banks [160].

3.3.1.6 Bulk density

Bulk density (g/cm^3) was determined by weighting the mass of the dried samples and by dividing it for their geometric volume. The drying procedure consisted in a oven heating up to 100 °C for 24 hours (or until the samples reached constant mass ± 0.1%).

3.3.1.7 Workability test

Workability test was performed on mortar at the fresh state according to EN 1015-3 [165]. The standard flow tests uses a standard conical frustum shape of mortar having a height of 60 mm with a top diameter of 60 mm and a bottom diameter of 100 mm. This mortar sample is placed on a flow table and dropped 15 times within 15 seconds. As the mortar is dropped, it spreads out on the flow table. The initial (d_i) and final diameters (d_f) of the mortar sample are used to calculate the flow. Flow is defined as the increase in diameter divided by the original diameter multiplied by 100, as in the following equation:

$$Flow = \frac{(d_f - d_i)}{d_i} \cdot 100$$

Laboratory mixed mortar should have a flow of approximately 110, while in the field mortar is usually mixed to a flow of about 130 - 150. The equipment used for this test is shown in Figure. 3.21.

a) b)

Figure. 3.21 Flow table (a); conical frustum and pestle (b).

3.3.1.8 Compressive and flexural mechanical strength

Mechanical tests were performed on prismatic samples with dimension of 40x40x160 mm^3. Flexural (three point bending mode) and compressive strengths were determined by an Amsler–Wolpert machine (maximum load: 100 kN) at a constant displacement rate of 50 mm/min. Stated flexural and compressive strengths are average values of 3 and 5 measurements, respectively. The tests were performed according to standard EN 196-1

[148] procedure.

Prisms were placed in the testing machine with one side face on the supporting rollers and with the longitudinal axis normal to the supports. The distance between supports is 100 ± 0.5 mm. The load was applied vertically by means of the loading roller to the opposite side face of the prism and increased smoothly at the rate of 50 ± 10 N/s until fracture. Flexural strength R_f was the calculated according to the following equation:

$$R_f = max\sigma_f = \frac{maxM}{W}$$

where:

- R_f = flexural strength (MPa);
- σ_f = maximum flexural stress (MPa);
- M = bending moment (N·mm);
- W = section modulus (mm^3).

The prism halves (after test of flexural strength) were tested in compression. The prism halves were centered laterally to the auxiliary platens of hard steel, which exactly determine the compressive area (because the prism halves have an irregular form). The size of the platens is 40x40 mm^2 and they are at least 10 mm thick. During loading the relative attitude of the upper and lower platens shall remain fixed. The resultant of the forces shall pass through the center of the specimen. The load has been smoothly increased until fracture and compressive strength ass calculated from the following equation:

$$R_c = max\sigma_c = \frac{F_c}{1600}$$

where:

- R_c = compressive strength (MPa);
- σ_f = maximum compressive stress (MPa);
- F_c = maximum load at fracture (N);
- 1600 = the area of the platens (40 x 40 mm^2).

3.3.1.9 Water Absorption

Water Absorption (WA%) at atmospheric pressure was determined on geopolymer and mortar samples according to UNI 7699 [166].

The sample is placed within a heater (GTherm 035) at a temperature of 100 °C and dried for 24 hours (or until reaching constant mass ± 0.1%) obtaining the value of the dry mass (m_0), then immersed in water for further 24 hours (or until reaching constant mass ± 0.1%), buffered with damp cloth and weighed, obtaining the weight in conditions of saturated surface dry condition (m_{SSD}).

The percentage of water absorption is obtained, then, through the following expression:

$$WA\% = \frac{m_{SSD} - m_0}{m_0} \cdot 100$$

This test gives an indication about the total open porosity.

3.3.1.10 Capillary absorption

Two different tests were performed to determine water absorption properties by capillarity. The first test was accomplished with a procedure similar to the one described in UNI EN 1015-18 [167] on prismatic samples after flexural test. First, the two half parts (about 40x40x80 mm^3) were longitudinally sealed with an epoxy resin, then the freshly fractured section of each sample was partially immersed in a 5 mm water head and sample mass was measured after 10 (W_1) and 90 (W_2) min of partial immersion. Capillary coefficient was then determined according to the formula:

$$C = 0.1 \cdot (W_2 - W_1) kg/m^2 \cdot min^{0.5}$$

and the height of water capillary penetration was measured at the end of the test by longitudinally splitting the samples.

The second test continued over 8 days and was performed according to UNI EN 15801 [168]. It consisted in monitoring at intervals the weight gain of pre-dried regular form samples, partially immersed in a constant 5 mm water head. The amount of water absorbed per unit area Q_i (kg/m^2) at time t_i is calculated as follows:

$$Q_i = [(m_i - \mathrm{m}_0)/A]$$

where m_i = mass at time t_i and m_0 = mass under pre-dried conditions, while A = area of the specimen in contact with water. For the determination of the capillary absorption curve, the calculated Q_i values were plotted as a function of $\sqrt{t}$.

3.3.1.11 Pore size distribution

Pore size distribution measurements were carried out on geopolymers by Mercury Intrusion Porosimetry (MIP) (Carlo Erba 2000) equipped with a macropore unit (Model 120, Fison Instruments). A mercury surface tension of 0.48 N/m and a contact angle of 141.3° were set for the MIP measurement [169]. Samples, about 1 cm^3, were cut by a diamond saw, dried under vacuum and kept under a P_2O_5 dried atmosphere in a vacuum dry box until testing.

The test gives information about the porous characteristics of a material: porosity, pore volume, pore size distribution and density. During a typical porosity analysis in a mercury porosimetry analyzer, a higher pressure is needed to force intrusion of mercury in smaller pores, whereas mercury intrusion in larger pores already occurs at low pressure. In this way a wide range of pore sizes can be explored and a pore size distribution can be obtained starting from 4 nm (pressure = 1000 MPa) up to approximately 800 μm. As a consequence, mercury porosimetry is extremely suitable for materials showing broad distributions of pore sizes.

The porosity of a material affects its physical properties and, subsequently, its behaviour in its surrounding environment. The adsorption, permeability, strength, density, and other factors influenced by a material's porosity determine the manner in which it can be appropriately used. Since mercury does not wet most substances and will not spontaneously penetrate pores by capillary action (and therefore is a non-wetting liquid with a high surface tension, that almost uniquely qualifies it for use in probing pore space), it must be forced into the pores by the application of external pressure. The required equilibrated pressure is inversely proportional to the size of the pores, only slight pressure being required to intrude mercury into large macropores, whereas much greater pressures are required to force mercury into small pores. Mercury porosimetry analysis is the progressive intrusion of mercury into a porous structure under stringently controlled pressures. From the pressure versus intrusion data, the instrument generates volume and

size distributions using the Washburn equation:

$$r = \frac{-4\gamma cos\theta}{P}$$

where:

- r = pore radius;
- γ = surface tension of liquid (480 mN/m);
- θ = contact angle of intrusion liquid (141.3°);
- P = pressure of liquid.

Clearly, the more accurate the pressure measurements, the more accurate the resulting pore size data. By measuring the volume of mercury that intrudes into the sample material with each pressure change, the volume of pores in the corresponding size class is known.

The volume of mercury that enters pores is measured by a mercury penetrometer (an electrical capacitance dilatometer). These devices are very sensitive and can detect a change in mercury volume of under 0.1μL. The dilatometer is constructed of glass (an insulator) and filled with mercury (a conductor). The stem of the dilatometer is a capillary that acts as a reservoir for the analytical volume of mercury. The stem is plated with metal (a conductor). The two conductors, mercury, and the metal plating, are separated by glass, thus forming a coaxial capacitor. As pressure forces mercury out of the capillary and into the sample, the mercury inside the capillary decreases and so is the capacitance. The decrease in capacitance, therefore, is proportional to the volume of mercury leaving the capillary with each change in pressure [170].

All the MIP equipment used in this work is shown in Figure. 3.22.

a)

b)

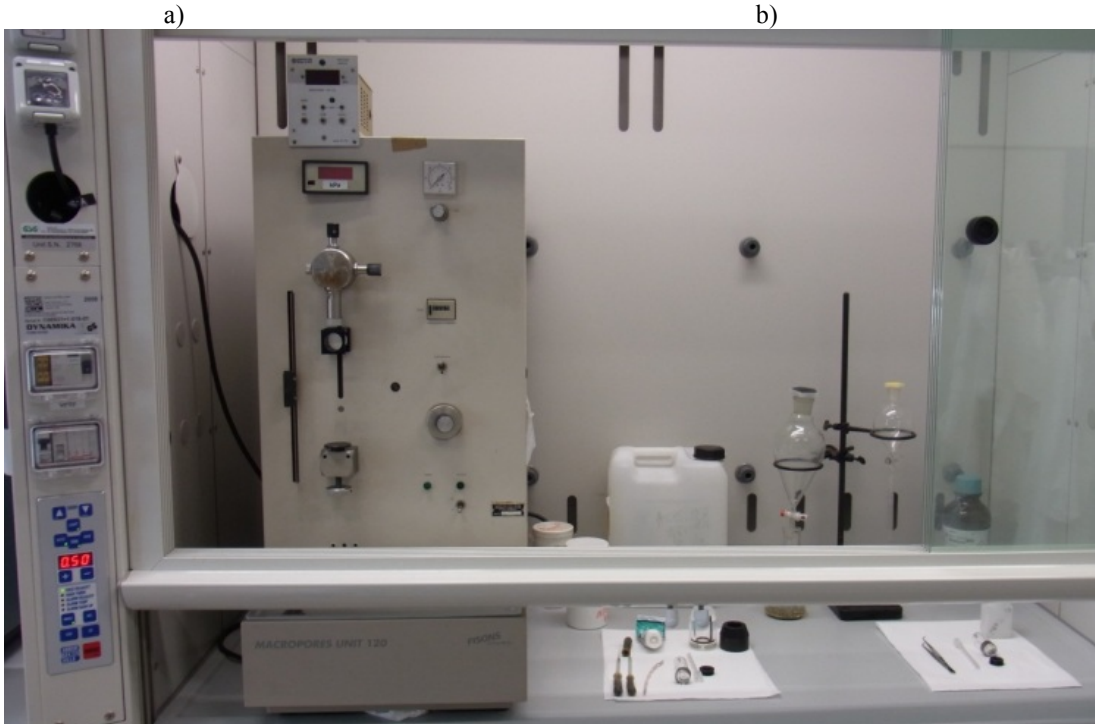

c)

Figure. 3.22 MIP equipment: dilatometer (a); micropore unit (b); macropore unit (c).

3.3.1.12 Dynamic elastic modulus

Dynamic elastic modulus (E_d) was calculated on mortar samples according to the following formula:

$$E_d = \rho V^2$$

where ρ is the sample's density and V is the pulse velocity, measured by a Matest instrument with 55 kHz transducers. Minimum of three readings was noted for each system and the average value was reported.

3.3.1.13 Shrinkage

Shrinkage was determined according to EN 12617-4 [171]. This test allows to determine the dimensional stability (shrinkage) resulting from any variations in the moisture content of the mortar and consists in measuring the linear variation after drying of prismatic specimens (40x40x160 mm^3) from 24 hours to 56 days after casting. Those specimens are cast in specific moulds according to the standard with compartments provided with hole in the center of each end face for inserting a pin measurement to be encapsulated in the sample.

After 48 hours from casting the specimens were removed from the molds, and the initial length L_0 and initial mass M_0 were obtained. All measurements relating to the length were carried out with a precision length comparator (Borletti model, Figure. 3.23) which guarantees an accuracy of measurement of ± 0.001 mm. Further length and weight measurements were then carried out after 3, 7, 14, 28, 56 days from casting, and it was possible to calculate the variation of a specific length (c) and the variation of specific mass (m) with the following formulas:

$$c = \frac{\Delta L \cdot 100}{L_g}$$

where:

- c = specific length variation (%);
- $\Delta L = L_0 - L_g$;
- L_g = samples length at specific day;

$$m = \frac{\Delta M \cdot 100}{M_g}$$

where:

- m = specific mass variation (%);
- $\Delta M = M_0 - M_g$;
- M_g = samples mass at specific day.

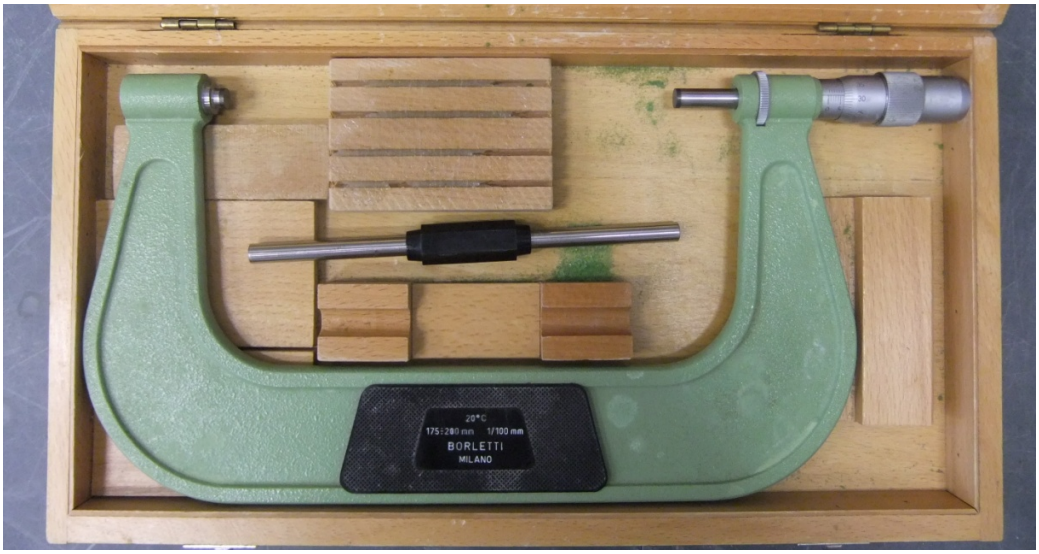

Figure. 3.23 Precision length comparator.

3.3.1.14 Weight loss after calcining

Weight loss (%) of geopolymers was measured after calcining at 800 °C in an electric muffle furnace (Catterson-Smith model, Figure. 3.24). The thermal treatment was in 3 steps: heating up to 800 °C (heating rate: 8 °C/min), hold for 2 hours at 800 °C and then furnace cooling naturally to room temperature.

Figure. 3.24 Electric muffle furnace.

3.3.1.15 Termogravimetrical Analysis

Thermogravimetrical Analysis (TGA) was performed on geopolymers using a TGA

Q50, TA Instrument (Figure. 3.25). Approximately 40 mg of the sample, previously milled and dried at 80 °C for 1 hour, were placed in a platinum pan and heated up to 900 °C with a constant heating rate of 20 °C/min under a nitrogen atmosphere. Pre-drying treatment was carried out in order to eliminate free water superficially adsorbed on sample surfaces thus allowing a better comparison of each sample's weight loss.

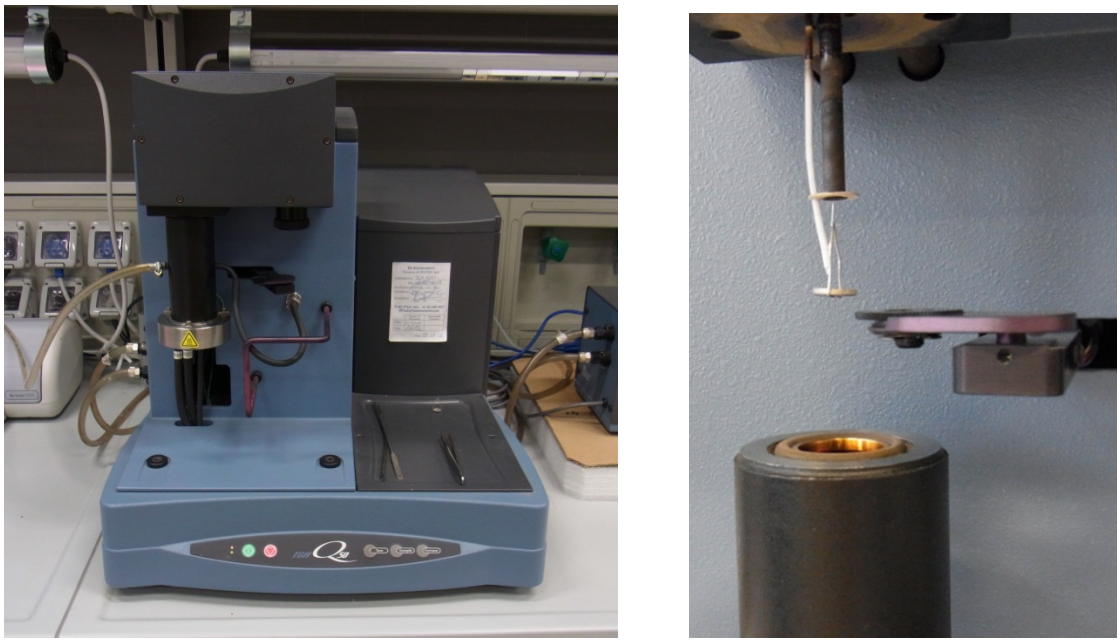

a) b)

Figure. 3.25 TGA equipment: Q50, TA Instrument (a); platinum crucible for sample analysis (b).

TGA is a method of thermal analysis in which changes in physical and chemical properties of materials are measured as a function of increasing temperature (with constant heating rate), or as a function of time (with constant temperature and/or constant mass loss) [172]. TGA can provide information about physical phenomena, such as second-order phase transitions, including vaporization, sublimation, absorption and desorption. Likewise, TGA can provide information about chemical phenomena including chemisorptions, desolvation (especially dehydration), decomposition, and solid-gas reactions (e.g., oxidation or reduction) [172].

TGA is commonly used to determine selected characteristics of materials that exhibit either mass loss or gain due to decomposition, oxidation, or loss of volatiles (such as

moisture). Common applications of TGA are: materials characterization through analysis of characteristic decomposition patterns, studies of degradation mechanisms and reaction kinetics, determination of organic content in a sample, and determination of inorganic (e.g., ash) content in a sample, which may be useful for corroborating predicted material structures or simply used as a chemical analysis.

3.3.1.16 Dilatometric analysis

Dilatometric analyses were conducted using an horizontal optical dilatometer ODLT-Expert System Solutions (Figure. 3.26). Measurements were conducted over a temperature range of 20 - 1000 °C with a heating rate of 10 °C/minute. After this first thermal treatment samples where subjected to a second treatment up to 1200 °C with a heating rate of 10 °C/minute.

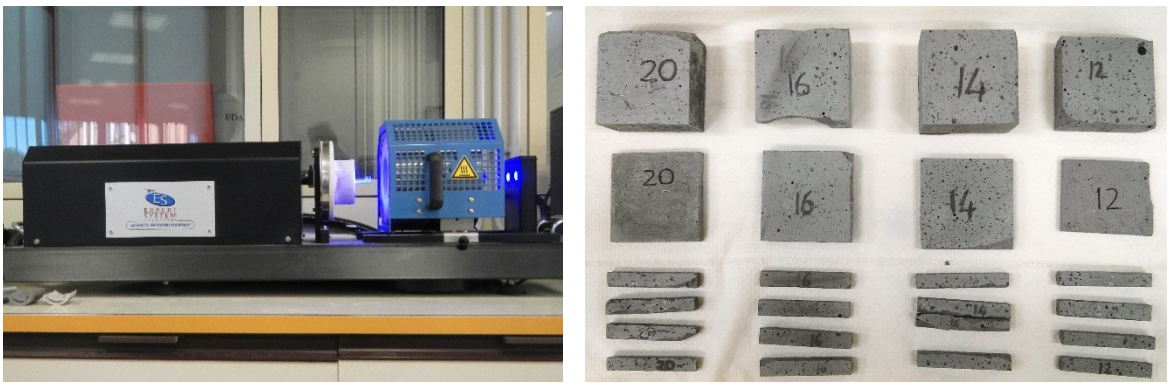

a) b)

Figure. 3.26 Optical dilatometer ODLT-Expert System Solutions (a); selected samples for dilatometric analysis (b).

An optical dilatometer is a non-contact device able to measure thermal expansions or sintering kinetics of any kind of materials. Unlike traditional push rod dilatometer, it can push up to the dilatometric softening of the specimen throughout the entire industrial firing cycles (up to 1750 °C on sample). The instrument is capable to determine expansion and shrinkage curve, coefficient of thermal expansion, glass transition temperature and dilatometric softening point. It is also able to handle small dimensional variations, thus, it is the ideal instrument to study all materials that present reduced or considerable expansions and contractions [173].

The instrument consists of three principal units mounted on an optical bench: two beams of blue light, an electric furnace with sample carriage and an observation unit with two digital cameras and a recording facility. The monochromatic light source illuminates the specimen. Some of the light is reflected by the specimen and interferes with the incoming light, creating optical interference fringes. As the specimen contracts or expands, there is a proportional movement of the interference fringes, which can be measured using a camera system. The measurement resolution is determined by the wavelength of the light, and is typically 0.5 μm for blue light [174].

Moreover, the optical technique simplifies the preparation of sample pieces: a very precise parallelism between the two ends of the specimen is not strictly required, the dimensions of the sample do not need to be very precise and the real ones are measured and introduced into the software before the test begins. Then, the software automatically aligns the optical paths to the ends of the sample [173].

3.3.1.17 Accelerated carbonation

The test consisted in exposing samples to an accelerate carbonation in a carbonation chamber (CO_2 = 1%, T = 30 °C, R.H. = 65%) for a predicted test time.

3.3.1.18 Carbonation depth

According to EN 13295 [175], carbonation depth is assessed using a solution of phenolphthalein indicator (1% concentration in ethylic alcohol) that appears pink in contact with alkaline concrete with pH > 9 and colorless at lower levels of pH. The test was carried out by spraying the indicator on freshly exposed surfaces.

3.3.1.19 pH measurements

The pH value of the pore electrolyte in the samples innermost core was estimated by leaching technique consisting in measuring the pH of the leachate solution of 5 g ground samples mixed in 5 cm^3 distilled water, at ambient temperature. The pH of the obtained leachate solution was deemed an acceptable approximation of the pH of the mortar pore electrolyte [176]. The pH was measured using a portable pH meter (Eutech Instrument, Cyberscan pH 310, Figure. 3.27) calibrated for high pH values.

Figure. 3.27 pH meter, Eutech Instrument, Cyberscan pH 310.

3.3.1.20 Raman analysis

The corrosion products formed on the rebars embedded in reinforced slabs were analyzed through Raman measurements by a Renishaw Raman Invia instrument, under conditions that avoided the thermal degradation of iron compounds. An Ar+ laser (514.5 nm) was adopted, with integration time (*t*) of 10 s, number of accumulations (*n*) of 4 and laser power (Pout) of 3 mW.

Raman spectroscopy is a spectroscopic technique used to observe vibrational, rotational, and other low-frequency modes in a system. Raman spectroscopy is commonly used in chemistry to provide a fingerprint by which molecules can be identified. It relies on inelastic scattering, or Raman scattering, of monochromatic light, usually from a laser in the visible, near infrared, or near ultraviolet range. The laser light interacts with molecular vibrations, phonons or other excitations in the system, resulting in the energy of the laser photons being shifted up or down. The shift in energy gives information about the vibrational modes in the system [177].

3.3.1.21 Total chloride content and diffusion coefficient

Two different tests were performed to analyze chlorides ingress throughout the mortars.

The first test mainly takes in account chlorides penetrated in the mortars by capillary suction. At specific timing the bare mortar surface was cut from main sample by drilling in order to measure the chloride concentration at different time intervals (as done for

slabs, see Figure. 3.8) and at different depths variation from the inner to the outer core of each sample (as done for cylinders, see Figure. 3.13).

The second test takes in account chlorides penetrated by diffusion and was performed on cubes (see Figure. 3.11) exposed to 165 g/l NaCl solution (2.8 M, according to ASTM C1556 [151]) by determining the values of surface concentration at eight recommended depth intervals (from 0 - 1 mm to 20 - 25 mm) at the end of the predicted exposure time (38 days). Apparent chloride diffusion coefficient (D_a, m^2/s) was determined by fitting chloride profiles to the error-function solution according to Fick's second law.

For both analyses, the total chloride content measurements were carried out on powdered samples according to ASTM C1152/C1152M [178] and ASTM C114 [179], by potentiometric titration.

3.3.2 Electrochemical tests

Electrochemical tests were performed by a 273A PAR instrument and consisted in corrosion potential (E_{cor}) and polarization resistance (R_p) measurements, always carried out on all the embedded rebars (4 repetitions). Before each potentiostatic test, E_{cor} was measured both versus the inner Ti quasi-reference electrode and versus an external Saturated Calomel Electrode (SCE), applied on the mortar surface in correspondence of the rebar. An interlaying wet pad minimized the ohmic drop. The software used to set the setup is CorrWare, while for data processing CorrView2 was used.

The polarization resistance values were obtained by a potentiostatic method, that is by applying an anodic 20 mV potentiostatic step lasting 300 s and by measuring the obtained final constant anodic current. Corrections for ohmic drop were not necessary because, as assessed by preliminary Electrochemical Impedance Spectroscopy (EIS) tests, the ohmic drop between the working and quasi-reference electrodes was always negligible with respect to the obtained R_p values.

3.3.2.1 Polarization Resistance test

Linear Polarization Resistance (LPR) is a quick, nondestructive testing technique commonly used in material corrosion studies to gain corrosion rate data. For this method the material is polarized, typically on the order of ± 10mV, relative to its Open Circuit

(OC) potential, which is the potential measured when no net current is flowing. As the potential of the material (working electrode) is changed, a current will be induced to flow between the working and counter electrodes, and the material's resistance to polarization can be found by taking the slope of the potential versus current curve. This resistance can then be used to find the corrosion rate of the material using the Stern-Geary equation.

An electrode is polarized when its potential is forced away from its value at open circuit or corrosion potential. Polarization of an electrode causes current to flow due to electrochemical reactions it induces at the electrode surface. The polarization resistance R_p is defined by the following equation:

$$R_p = \frac{\Delta E}{\Delta I}$$

where, ΔE is the variation of the applied potential around the corrosion potential and ΔI is the resulting polarization current.

Polarization resistance behaves like a resistor and can be calculated by taking the inverse of the slope of the current potential curve at open circuit or corrosion potential. During the polarization of an electrode, the magnitude of the current is controlled by reaction kinetics and diffusion of reactants both towards and away from the electrode.

In the Butler-Volmer equation E is the applied potential and i the measured current density:

$$i = i_{corr} = \left(e^{2.303\frac{\eta}{b_a}} - e^{2.303\frac{\eta}{b_c}} \right)$$

$$\eta = E - E_{corr}$$

The overpotential, η, is defined as the difference between applied potential and the corrosion potential E_{corr}, which is the open circuit potential of a corroding metal. The corrosion current, i_{corr}, and the Tafel constants b_a and b_c, can be measured from the experimental data.

For small η, i.e., for potentials close to corrosion potential, the above equation can be reduced to:

$$i_{corr} = \frac{1}{2.3} \frac{b_A b_C}{(b_A+b_C)} \left(\frac{\Delta I}{\Delta E}\right)_{E=Ecorr}$$

Or, when the expression is rearranged:

$$R_p = \frac{1}{2.3} \frac{b_A b_C}{(b_A+b_C)} \left(\frac{1}{i_{corr}}\right)$$

which can be rewritten using the Stern-Geary constant:

$$i_{corr} = \frac{B}{R_p}$$

If the Tafel slopes are known, it is possible to can calculate the corrosion currents from the polarization resistance R_p using the above equations. If the Tafel slopes are not known (e.g., when corrosion mechanism is not known), it can still be used as a quantitative parameter to compare the corrosion resistance of metals under various conditions. High R_p of a metal implies high corrosion resistance and low R_p implies low corrosion resistance [180].

3.3.2.2 Electrochemical Impedance Spectroscopy

Electrochemical Impedance Spectroscopy (EIS) studies the system response to the application of a periodic small amplitude alternating current (*ac*) signal. These measurements are carried out at different *ac* frequencies and, thus, the name impedance spectroscopy was later adopted. Analysis of the system response contains information about the interface, its structure and reactions taking place there.

At the base of this method there is the concept of electrical resistance, which is the ability of a circuit element to resist the flow of electrical current. Ohm's law defines resistance in terms of the ratio between voltage, *E*, and current, *I*:

$$R = \frac{V}{I}$$

While this is a well-known relationship, its use is limited to only one circuit element - the ideal resistor. An ideal resistor has several simplifying properties:

- it follows Ohm's Law at all current and voltage levels;

- its resistance value is independent of frequency;
- *ac* current and voltage signals though a resistor are in phase with each other.

However, the real world contains circuit elements that exhibit much more complex behaviour. These elements force to abandon the simple concept of resistance, and in its place impedance is used, which is a more general circuit parameter. Like resistance, impedance is a measure of the ability of a circuit to resist the flow of electrical current, but unlike resistance, it is not limited by the simplifying properties listed above [181].

Electrochemical impedance is usually measured by applying an *ac* potential to an electrochemical cell and then measuring the current through the cell. Assuming applying a sinusoidal potential excitation, the response to this potential is an *ac* current signal. This current signal can be analyzed as a sum of sinusoidal functions (a Fourier series).

Electrochemical impedance is normally measured using a small excitation signal. This is done so that the cell's response is pseudo-linear. In a linear (or pseudo-linear) system, the current response to a sinusoidal potential will be a sinusoid at the same frequency but shifted in phase (see Figure. 3.28) [181].

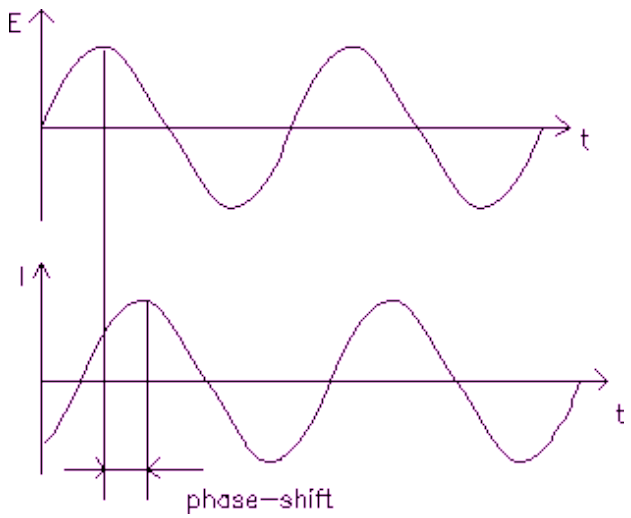

Figure. 3.28 Sinusoidal current response in a linear system [181].

The excitation signal, expressed as a function of time, has the form:

$$E_t = E_0 \sin(\omega t)$$

where E_t is the potential at time t, E_0 is the amplitude of the signal, and ω is the radial frequency. The relationship between radial frequency ω (expressed in radians/second) and

frequency *f* (expressed in hertz) is:

$$\omega = 2\pi f$$

In a linear system, the response signal, I_t, is shifted in phase (φ) and has a different amplitude than I_0 :

$$I_t = I_0 \sin(\omega t + \varphi)$$

An expression analogous to Ohm's Law allows to calculate the impedance of the system as:

$$Z = \frac{E_t}{I_t} = Z_0(\cos\varphi + j\sin\varphi) = Z^I + jZ^{II}$$

The expression is composed of a real (Z^I) and an imaginary part (Z^{II}). If the real part is plotted on the x-axis and the imaginary part is plotted on the y-axis of a chart, it is possible to get a "Nyquist plot" (see Figure. 3.29). In this plot the y-axis is negative and each point corresponds to the impedance at one frequency.

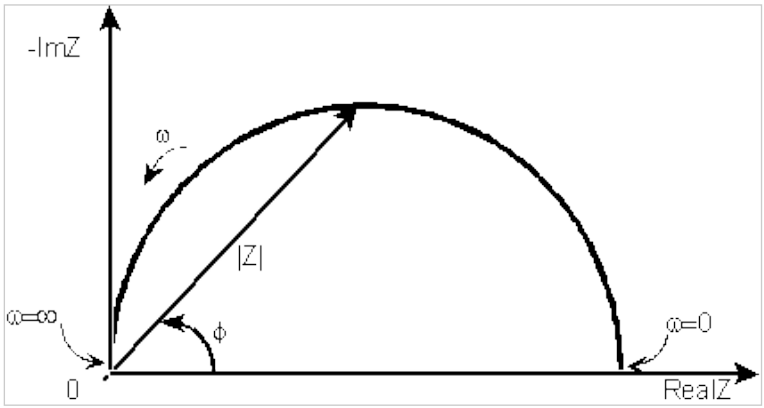

Figure. 3.29 Nyquist plot with impedance vector [181].

From a theoretical point of view, the situation of a reinforcing rebar embedded in a mortar (or more generally in a concrete) that starts to corrode, should be represented, in a Nyquist plot, by three semicircles more or less well defined and distinguishable; specifically, a half circumference for the cement at high frequencies (> 104 Hz), one for the corrosion process at low frequencies (< 102 - 101 Hz) and one for the corrosion products at intermediate frequencies (104 - 102 Hz).

For the impedance determination the software Zplot was used by applying an alternating potential of ± 10 mV in a frequency spectrum from $1 \cdot 10^{-5}$ to $1 \cdot 10^{-3}$ Hz. The software for data processing is ZView which allows to obtain the polarization resistance R_p.

4 EXPERIMENTAL RESULTS AND DISCUSSION: FLY ASH

This Chapter presents the comparative results obtained from the characterization of the different types of fly ash used in this study. The first part is dedicated to the analysis of the main physical-chemical and morphological differences between IFA and AFA, including their mineralogical phase composition. The second part gives an insight on the variability in aluminosilicate glass chemistry of the considered fly ashes, extending the analysis to other types of precursors (five FA in total) through the use of X-ray and neutron Pair Distribution Function analysis. Results have been discussed in light of the complementary information provided by the two methods in order to give a comprehensive overview of FA structure at the nanoscale. The obtained experimental results fill a deficit in literature in the atomic structure and associated variability for class F FA, which is extensively used in several industrial applications including as raw material in alkali-activated cements.

4.1 IFA and AFA main characterization

Figure. 4.1 shows the particle size distribution of the two fly ash samples while Figure. 4.2 shows their morphology. Both the fly ashes were primarily composed of spherical shaped particles with the AFA being finer than IFA with a D_{50} of 15.0 μm compared to 22.1 μm.

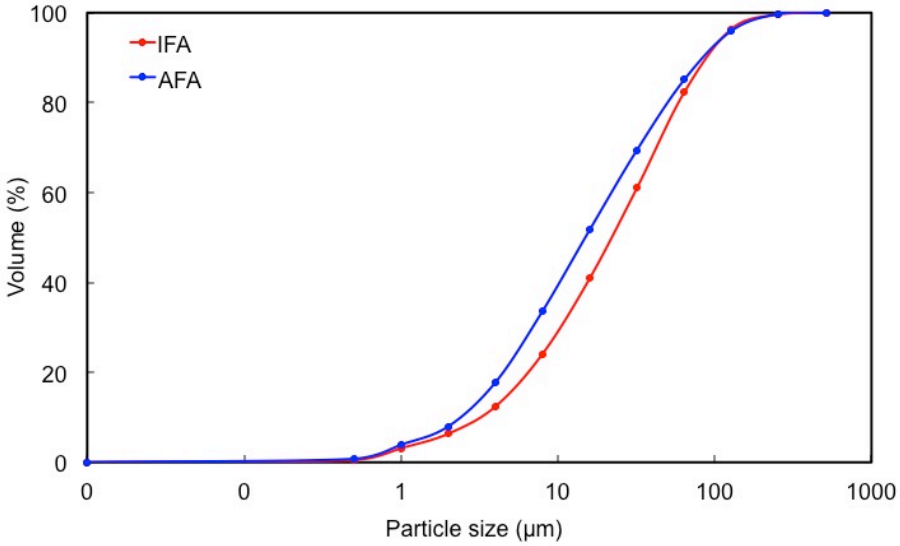

Figure. 4.1 Particle size distribution of IFA and AFA samples [44].

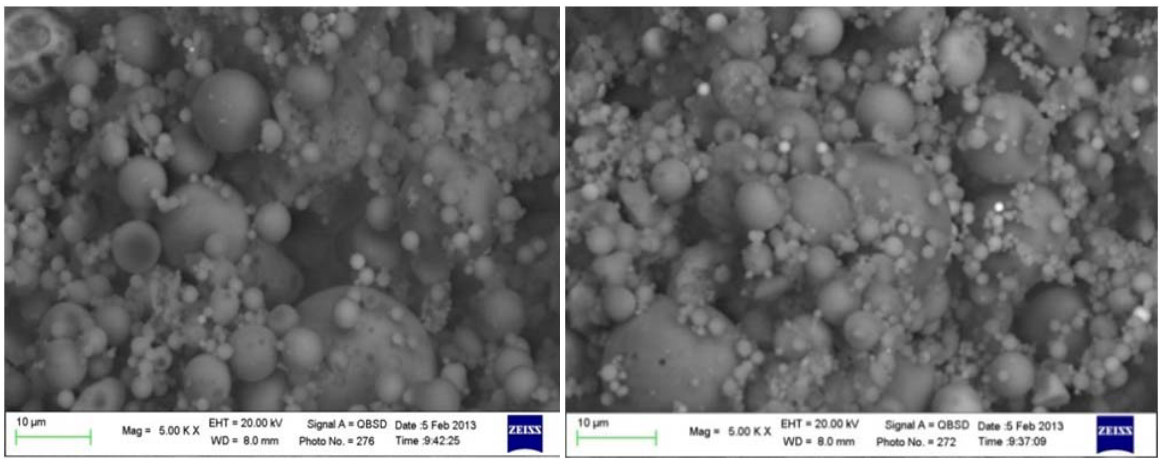

a) b)

Figure. 4.2 SEM images of IFA (a) and AFA (b) [44].

Table. 4.1 shows the composition, as oxides, of both the fly ashes. They have similar levels of SiO_2, K_2O, Na_2O, MgO and TiO_2 but IFA is richer in Al_2O_3 and CaO and poorer in Fe_2O_3.

The XRD pattern of IFA (Figure. 4.3) clearly shows crystalline phases of quartz, mullite and maghemite plus a broad amorphous hump in the 2θ region between 10° and 30°. The amorphous and crystalline phase content of both IFA and AFA are presented in Table. 4.2. The IFA was found to have 65.32 ± 0.75 wt.% amorphous phase, made up of SiO_2 (35.1 wt.%), Al_2O_3 (13.5 wt.%), CaO (6.6 wt.%, Fe_2O_3 (1.3 wt.%) and other oxides (8.8 wt.%). It is worth highlighting that none of the calcium oxide in the IFA was detectable as crystalline material by XRD and hence is included in the amorphous component. The amorphous phase of AFA was 53.49 ± 0.45 wt.%, composed of SiO_2 (20.9 wt.%), Al_2O_3 (15.4 wt.%), Fe_2O_3 (9.1 wt.%) and other oxides (8.09 wt.%), and crystalline phases included quartz, mullite, magnetite and hematite (Figure. 4.4) [182].

Oxide	IFA (wt.%)	AFA (wt.%)
SiO_2	49.37	48.21
Al_2O_3	29.23	25.01
TiO_2	1.59	1.30
Fe_2O_3	2.71	15.20
CaO	6.63	1.67
MgO	1.05	1.02
K_2O	0.60	0.60
Na_2O	0.05	0.06
BaO	0.07	0.12
Cr_2O_3	0.02	0.01
SO_3	0.33	0.43
LOI	3.28	0.51
Insoluble residue	5.07 (black)	5.86 (black)

Table. 4.1 Fly ash composition (oxide wt.%) [44].

Phase	IFA (wt.%)	AFA (wt.%)
Amorphous	65.32 ± 0.75	53.49 ± 0.45
Quartz	8.83 ± 0.19	26.19 ± 0.39
Mullite	21.13 ± 0.51	15.80 ± 0.18
Maghemite	1.44 ± 0.17	/
Magnetite	/	2.51 ± 0.83
Hematite	/	1.50 ± 0.64

Table. 4.2 Crystalline and amorphous phase content of IFA and AFA (wt.%) [44].

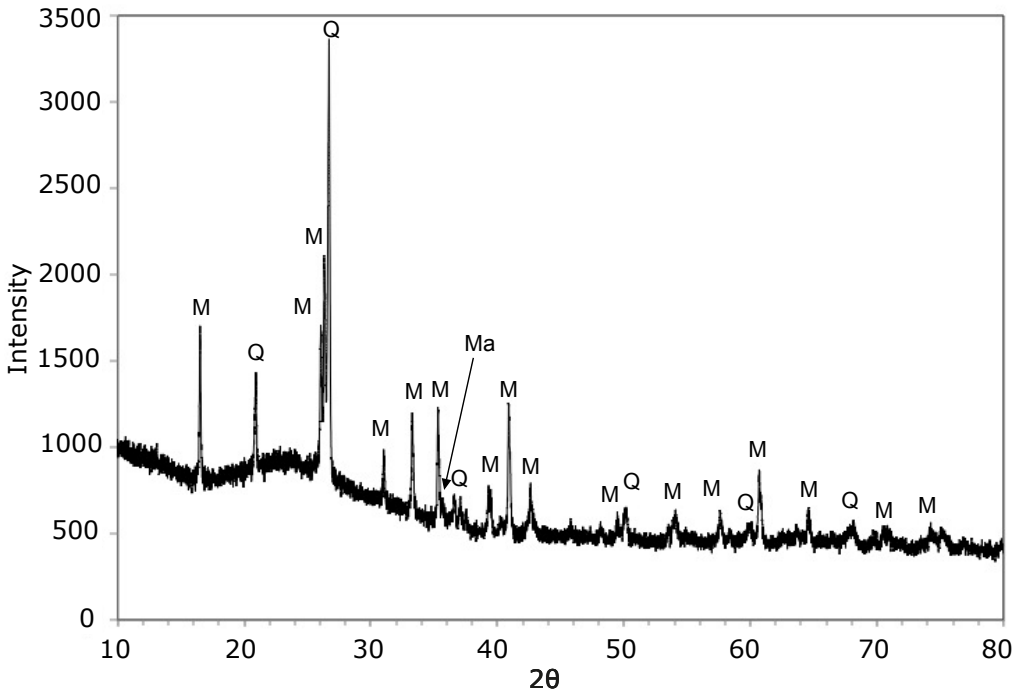

Figure. 4.3 XRD pattern of IFA (M = mullite (PDF #00-015-0776); Q = quartz (PDF #04-012-0490); Ma = maghemite (PDF #00-039-1446)) [44].

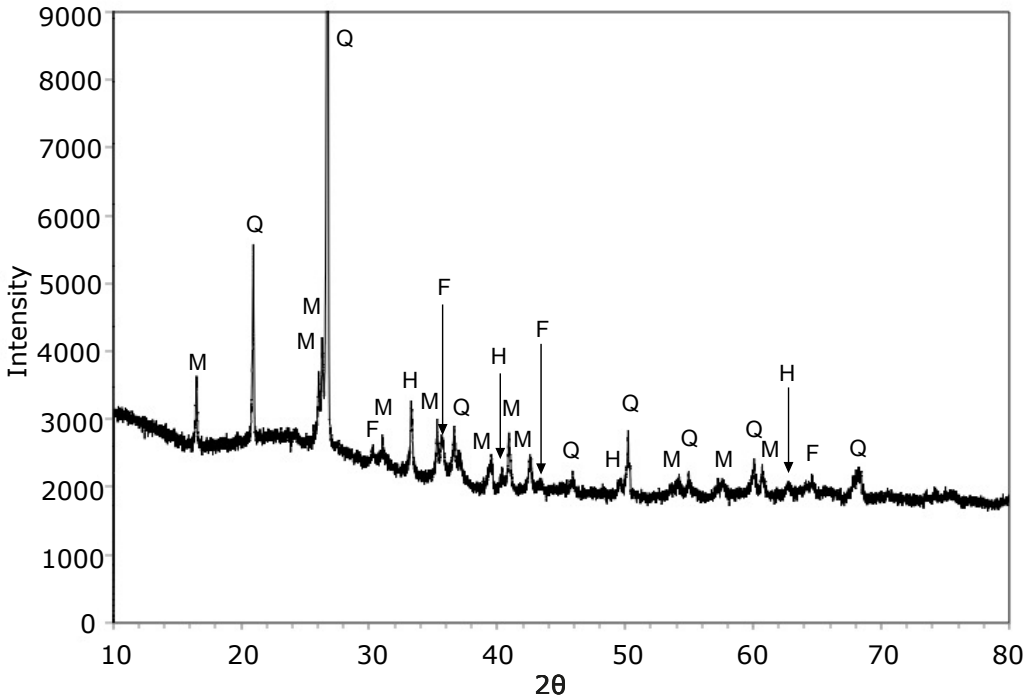

Figure. 4.4 XRD pattern of AFA (M = mullite (PDF #00-015-0776); Q = quartz (PDF #04-012-0490); F = magnetite (PDF #04-012-7038); H = hematite (PDF #00-033-0664)) [44].

4.2 Reciprocal space X-ray and neutron data

A comparison of the FA reciprocal space diffraction patterns, with the major crystalline phases identified, is presented in Figure. 4.5 and Figure. 4.6, where both X-ray (Figure. 4.5) and neutron data (Figure. 4.6) are reported. All the FA samples exhibit the typical amorphous broad hump between a Q value of 1 and 2.5 $Å^{-1}$, which corresponds to a 2θ region of 15° to 35° for Cu-Kα radiation. In addition to the amorphous component there are a number of crystalline phases present including quartz (SiO_2, PDF #00-001-0649), mullite ($Al_6SiO_2O_{13}$ PDF #00-001-0613) and iron oxides such as maghemite (Fe_2O_3, PDF #00-013-0458) or magnetite ($Fe^{2+}Fe^{3+}{}_2O_4$, PDF #00-019-0629) and, particularly in case of AFA and AMFA, hematite (Fe_2O_3, PDF #00-002-0915). Due to similarities in the Bragg scattering for maghemite and magnetite, it is difficult to distinguish between these two phases using reciprocal space analysis. In the proceeding sections it will be shown that by using PDF analysis it is possible to distinguish between these two iron oxide phases [74].

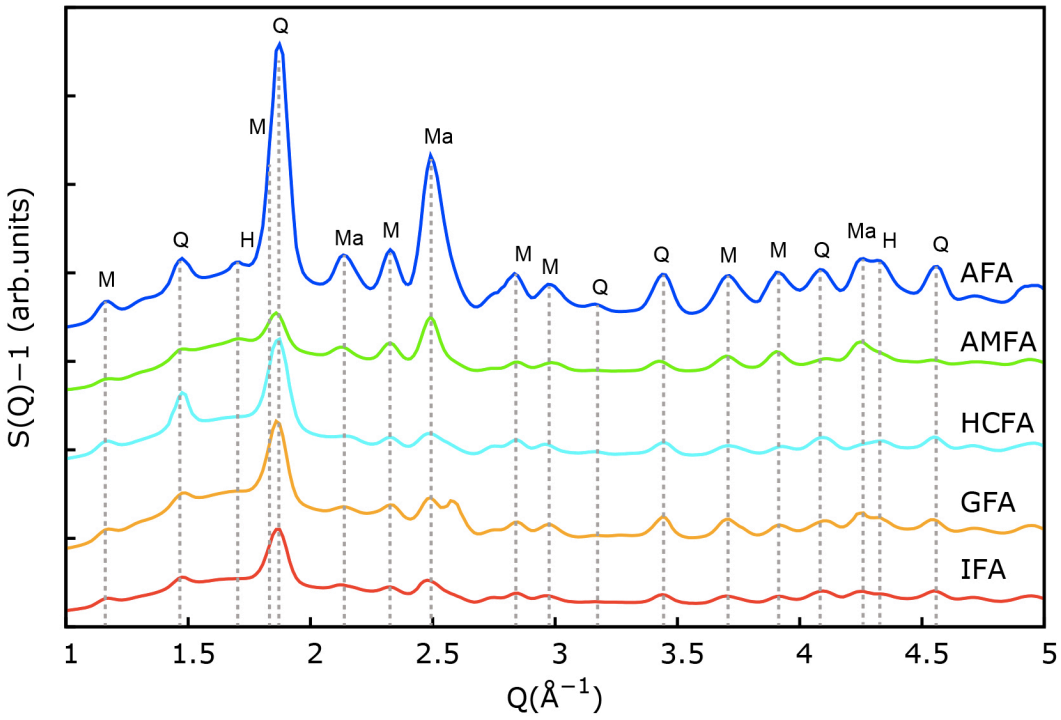

Figure. 4.5 X-ray synchrotron based diffraction patterns of the analyzed FA (Q = quartz (PDF #00-001-0649); M = mullite (PDF #00-001-0613); Ma = maghemite/magnetite (PDF #00-013-0458/#00-019-0629); H = hematite (PDF #00-002-0915)) [74].

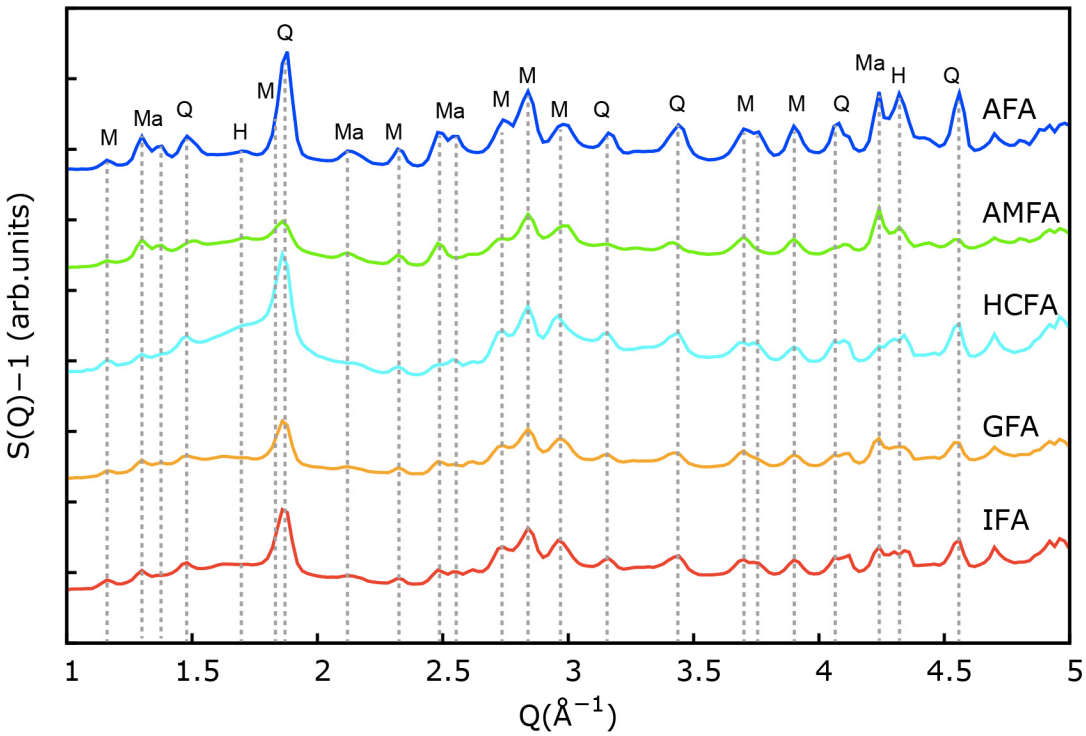

Figure. 4.6 Neutron diffraction patterns of the analyzed FA (Q = quartz (PDF #00-001-0649); M = mullite (PDF #00-001-0613); Ma = maghemite/magnetite (PDF #00-013-0458/#00-019-0629); H = hematite (PDF #00-002-0915)) [74].

4.3 X-ray Pair Distribution Functions

To isolate the amorphous glassy contributions in the X-ray PDFs, crystalline phases have been subtracted from the experimental data. The crystalline atomic structures chosen for the subtraction process were the one proposed by Gualtieri for the structure of quartz [183] (ICSD #90145), by Ďurovič for mullite [184] (ICSD #237026), by Shmakov et al. for maghemite [185] (ICSD #79196) and by Iizumi et al. for magnetite [186] (ICSD #35000). Concerning the iron oxide crystalline phases, maghemite was chosen for all FA samples except for AFA, where the magnetite structure was used for refinement since it led to better agreement with the experimental data (i.e., lower value for the goodness of the fit, R_w, as defined in PDFgui [159]). Given the low concentration of hematite in the samples, together with the relatively low Q space resolution (and therefore resolution in the PDFs), this phase was not chosen for the refinement, as preliminary analysis revealed that including this phase did not lead to a significant reduction in R_w. A spherical form factor (spherical particle diameter, *spdiameter*, as defined in PDFgui [159]) for both the mullite and maghemite/magnetite phases led to a reduced R_w value for all X-ray FA data,

indicating the possible presence of nanocrystalline mullite and maghemite/magnetite in these samples (with a spherical particle diameter of ~ 70 Å). Scale factors for the crystalline phases, as determined using PDFgui [159], are reported in Table. 4.3, while peaks positions for the nearest-neighbor atom-atom correlations before and after crystalline subtraction are reported in Table. 4.4.

Type of FA		Quartz	Mullite	Maghemite	Magnetite
IFA	X-ray	0.13	0.16	0.06	/
	Neutron	0.08	0.06	0.02	/
AFA	X-ray	0.19	0.23	/	0.14
	Neutron	0.12	0.06	/	0.05
GFA	X-ray	0.11	0.14	0.05	/
	Neutron	0.06	0.04	0.02	/
AMFA	X-ray	0.08	0.18	0.12	/
	Neutron	0.04	0.04	0.03	/
HCFA	X-ray	0.13	0.15	0.02	/
	Neutron	0.10	0.05	0.02	/

Table. 4.3 Scale factors after refinement of the principal crystalline components, obtained by refinement of the X-ray/neutron PDF data [74].

Type of FA		Atom-atom correlation						
		TR	T-O	Al-O	Fe-O /TR	O-O	T-T	Al-Al
IFA	B	1.26	1.63	1.92	2.22	2.63	3.06	/
	A	1.26	1.62	1.96	2.22	2.60	3.07	3.31
AFA	B	1.24	1.61	1.93	2.21	2.63	3.02	3.43
	A	1.21	1.61	1.95	2.19	2.63	3.05	3.33
GFA	B	1.25	1.62	1.94	2.20	2.62	3.03	3.42
	A	1.22	1.62	1.96	2.19	2.61	3.04	3.32
AMFA	B	1.22	1.62	1.94	2.20	2.62	3.03	3.42
	A	1.22	1.62	1.96	2.19	2.61	3.04	3.32
HCFA	B	1.28	1.62	1.92	2.19	2.62	3.06	/
	A	1.28	1.61	1.95	2.19	2.56	3.07	3.29

Table. 4.4 Peak position from X-ray PDFs before (B) and after (A) removal of the crystalline phases (TR = termination ripple) [74].

The results of the real space analysis are provided in Figure. 4.7 - Figure. 4.10. All the datasets have been normalized to the total amount of silicon and aluminum (Si + Al in molar %), as determined from the total molar content (%) of the major elements present in each FA composition (Si, Al, Fe and Ca) given in Table. 3.2. The PDF atom-atom

correlation that provides a direct measure of the total Si + Al content in the FA is the T-O correlation (tetrahedral Si and Al) located at ~ 1.62 Å, as visible in Figure. 4.8 and Figure. 4.10.

This normalization method assumes that all aluminum exists as IV-coordinated in the samples. This assumption is based on previous work investigating the coordination state of aluminum in aluminosilicate glassy phases [68,187,188], however, the coordination of aluminum in mullite, as well in the other crystalline phases such as sillimanite and kyanite, is known to also contain VI-coordinated sites [184,189]. Nevertheless, given the relative low percentages of these crystalline phases in comparison to the dominant glassy component, together with the fact that some of the aluminum in the crystalline phases exists as IV-coordinated, this normalization process is a good approximation for the behaviour of the scattering data [74].

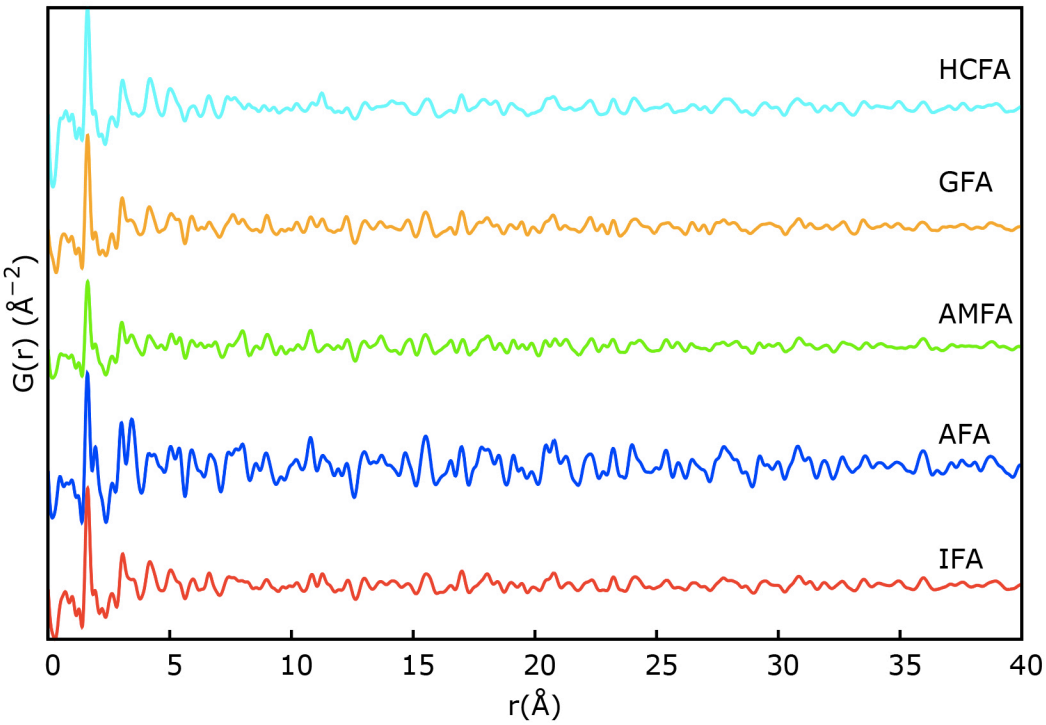

Figure. 4.7 X-ray PDFs of all the analyzed FA up to 40 Å [74].

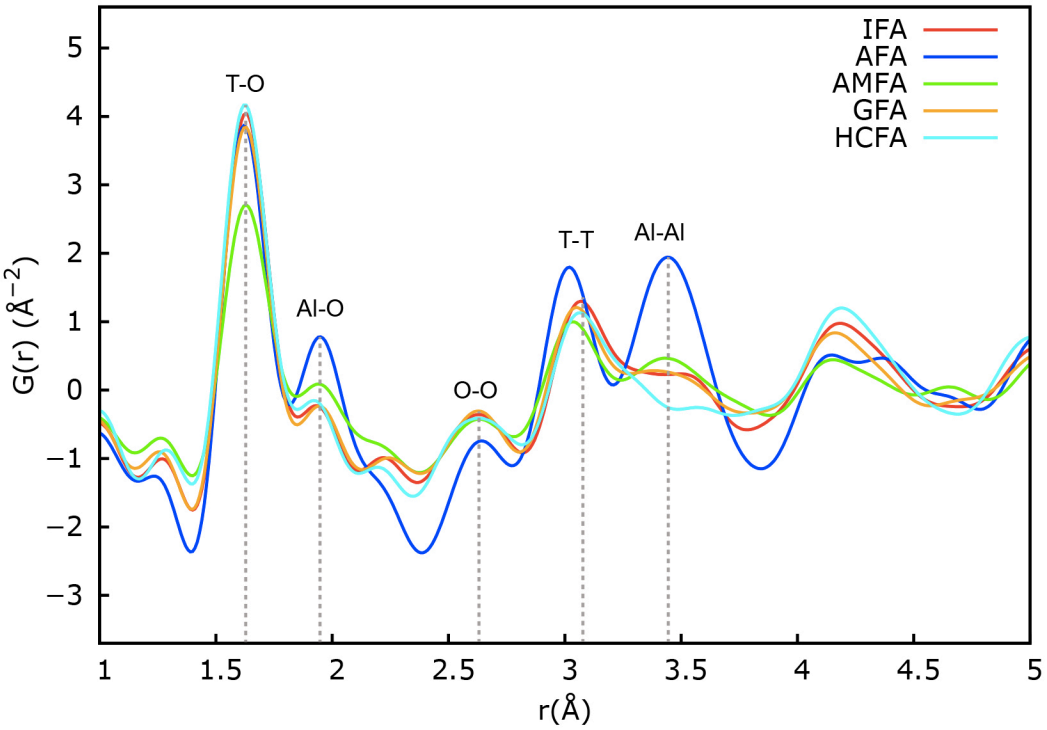

Figure. 4.8 X-ray PDFs of all the analyzed FA over the region $1 \leq r \leq 5$ Å [74].

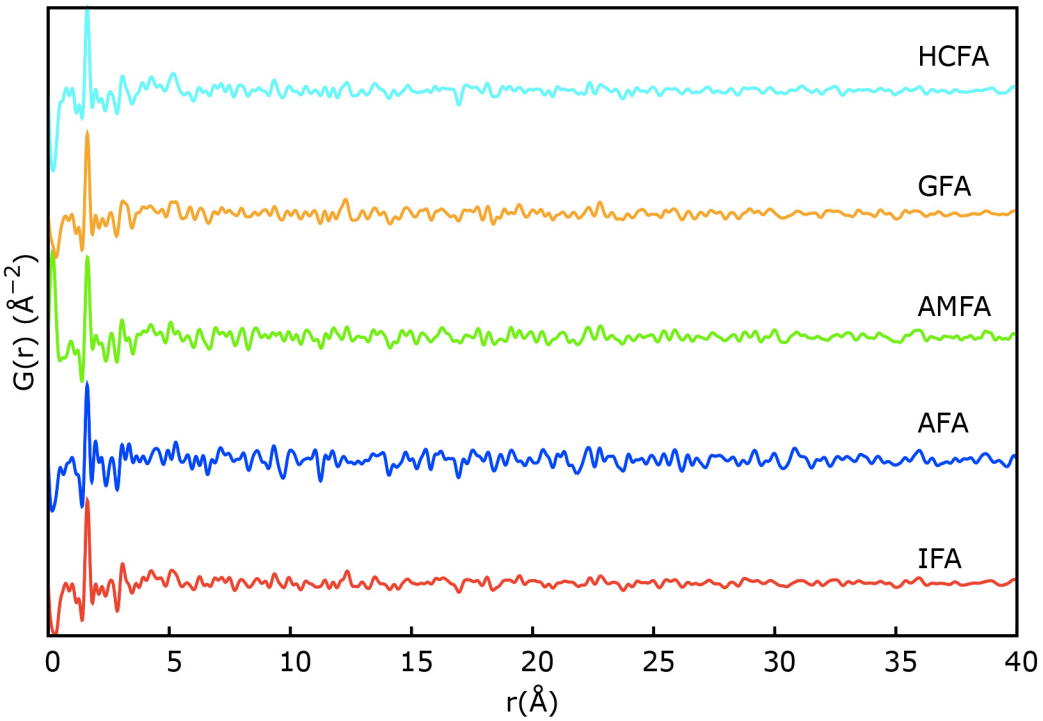

Figure. 4.9 X-ray PDFs of all the analyzed FA after subtraction of the crystalline phases up to 40 Å [74].

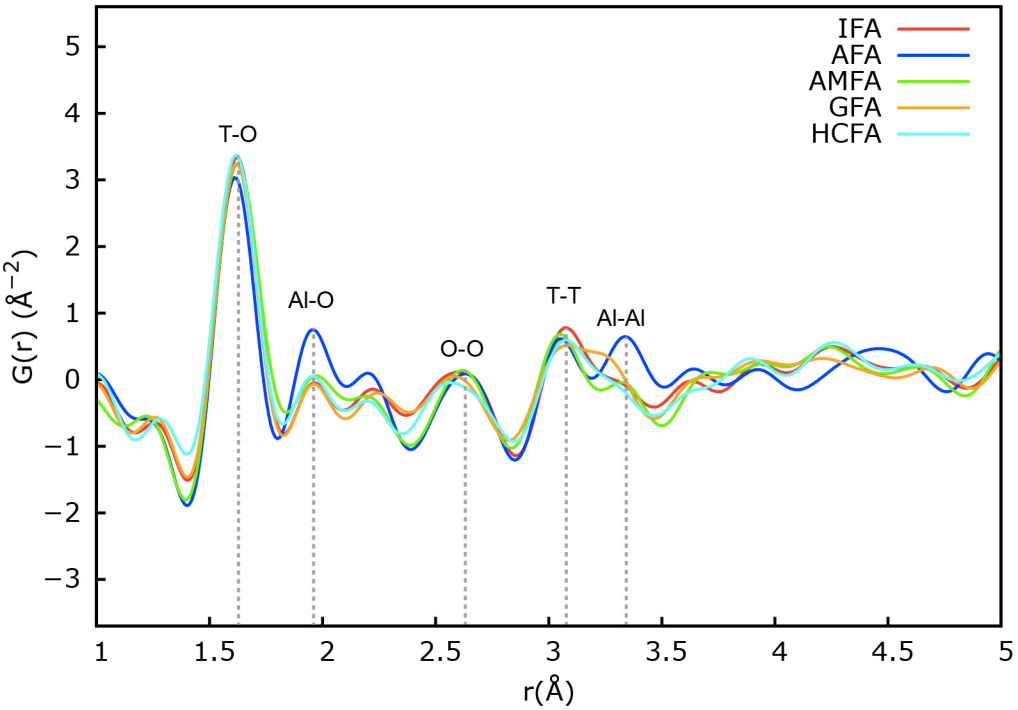

Figure. 4.10 X-ray PDFs of all the analyzed FA after subtraction of the crystalline phases over the region $1 \leq r \leq 5$ Å [74].

Figure. 4.7 and Figure. 4.8 display the X-ray PDFs of the FA samples measured in this study after Fourier transformation of the total scattering patterns, while Figure. 4.9 and Figure. 4.10 show the glassy aluminosilicate phases in the FA (crystalline phases have been subtracted). As is visible from the long-range information (Figure. 4.7 and Figure. 4.9, above ~ 10 Å) the intensity of the atom-atom correlations decreases relatively rapidly with increasing atom-atom distance (r), with the FA samples losing a significant amount of atomic ordering above 5 Å. This indicates a mostly amorphous structure for all the considered FA, especially after subtraction of the crystalline phases (Figure. 4.9 and Figure. 4.10 show). The short-range information ($1 \leq r \leq 5$ Å) is representative of the local bonding environments present in these amorphous systems (Figure. 4.8 and Figure. 4.10). It is clear from Figure. 4.8 and Figure. 4.10 that the majority of the disagreement in local atomic ordering in the samples is attributed to the presence of crystalline phases, and that, after removal of these phases, there is generally good agreement in the local atomic ordering of the glassy components, with no strong atom-atom correlations above 3.5 Å. The nearest-neighbor atom-atom correlation is present at ~ 1.62 Å in Figure. 4.10, which is attributed to the tetrahedral silicon and aluminum atoms (T-O). Previous literature on aluminosilicate glasses (which consist of mainly tetrahedrally-coordinated

silicon and aluminum) reveals that as the aluminum content increases, the average T-O distance increases (Si-O ~ 1.60 Å and Al-O ~ 1.75 Å) [190]. Hence, analysis of the T-O correlation in the FA glassy components in Figure. 4.10 reveals the presence of an aluminosilicate tetrahedral network similar to the one found by Meral et al. [68]. It is clear from Figure. 4.10 that the majority of the FA samples contain similar T-O correlations, however, the AFA sample contains an aluminosilicate glassy network with a slightly lower percentage of alumina, as seen by a shift in the T-O peak to lower *r* values.

The peak at ~ 1.95 Å in Figure. 4.8 can be attributed to an Al-O correlation (in case of VI-coordinated alumina present in mullite structure [184]) and/or to Fe-O for Fe^{3+} with coordination number of V [191-193] or even to a mix of Fe-O correlations as reported by Weigel et al. [194]. Although crystalline mullite has been removed from the PDF data in Figure. 4.10, it is possible that VI-coordinated Al is still present in the glassy phases as amorphous mullite [25] or amorphous alumina and the Al-O distance of 1.95 Å from Figure. 4.10 is in agreement with the mullite data proposed by Fisher [195]. As will become evident during the discussion of the neutron data (Section 4.4), the iron-containing correlations are present at different *r* values compared to the peaks visible in the X-ray data in Figure. 4.8 and Figure. 4.10. Therefore, the peaks at 1.95 Å and 3.42 Å in the X-ray PDF data are attributed to Al-O and Al-Al, respectively, for VI-coordinated aluminum existing in an amorphous alumina phase such as amorphous mullite. The atom-atom correlation at ~ 2.62 Å is attributed to O-O [68], while the correlation at ~ 3.08 Å is related to T-T environments (i.e., Si-Si and Si-Al, with Al-Al correlations absent due to Löwenstein's rule for tetrahedral aluminum) [68,196]. Subtle differences are seen in Figure. 4.10 for the T-T correlation according to the FA source. There is a slight shift to higher T-T correlations for IFA, which correlates with a higher Al content in the bulk chemical composition for this FA sample (Table. 3.2). Therefore, this FA sample contains a higher amount of Si-O-Al linkages compared to the other samples. An evident correlation at ~ 4.15 Å is visible in Figure. 4.8, which mainly disappears after subtraction of the crystalline phases and is attributed to either quartz or mullite [74].

As mentioned in the literature, the glassy spherical particles that constitute FA are known to be heterogeneous in terms of chemical composition [24-28]. Therefore, the reactivity of individual FA particles in a source of FA can be significantly different, with some particles dissolving during the alkali-activated reaction, while others remain

completely intact [197]. Therefore, there will be a range of glassy structures in the FA samples studied in this investigation, with the PDF data providing the average glassy structure of each FA source (i.e., the average amorphous structure after subtraction of the crystalline phases, as shown in Figure. 4.10). Ideally the distribution of amorphous structures throughout the FA sample would be accessible, and with recent developments in micron-resolved PDF analysis [198], this analysis approach may become readily accessible within the next couple of years. Nevertheless, the PDF data presented in the current investigation has shed light on the variability in the average glassy structure for different sources of class F FA. The X-ray PDF results shown in Figure. 4.9 and Figure. 4.10 reveal that there is relatively little difference in atomic ordering among the different types of FA, apart from those FA samples containing high levels of amorphous mullite/alumina (as is the case for AFA) [74].

4.4 Neutron Pair Distribution Functions

Neutron PDFs have been obtained to provide complementary data to the X-ray PDFs, particularly since iron, carbon and oxygen atoms have relatively large coherent neutron scattering lengths compared to silicon and aluminum. Given the difference in the neutron scattering lengths between silicon and aluminum, a different normalization process has been used compared to the X-ray data, specifically by taking into consideration the different coherent neutron scattering length densities (b) of the major atoms (Si, Al, Ca and Fe). All datasets have been normalized to the T-O correlation considering the amount of silicon and aluminum in the sample weighted by the scattering strength of each element, as depicted in the following equation:

$$Si(molar\ \%)\times b_{Si} + Al(molar\ \%)\times b_{Al}$$

The neutron PDFs are shown in Figure. 4.11 and Figure. 4.12. As for the X-ray data, a crystalline subtraction process has been performed on each dataset, with the results given in Figure. 4.13 and Figure. 4.14. Scale factors for the crystalline phases for neutrons, as determined using PDFgui [159], are reported in Table. 4.3. It is apparent that there are differences in the scale factors according to the type of radiation used (X-rays versus neutrons), especially for mullite, which is attributed to the relatively weak scattering of neutrons from aluminum atoms. Such discrepancies in scale factors

according to the type of radiation used have been previously reported in the literature [199]. Peaks positions for the nearest-neighbor atom-atom correlations before and after crystalline subtraction are reported in Table. 4.5 [74].

Type of FA		Atom-atom correlation								
		TR	C-C	T-O	Fe-O	Fe-O	Ca-O	O-O	T-T	Fe-Fe
IFA	B	1.35	/	1.61	1.87	2.08	2.36	2.61	3.00	3.55
	A	1.35	/	1.61	1.87	2.08	2.37	2.61	2.82	3.53
AFA	B	1.33	/	1.60	1.87	2.05	2.33	2.61	2.96	3.48
	A	1.31	/	1.60	1.89	2.07	2.33	2.61	2.84	3.45
GFA	B	1.34	/	1.60	1.86	2.09	2.34	2.60	2.97	3.49
	A	1.34	/	1.61	1.87	2.09	2.35	2.60	2.98	3.49
AMFA	B	1.36	/	1.62	1.88	2.09	2.33	2.62	3.02	3.49
	A	1.36	/	1.62	1.87	2.08	2.34	2.59	2.99	3.45
HCFA	B	/	1.39	1.61	1.87	2.11	/	2.55	3.01	/
	A	/	1.38	1.61	1.89	2.11	/	2.55	3.01	/

Table. 4.5 Peak position from neutron PDFs before (B) and after (A) removal of the crystalline phases (TR = termination ripple) [74].

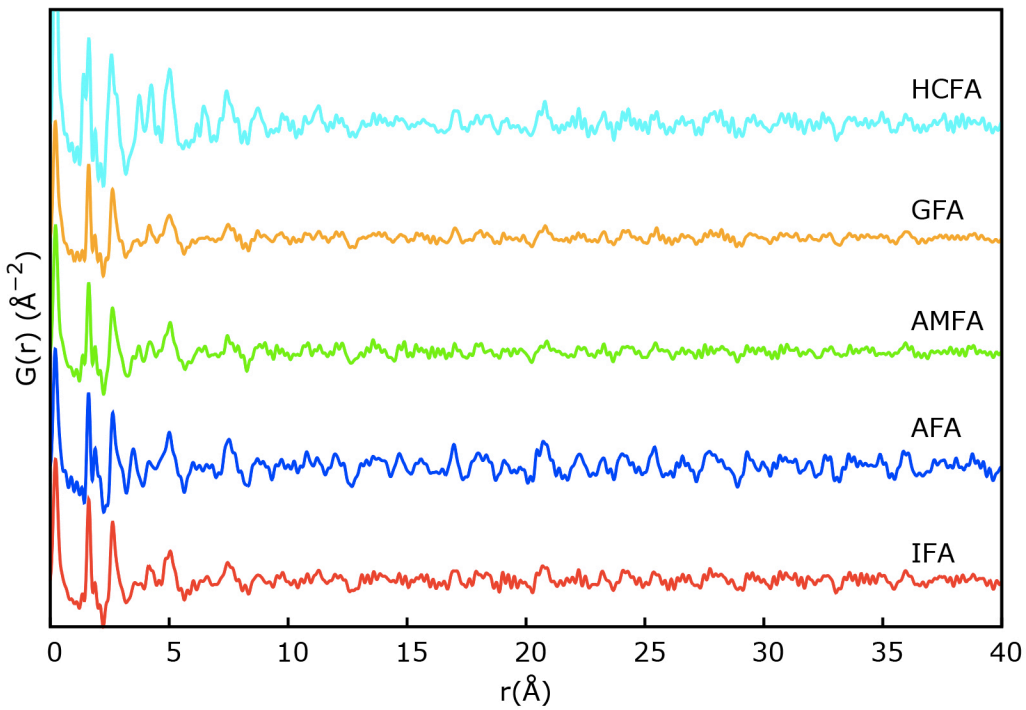

Figure. 4.11 Neutron PDFs of all the analyzed FA up to 40 Å [74].

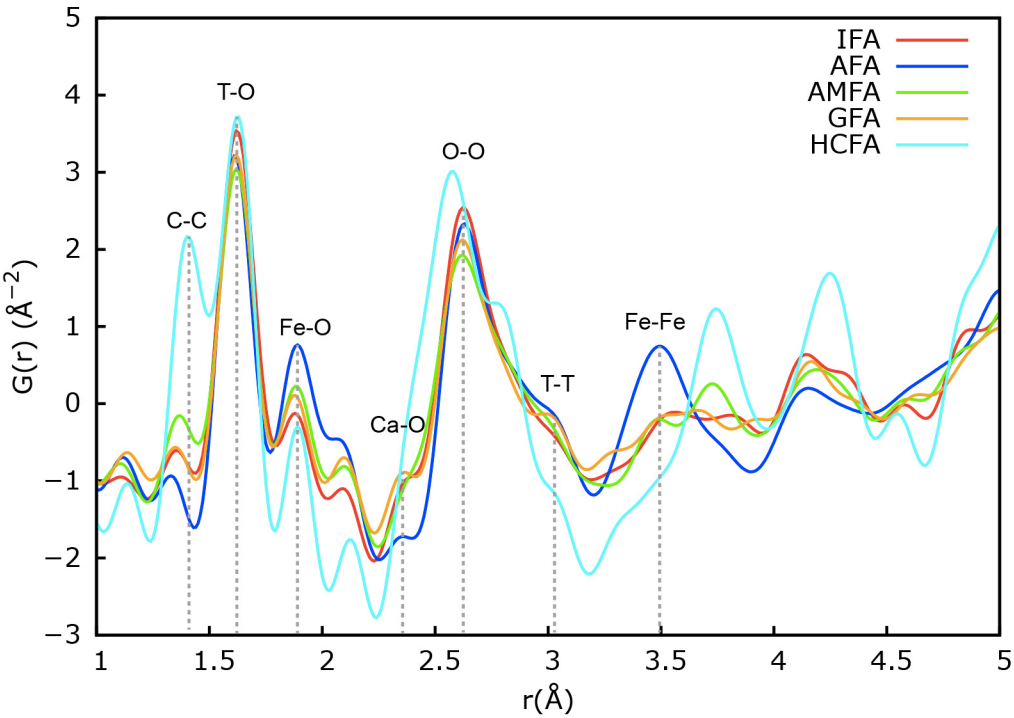

Figure. 4.12 Neutron PDFs of all the analyzed FA over the region $1 \leq r \leq 5$ Å [74].

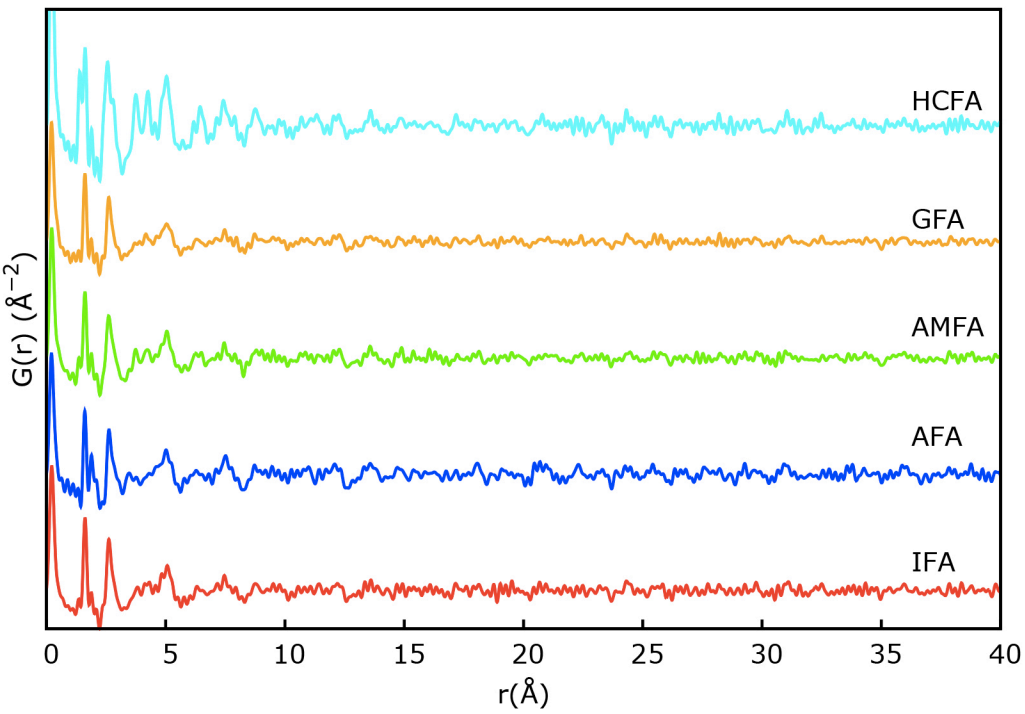

Figure. 4.13 Neutron PDFs of all the analyzed FA after crystalline phases subtraction up to 40 Å [74].

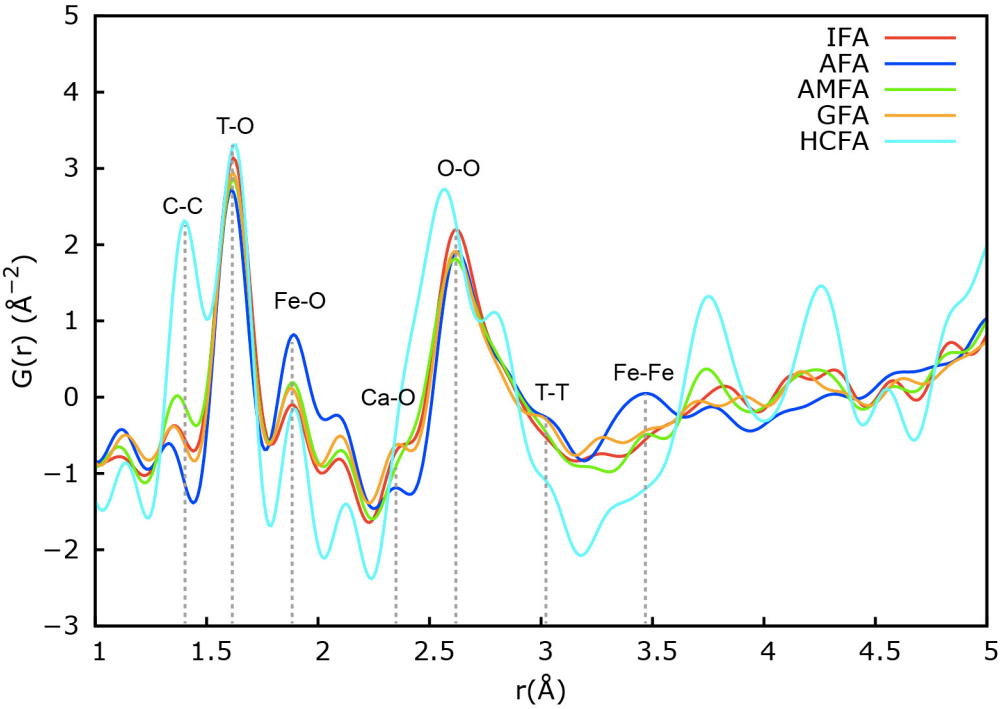

Figure. 4.14 Neutron PDFs of all the analyzed FA after crystalline phases subtraction over the region $1 \leq r \leq 5$ Å [74].

The neutron PDF data in Figure. 4.11 and Figure. 4.13 reveal the lack of long-range ordering above ~ 10 Å, which confirms that the FA samples are predominately amorphous. The presence of strong scatterers (e.g., Fe and C) in the neutron data is particularly evident for HCFA and AFA, where the PDF data show the most differences relative to the other samples. In fact, HCFA exhibits distinct atom-atom correlations at different *r* values compared to the other FA samples, which is attributed to carbon-containing correlations. Furthermore, AFA contains specific peaks related to iron-containing correlations due to the higher scattering strength of iron compared to aluminum for the case of neutrons (b_{Fe} = 9.45 *vs* b_{Al} = 3.44). The majority of peaks at low *r* in Figure. 4.12 and Figure. 4.14 ($1 \leq r \leq 1.5$ Å) are termination ripples as their position has been shown to shift with a change in the Q_{max} used to produce the PDF data. However, for HCFA an intense peak appears at ~ 1.39 Å, which is attributed to the C-C correlation found in a graphene sheet at ~ 1.42 Å [200]. This seems to be directly linked to the LOI content (i.e., LOI_{HCFA} of 11.37 wt.%, which is the highest among all the FA samples investigated here). The high carbon content in this type of FA seems to particularly affect its nanoscale structure (Figure. 4.14), although no evidence of crystalline carbon phases was observed in the total scattering pattern (Figure. 4.6).

The local atomic ordering in the FA samples (Figure. 4.14) reveals the presence of two distinguished peaks at ~ 1.87 Å and ~ 2.08 Å, which were not evident in the X-ray data. The intensities of these two peaks follow the iron content (Table. 3.1) and their *r* values are in good agreement with the correlations found by Weigel et al. [194] for Fe-O correlations in Fe-aluminosilicate glasses. According to the investigation by Weigel et al., the shorter distance can be assigned to IV-coordinated Fe^{3+} and the second either to V-coordinated Fe^{3+} either to V-coordinated Fe^{2+}. Given that the neutron data are more strongly affected by the iron content compared to X-rays (due to the large neutron coherent scattering length of Fe), the conclusions drawn from the PDF data in this investigation is highly dependent on the type of radiation used in the analysis, with the presence of both amorphous mullite/alumina and amorphous iron-containing structural features being identified using X-rays and neutrons. If only one form of radiation was used, then an incomplete understanding of the bulk amorphous structure would have been obtained.

Except for HCFA, which exhibits a broad peak at ~ 2.55 Å, all the samples possess an atom-atom correlation at ~ 2.35 Å, especially for GFA and IFA samples (Figure. 4.14). This peak may be attributed to the Ca-O correlation [65], and is seen to be more intense for the higher calcium content FA samples of GFA and IFA. The presence of this peak, which was not evident in X-ray PDFs, might be linked to the slightly higher scattering length density of Ca compared to other atoms, which allows it to be more visible in neutron data (e.g., $b_{Ca} = 4.70$ *vs* $b_{Al} = 3.44$). Above an *r* spacing of 2.5 Å, HCFA exhibits a different local atomic structure compared to the other samples (Figure. 4.14). In fact, while the O-O and Si-Si correlations are clear for all the other FA samples, HCFA possesses a broad peak at ~ 2.5 to 2.7 Å along with two distinct peaks at ~ 3.7 Å and ~ 4.2 Å. As will be discussed in the next paragraph, these correlations are associated with the carbon phase(s) present in the sample. The broad correlation at ~ 3.5 Å in the AFA sample is attributed to Fe-Fe. This peak decreases in intensity for all the other types of FA and disappears in case of HCFA (which has the lowest amount of iron oxide, see Table. 3.1 for details). A previous investigation on alkali iron-containing aluminosilicate glasses [194] using neutron total scattering and empirical potential structure refinement modeling revealed that the glasses investigated, when containing iron in a range of coordination environments, is seen to possess a broad distribution of Fe-Fe correlations between 2.6 and 3.8 Å [74].

To determine the type of carbon present in the HCFA sample, the carbon contributions were isolated by assuming that the remaining amorphous components in the HCFA possess similar atomic structural arrangements to the amorphous glassy structure for GFA. This enabled a subtraction procedure to be carried out, resulting in a difference PDF curve where only the atom-atom contributions from the carbon phase(s) are present (Figure. 4.15).

Comparison of the atom-atom correlations in Figure. 4.15 to a range of carbon based phases reveals that the local atomic ordering of the carbon phase(s) in HCFA is very similar to graphite. Figure. 4.15 also displays the simulated neutron PDF of crystalline graphite with a spherical particle diameter of ~ 10 Å to mimic an amorphous/nanostructured phase of graphite. This particle diameter value was obtained by performing a real space refinement (PDFgui [159]), using the graphite crystal structure (ICSD #76767 [201]). Other parameters were refined as follows: scale factor = 0.42, atomic displacement parameters u_i = 0.0092 Å^2, lattice parameters a = 2.46 Å and c = 6.94 Å.

From Figure. 4.15 it is evident that the carbon present in HCFA is highly disordered, most likely due to disordered graphene sheets. However, the level of agreement achieved between the experimentally derived data and the simulated neutron PDF is quite good, especially given that the experimental dataset assumed that the non-carbon containing amorphous structure in HCFA was the same as that found in GFA, which is an approximation given the differences seen in the X-ray PDF data in Figure. 4.10. Figure. 4.15 reveals that the C-C correlation in the experimental data is located at ~ 1.42 Å [200] and the atom-atom correlations positioned at ~ 3.70 Å and ~ 4.25 Å are very similar to the local structural ordering found in graphite.

Therefore, based on these results it is clear that the unburnt carbon in the high carbon content class F FA sample studied in this investigation possesses atomic structural ordering similar to disordered graphitic layers [74].

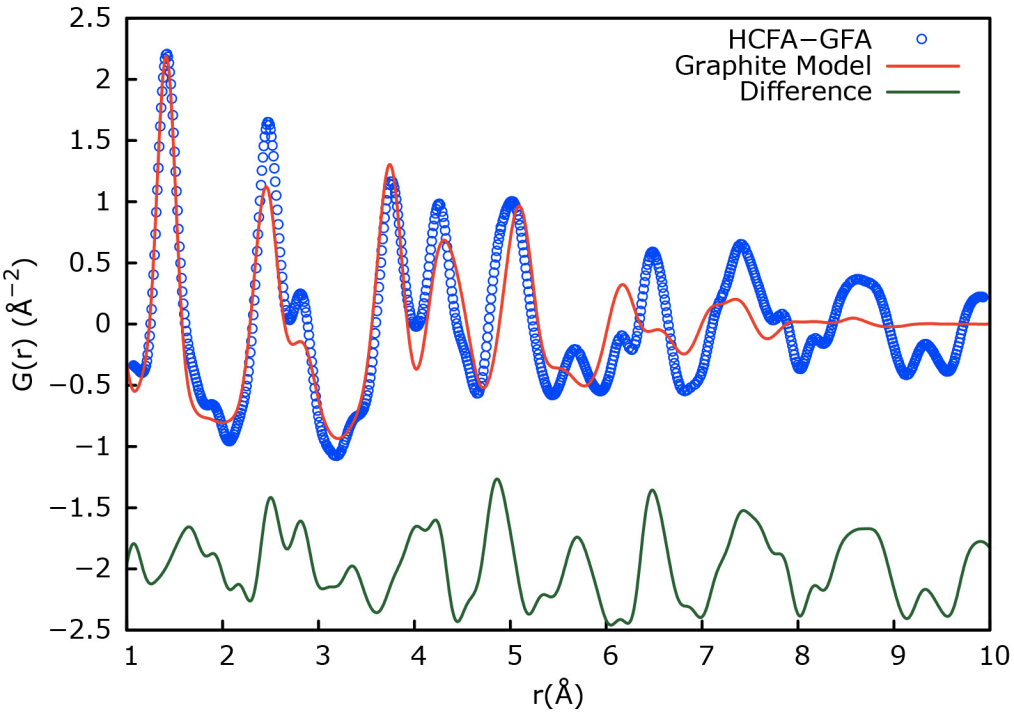

Figure. 4.15 Neutron PDF for HCFA-GFA data (blue curve), the simulated graphite crystalline structure (red line [201]) and their difference (green line) over the region $1 \leq r \leq 10$ Å [74].

4.5 Main remarks

This work allowed to obtained different information on the main characteristics of the considered FA samples.

Regarding the first part of the analysis, and considering the IFA and AFA, it was observed they differ mainly in: (i) chemical composition (i.e., IFA is richer in CaO and AFA in Fe_2O_3), (ii) fineness (IFA D_{50} = 22.1 μm *vs* AFA D_{50} = 15.0 μm) and (iii) amorphous phase % (IFA = 65.32% *vs* AFA = 53.49%) [44].

Regarding the atomic structure and associated variability in FA aluminosilicate glass chemistry, PDF analysis, obtained by Fourier transformation of high-energy X-ray and neutron total scattering data, has been used to determine the average atomic ordering present in the considered IFA and AFA samples, including other types of fly ash. The complementarity of X-rays and neutrons allowed to pinpoint the exact atom-atom correlations present in the samples. All FA samples showed a significant loss in atomic ordering above ~ 5 Å in both the X-ray and neutron data, which is consistent with a mainly amorphous structure. The majority of the disagreement in local atomic ordering

between samples is attributed to the presence of crystalline phases such as quartz, mullite and iron-components (maghemite, magnetite and hematite). After removal of crystalline phases, analysis of the short range atom-atom correlations revealed that the bulk glassy structure of the different FA sources are relatively similar, apart from those containing (i) amorphous mullite/alumina, (ii) high levels of iron in the glassy component and (iii) carbon [74]. The presence of VI-coordinated aluminum (in the form of amorphous mullite or amorphous alumina) was unequivocally detected using X-rays, while neutrons, which are more sensitive to iron, showed the presence of amorphous iron (together with amorphous graphite in the high carbon-containing sample). The importance of combining the two methods was so evident, allowing a deep and exhaustive understanding on the local atomic ordering of the considered samples [74].

5 EXPERIMENTAL RESULTS AND DISCUSSION: GEOPOLYMERS

In this Chapter, the first part is dedicated to evaluation of the performances obtained by IFA and AFA based geopolymers activated at room temperature. Formulations were modified in order to obtain Na_2O/SiO_2 molar ratio ranging form 0.12 to 0.20 and results were compared from a physical, microstructural and mechanical point of view. In the second part, the research was focused on the only use of IFA as geopolymer precursor and on the behavior of the relevant geopolymer depending on curing conditions. Results have been discussed pointing out, among the other characteristics, the thermal properties shown by the obtained products.

5.1 IFA and AFA geopolymers

The first step of this study was aimed at investigating the potential of an Italian fly ash as precursor for geopolymers, along with their thermal properties, in comparison to an Australian fly ash, which has already been studied and used as a precursor for inorganic polymer binders/geopolymers in previous works [78,112,117].

Four different formulations for each FA were prepared at this purpose, with molar ratios of Na_2O/SiO_2 ranging from 0.12 to 0.20, according to Table. 3.3.

A first consideration was made about the fresh state workability, which has been visually estimated. As a general trend, AFA based samples exhibited better workability compared to the samples prepared with IFA. Moreover, workability was observed to increase with increase of the Na_2O/SiO_2 molar ratio. The superior workability shown by AFA based materials is likely due to the higher content of fines present in this fly ash, as it was observed to be the main difference, in terms of morphology, between the two used precursors (Figure. 4.1).

5.1.1 Microstructural characterization

After 7 days of curing, hardened geopolymers were tested for mechanical properties and exposed to high temperature (calcining at 800 °C for 2 hours, as described in paragraph 3.3.1.14). Calcined geopolymers are identified by the addition of the letter C at the end of their sample name. Microstructural characterization by SEM and MIP was carried out before and after calcining in order to determine the effect of Na_2O/SiO_2 molar ratio on the thermally induced changes.

The weight loss due calcination at 800 °C for the different Na_2O/SiO_2 molar ratio of IFA and AFA samples is reported in Figure. 5.1. IFA geopolymer samples exhibited a weight loss between 8.5 - 9.1 %, whereas AFA samples exhibited lower mass loss values (4.5 - 5.5 %). Weight loss was not found to be strongly dependent on Na_2O/SiO_2 molar ratio, however for both fly ashes the lowest measured value corresponded to the highest Na_2O/SiO_2 level of 0.20.

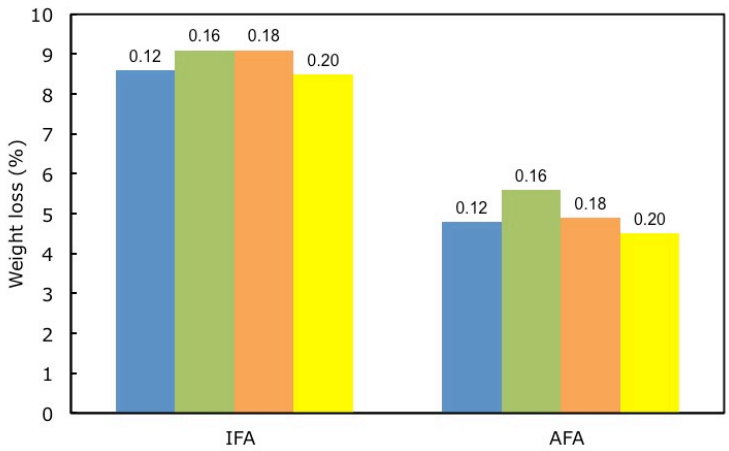

Figure. 5.1 Weight loss % after calcining to 800 °C for IFA and AFA geopolymer samples (uncertainty: ±1%) [44].

The different weight loss behaviour of the two fly ash systems might be influenced by several factors: (i) the LOI value of the starting fly ash (i.e., IFA_{LOI} = 3.28 *vs* AFA_{LOI} = 0.51, see Table. 4.1); (ii) the phases formed during the geopolymerization reaction and their thermal stability, which will be discussed in the further paragraphs; (iii) the water content, which increases with the amount of 8 M NaOH solution in the mix [44]. Moreover, no dimensional changes were observable after calcining and a shift to red color was more pronounced in AFA samples due to the higher iron content (Figure. 5.2).

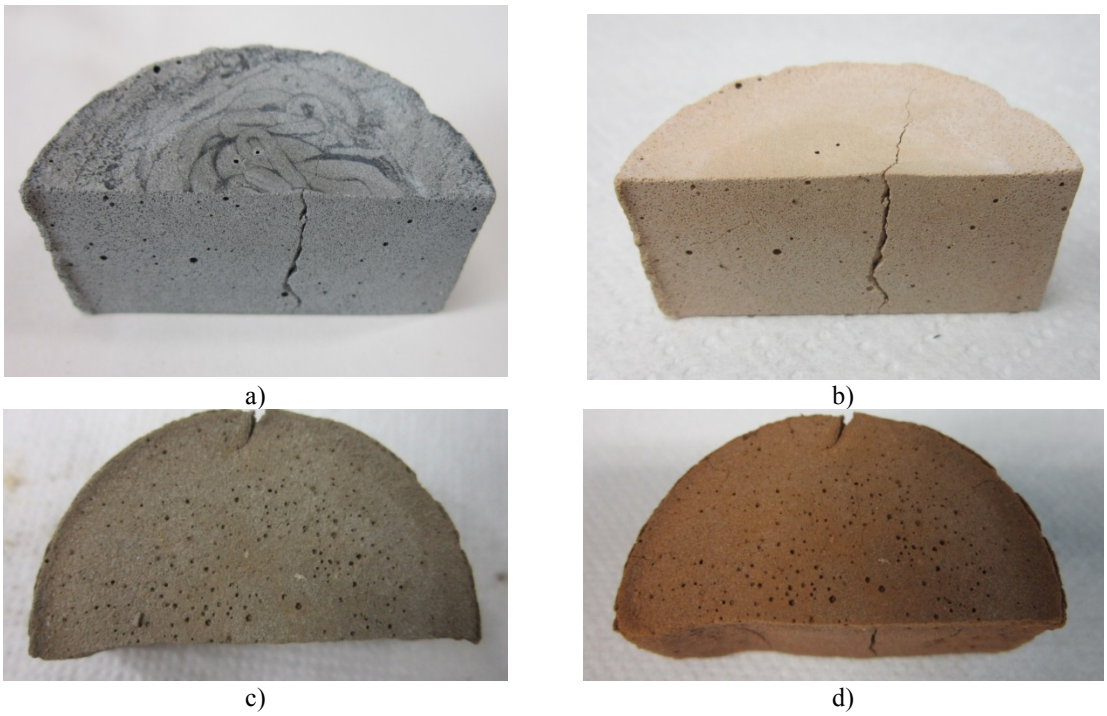

Figure. 5.2 IFA and AFA geopolymers after calcining: IFA12 (a); IFA12C (b); AFA12 (d); AFA12C.

XRD patterns from the samples prepared with Na_2O/SiO_2 = 0.12 and 0.20 based on IFA and AFA are presented in Figure. 5.3 as typical examples of the investigated geopolymers before and after calcining.

Quartz and mullite phases, originating from the fly ash precursors (see Figure. 4.3 and Figure. 4.4), are evident for both the geopolymers. AFA based geopolymers also exhibit characteristic peaks of hematite according to the higher Fe_2O_3 content in the precursor fly ash. Both fly ashes also exhibited characteristic amorphous humps for 2θ values between 15^o and 40^o.

The calcining treatment has different effects on IFA and AFA geopolymers. For the latter, new crystalline phases were not detected, but an increase in the peak intensity of hematite was registered according to its crystallization from amorphous iron (oxide) in the fly ash (as previously observed by Rickard et al. [182]). For IFA geopolymers, except for IFA12 mix, peaks characteristic of nepheline ($NaAlSiO_4$) have been identified after calcining. Nepheline usually improves sample thermal resistance due its high melting point (1257 °C) and its formation might be related to the presence of free sodium for the mixes prepared with $Na_2O/SiO_2 \geq 0.16$.

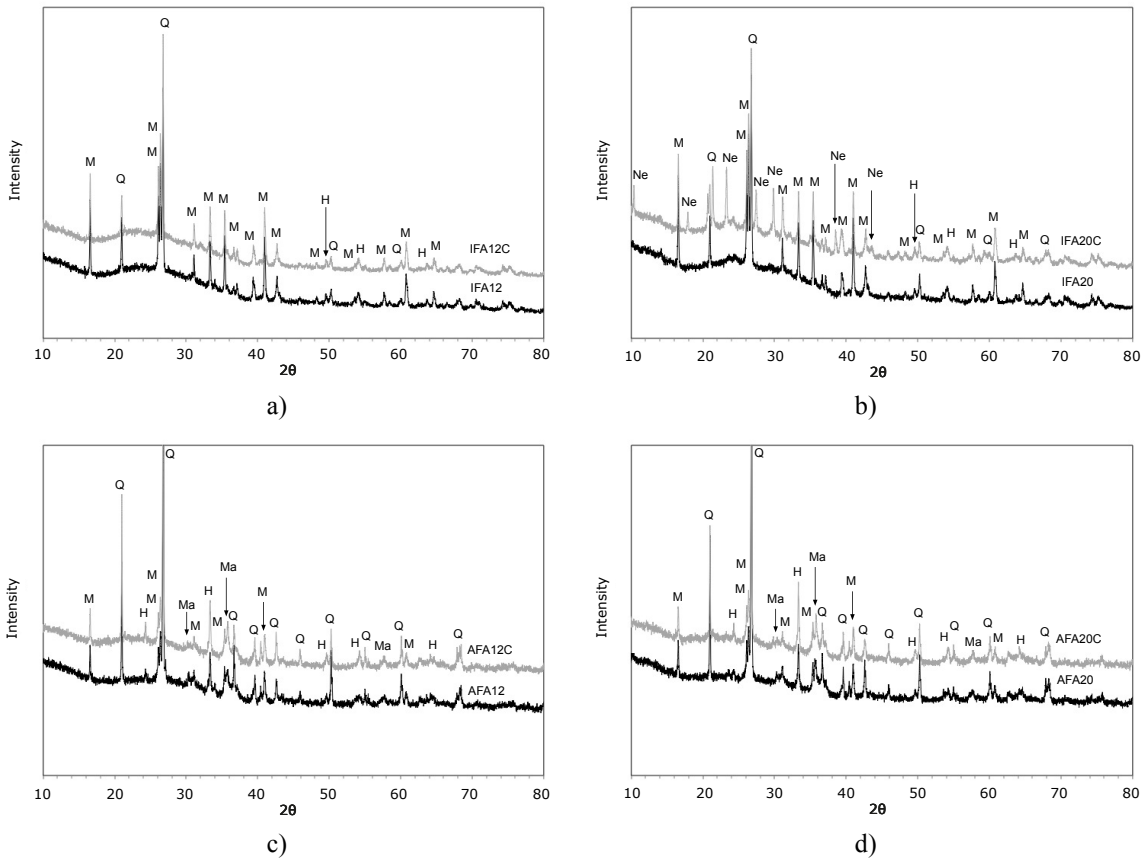

Figure. 5.3 X-ray diffraction of IFA12 (a), IFA20 (b), AFA12 (c) and AFA20 (d) before (black line) and after (grey line) calcining (M = mullite (PDF #04-016-1588); Q = quartz (PDF #04-012-0490); H = hematite (PDF #04-003-2900); Ma = maghemite (PDF #01-089-5894); Ne = nepheline (PDF #04-012-4977)).

SEM analysis allows observations of the microstructures formed during the alkali-activation process. In Figure. 5.4 micrographs of samples based on IFA and AFA prepared with Na_2O/SiO_2 molar ratio equal to 0.12 and 0.20 are reported for comparison. For all the samples, unreacted fly ash particles are evident in the microstructures and their

content increases with increasing Na_2O/SiO_2 molar ratio in the activator. IFA20 and AFA20 contained more unreacted fly ash particles compared to the relevant samples IFA12 and AFA12. Such behaviour can be ascribed to the low amount of sodium silicate present in the activating solution. According to the literature [9,21] soluble Si atoms are extremely important for the geopolymerization process.

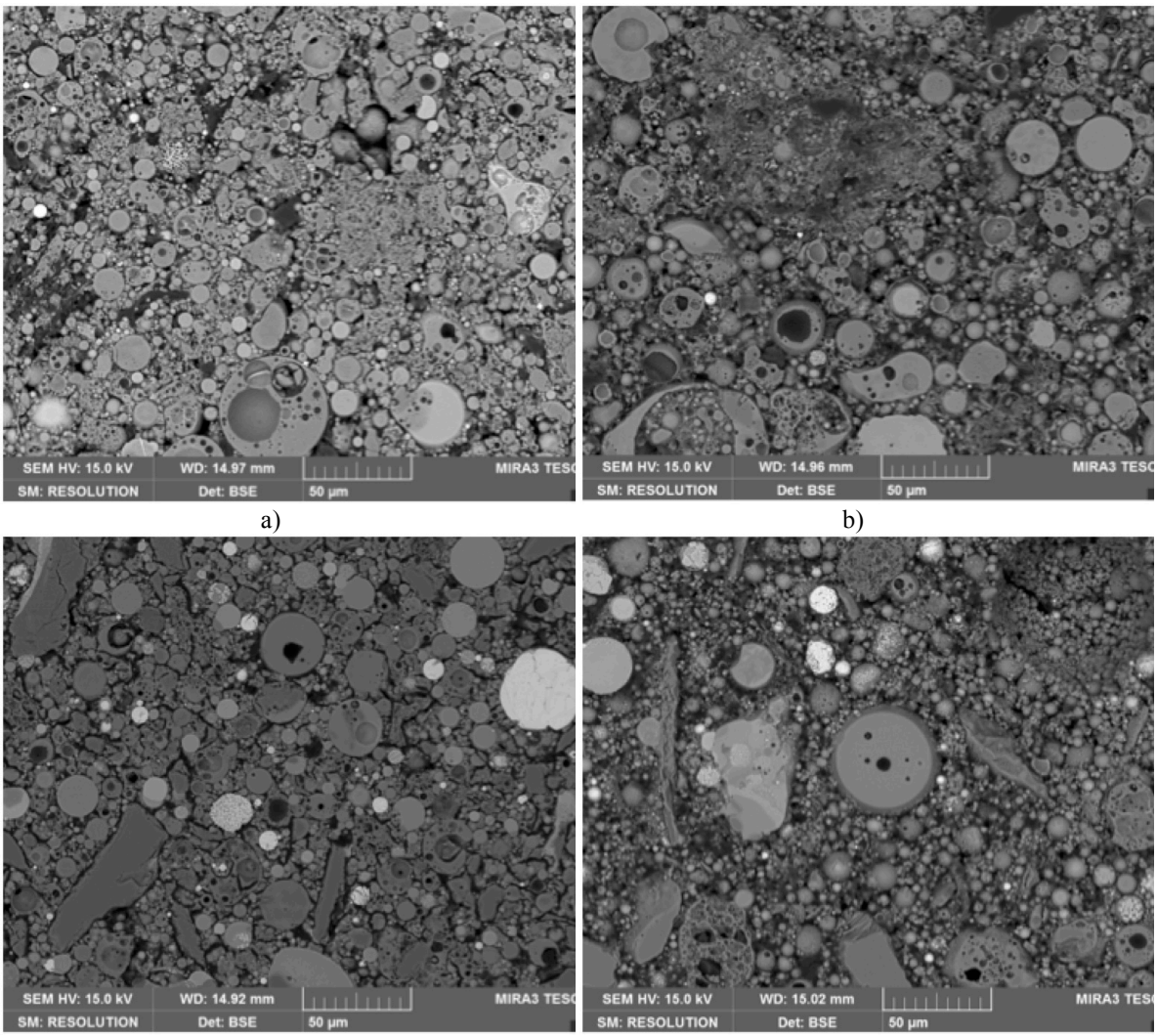

Figure. 5.4 Micrographs of samples IFA12 (a), IFA20 (b), AFA12 (c) and AFA 20 (d) [44].

As a general statement, geopolymer gel amongst the unreacted fly ash particles can be observed in all the samples, however the identification of its chemical composition by EDS analysis was not reported as the binder compositions varied significantly from point to point even on polished surfaces [44].

The total open porosity determined by MIP is reported in Figure. 5.5 for IFA (a) and

AFA (b) based geopolymers. As a general trend, the total open porosity increases with increasing Na_2O/SiO_2, before and after calcining.

When IFA samples are considered, the total open porosity increases very slightly for $Na_2O/SiO_2 > 0.16$ and it is almost constant for 0.18 and 0.20 molar ratios. Conversely, for AFA geopolymers the porosity rises almost linearly from $Na_2O/SiO_2 \geq 0.16$. Before calcining, for Australian fly ash geopolymers, the total porosity increased by 65% as Na_2O/SiO_2 went from 0.12 to 0.20, while for the calcined geopolymer it increased by 71%. The corresponding porosity increases for the Italian fly ash with increase in Na_2O/SiO_2 were 43% for samples before calcining and 13% for calcined geopolymers [44].

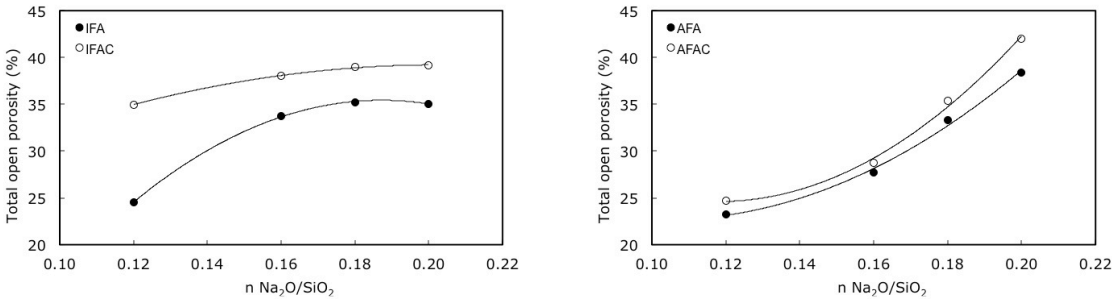

Figure. 5.5 Total open porosity of IFA (a) and AFA (b) based geopolymers before and after calcining [44].

This significant difference in porosity with increase in Na_2O/SiO_2 molar ratio is directly attributable to an incomplete geopolymerization process, becoming more evident as the content of sodium silicate decreases in the mix. This effect is more remarkable for AFA based samples. For IFA samples, the less evident increase in porosity with the increase in Na_2O/SiO_2 molar ratio may be due to the presence of calcium in the gel, which mitigates such effect. As CaO in IFA is present as an amorphous component, the formation of C-N-A-S-H and C-S-H gel in the relevant geopolymers is expected [77,202-204].

IFA and AFA calcined based geopolymers exhibit the same trend as the equivalent samples before calcining, confirming that the determined porosity trend is strictly related to the precursor type, its chemical composition/reactivity as well as the microstructure of the final products. For both the series the total open porosity increased after calcining. This has been observed previously [49,182] and is reported to be due to the exposure of

previously closed pores within unreacted fly ash particles after viscous flow on heating.

Exploiting the IUPAC classification system for porosity, as reported in other works [205,206], pores can be categorized as a function of size (Figure. 5.6). For IFA geopolymers, macropores (with pore radius, *r*, between 25 - 5000 nm) dominate, regardless of the Na_2O/SiO_2 used in the mix. Conversely, for AFA geopolymers, mesopores (with pore radius, *r*, between 1.25 - 25 nm) were the most common in AFA12 and AFA16, whereas macropores dominate in AFA18 and AFA20 samples [44].

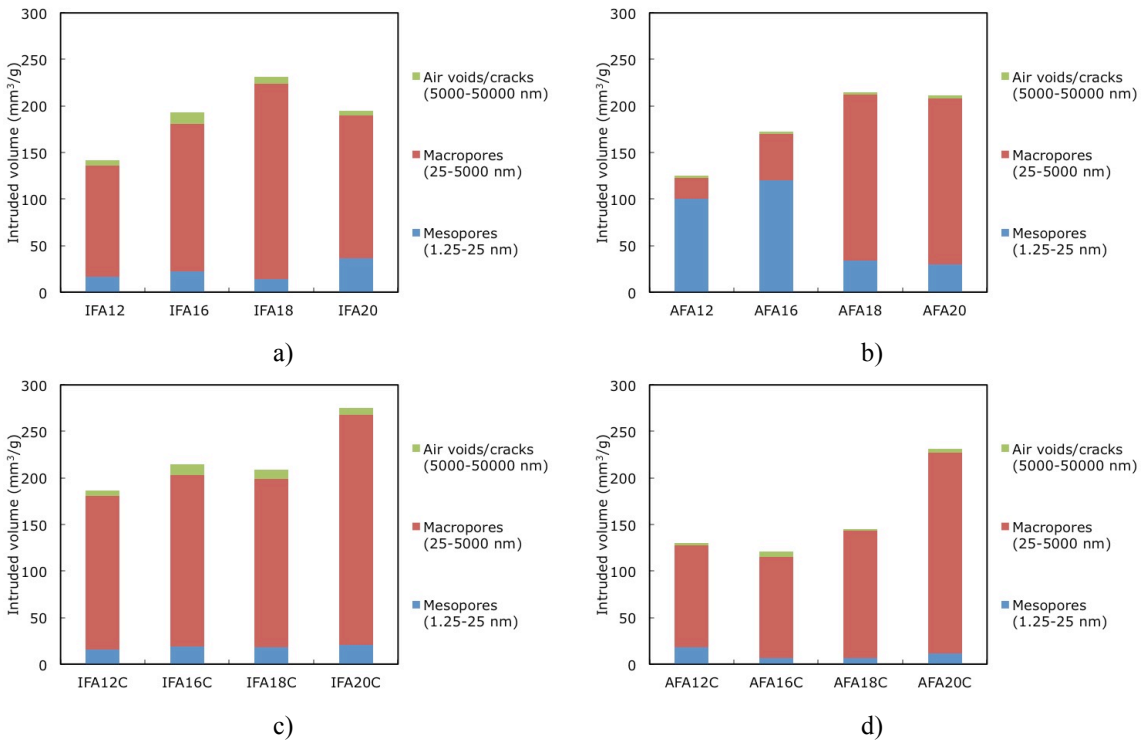

Figure. 5.6 Pore size categories for IFA and AFA geopolymers before (a,b) and after calcining (c,d) process [44].

MIP results indicate that the porosity and pore size distribution are influenced by the chemical composition and nature of the two starting fly ashes and by the proportion of the alkaline solutions. For IFA based samples, porosity is sensitive to the increase of Na_2O/SiO_2 molar ratio from 0.12 to 0.18, whereas it only slightly increases for higher ratios. Conversely, for AFA geopolymers, the porosity dramatically changes with Na_2O/SiO_2 increase. For Na_2O/SiO_2 equal to 0.12 and 0.16, the resulting microstructure is very compact, mainly characterized by mesopores. However, decreasing sodium silicate content in the activating solution, resulting in less available soluble Si atoms, lead to an incomplete geopolymerization process promoting the formation of a microstructure

characterized by macroporosity. Calcining mainly led to the dehydration of the gels for both IFA and AFA based geopolymers, however the formation of crystalline nepheline detected in IFA16, IFA18 and IFA20 could also be the cause for porosity increasing with size > 5 μm. It is worth highlighting that for geopolymers AFA12C and AFA16C, a reorganization of the pores (from meso to macropores) was found. This change in pores size distribution is probably due the collapse of mesopores at high temperature, as reported elsewhere [205].

5.1.2 Thermal behaviour

The thermograms of IFA and AFA geopolymers are collectively reported in Figure. 5.7. Samples were dried at 80 °C prior to analysis.

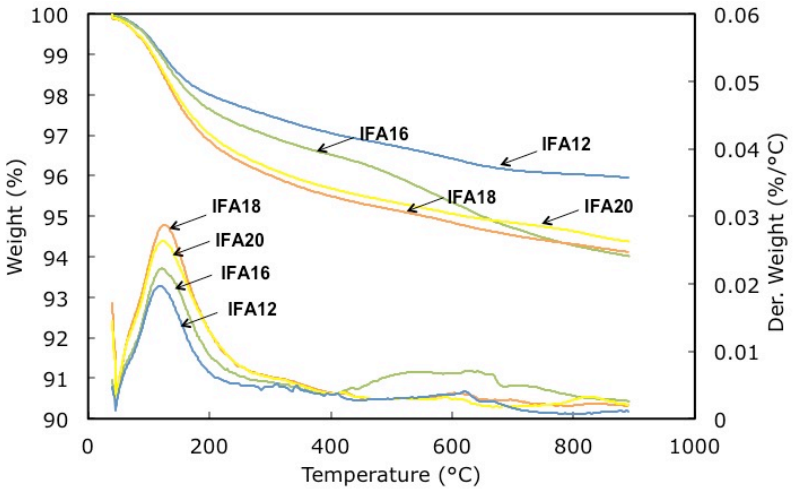

a)

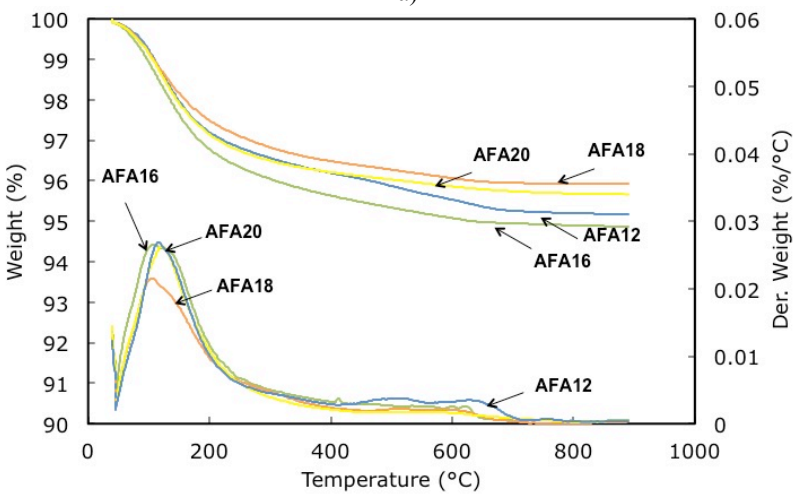

b)

Figure. 5.7 Thermal analysis for IFA (a) and AFA (b) geopolymers [44].

There is a continuous loss of weight up to 700 °C for all the AFA based samples, above which it remains constant up to 900 °C with a total weight loss of 4 - 5 wt.%. The weight loss was mainly due to the dehydration process of physically adsorbed (at T < 200 °C) and chemically bound water (200 °C < T < 700 °C). A similar behaviour for Australian fly ash based geopolymers, prepared with different amounts and concentrations of activating solutions, is reported elsewhere [205]. The weight loss of IFA geopolymers resembles the behaviour determined for the total open porosity of these samples: IFA12 shows the lowest weight loss (less than 4 wt.%), whereas IFA16, IFA18 and IFA20 exhibit very similar values of about 5.5 wt.%. As for Australian fly ash based geopolymers, the weight loss was due to the dehydration process which may be influenced, in part, by the adsorbed water and the dimensions and amount of pores present in the final microstructure [44].

5.1.3 Physical and mechanical characterization

The water absorption and the mechanical strength data determined for the series of geopolymers samples based on IFA and AFA are reported in Table. 5.1. Water absorption increases and mechanical strength (both flexural and compressive) decreases with the increase in Na_2O/SiO_2. Such behaviour agrees with the results of the above-described characterizations showing less compact microstructures and higher porosity with the decrease of sodium silicate in the activator. The best performance in terms of mechanical strength was exhibited by AFA12 and AFA16 samples. This behaviour is in agreement with the results obtained on the microstructure of these samples, which was characterized by mesopores (Figure. 5.6).

	7 days of curing		
Sample	WA%	Flexural strength (MPa)	Compressive strength (MPa)
IFA12	15.7	7.6 ± 0.7	9.7 ± 1.0
IFA16	20.2	2.6 ± 0.3	5.6 ± 0.3
IFA18	21.9	1.2 ± 0.1	4.3 ± 0.2
IFA20	25.6	0.8 ± 0.1	2.3 ± 0.1
AFA12	15.7	10.6 ± 0.5	11.2 ± 0.3
AFA16	16.6	5.0 ± 0.7	10.1 ± 1.9
AFA18	22.9	1.3 ± 0.4	3.7 ± 0.6
AFA20	27.5	1.1 ± 0.2	3.6 ± 0.2

Table. 5.1 Water absorption, flexural and compressive strength of the investigated geopolymers samples [44].

5.1.4 Main remarks

The studied geopolymers were prepared by alkali-activation at room temperature of two types of class F fly ash (IFA and AFA) which differ in origin (coming from Italian and Australian power plants), chemical and mineralogical composition.

The obtained results allow the following observations:

- the different fineness of the Italian and Australian fly ash plays an important role in influencing the properties of the investigated samples. Specifically, AFA exhibited a higher content of particles in the range 2 - 100 μm compared to IFA, promoting mixes with a good workability in the fresh state and higher strength/lower porosity after curing;
- increasing the proportion of sodium silicate solution in the formulations encourages geopolymer gel formation and, consequently, higher physical and mechanical performances;
- the investigated samples show good results in terms of thermal stability, directly linked to the formation of new crystalline phases after calcining as nepheline, which increase the thermal properties of the samples.

In view of finding alternative solutions to the use of hydraulic binders such as hydraulic lime and Ordinary Portland Cement, alkali-activation of fly ash at room temperature represents a valid approach in developing market ready products. Developing comprehensive knowledge of geopolymer precursors is a fundamental and critical step in commercializing geopolymer products [44].

5.2 IFA sealed and oven cured samples

For this second step of research, only IFA was used as precursors and Na_2O/SiO_2 molar ratios ranging from 0.12 to 0.20 were investigated. The curing conditions of those samples were varied in order to evaluate their influence on samples properties. Thus, those samples, as already reported in Chapter 3.2.1.2 and Table. 3.5, were sealed after casting and maintained at T = 25 °C, T = 50 °C or T = 70 °C for the first 24 hours, then maintained sealed till testing (after 28 days of curing).

As in the previous case, a first observation was made on samples workability, confirming that geopolymer fluidity tended to increase with increasing Na_2O/SiO_2 molar ratio. In fact, while IFA12 and IFA14 exhibited a fairly thick consistency, FA16, FA18 and FA20 were very smooth and easily pourable into molds. This difference is justified by the reduced fluidity of sodium silicate with respect to the NaOH solution whose consistency is comparable to that of water. Increasing the percentage of sodium hydroxide was, however, observed to be also related to a reduction of workability time, especially for IFA16 and IFA18 formulations, whose margins have been reduced to 10-15 minutes compared to 25 - 30 minutes of other geopolymer types.

After 28 days of curing it was found that both the chosen process parameters (Na_2O/SiO_2 molar ratio and curing temperature for the first 24 hours) influenced the formation of efflorescences on samples surface. In fact, with increasing temperature, but especially for low Na_2O/SiO_2 values, a significant decrease in the presence of salts on the samples surface was noticed.

In Figure. 5.8 fresh cut surfaces are reported while microscope magnifications (10x) are shown in Figure. 5.9. The surfaces appear grey and the presence of macroporosity with diameters ranging from tenths of mm to several mm is clearly observable. At RT, the presence of large visible pores seems to decrease by increasing Na_2O/SiO_2 ratio and to increase with temperature especially for IFA12 and IFA14. These big pores seem not to be interconnected. IFA16, IFA18 and IFA20 show a reduced visible porosity and a smooth surface, which seems not to be affected by curing temperature. The presence of such big pores in IFA12 and IFA14 seems to be connected to the viscosity of these slurries compared to the others. A sticky slurry is, in fact, more easily affected by air entrapment during casting and, even after vibration, entrapped air is not facilitated to exit due to viscosity. Heating process increases fluidity so that bubbles tend to move and connect to each other resulting in bigger pores, which still remain entrapped in the slurry. On the contrary, in the case of a fluid slurry, the chance to include air is much more reduced resulting in a homogenous product (as for IFA16-IFA20). Some cracks are observable in IFA20-50 and IFA20-70 (Figure. 5.9) while no cracks are reported for the other formulations.

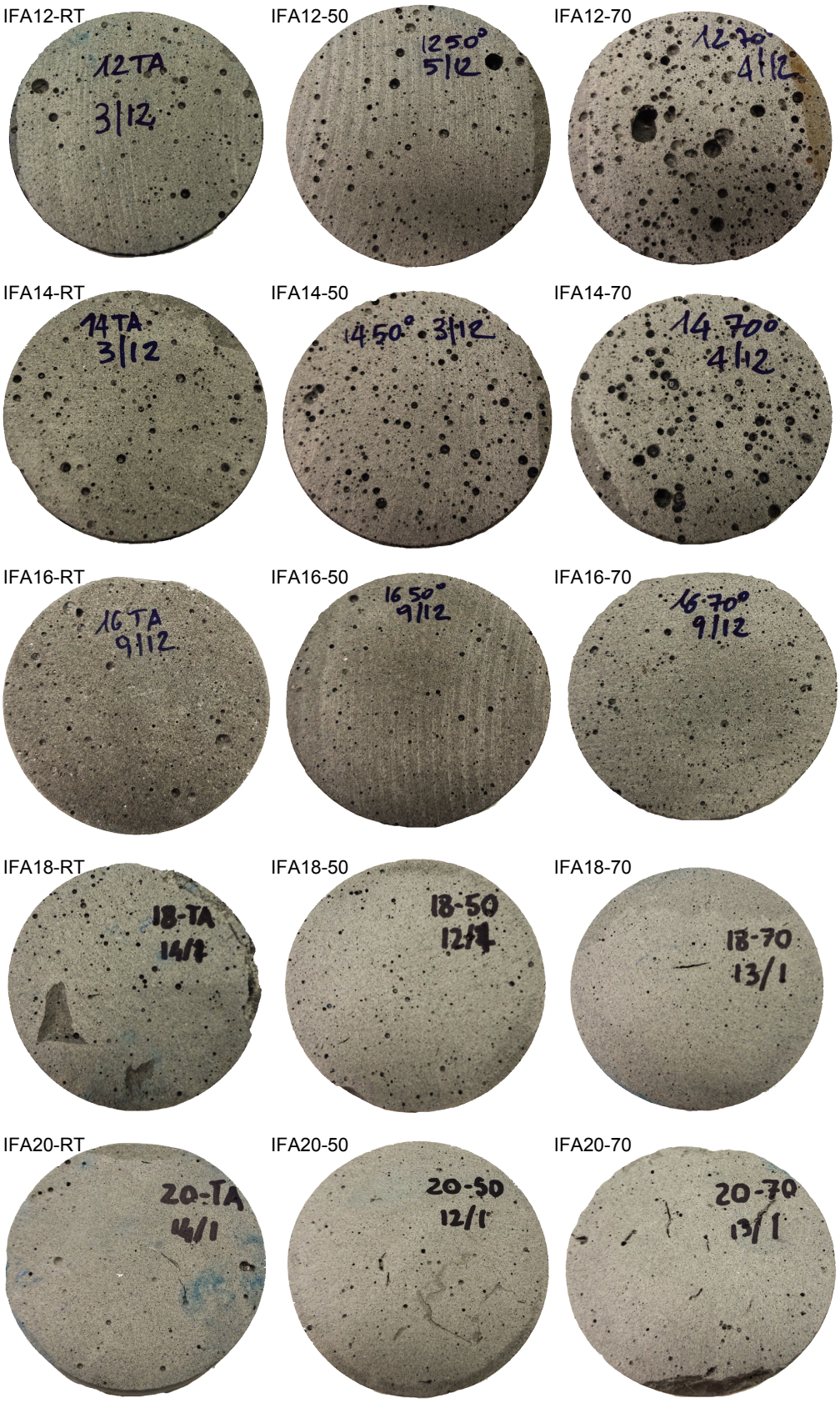

Figure. 5.8 Samples cross-sections after 28 days of curing (ϕ = 50 mm) [149].

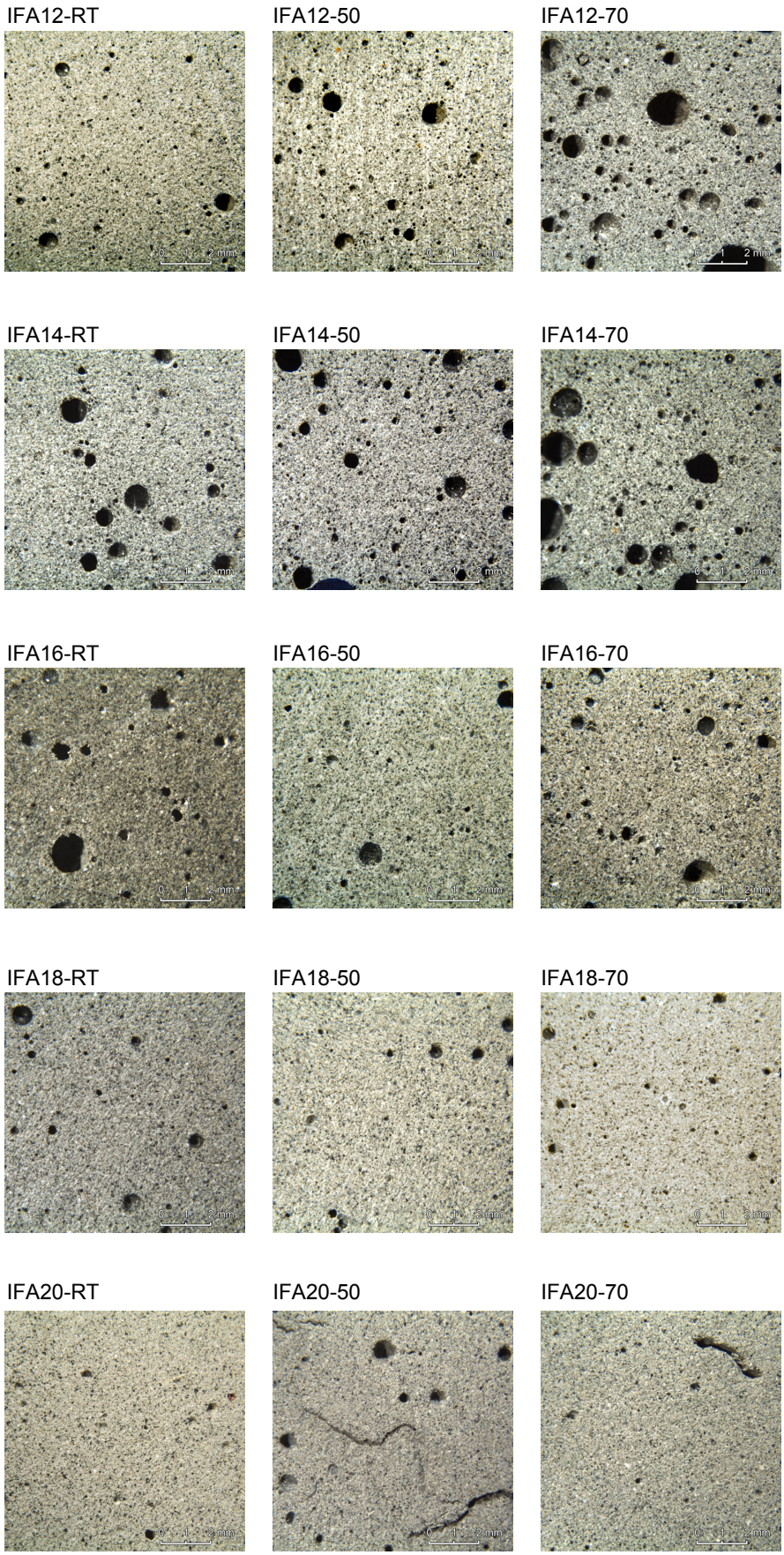

Figure. 5.9 Optical microscope images for the samples cross-section, magnification 10x.

5.2.1 Physical characterization

After 28 days of curing geopolymers were dry-weighted to determine their bulk density ρ (g/cm^3) and subjected to water absorption test. Figure. 5.10 shows the histograms relating the two parameters: ρ (in red with inverted axis) and WA% (in blue). Bulk density, whereas samples with identical formulations, varies with curing conditions. In particular, by increasing the temperature of the first 24 hours, it decreases. WA% is included within a range that varies from 8.2% (IFA16-RT) to 16.9% (IFA16-70) and seems to be most influenced by curing temperature rather than by Na_2O/SiO_2 molar ratio. In fact, it can be noted that for all geopolymer types WA% increases with increasing curing temperature. It is clear that a decrease in density corresponds to an increase of the water-absorbed percentage. It is also notable that, by increasing Na_2O/SiO_2 molar ratio, density tends to decrease while WA% tends to increase. This trend is particularly evident for IFA12 formulation.

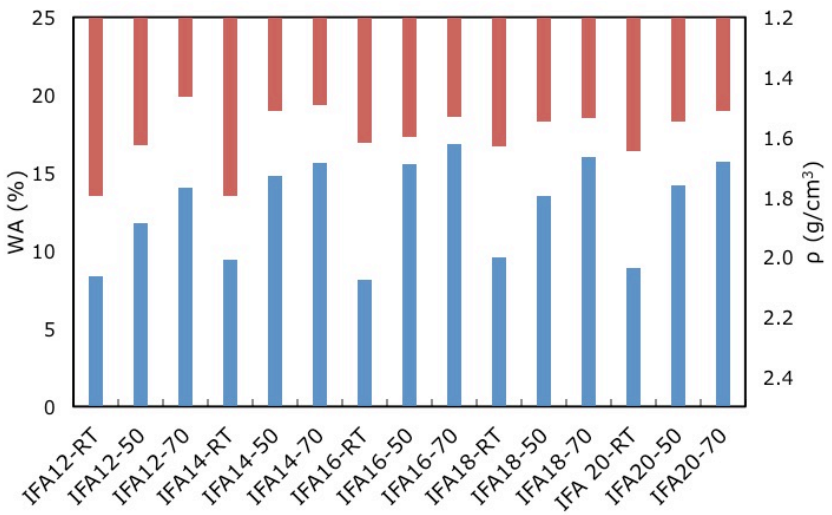

Figure. 5.10 Water absorption and bulk density for the considered samples [149].

5.2.2 Thermal behaviour

Dilatometric analyses were carried out on selected samples cured at room temperature (IFA12-RT, IFA14-RT, IFA16-RT) and at 70 °C (IFA12-70, IFA14-70, IFA16-70 and IFA20-70). The test was performed on 50x7x6 mm^3 samples obtained from the cubic ones and results are reported in Figure. 5.11 - Figure. 5.13.

Figure. 5.11 shows the dilatometric curves of room temperature cured samples. At

the end of the test all the samples show a relevant expansion. In particular, IFA12-RT exhibits an expansion of about 5% while for the other two samples (IFA14-RT and IFA16-RT), the test was interrupted around 750 °C for over-expansion, probably due to a partial melting resulting in the softening of the specimens.

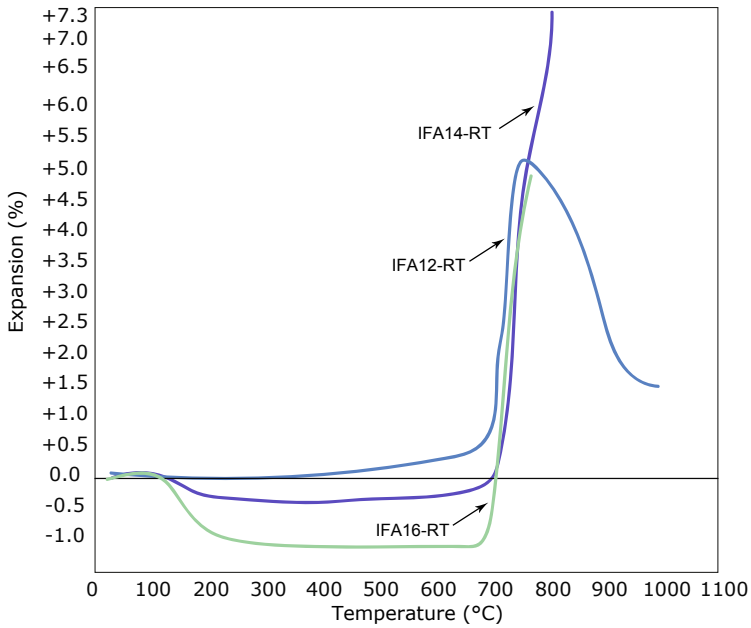

Figure. 5.11 Dilatometry results for ambient temperature cured representative samples [149].

The behaviour of oven cured samples (Figure. 5.12) is very different from the one observed for RT. All the samples show a similar curve, exception for FA20-70, which follows a different performance. The trend shown by IFA12-70, IFA14-70, IFA16-70 is very similar to the one obtained by Rickard et al. [112] in a study conducted on geopolymers obtained by the activation of fly ash by means of hydroxide and sodium silicate with similar curing conditions. As done in the aforementioned paper, is it possible to split the plot in six different regions, separated by changes in trend curves. Region I is characterized by the evaporation of absorbed water without any related shrinkage. Region II shows a start of shrinkage generated by the pore collapse due to capillary strain and dehydration, while region III shows a plateau of thermal stability potentially related to a slow dehydroxylation of hydroxyl groups [207]. This phase of stability is not detected for FA20-70 sample, which continues to shrink with less intensity. The following shrinkage of region IV is in accordance with the densification observed by Rickard [112] and potentially related to a glass transition temperature for geopolymers. In the study of Duxson et al. [207] a similar densification was observed for metakaolin samples by a

Si/Al ratio between 1.15 and 2.15 and the onset was observed to reduce as the Si/Al increased, which is in accordance with what was recorded in the studied samples. In fact, the starting temperature of the densification phase (region IV) seems to be smaller for IFA12-70 sample (which is characterized by a Si/Al = 1.74) compared to that for IFA14-70 sample (Si/Al = 1.67), which in turn is lower than the one for IFA16-70 (Si/Al=1.61). This link between Si/Al ratio and phase densification is also emphasized by the derivate peaks. The thermal expansion of region V, which is not present in IFA20-70 where a constant shrinkage is recorded, can be related either to crack formation, crystallization or to an increase in porosity [112] while the further shrinkage of region VI may be related to the collapse of the pores which were formed in the previous region. Sample IFA20-70 exhibits a complete different behaviour with a constant shrinkage between regions IV and V and a further dilatation in region VI. This difference can be ascribed to intrinsic differences in gel types developed by the different systems depending on activators balance [149].

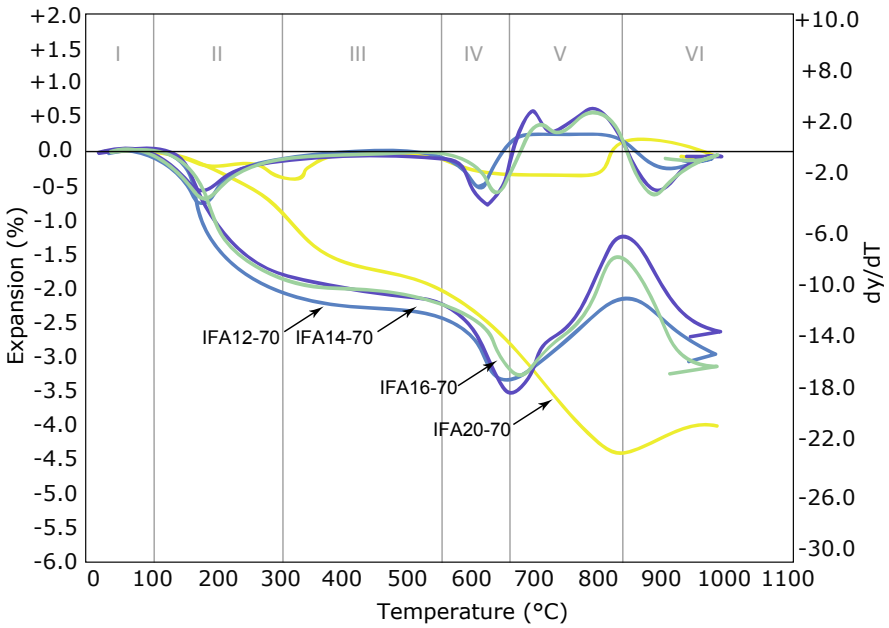

Figure. 5.12 Dilatometry results for oven cured (70 °C) representative samples [149].

After this first dilatometric test, selected samples were subjected to a second calcining and Figure. 5.13 reports the comparison between the first and second test.

IFA12-70C is characterized by a linear behaviour with a negligible expansion of 0.5 - 1% at the end of the test (1200 °C) while IFA20-70C exhibit a linear expansion till 1000

°C followed by a sharp shrinkage with a final contraction of about -1%. It is clear how, after calcining, samples gain thermal resistance and become more stable.

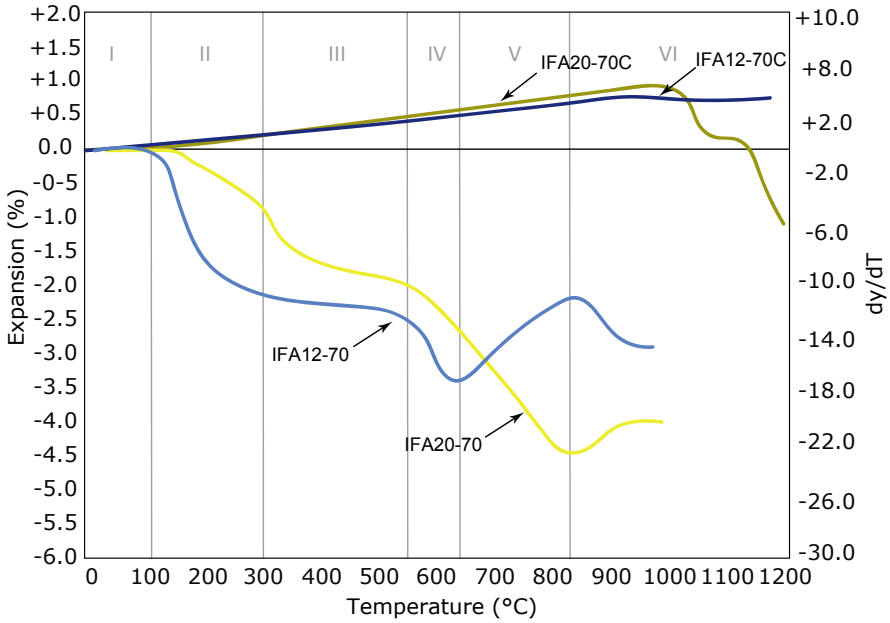

Figure. 5.13 Dilatometry results for IFA12-70 and IFA20-70, curves for the first and second (C) calcination cycle [149].

Figure. 5.14 shows samples before and after the calcining process: the colour clearly shifts into red and no cracks or any sign of deterioration are observable.

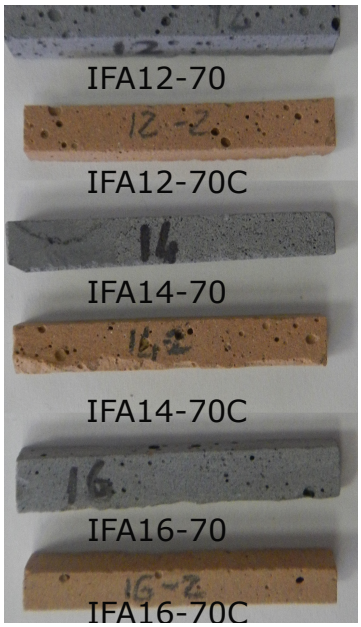

Figure. 5.14 Samples before and after calcining [149].

This behaviour can be ascribed to the formation of different crystalline phases, which were confirmed by XRD analysis before and after calcining.

5.2.3 Microstructural characterization

Figure. 5.15 shows how calcination process allows the formation of albite, which can improve the thermal resistance of geopolymers due to its high meting point (1118 °C [208]). Before calcining, the intrinsic difference between the two boundary systems is evidenced by the presence of chabazite-Na in FA20-70 compared to FA12-70. This result is in accordance with the results obtained by Temuujin et al. [209] for samples with low Si/Al ratio (1 - 2), which show zeolitic compounds, compared to geopolymers with Si/Al >2. Moreover, the formation of chabazite-Na is related to an excess of free Na in this latter formulation compared to the others.

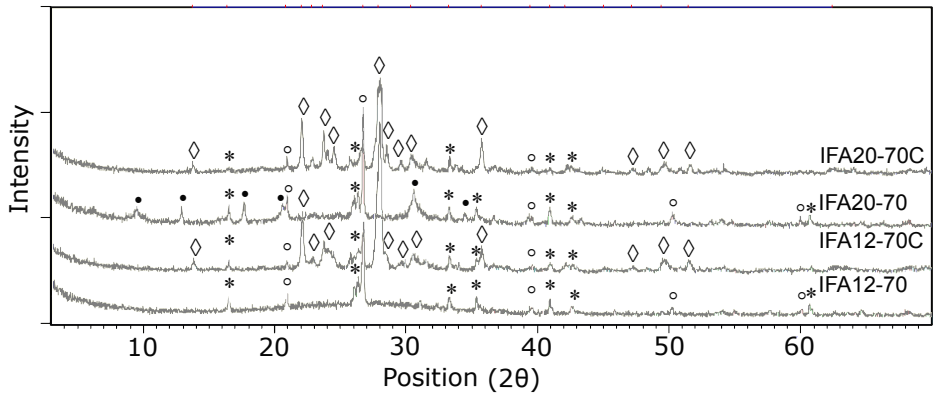

Figure. 5.15 XRD patterns of the geopolymer composition before and after calcining. (✻ = mullite ($Al_6SiO_2O_{13}$); ○ = quartz (SiO_2); ● = chabazite-Na ($NaAlSi_2O_6*3H_2O$); ♢ = albite ($NaAlSi_3O_8$)) [149].

The mercury intrusion porosimetry was performed on all types of geopolymers and on two selected calcined samples (FA14-70C and FA16-70C). For each sample values are reported in Table. 5.2 and Figure. 5.16. It is clear how oven curing results in a drastic drop of pore size for all the samples and in an increase of total porosity %. This effect is more evident for IFA12 and IFA14 formulations and it is consistent with the results obtained by WA%, where an increase in absorption was observed for oven-cured samples. The different curing conditions are so directly responsible for the development of a different pore system which consist, in the case of oven-cured samples, in long percolative chains of small pores which can be accessed only by a breakthrough effect of an high mercury pressure.

It must be highlighted, as reported by Pastorino et al. [210], that MIP measures the threshold diameter of the pore which allows mercury penetration, rather than the pore diameter itself thus, as in this case, the presence of large cavities connected by smaller neck opening is registered as unimodal porosity having the diameter of the neck (ink-bottle effect). The presence of those percolative chains in oven-cured samples, compared to RT ones, may be also linked to a higher geopolymerization grade and to the formation of a more coherent and resistant gel which allows the formation of a more stable product (as observed in the case of dilatometric analyses).

The possibility shown by MIP to determine the accessibility of the pore network is relevant when durability is taken in account, as pores are directly responsible of external agent penetration in the matrix [52,210]. The reduction of pore size (one order of magnitude on average) is so a relevant aspect determined by a different curing.

After calcining (Figure. 5.16f) a sensible increase in pore size is observed, which is related to the formation of the new crystalline phases described in the previous paragraphs.

Sample	Mean pore radius (μm)	Bulk density (g/cm^3)	Total porosity (%)
IFA12-RT	0.368	1.77	17.6
IFA12-50	0.031	1.67	19.9
IFA12-70	0.010	1.63	25.7
IFA14-RT	0.212	1.83	21.5
IFA14-50	0.010	1.67	22.9
IFA14-70	0.014	1.49	30.0
IFA16- RT	0.122	1.59	27.2
IFA16-50	0.031	1.57	28.5
IFA16-70	0.030	1.56	31.9
IFA18-RT	0.071	1.54	19.2
IFA18-50	0.053	1.59	33.6
IFA18-70	0.053	1.59	32.6
IFA20-RT	0.071	1.50	27.4
IFA20-50	0.120	1.66	28.1
IFA20-70	0.014	1.43	24.3
IFA14-70C	1.094	1.44	28.3
IFA16-70C	1.078	1.67	30.3

Table. 5.2 Mean pore radius, bulk density and total open porosity for the investigated samples; results obtained by MIP analysis [149].

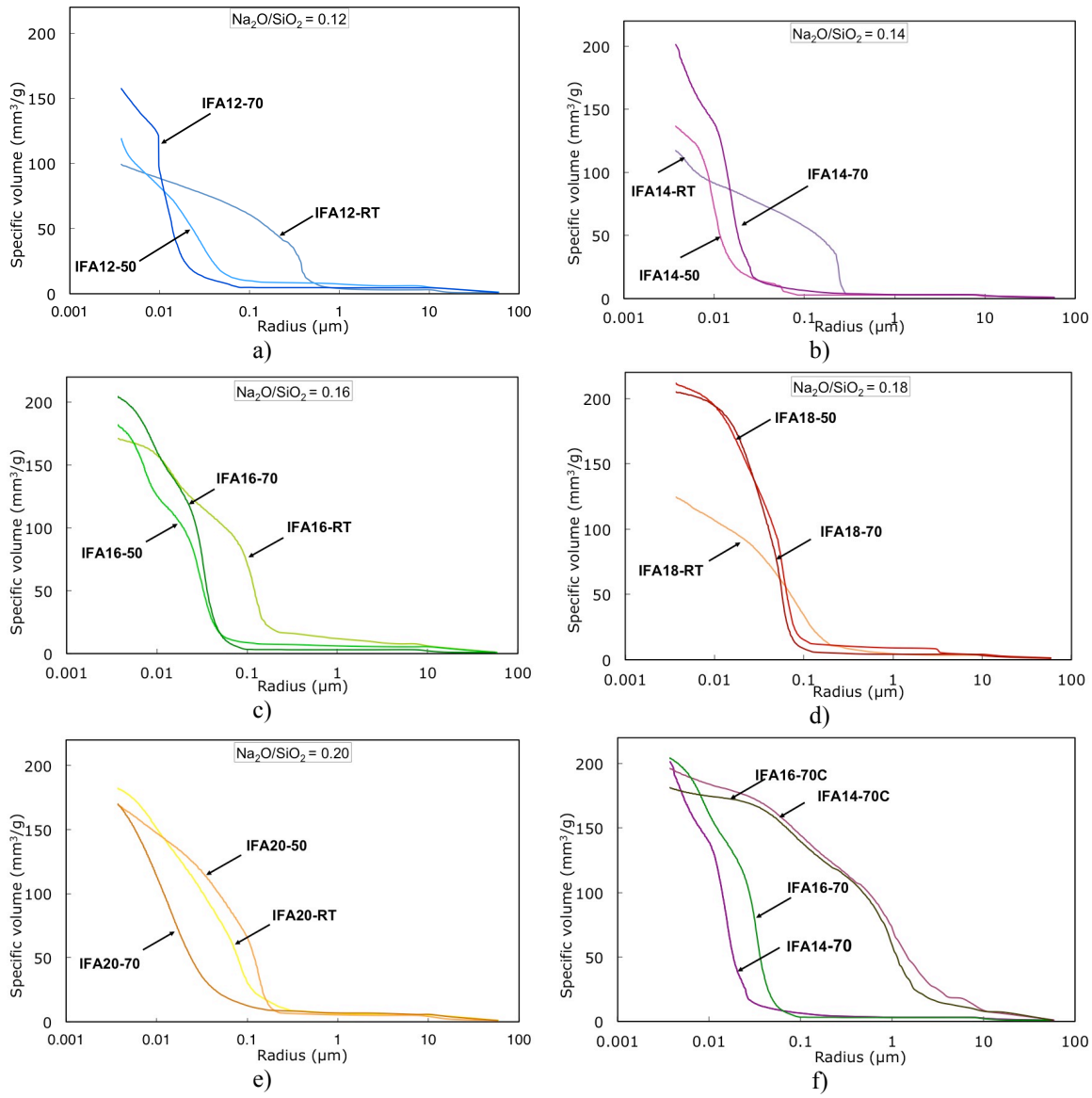

Figure. 5.16 MIP curves for the investigated samples: IFA12 (a); IFA14 (b); IFA16 (c); IFA18 (d); IFA20 (e); IFA14-70 and IFA16-70 before and after calcining (f) [149].

5.2.4 pH and carbonation

Another parameter that was monitored in this study is the evolution of pH of the pore electrolyte in the samples. This measurement was performed for each sample after 90 days of natural carbonation and after a further 90 days curing in carbonation chamber (CO_2 = 1%, T = 30 °C, R.H. = 65%). The results for this test are reported in Table. 5.3.

Regardless of the formulation and of the initial curing conditions, it is possible to observe that the pH of all the samples is set around 11 and a drop of 2 pH points on average is recorded after subjecting the samples to further 30 days of accelerated

carbonation. Even in this case no sensible differences are distinguishable among the formulation/curing conditions.

In order to monitor the evolution of pH more in detail, another measurement was performed on specimens which were specifically prepared and subjected to two different curing conditions: a series of samples for each formulation was poured in moulds and immediately sealed, maintained sealed at room temperature and then unsealed and demoulded and at the due testing day, another parallel series was cast, stored unsealed in carbonation chamber, demolulded after three days and tested in the predicted days. Results are reported in Figure. 5.17. It is clear that carbonation in the specimens is completely attributed to the exposure to CO_2, as no sensible drop is recorded for sealed samples, which maintain a constant pH over 12. The geopolymerization process itself has so no consequences in "pH consuming". However, when exposed to carbonation, samples with lower amount of NaOH (e.g., IFA12) have a fast drop below 10 (this drop is already measured after 14 days) and results tend to flatten and reach a plateau around 9.5 at the end of testing, as already shown for natural carbonation. The tendency to fast carbonation for geopolymers has been already highlighted in literature [57,211,212] and it is clear how accelerated carbonation can lead to an overestimation of results compared to the natural CO_2 concentration. Nevertheless, is also clear that, for a broad range of application, this is a crucial parameter, which has to be deeply assessed, as carbonation is one of the main problems affecting service life of reinforced structures [213].

Sample	pH after 90 days of natural carbonation	pH of the previous samples after further 90 days of accelerated carbonation
IFA12-RT	10.880	9.385
IFA12-50	11.420	9.570
IFA12-70	11.033	9.526
IFA14-RT	11.740	9.394
IFA14-50	11.185	9.560
IFA14-70	11.235	9.698
IFA16-RT	11.600	9.392
IFA16-50	11.456	9.451
IFA16-70	11.551	9.507
IFA18-RT	11.100	9.346
IFA18-50	11.402	9.168
IFA18-70	11.343	9.370
IFA20-RT	11.580	8.985
IFA20-50	10.772	9.349
IFA20-70	11.122	9.418

Table. 5.3 pH values for the investigated samples [149].

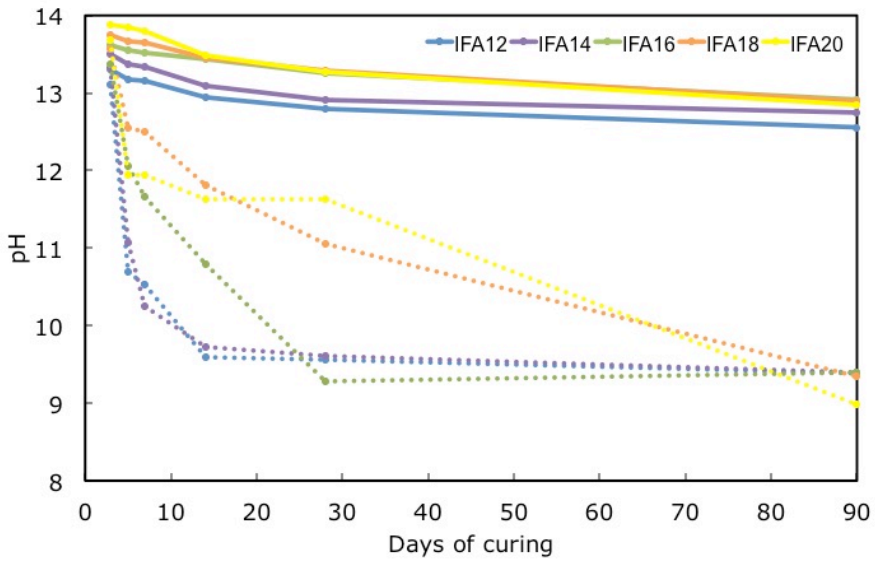

Figure. 5.17 pH measurement for sealed samples (full line) and samples cured in carbonation chamber (dotted lines) [149].

5.2.5 Main remarks

This part of the research was aimed at investigating the influence of curing conditions in physical and microstructural properties of different formulations of IFA based geopolymers, with specific attention on thermal behaviour. The formulations were varied by modifying the total Na_2O/SiO_2 molar ratio from 0.12 to 0.20 and samples were maintained sealed till the selected testing day and subjected to three different curing conditions for the first 24 hours: ambient temperature, oven curing at 50 °C and oven curing 70 °C. Results can be summarized as follows:

- among the two considered process parameters (Na_2O/SiO_2 molar ratio and curing temperature for the first 24 hours) the one with the greatest influence on the microstructure of the resultant geopolymers is the curing condition. A more compact structure, which also shows a higher geopolymerization degree, was observed in thermally treated samples;
- the dilatometric analysis showed a better behaviour in terms of dimensional stability for the samples cured at 70 °C with respect to the RT cured geopolymers. Moreover, after the first calcination, specimens showed a sensible increase in thermal stability and a vey low shrinkage (~ 1%), which is a behaviour that is close to that of refractory materials for industrial application;

- XRD analysis allowed to observe the formation of different phases before and after calcining, depending on the increase of Na_2O/SiO_2 molar ratio: in particular, comparing IFA12-70 with IFA20-70, it is clear how the increase in sodium hydroxide, with respect to sodium silicate, leads to the shift from a mainly amorphous to a crystalline and zeolite-like product. Calcination, in addition, leads to the formation, for all sample types, of new crystalline phases which involve an increase of the high temperature performance;
- MIP analysis highlights a drastic drop of pore size samples and an increase of total porosity % for all the oven-cured samples, which is sign of a different refinement of the pore structure due to heating and of a different geopolymerization grade and which is a relevant issue when durability is taken in account;
- pH measurements show how all geopolymers, regardless the formulation and curing, are prone to carbonation when in contact with CO_2. This is a remarkable point, which must be carefully considered in case of reinforced applications.

The studied geopolymer formulations, although not classifiable as refractory materials, showed a good behaviour for high temperature applications and are so encouraging in demonstrating how, with the optimization of curing and formulation it is possible to obtain performing products, which can open new perspective in the field of sustainable materials.

6 EXPERIMENTAL RESULTS AND DISCUSSION: MORTARS

In this Chapter an evaluation of the performances of the studied geopolymer formulations as mortar is reported. A first analysis was performed comparing the behavior of IFA and AFA mortar samples from a microstructural and mechanical point of view. Then, the research was focused on the only use of IFA as geopolymer precursor and on the behavior of the relevant geopolymer mortars in reinforced systems and aggressive environments. Results have been compared to the one obtained by a traditional cement-based mortar and interpreted in the light of their physical and microstructural characteristics, pointing out the main discovered discrepancies in the two different systems.

6.1 Mortar Type 1: IFA and AFA samples

In this section, IFA and AFA formulations, previously tested as geopolymers, are compared as mortars (M1, as reported in Chapter 3.2.2.2) in order to evaluate how the different raw material can influence the final performances of the related mortar product.

A first observation was made on the different workability offered by the two systems: additional water was needed in IFA samples in order to obtain the same workability offered by AFA samples. An increase in L/FA ratio by 15% (i.e., 0.52 for IFA *vs* 0.45 for AFA, see Table. 3.7) led to a decrease in mechanical performances compared to AFA.

6.1.1 Microstructural and mechanical characterization

From a microstructural and mechanical point of view, mortar samples exhibited the same trend for water absorption and mechanical strength which was previously determined for pastes (see Chapter 5). However, for IFA mortars, increasing the L/FA ratio led to a decrease in properties, in particular, a significant lowering of compressive strength compared to AFA.

In general, Australian fly ash mortar samples had marginally lower water absorption and had higher strength (both compressive and flexural) than the equivalent mortars prepared with Italian fly ash (Table. 6.1).

28 days of curing			
Sample	WA %	Flexural strength (MPa)	Compressive strength (MPa)
M1_IFA12	5.7	11.0 ± 0.8	26.7 ± 2.5
M1_IFA16	6.3	8.9 ± 0.3	24.0 ± 1.3
M1_IFA18	7.2	6.4 ±0.5	24.5 ± 4.7
M1_IFA20	8.6	3.5 ± 0.1	13.7 ±1 .4
M1_AFA12	4.8	9.3 ± 0.2	66.1 ± 3.3
M1_AFA16	5.7	7.1 ± 0.2	41.9 ± 2.1
M1_AFA18	6.8	6.8 ± 0.2	32.4 ± 2.1
M1_AFA20	7.1	6.2 ± 0.1	30.2 ± 2.7

Table. 6.1 Water absorption, flexural and compressive strength of the investigated mortar samples [44].

6.1.2 Main remarks

The results obtained for mortars confirms the sensitivity of the investigated systems to the Na_2O/SiO_2 molar ratio used in the feed and highlights how the water added during mixing can play a further and important role in affecting the final performances of the products. In fact, the addition of water needed for IFA based mortars to reach acceptable workability leads to a dramatic decrease in compressive strength compared to AFA mortar samples. As workability is one of the main requirements for building materials such as mortar and concrete, the research on admixtures such as superplasticizers suitable for geopolymers should be emphasized in order to enable strength retention. The mechanical strength results obtained for the investigated mortar samples clearly demonstrate the potential of using fly ash based binders to prepare plasters and mortars

useful for the civil engineering field as the reported properties were similar or better of those usually exhibited by traditional hydraulic binders (e.g., hydraulic lime, Ordinary Portland Cement) [44].

6.2 Mortar Type 2: IFA and CEM samples

The aim of this part of the work was to study the corrosion behaviour of room temperature cured steel-reinforced geopolymer mortars (M2) based on IFA by an integrated approach including mechanical, physical, microstructural and electrochemical tests. In particular, formulations with Na_2O/SiO_2 molar ratio ranging from 0.12 to 0.16 (see Chapter 3.2.2.2 and Table. 3.8) were prepared in order to evaluate its effect on mechanical strength, porosity distribution and rebar corrosion behaviour in a chloride-rich environment (NaCl 3.5 wt.%). During the exposure, the chloride content in close proximity of the rebars and the initial and final pH values were also assessed. A comparison was made between geopolymer performances and those characterizing a cement-based mortar and the different behaviour observed was justified on the basis of tests carried out in leachate solutions obtained from the different mortar types in contact with water.

6.2.1 Microstructural and mechanical characterization

Geopolymer and cement M2 mortars showed similar values of bulk density (i.e., 2.04 ± 0.01 g/cm^3 for geopolymers and 2.07 ± 0.01 g/cm^3 for CEM). The compressive strength values of the investigated mortars were evaluated at different curing times and results are reported in Figure. 6.1. Figure. 6.1a shows that the compressive strength values of geopolymers increased with curing time for up to 28 days of curing, as occurs in traditional mortars. As a consequence, 28 days can be considered as a representative curing time for estimating geopolymer strength, similarly to cement standard compressive strength determined according to EN 196-1 [148]. The compressive strength values at 28 days of curing (σ_{c28}) increased for geopolymers following this order: σ_{c28}IFA16 < σ_{c28}IFA14 < σ_{c28}IFA12 (i.e., 17.2 ± 0.9 < 18.9 ± 0.6 < 23.3 ± 0.3 MPa) and were in line to those obtained in the previous Chapter (6.1.1) and by other authors on similar materials cured at room temperature or by mild heating [96,97]. At decreasing Na_2O/SiO_2 molar ratio, compressive strength increased linearly (Figure. 6.1b). The increase of σ_c values at

higher silicate contents was more evident at early curing time, suggesting that a high silicate concentration stimulated the rate of geopolymerization [93]. The effect of sodium silicate in promoting the geopolymer net formation and in reducing the total porosity (at least in specific Na_2O/SiO_2 ranges) is also elsewhere highlighted [14,29,44,138]. In particular, in a research carried out on geopolymers with a constant Na/Al ratio, an increase in Si/Al (and therefore Si/Na) ratio induced an increase in gel volume, homogeneity and strength and, likely, also an increase in the intrinsic binder strength, because the stronger Si-O-Si linkages substituted the weaker Si-O-Al and Al-O-Al bonds [29]. Conversely, a too high Si/Al ratio produced a highly unreacted phase fraction and induced a decrease of mechanical performances [29]. CEM exhibited a compressive strength of 34.4 ± 0.5 MPa at 28 days of curing (Figure. 6.1a), which was higher than that of geopolymer mortars. This value, which is quite low for a CEM 42.5 R, was due to factors such as: (i) the relatively high L/B ratio, (ii) the use of non-standard sand and (iii) the use of non-standard curing conditions (R.H. = 35% *vs* R.H. > 95%) [52].

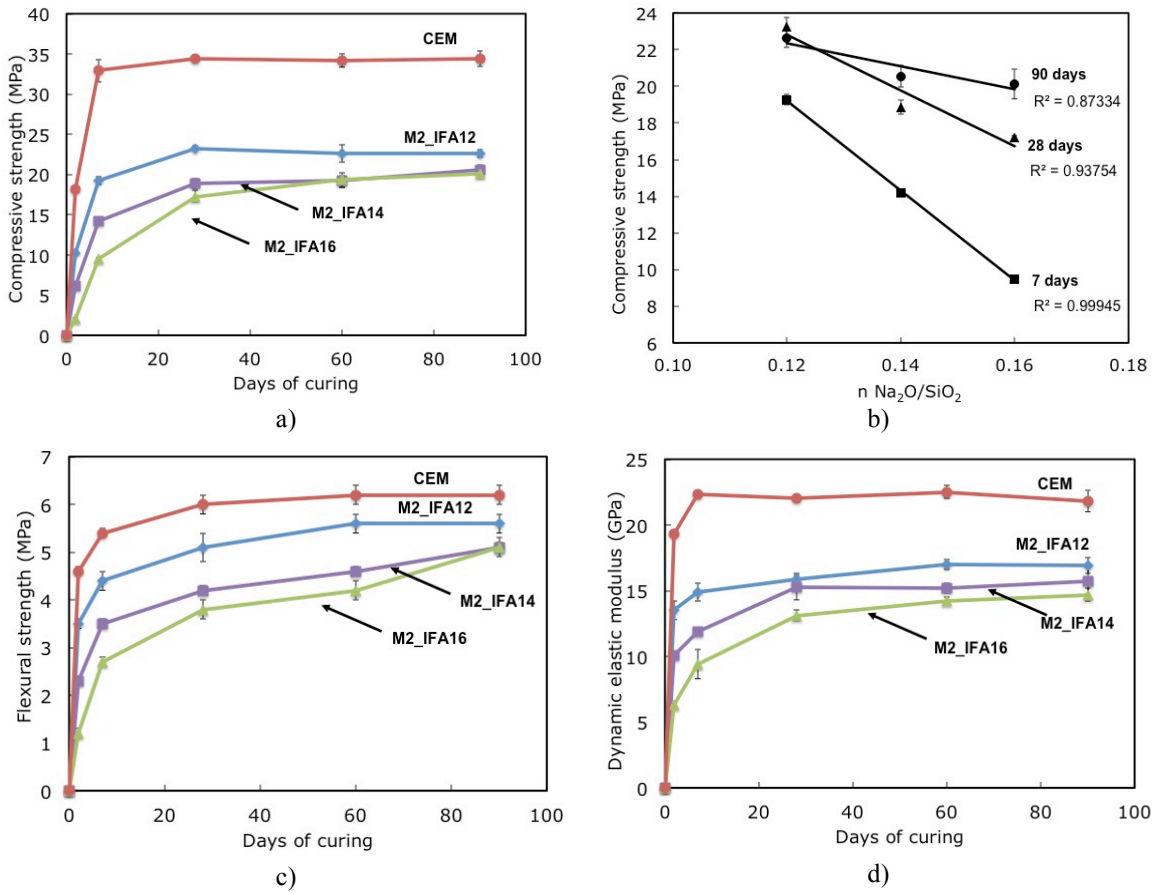

Figure. 6.1 Mechanical properties for the investigated mortar samples at different times of curing (2, 7, 28, 60 and 90 days): compressive strength (a); compressive strength as a function of the Na_2O/SiO_2 molar ratio (b); flexural strength (c); dynamic elastic modulus (d) [52].

Flexural strength results (σ_f) are reported in Figure. 6.1c. Although three point bending test on porous materials can be affected by high degree of uncertainties, the trend determined for geopolymer and CEM mortar samples is similar to that one obtained by compressive test. Again, M2_IFA12 mix shows the best values among geopolymer mixes, still remaining lower then CEM sample.

The results of the dynamic elastic modulus (E_d) are reported in Figure. 6.1d. For geopolymers E_d values show the same trend of mechanical strength tests: a linear increase in stiffness is observed with the decrease of Na_2O/SiO_2 molar ratio (Figure. 6.1b). M2_IFA12 exhibits the higher E_d value among the geopolymer formulations, which is in its turn lower compared to CEM. The lower E_d value determined for geopolymers corresponds to a higher elastic deformation at constant load and a to a lower stiffness. This property could prevent the formation of microcracks if geopolymers are used as a repair mortar.

The sample microstructure was investigated by means of water absorption and MIP measurements.

Regarding water absorption the first test, which is a short test investigating the absorbed water after 90 min of partial immersion, was conducted according to UNI EN 1015-18 [167]. After 90 min, the absorbed water reached penetration heights of about 45 mm in all geopolymer mortars, while a lower height of 25 mm was measured for CEM (Figure. 6.2). The capillary water absorption coefficients, reported in Figure. 6.3a, were quite similar for all geopolymer mortars (with a maximum value of 0.43 $kg/m^2 \cdot min^{0.5}$ for M2_IFA16), while a lower value was registered for CEM (0.36 $kg/m^2 \cdot min^{0.5}$). These results suggest that the latter mortar has a refined and perhaps more tortuous pore structure than that of FA mortars [214].

In spite of the slow water uptake rate detected on CEM at short exposure times, the longer lasting water absorption tests according to UNI EN 15801 [168] (Figure. 6.3b) evidenced that the final water uptake of CEM was comparable or even higher than that exhibited by geopolymers (Q_i = 7.2 kg/m^2 in CEM and Q_i = 6.7 kg/m^2 in M2_IFA16). In fact, after 8 days the water uptake of CEM was twice than that obtained after 90 min, while that achieved by geopolymer mortars did not increase much. These data indicated that in both mortar types a significant water absorption occurred, which was faster in

geopolymer materials.

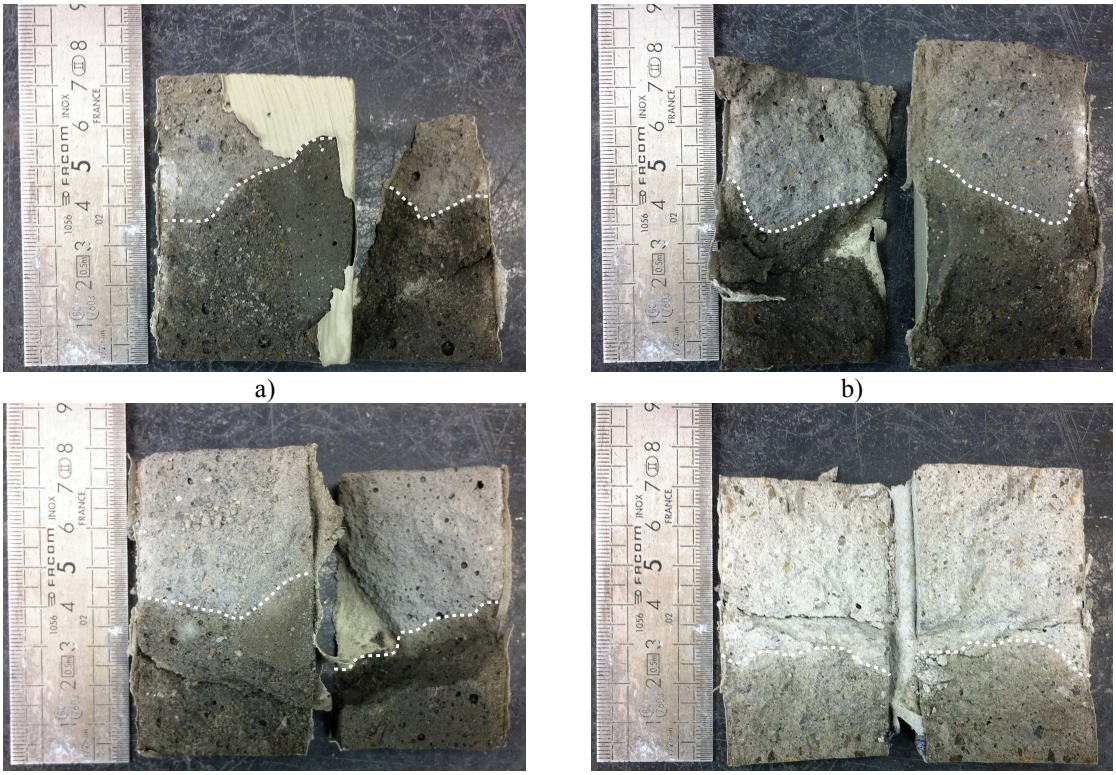

Figure. 6.2 Split samples after 90 min of partial immersion with a 5 mm water head according to UNI EN 1015-18 [167]: M2_IFA12 (a); M2_IFA14 (b); M2_IFA16 (c); CEM (d).

The pore size distributions of all mortars were assessed by MIP analysis after 28 days of curing and the results are reported in Figure. 6.3c. In this plot, three different pore size regions can be distinguished: gel pores below 0.015 μm (which do not affect permeability [215]), capillary pores ranging between 0.015 - 0.5 μm (affecting fluid permeability and mechanical properties [216,217]) and macropores with radius ≥ 0.5 μm, mainly influencing mechanical properties [218]. The Figure shows that the main observable difference between geopolymer and cement-based mortars was the large presence of macropores in geopolymers and the predominance of capillary pores in CEM. Among geopolymers, M2_IFA16 exhibited the most porous microstructure, while similar pore size distributions were observed for M2_IFA12 and M2_IFA14. Other important information can be drawn by the comparison of the $r_{50\%}$ values, which are the pore radii at which 50% of the pore volume is intruded in the different matrices. Figure. 6.3d reports the normalized pore size distributions for all the investigated mortar types and shows that the $r_{50\%}$ of CEM mortar was 0.19 μm, much lower than that obtained for geopolymers (around 1 μm for all mixes), in agreement with the slower observed water uptake detected

during absorption tests in CEM mortar. Among geopolymers, a slightly higher $r_{50\%}$ value was found in M2_IFA16 (i.e., M2_IFA12 = 1.23 µm; M2_IFA14 = 1.27 µm and M2_IFA16 = 1.36 µm), suggesting that this mortar is more vulnerable to the penetration of aggressive species from aqueous solutions [52].

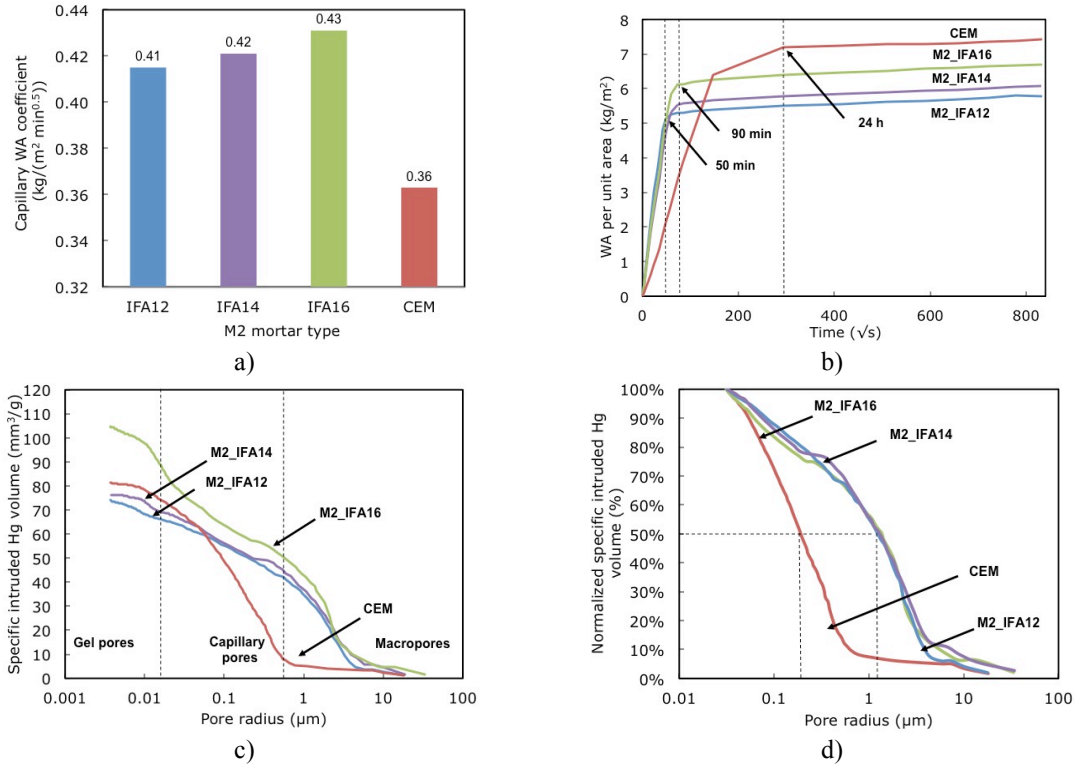

Figure. 6.3 Capillary water absorption coefficients according to UNI EN 1015-18 [167] (a); amount of water absorbed per unit area according to UNI EN 15801 [168] (b); pore size distribution curves of the investigated samples at 28 days of curing (c); normalized pore size distribution curves of the investigated samples at 28 days of curing. Mean pore radius values ($r_{50\%}$) are highlighted by dashed lines (d) [52].

6.2.2 Tests under partial immersion conditions

Tests under partial immersion conditions were performed on reinforced and unreinforced slabs, as previously described in Chapter 3.2.2.2. The setup for the test is reported in Figure. 3.9.

During the 90 days exposure to 3.5% NaCl solution, chlorides penetrated through the mortars by a combination of capillary suction and diffusion. Capillary suction is the fastest process and, on the basis of absorption tests, the chloride solution was expected to reach the reinforcing bars (height of 33 mm, Figure. 3.9) in less than 1 day in all mortars.

Figure. 6.4 shows the average E_{cor} (Figure. 6.4a) and R_p (Figure. 6.4b) trends

obtained in all mortars. Within 2 days of exposure, the average E_{cor} values of rebars in CEM underwent a fast drop from about -0.1 V_{SCE} down to values more negative than -0.276 V_{SCE} (Figure. 6.4a) that is the limit that, according to ASTM C876 [219], indicated a high probability of active corrosion. The same occurred within about 6 days of exposure in M2_IFA12 and M2_IFA14 and after only 1 day in M2_IFA16 mortars. Later, values around -0.55 V_{SCE} on average were obtained in CEM and even more negative in M2_IFA12 and M2_IFA14 and particularly in M2_IFA16 (on average -0.60 ÷ -0.65 V_{SCE}, Figure. 6.4a) [52].

On the basis of a generally accepted Stern-Geary constant of 26 mV, the i_{cor} limit for active corrosion (i_{cor} of $0.2 \cdot 10^{-6}$ A cm^{-2}, according to [220]) is reached in correspondence of a R_p value of $1.3 \cdot 10^5$ ohm·cm^2. Figure. 6.4b shows that the average R_p values of the rebars decreased from initial values close to $3 \cdot 10^6$ ohm·cm^2 to values lower than about 10^5 ohm·cm^2 within 1 - 2 days of exposure in CEM and M2_IFA16 and after about 40 days, in the case of M2_IFA12 and M2_IFA14. At the end of the exposure period, low and comparable average R_p values ($3 \cdot 10^4$ ÷ $4 \cdot 10^4$ ohm·cm^2) were recorded in all mortar types [52].

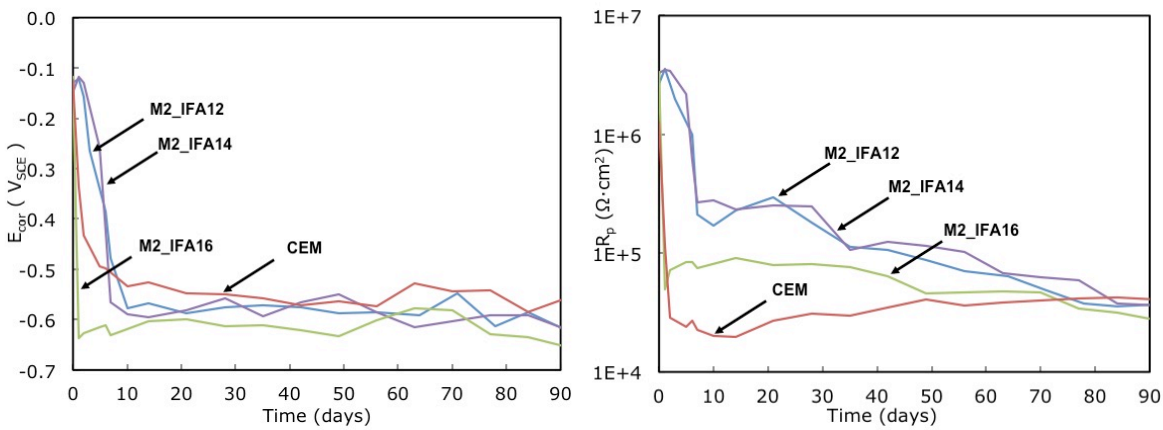

Figure. 6.4 Average E_{cor} (a) and R_p (b) values recorded in the different mortar types during partial immersion in 3.5% NaCl solution [52].

These findings suggested that a corrosion attack developed in all mortars, but a less severe one occurred in M2_IFA12 and M2_IFA14 formulations. These mortars exhibited a lower porosity than M2_IFA16 (Figure. 6.3a), so justifying their better protectiveness towards the rebars. However, their cumulative porosity was similar to that of CEM, which also exhibited finer pores. So the worse behaviour of CEM towards degradation was

unexpected.

In order to elucidate this apparent inconsistency, further tests were performed, starting with the measurement of the pH and the chloride content of the pore electrolytes in contact with the rebars.

The pH values of the mortar pore electrolyte at the rebar level were measured at the end of the 90 days exposure to the NaCl solution. In Table. 6.2, these pH values are compared to the initial values, measured after 1 day curing. A negligible pH decrease was detected in CEM and a pH reduction of about 0.5 pH unit was found in FA mortars. Anyway, all pH values remained higher than 12, suggesting that significant carbonation was not experienced and did not affect the corrosion behaviour.

Sample	After 1 day of curing	After 90 days of partial immersion in 3.5% NaCl solution
M2_IFA12	12.73	12.38
M2_IFA14	12.74	12.36
M2_IFA16	12.73	12.17
CEM	12.99	12.88

Table. 6.2 Core pH values of the mortar specimens after 1 day curing and after 90 days of partial immersion in the chloride solution [52].

The total Cl- content (% *vs* binder) again at the rebar level in the mortars was determined after different exposure times (Figure. 6.5). In all mortars, the chloride amounts increased up to 60 days and then remained more or less constant until the end of the test. Higher chloride contents were detected in CEM (5% *vs* binder at the end of the test) than in geopolymers (1.4 - 1.8% *vs* binder at the end of the test). This was caused by the lower solubility of calcium-containing chloride salts formed in CEM (e.g., Friedel salts), in comparison to the sodium-containing chloride salts present in FA mortars. In the latter case, the salts were leached away by the contact solution, ensuring the maintenance of a lower chloride concentration. Chloride concentrations in AAMs similar to those reported in Figure. 6.5 were achieved after 7 days of exposure to saturated NaCl solution by [214]. Moreover, analyses carried out after 300 days of full or partial immersion of traditional mortar (obtained with water/cement ratio of 0.65 and moist curing) in 3.5% NaCl solution revealed chloride concentrations (expressed as of mass fraction of chloride ions in cement mortar) close to those here reported in CEM at saturation [221]. In that research, the authors stressed that during partial immersion exposures much higher

chloride amounts penetrated inside the mortars with respect to full immersion conditions because of the concomitant effect of continuous capillary penetration and water evaporation [221].

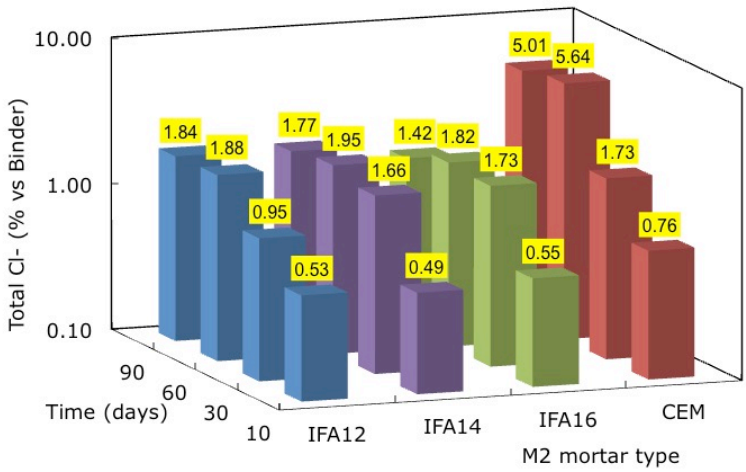

Figure. 6.5 Total Cl^- content (wt.% *vs* binder) at the rebar section for the investigated samples [52].

After just 10 days of exposure in 3.5% NaCl solution, the Cl- content in CEM and FA mortars was quite high: about 0.7 and 0.5% *vs* binder, respectively. The achieved chloride concentrations are higher than the commonly accepted critical chloride content capable to initiate corrosion in traditional concrete [127] and were actually found to be sufficient to start corrosion in CEM and M2_IFA16. On the contrary, a significant corrosion rate in M2_IFA12 and M2_IFA14 was measured only after 40 - 50 days when the chloride content was in the range 1 - 1.7 % *vs* binder. A higher critical content is likely to characterize the more compact geopolymers [52]. The reason for this different behaviour was unclear and was elucidated by recording polarization curves on steel in leachate solutions, as in Chapter 6.2.4.

6.2.3 Rebar surface analyses

Figure. 6.6 shows the surface aspect of the rebars after 90 days of partial immersion in 3.5% NaCl solution. In agreement with the active E_{cor} values and relatively low R_p measured by the electrochemical tests, significant corrosion attacks were detected in all rebars. In particular, a significant localized corrosion attack was present in CEM mortar, with pit depths around 300 μm (Figure. 6.7), while a widespread general non-uniform corrosion attack occurred in FA mortars and particularly in M2_IFA16. As an example,

Figure. 6.8 reports a SEM image showing a uniform corrosion layer (200 - 400 μm thick), which covered part of the reinforcing bar in M2_IFA16 (as shown in Figure. 6.6).

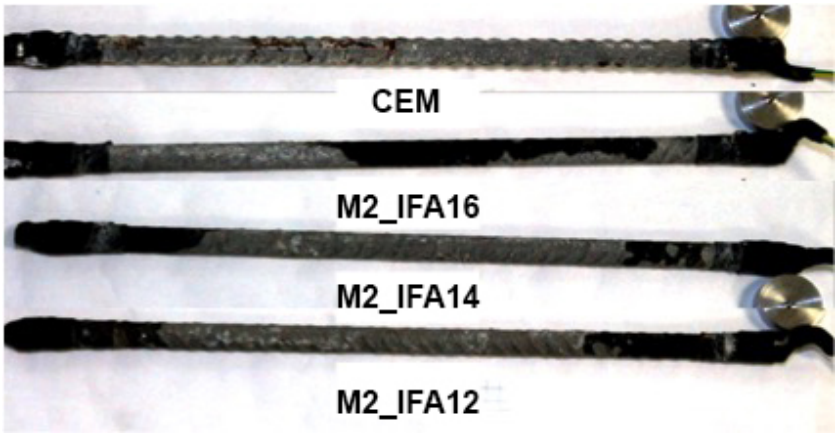

Figure. 6.6 Reinforcing bars extracted from the slabs at the end of the corrosion tests [52].

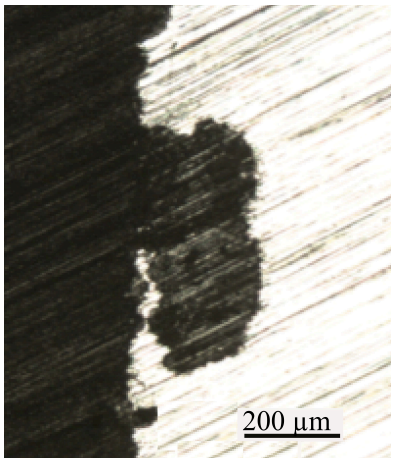

Figure. 6.7 Cross-section optical micrograph of rebar in reinforced CEM slab at the end of the corrosion tests [52].

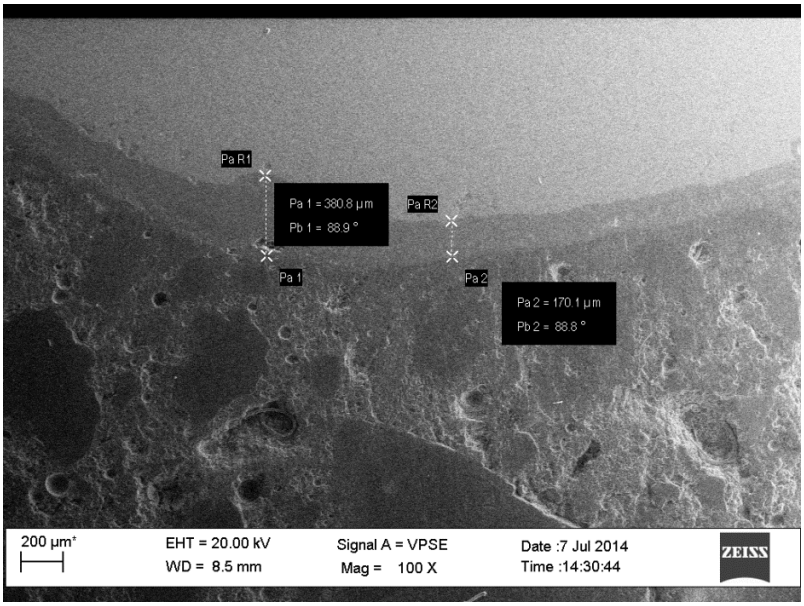

Figure. 6.8 Cross-section SEM micrograph of rebar in reinforced M2_IFA16 slab at the end of the corrosion tests [52].

The Raman analysis of the corrosion products formed in the different mortar types (Table. 6.3) revealed the presence of maghemite (γ-Fe_2O_3) and δ-FeOOH in all samples, while akaganeite (β-FeOOH) was found only in the geopolymer matrices. This latter corrosion product, usually connected to chloride-contaminated environments [222], is characterized by a low protectiveness and justifies the occurrence of a general corrosion attack in geopolymer mortars, instead of a localized attack, as detected in CEM [52].

Sample	Akaganeite	Hematite	Maghemite	δ-FeOOH	Fluor.
M2_IFA12	+		+	+	++
M2_IFA14	+	+	+	+	++
M2_IFA16	+	+	+	+	++
CEM			+	+	++

Table. 6.3 Raman quantitative analysis for corrosion products formed on rebars in reinforced slabs exposed to 3.5% NaCl solution; + = small values detected; ++ = high values detected; Fluor. = fluorescence [52].

6.2.4 Tests in leachate solutions

Figure. 6.9 collects the polarization curves recorded in the leachate solutions obtained from the different mortars. It clearly shows that in all cases steel exhibits a passive behaviour at E_{cor}, which is close to -0.38 V_{SCE}, independently of the mortar type. Passivity persists up to a potential of about 0.6-0.7 V_{SCE}, where oxygen evolution occurs [215] and it is slightly stronger in solutions obtained from geopolymers. In fact, passive

currents are smaller than in solutions extracted from CEM. Also cathodic polarization curves recorded in geopolymer leachate solutions are shifted to lower currents. Consequently, i_{cor} values in solutions extracted from geopolymers are about one half of that obtained in CEM extracts ($2.4 \cdot 10^{-8}$ A cm^{-2} towards $5.1 \cdot 10^{-8}$ A cm^{-2} on average) [52].

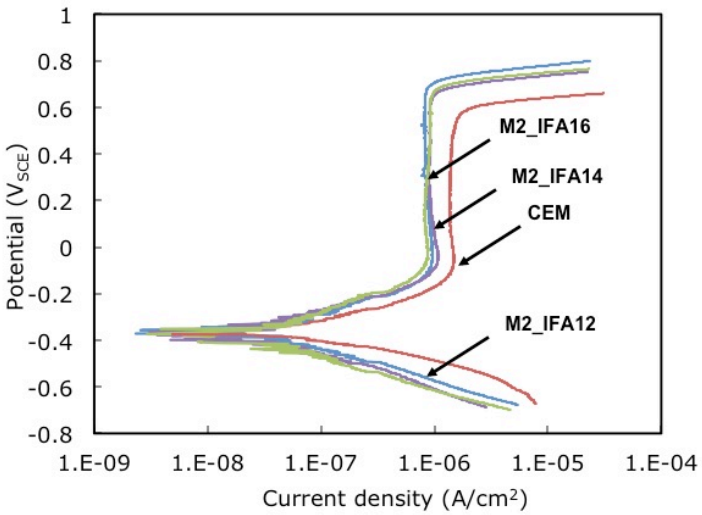

Figure. 6.9 Polarization curves recorded in the leachate solutions obtained from the different mortar types [52].

This means that, in spite of the presence of a pH value slightly lower than that detected in CEM, a corrosion inhibitor is present in the FA mortar pores electrolyte, which hinders steel corrosion [52].

ICP-OES analyses reported in Table. 6.4 show that leachate solutions deriving from FA mortars differ from those extracted from CEM essentially for the presence of relevant amounts of silicates in the former case (i.e., Si = 0.02 - 0.03 M in FA mortars, absent in CEM). Silicates are known to be corrosion inhibitors for iron and steel [224,225] and are reputed the origin of the observed slightly better corrosion behaviour of steel in geopolymers [52].

Element	Sample			
	M2_IFA12	M2_IFA14	M2_IFA16	CEM
Si	540	840	500	< 0.5
Al	0.3	1.4	0.7	1.1
Ca	< 0.1	< 0.1	< 0.1	60
K	110	130	130	430
Na	3900	5460	5300	420

Table. 6.4 Elemental analysis (in ppm) of leachate solutions provided by ICP-OES [52].

6.2.5 Main remarks

Reinforced and unreinforced IFA based mortar samples were prepared at RT with a constant L/B ratio of 0.52 and decreasing Na_2O/SiO_2 ratios in the activating solutions. Their microstructure and mechanical behaviour, along with their corrosion and chloride penetration resistance, were analyzed and compared to those exhibited by a cement-based mortar with the same L/B ratio. The multiple characterization techniques used in this work permitted to draw the following conclusions [52]:

- the mechanical properties of IFA mortars were found to be inversely proportional to the Na_2O/SiO_2 molar ratio. This result was already observed in the previous formulations confirming the role of silicate, which appears to stimulate the rate of geopolymerization and densification. However, all geopolymer mortars showed higher porosity and lower mechanical performances compared to CEM mortar;
- during exposure to NaCl solution, no carbonation was detected at the rebar level. Chloride concentrations were higher in CEM than in geopolymer mortars, due to the formation of scarcely soluble calcium-containing chloride salts (Friedel salts), which can't form in the case of geopolymers because of the low Ca content in the gel phase;
- electrochemical tests showed that the most compact geopolymers (M2_IFA12 and M2_IFA14) were more protective than M2_IFA16 and CEM towards steel rebars. The lower chloride contents generally present in geopolymers with respect to CEM can help to justify these differences. The lower protectiveness of M2_IFA16 was due to its higher porosity;
- M2_IFA12 and M2_IFA14 showed a higher critical chloride content for corrosion onset (about 1 - 1.7% *vs* binder), than CEM (around 0.5%). The better performance of these denser geopolymer mortars was connected to the presence of soluble silicate ions in geopolymer pore electrolytes which exerted a specific inhibition of rebar corrosion;
- at the end of the partial immersion test, a corrosion attack started on all rebars, independently of the mortar type. In geopolymers, the surface film contained akaganeite, which induced a general non-uniform corrosion attack. In CEM, different surface conditions occurred which caused the localization

of the attack in deep pits.

6.3 Mortar Type 3: IFA and CEM samples

This third part of the research on mortars investigates the corrosion protection afforded to the embedded rebars by room temperature cured alkali-activated mortars, based on IFA, during wet and dry exposures to 0.1 M NaCl solution. The results were compared to those obtained in a traditional cement-based mortar. The rebar corrosion behaviour was characterized by E_{cor} and potentiostatic R_p measurements, polarization curve recording and EIS. A concomitant physical-chemical investigation of the mortar microstructures and characteristics helped the interpretation of electrochemical test results.

6.3.1 Microstructural and mechanical characterization

Bulk density results, together with compressive strengths, elastic moduli and shrinkage values collected after 28 days of curing are reported in Table. 6.5.

In this case, a standard curing was used for CEM (T = 25 °C, R.H. = > 95%) and standardized sand was used for all the mortar samples. Results evidence again higher mechanical performances for CEM mortar, which show also a good dimensional stability in terms of shrinkage. Among geopolymers, M3_IFA12 is confirmed as the formulation leading to best properties and the compressive strength value obtained with standardized sand (34.2 ± 2.9 MPa) allows to classify this formulation as a 32.5 strength class, according to EN 196-1 [148]. With regard to shrinkage, a -0.3% variation was observed in M3_IFA12 and M3_IFA14, while a -0.1% was observed in M3_IFA16 mortar, which is the most stable geopolymeric formulation. The different curing conditions adopted for geopolymers (T = 25 °C and R.H. = 35%) and cement-based mortar (T = 25 °C and R.H. > 95%) partially explain the different shrinkage behaviour of geopolymers and CEM. Shrinkage values for geopolymers higher than those usually exhibited by cement-based mortars were already reported [226,227] where this behaviour was also ascribed to weight loss of water from the unreacted porous FA particles and to pore size distribution and relevant interconnectivity.

Sample	Bulk density (g/cm^3)	Compressive strength (MPa)	Dynamic elastic modulus (GPa)	Shrinkage (%)
M3_IFA12	2.11 ± 0.01	34.2 ± 2.9	15.6 ± 1.7	-0.36 ± 0.13
M3_IFA14	2.07 ± 0.01	27.0 ± 3.1	15.9 ± 2.5	-0.37 ± 0.02
M3_IFA16	1.78 ± 0.13	22.5 ± 0.8	14.2 ± 2.2	-0.11 ± 0.02
CEM	2.11 ± 0.02	47.0 ± 5.7	30.2 ± 2.2	-0.02 ± 0.01

Table. 6.5 Physical-mechanical characterization of the considered mortars after 28 days of curing [150].

In order to justify the different physical-mechanical properties of CEM and geopolymers, MIP was used to determine the pore distribution curves of the different mortars (Figure. 6.10). The total specific Hg volume intruded in geopolymer mortars, and particularly in M3_IFA16, was higher than that in CEM, suggesting a higher total porosity and a greater vulnerability of geopolymers to degradation. More in detail, the pore size distribution curves of M3_IFA16 shows the highest total porosity of about 85 mm^3/g (inducing the low measured bulk density of this mortar) and a bi-modal pore size distribution positioned at about 1 μm and in the range 0.3 - 0.03 μm. The pore distribution curves of M3_IFA12 and M3_IFA14 are rather similar to each other and are characterized by a total porosity of 57 - 60 mm^3/g and pore radii mostly around 1 - 3 μm. In the case of CEM, the total porosity is smaller (about 50 mm^3/g) and mainly consists in pores smaller than 0.5 μm and nanometric gel pores. As pores exceeding 1 μm are directly responsible for the rate of mass transfer through the porous system, the CEM pore network will induce slower water saturation and mass transfer processes [150].

The higher scale porosity of geopolymers can be ascribed to the different nature of the gels formed during hardening in these mortar types, in comparison to CEM. In fact, whereas C-S-H is the main product formed in the latter mortar type, binding phases formed by alkali-activation of IFA are constituted, as already reported in the previous Chapters, by gels such as C-A-S-H, N-A-S-H and C-S-H [44,77]. The pores associated with C-A-S-H and N-A-S-H gel are larger, mainly due to IFA grain dissolution after alkali-activation, even if they are often accessed via narrow constrictions caused by ink-bottle pores [228,229]. It is well known that the mortar porosity is the pathway through which aggressive species, such as oxygen, chlorides and carbon dioxide, penetrate and induce corrosion attack on the reinforcing bars.

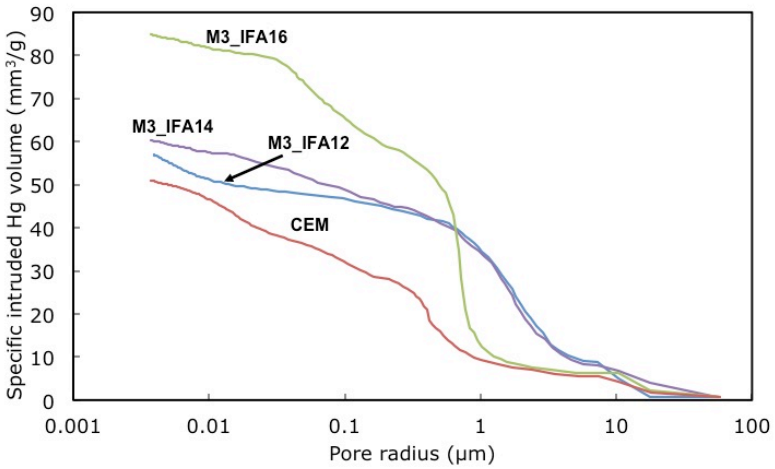

Figure. 6.10 Pore size distribution curves at 28 days of curing [150].

A clear consequence of the different pore size distribution between the two systems is given by the higher apparent chloride diffusion coefficients, D_a, measured for geopolymer mortars, which give information about the relative chloride mobility under pure diffusion conditions affected by pore dimensions, tortuosity and interconnectivity. D_a for CEM is smaller than those obtained for geopolymers, which in turn increase going from M3_IFA12 to M3_IFA14 and M3_IFA16 (Table. 6.6). The last one is one order of magnitude higher than that obtained for CEM, following the total porosity values.

Sample	D_a (m^2/s)
M3_IFA12	$9 \cdot 10^{-13}$
M3_IFA14	$1.6 \cdot 10^{-12}$
M3_IFA16	$3.6 \cdot 10^{-12}$
CEM	$3 \cdot 10^{-13}$

Table. 6.6 Apparent chloride diffusion coefficients in the different mortars [150].

6.3.2 pH and chloride content measurements

Another insight on the consequences of the different pore size distribution characterizing the two systems was provided by monitoring the pH variation and chloride concentration before and after the w/d cycles.

Table. 6.7 collects the pH of the pore electrolytes measured in the core of unreinforced cylinders after 28 days of curing in the absence of carbonation (curing in plastic bags for geopolymers/in the moist room at T = 25 °C and R.H. > 95% for CEM) and after 2 and 14 w/d cycles. The initial values obtained in the absence of carbonation in

M3_IFA12 and M3_IFA14 are similar to those obtained in CEM (12.80 - 12.97). Instead, M3_IFA16 exhibits a higher pH value (13.25), likely connected to the high Na_2O content in the activating solution [150].

Sample	pH after 28 days of curing	pH after 2 w/d cycles	pH after 14 w/d cycles
M3_IFA12	12.80 [(a)]	11.89	10.76
M3_IFA14	12.90 [(a)]	11.96	10.54
M3_IFA16	13.25 [(a)]	12.07	10.72
CEM	12.97 [(b)]	12.66	12.18

Table. 6.7 pH measurements for the investigated mortar samples. Curing in plastic bag (a); curing in a moist room at RT and R.H. > 95% (b) [150].

During the w/d cycles, all IFA mortar cylinders underwent a significant carbonation process. In particular, Table. 6.7 evidences that the pH of the pore electrolyte in the cylinder cores decreased to about 12 after 14 days (2 cycles) and dropped to a common limit of 10.5 - 10.8, after 98 days (14 cycles), in agreement to the results obtained by geopolymers in the previous Chapters (5.2.4 and 6.2.2).

In contrast, the pH always remained well over 12 in the case of CEM samples. This different behaviour is due to the formation of different reaction products after the reaction of the penetrated CO_2 with the alkaline components of the mortars: soluble sodium carbonate salts in geopolymers and insoluble calcium carbonate, capable to partially obstruct the mortar pores and to hinder effectively the CO_2 penetration, in the case of CEM [230]. The phenolphthalein test for carbonation depth assessment applied on the mortar cylinders after 14 days (2 cycles, Figure. 6.11) shows that among geopolymers the depth of carbonation decreased going from M3_IFA12 to M3_IFA14 and M3_IFA16, that is at increasing Na_2O/SiO_2 ratio in the activating solution confirming that a high Na_2O content can slightly slows down the carbonation rate.

Figure. 6.11 Carbonation depth assessment (by phenolphthalein method) on sectioned mortar cylinders exposed for 14 days (2 cycles) to the 0.1 M NaCl solution [150].

Concerning chloride content, the measurements carried out after 2, 4, 6, 8, 11 w/d cycles evidenced that total concentration was always independent of the depths in all mortar types. For this reason, Figure. 6.12 collects the average chloride contents measured inside the mortars, as a function of exposure time. In CEM, the chloride content strongly augmented with time, reaching a concentration of 0.75 wt.% (*vs* binder) after 11 w/d cycles, while in IFA samples, the average chloride content remained more or less constant during the exposure period, in the range of 0.06 - 0.18 wt.%, independently of the specific geopolymer considered. This different trend can be connected to the different chloride binding capacity of the two mortar systems. In CEM, chlorides form low solubility calcium-containing compounds (e.g., Friedel salts, FS, calcium salts), while, as already observed, in geopolymers FS are prevented by the low calcium content in IFA and the obtained sodium salts are characterized by a much higher leachability.

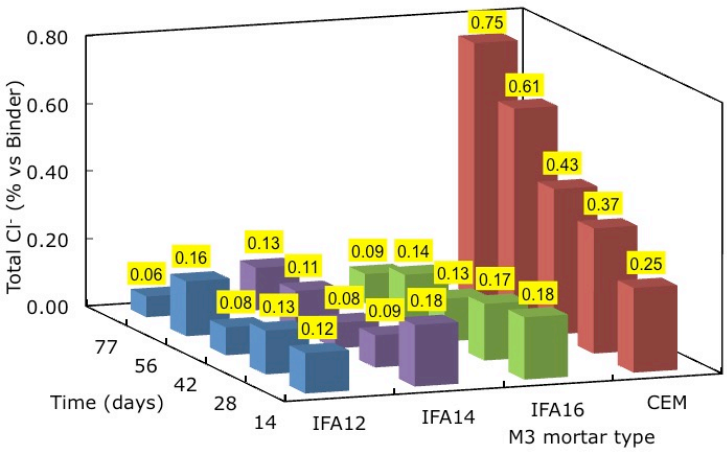

Figure. 6.12 Average total chloride contents (wt.% *vs* binder) in the investigated mortar samples after different exposure periods [150].

6.3.3 Electrochemical tests

Figure. 6.14 collects, respectively, the average corrosion potential (E_{cor}) values and polarization resistance (R_p) values obtained during tests carried out during w/d cycles in 0.1 M NaCl solution.

The time trends oscillate due to the different oxygen level in contact with the rebars during the immersion and emersion steps of each cycle. In particular, nobler E_{cor} values are recorded during the dry stage of each cycle. The E_{cor} values of the rebars embedded in the geopolymer mortars are quite similar to each other, independently of the mortar type. During the first cycle they are noble (around -0.1 - -0.2 V_{SCE}), although slightly more active than those shown by CEM. After 10 days, E_{cor} of rebars in geopolymers constantly decreases and reaches values lower than -0.276 V_{SCE} (the limit reported by ASTM C876 [219] below which the corrosion probability is greater than 90%) in about 20 days. The E_{cor} values of rebars in CEM decrease more slowly and up to the end of the exposure period they remain nobler or equal to -0.30 V_{SCE}. Concerning R_p, during the first two cycles, values for geopolymers were slightly higher compared to CEM mortar (i.e., $3 \cdot 10^{-6}$ *vs* $1 \cdot 10^{-6}$ ohm·cm^2). As w/d cycles number increased, a marked drop was exhibited after 15, 43 and 57 days by M3_IFA16, M3_IFA14 and M3_IFA12 by reaching the constant values of $9 \cdot 10^{-3}$ - $1 \cdot 10^{-4}$ ohm·cm^2 after 50, 58 and 72 days, respectively. Those results indicate a fast corrosion occurrence in geopolymers following the previously described order (in M3_IFA16 corrosion starts earlier compared to M3_IFA12). Meanwhile, R_p in CEM samples remains almost constant and a starting decrease is only detected after 90 days of exposure.

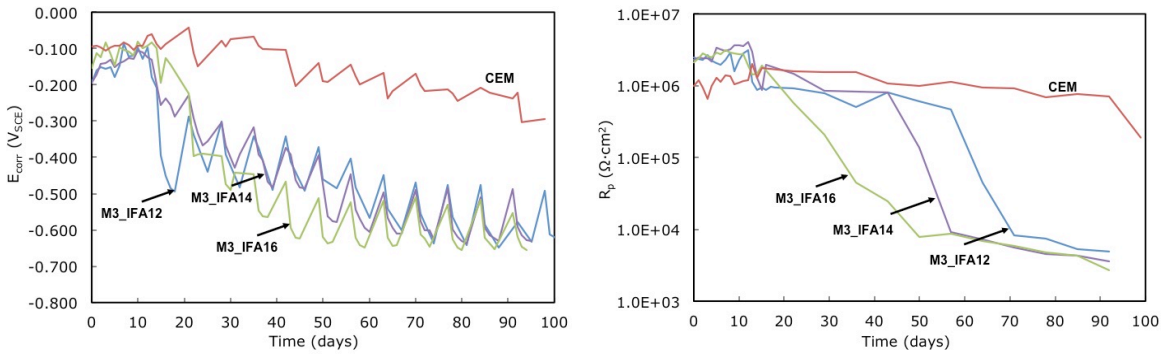

Figure. 6.13 Average E_{cor} (a) and R_p (b) values recorded in the different mortar types during w/d cycles [52].

6.3.3.1 Potentiostatic R_p measurements

Going further in understanding the obtained results, Figure. 6.14 collects representative time trends of E_{cor} and R_p values obtained in M3_IFA12 (a), M3_IFA14 (b), M3_IFA16 (c) and CEM (d) mortars, during w/d cycles, highlighting the time at which rebar depassivation was achieved. In fact, initially, the rebar E_{cor} values were quite noble. They oscillated in the range -0.15 / -0.06 V_{SCE} for M3_IFA16 and CEM, while showed an increasing trend from about -0.17 to -0.10 V_{SCE}, in the case of M3_IFA12 and M3_IFA14. During this first period, R_p values of about 1 MΩ cm^2 or higher were recorded, with the highest values recorded in IFA mortars. After 12 - 18 days the E_{cor} values in geopolymers started to decrease and reached values of -0.60 V_{SCE} or more active, while R_p values diminished progressively down to 1 kΩ cm^2, indicating the onset and propagation of a corrosion attack. In CEM, the E_{cor} values of rebars started to decrease after longer exposure periods (longer than 40 days) and a concomitant sharp R_p drop was recorded, but afterwards the rebars again underwent repassivation/depassivation events, as the concurrent E_{cor}/R_p oscillations denote (Figure. 6.14d) [150].

Corrosion in CEM is connected to the penetration of chlorides (Figure. 6.12) that, after exposures of 42 days or more, arrive at concentration values of 0.43% (*vs* binder) and at the end of the exposure period reach concentrations of 0.75% (*vs* binder). These chloride levels are comparable or higher than those reputed critical for the onset of corrosion in traditional non-carbonated mortars [127]. In geopolymers, in spite of the smaller penetrated chloride amounts, rebar depassivation was detected at shorter times, due to carbonation inside these mortars. Therefore, corrosion in geopolymers starts in correspondence of smaller critical chloride contents.

Figure. 6.15 shows the relationship between R_p and E_{cor} for the different mortars, independently of exposure time. As expected from Figure. 6.14, higher R_p mainly correspond to nobler E_{cor} values in all mortars and time evolution, as indicated in the Figure, confirms progression towards rebar corrosion, in the timeframe of the tests here described. However, in geopolymers passive conditions (that is conditions with noble E_{cor} values) correspond to higher R_p, in comparison to CEM, which can be connected to the relevant amounts of silicates present in the pore electrolyte of geopolymers, which can slightly inhibit the corrosion process and reinforce passivity, as already found in the previous Chapters [52]. As a result, the linear trends fitting log R_p/E_{cor} values in

M3_IFA12 and M3_IFA14 have higher slopes than that of CEM. In the case of M3_IFA16, the rebar behaviour is the same detected in M3_IFA12 and M3_IFA14 at the beginning of the test (that is under passive conditions), but as depassivation proceeds R_p values higher than those measured in the other geopolymers were detected. Again, the rebar corrosion behaviour in M3_IFA16 becomes similar to those in the other geopolymers under severe corrosion conditions, reached towards the end of the test, when very low R_p and active E_{cor} values are detected. The relatively high R_p values detected in this geopolymer, during an intermediate period during depassivation, are likely connected to its high Na_2O content, which slows down the penetration of carbonation and, for a while, favours slightly lower corrosion rates [150].

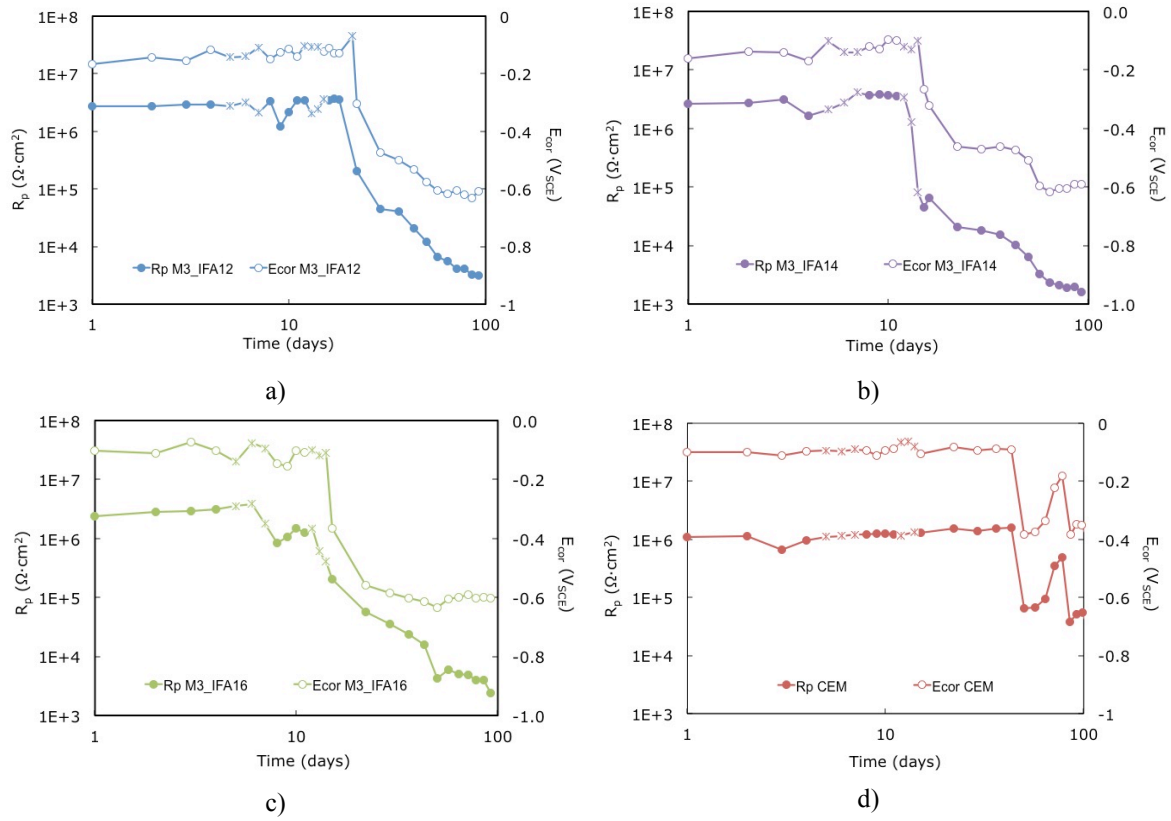

Figure. 6.14 Representative time trends of the corrosion potential and polarization resistance values obtained in M3_IFA12 (a), M3_IFA14 (b), M3_IFA16 (c) and CEM (d) mortars, during w/d cycles in 0.1 M NaCl solution. Most data were obtained during the wet step of the cycles. Those collected in the dry step are indicated by the symbol * [150].

Figure. 6.15 describes the R_p/E_{cor} dependence while depassivation proceeds, but it does not give any information about the speed of depassivation. In order to compare the depassivation rate in the different mortar types on a statistical basis, Figure. 6.16 shows the time evolution of the fraction of rebars with corrosion probability greater than 90%,

that is the fraction of rebars characterized by E_{cor} values more active than -0.276 V_{SCE} [219]. The figure clearly evidences that CEM offers the highest corrosion protection to the reinforcements, as an exposure period longer than 95 days is necessary to induce corrosion attack on more than 50% of the rebars. In the case of geopolymer mortars this occurs after about 20 days. In M3_IFA12 and M3_IFA14, corrosion propagates in all rebars after about 60 days, while in the most porous M3_IFA16 (in spite of the slower carbonation process) this occurs after only 25 days. This suggests that the high M3_IFA16 porosity (Figure. 6.10) favours oxygen diffusion and reduces the positive effects of a slower carbonation rate. The higher diffusion rate in M3_IFA16 was also confirmed by chloride diffusion tests (see Table. 6.6).

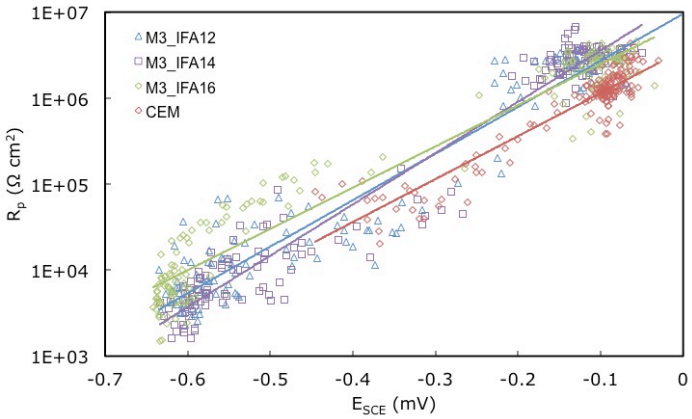

Figure. 6.15 Relations between R_p and E_{cor} measured during w/d exposures in the different mortars [150].

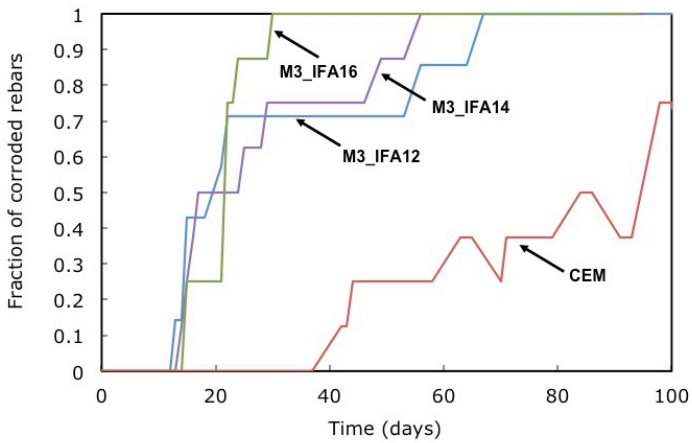

Figure. 6.16 Time dependence of the rebar fractions affected by corrosion in the different mortars during w/d cycles in 0.1 M NaCl solution [150].

6.3.3.2 Electrochemical Impedance Spectroscopy

The EIS spectra collected in M3_IFA12 and M3_IFA16 geopolymers at different exposure times are shown in Figure. 6.17a-b, in the form of Nyquist plots. Those obtained in M3_IFA14 are quite similar.

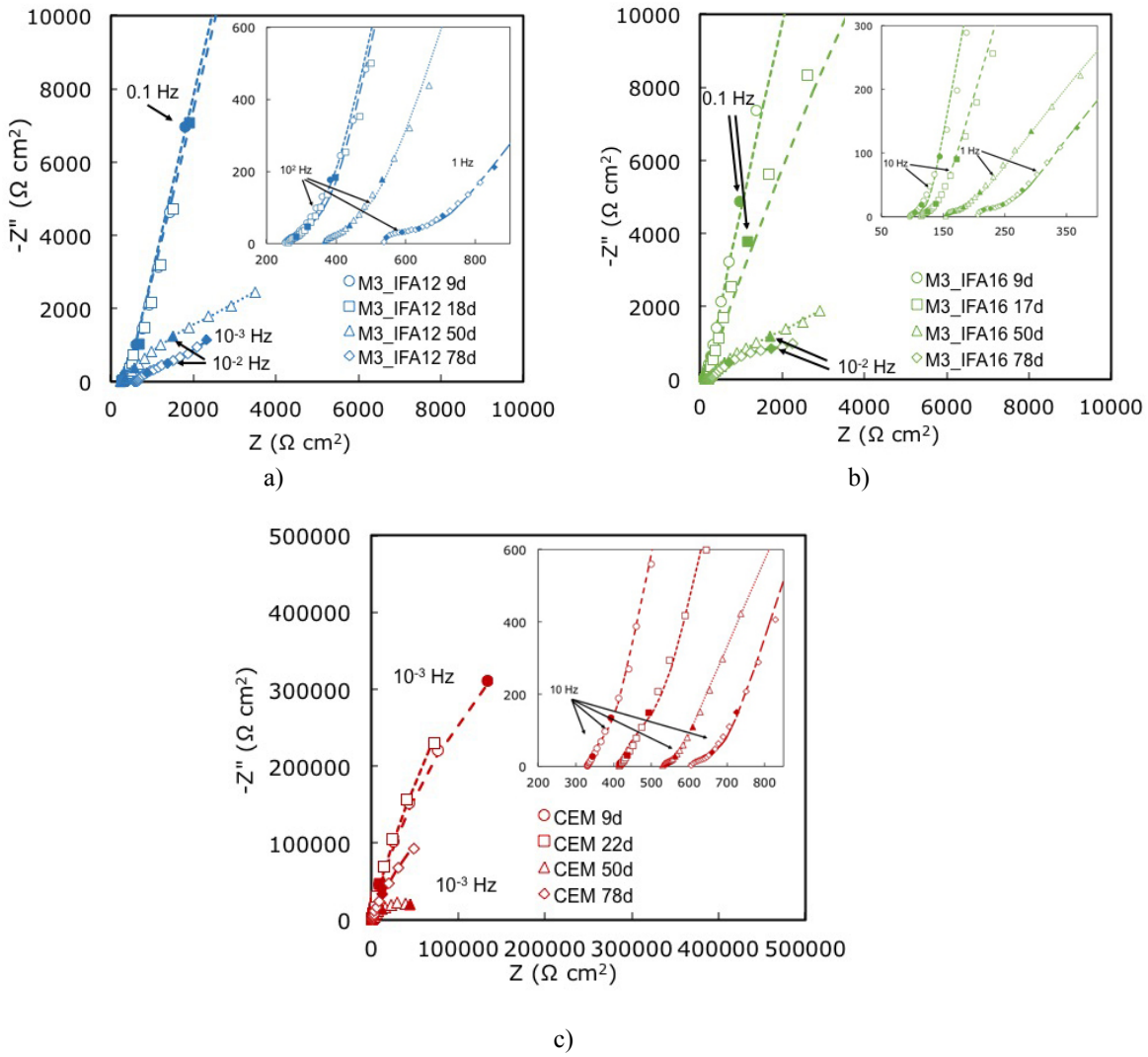

Figure. 6.17 Experimental (symbols) and simulated (lines) EIS spectra recorded in M3_IFA12 (a), M3_IFA16 (b) and CEM (c) mortars at different exposure times. Solid symbols refer to the first frequency in each decade [150].

Before the onset of corrosion, identified by R_p and E_{cor} drops (Figure. 6.14), the spectra comprised two capacitive arcs. The first one, at frequencies higher than 10^2 Hz,

was very small and often ill-resolved, particularly at short immersion times (boxes in Figure. 6.17a-b). Different interpretations were given to it (film of corrosion products [231] redox transformations on the corrosion product surface [232], presence of a cementitious film on the rebar surface, with specific characteristics different from that of bulk mortars [233,234]). As its presence was observed since the beginning of the exposures, when the rebars are still passive, the last interpretation connecting it to dielectric properties of an interfacial geopolymeric region appears correct. The second capacitive arc at frequencies lower than 10^2 Hz was connected to charge transfer reactions on the rebar surface [150].

These spectra were reasonably well fitted by the equivalent circuit (*EC*) in Figure. 6.18a [139,150,235-237], and the obtained fitting curves are superimposed on the experimental spectra of Figure. 6.17.

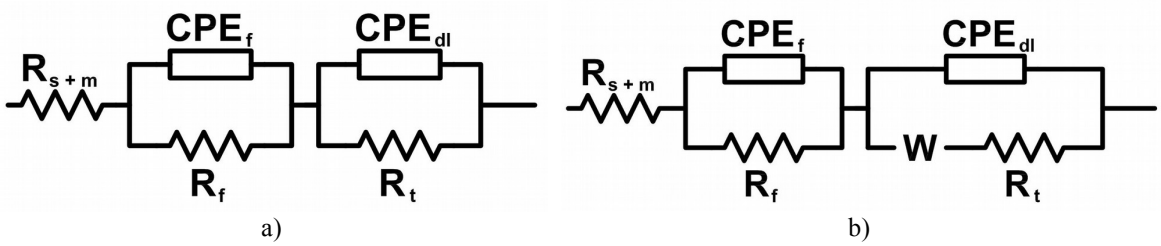

Figure. 6.18 Equivalent circuits used to fit EIS spectra: under passive conditions or limited corrosion attack (a); under active corrosion conditions (b) [150].

The first element in the *EC* is the resistance R_{s+m}, which corresponds to the sum of the pore electrolyte and mortar resistance between the pseudo-reference Ti electrode and the steel surface. Then, the *EC* shows two parallel combinations of a resistance (*R*) and a constant phase element (*CPE*), in series to each other. The first combination (R_f- CPE_f arm) fits the high frequency (*hf)* shoulder connected to the presence of the interface mortar film [236], while the low frequency (*lf*) combination (R_t- CPE_{dl}) is linked to the charge transfer resistance and double layer capacitance and gives information on the corrosion process [150]. In EC, the substitution of capacitances with Constant Phase Elements (*CPE*) aims at complying with inhomogeneities and discontinuities at interfaces. *CPE* is a distributed element with impedance expression shown in following

equation:

$$Z_{CPE} = [Y(j\omega)^n]^{-1}$$

where $0 \leq n \leq 1$ (for $n = 0$, *CPE* stands for a resistance, while for $n = 1$ it is a pure capacitance).

In the presence of a severe corrosion attack (active E_{cor} and low potentiostatic R_p values), impedance spectra were characterized by three capacitive arcs (Figure. 6.17a-b). Beside the *hf* one, related to the interfacial mortar film, two other arcs were present, connected to charge transfer (the medium frequency (*mf*) arc) and mass transfer (*lf* arc) processes. These spectra were correctly fitted by the *EC* of Figure. 6.18b [139,150,235,237,238] where in the R_t - CPE_{dl} arm a Finite-Length Warburg element was introduced to take into account the influence of diffusion on corrosion. Its impedance expression is expressed in the following equation:

$$W = R_w \cdot \frac{tanh\left[j\omega\left(\frac{\delta^2}{D}\right)\right]^P}{\left[j\omega\left(\frac{\delta^2}{D}\right)\right]^P}$$

where δ is the effective diffusion path length, D the effective diffusion coefficient and $0 \leq P \leq 1$ [237,239].

The fitting parameters related to all geopolymer spectra are reported in Table. 6.8 - Table. 6.10. R_{s+m} values are always very small, in the range 70 - 520 Ω cm^2, given the position of the reference electrode in close proximity of the steel electrode, and tend to increase with time, likely due to the going on of the mortar curing. The lowest values are recorded in M3_IFA16, characterized by the highest content of very conductive sodium hydroxide in the activating solution and by the most porous microstructure (Figure. 6.10). The geopolymeric interfacial film shows R_f values, which tend to increase with time. As the chloride content in the mortars is more or less constant with time, this could be due to the time evolution of the mortar compactness and, for times longer than 20 days, could be also connected to the pore obstruction with corrosion products in the proximity of the rebars. Also the interfacial film tends to become less resistive, passing from M3_IFA12 to M3_IFA16. Its pseudo-capacitance, Y_f, has values of 200 - 800 $\mu\Omega^{-1}cm^{-2}\ s^{nf}$, which are compatible with those found in the literature [232,238]. The decrease of Y_f found in the

less protective geopolymer mortars (M3_IFA14 and M3_IFA16) towards the end of the exposure period could be connected to the accumulation of corrosion products, which cause an increase in the interlayer thickness. The n_f exponent is always much smaller than unity, due to non-ideal capacitive behaviour of the film [150].

In geopolymer mortars, R_t values are higher (and often much higher) than 1 MΩ cm^2 for short exposure periods, meaning that charge transfer through the surface passive films controls the corrosion rates. As E_{cor} values become more active and reach values of -0.3 / -0.6 V_{SCE}, R_t values decrease concurrently, down to some kΩ cm^2 and double layer pseudo capacitances significantly increase up to a few mΩ^{-1}cm^{-2} s^{ndl}. These variations are connected, respectively, to the decrease of surface oxide film protectiveness and to the increase in real surface area of corroded rebars [150]. Under severe corrosion conditions, the Warburg parameter R_W, representing the resistance to diffusion processes, has always the same magnitude order of R_t, suggesting that corrosion rate is under a mixed charge transfer/diffusion control. M3_IFA16 presents slightly lower R_W and (δ^2/D) values, likely due to the lower resistance to diffusion and higher diffusion coefficient in the most porous M3_IFA16 microstructure.

Time (days)	2	9	18	50	78
E_{cor} (V_{SCE})	-0.128	-0.141	-0.13	-0.575	-0.621
R_{s+c} (Ω cm^2)	165	250	250	360	520
R_f (Ω cm$^{2)}$	64	150	150	220	220
Y_f (μΩ^{-1}cm^{-2} s^{nf})	300	370	320	540	360
n_f	0.6	0.53	0.5	0.42	0.40
R_t (kΩ cm^2)	6000	16000	20000	5.26	1.86
R_W (kΩ cm^2)	/	/	/	5.97	2.64
δ^2/D (s)	/	/	/	500	650
P	/	/	/	0.5	0.5
Y_{dl} (μΩ^{-1}cm^{-2} s^{ndl})	200	200	196	3740	3919
n_{dl}	0.87	0.87	0.87	0.65	0.6

Table. 6.8 Fitting parameters of EIS spectra and related E_{cor} values, obtained in M3_IFA12 mortar [150].

Time (days)	2	9	18	50	78
E_{cor} (V_{SCE})	-0.137	-0.128	-0.322	-0.596	-0.606
R_{s+m} (Ω cm^2)	124	140	143	227	423
R_f (Ω $cm^{2)}$	40	70	53	40	100
Y_f ($\mu\Omega^{-1}cm^{-2}$ s^{nf})	800	800	800	700	226
n_f	0.53	0.5	0.5	0.5	0.5
R_t ($k\Omega$ cm^2)	5300	10000	40.5	3.8	1.36
R_W ($k\Omega$ cm^2)	/	/	/	4.42	2.00
δ^2/D (s)	/	/	/	968	673
P	/	/	/	0.5	0.5
Y_{dl} ($\mu\Omega^{-1}cm^{-2}$ s^{ndl})	230	221	316	1800	2240
n_{dl}	0.88	0.87	0.8	0.6	0.57

Table. 6.9 Fitting parameters of EIS spectra and related E_{cor} values, obtained in M3_IFA14 mortar [150].

Time (days)	2	9	17	50	78
E_{cor} (V_{SCE})	-0.134	-0.156	-0.364	-0.634	-0.601
R_{s+m} (Ω cm^2)	71	96	114	154	205
R_f (Ω $cm^{2)}$	15	34	35	51	69
Y_f ($\mu\Omega^{-1}cm^{-2}$ s^{nf})	600	600	821	878	463
n_f	0.6	0.5	0.5	0.5	0.5
R_t ($k\Omega$ cm^2)	4500	1150	220	3.50	2.50
R_W ($k\Omega$ cm^2)	/	/	/	4.5	1.51
δ^2/D (s)	/	/	/	270	193
P	/	/	/	0.5	0.5
Y_{dl} ($\mu\Omega^{-1}cm^{-2}$ s^{ndl})	266	297	370	1960	1800
n_{dl}	0.89	0.885	0.82	0.63	0.65

Table. 6.10 Fitting parameters of EIS spectra and related E_{cor} values, obtained in M3_IFA16 mortar [150].

The EIS spectra obtained in CEM mortar are collected in Figure. 6.17c. They are quite similar to those collected in geopolymer mortars before the development of severe corrosion, suggesting that diffusion phenomena do not influence the corrosion rates. Therefore, fitting of the spectra was done by the *EC* of Figure. 6.18a. The obtained *EC* parameters and the corresponding E_{cor} values are collected in Table. 6.11. The R_{s+m} are slightly higher than those measured in the most compact geopolymer (M3_IFA12), in agreement with the even denser CEM microstructure. Also in CEM, a continuous increase with time of R_{s+m} and R_f values is recorded, in spite of chloride penetration, due to the

ongoing curing process in both bulk and interfacial mortar regions. However, final R_f are smaller than those in M3_IFA12, because of a more limited formation of corrosion products, during the exposure period [150]. The more long lasting protectiveness of CEM, due to a much slower mortar carbonation, reflects in the persistence of relatively high R_t values till the end of the test and in the capability of repassivation, after onset of a corrosion attack. In fact, after 50 days R_t decreases to 60 kΩ cm^2 (and E_{cor} diminishes to -0.38 V_{SCE}) and then, after 78 days, it increases again up to 600 kΩ cm^2 (and E_{cor} ennobles up to -0.18 V_{SCE}). The permanence of a limited corrosion attack is also evidenced by the constancy of the pseudo-capacitance, Y_{dl}, which remains in the range 230 - 380 $\mu\Omega^{-1}cm^{-2}$ s^{ndl}, till the end of the exposure [150].

Time (days)	2	9	17	50	78
E_{cor} (V_{SCE})	-0.098	-0.11	-0.082	-0.382	-0.181
R_{s+m} (Ω cm^2)	238	328	416	525	600
R_f (Ω cm$^{2)}$	57	57	60	80	100
Y_f ($\mu\Omega^{-1}cm^{-2}$ s^{nf})	200	200	200	200	200
n_f	0.9	0.9	0.85	0.64	0.56
R_t (kΩ cm^2)	1200	1500	2500	60	600
Y_{dl} ($\mu\Omega^{-1}cm^{-2}$ s^{ndl})	258	243	235	381	262
n_{dl}	0.89	0.88	0.87	0.76	0.81

Table. 6.11 Fitting parameters of EIS spectra and related E_{cor} values, obtained in CEM mortar [150].

In conclusion, EIS analysis allows observing more in detail the results obtained by R_p measurements. R_{s+m} values increased with the mortar compactness and the highest values were obtained by CEM. The *hf* loop describing the dielectric properties of the interfacial mortar region in contact with the rebars showed R_f values depending on both the mortar porosity and the abundance of corrosion products inside the mortar pores. Therefore, the densest CEM mortar reached intermediate R_f values, because of the limited accumulation of corrosion products in the mortar region close to the rebar surface.

At frequencies lower than 10^2 - 10 Hz, the spectra described the corrosion processes affecting the embedded rebars. In the presence of rebar passive conditions or limited corrosion attack, the spectra exhibited a single arc with dimensions increasing at increasing protectiveness of the passive (or pseudopassive) film. In CEM, the spectra indicated the presence of a limited corrosion attack until the end of the exposure, because

of the persistence of a single *lf* arc, with relatively high R_t values. In geopolymer mortars, severe corrosion attack developed with time, and the corrosion process is described by two capacitive arcs and the appearance of a second *lf* arc, due to a mixed charge transfer/diffusion control on the corrosion rate [150].

6.3.3.3 Polarization curves

Figure. 6.19 shows the ohmic drop-compensated polarization curves recorded on reinforcing bars in geopolymer mortars (Figure. 6.19a) and CEM (Figure. 6.19b). They clearly evidence that at increasing exposure periods, variations in surface film stability (connected to the pore solutions modifications described in previous sections) modify the rebar electrochemical behaviour. In particular, the curves show that, after 8 days of exposure, stable passive films are present in both mortar types, inducing noble E_{cor} (around -0.1 V_{SCE}) and low i_{cor} values (varying within 0.06 - 0.1 μA/cm^2). Passivity persists up to potentials of about +0.6 V_{SCE} where an abrupt current increase was observed, due to oxygen evolution [223]. Instead, after 43 days, the polarization curves recorded in geopolymer mortars (Figure. 6.19a) exhibited much more active E_{cor} (in the range -0.5 / -0.6 V_{SCE}) and higher i_{cor} values (about 3 - 4 μA/cm^2). Under these conditions, high pseudo-passive currents (higher than 10^{-5} A/cm^2) were recorded, slowly increasing from E_{cor} up to the potential of oxygen evolution, without discontinuity. This curve suggests that a non-protective surface film forms on the rebars and permits significant corrosion at E_{cor} [150].

The conditions detected in CEM after the same exposure time (43 days) are quite different. In fact, the curves show E_{cor} and i_{cor} values close to those measured after 8 days (Figure. 6.19b), suggesting the permanence of passive conditions at E_{cor}. However, an abrupt current increase was recorded at about +0.135 V_{SCE}, due to pitting attack [51]. This means that the surface film has a smaller resistance towards the anodic polarization, owing to chloride accumulation (Figure. 6.12) [150]. After 100 days of exposure, a stronger corrosion attack affected the rebars already at E_{cor}, as higher i_{cor} (2 μA/cm^2) and rebars were under pseudo-passive conditions. Anyway, these currents remained smaller than those obtained in geopolymers after shorter times.

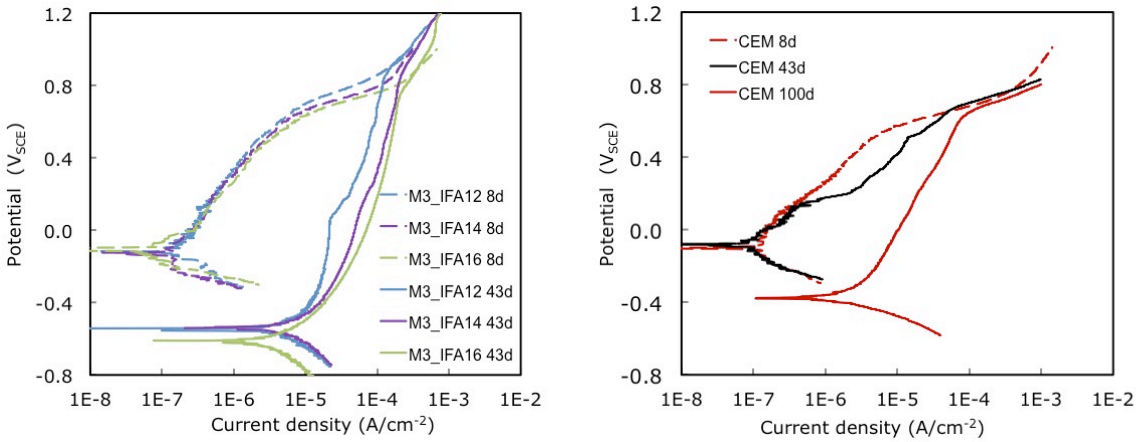

Figure. 6.19 Polarization curves recorded in the different mortars during the wet step of w/d cycles in 0.1 M NaCl solution [150].

6.3.3.4 Corrosion product analysis

At the end of the w/d cycles, rebars not used for polarization curve recording were used to visually evaluate the extent of the corrosion attack after mortar breakage. In agreement with the suggestions of electrochemical tests, widespread corrosion attacks and more abundant corrosion products were found in IFA mortars in comparison to CEM, as shown in Figure. 6.20.

Table. 6.12 reports the Raman results for corrosion products formed on the steel surface at the end of the w/d cycles. By analyzing the oxides composition, a range of diverse amorphous and crystalline structures was found, but abundance of akaganeite (β-FeO(OH,Cl)) was detected only in geopolymer mortars with the characteristic *cotton balls* and *rosette* shapes [240]. The presence of agakaneite confirms the chloride incorporation in the oxide structure, with the formation of a very scarcely protective surface film [222]. In CEM, the most abundant crystalline compound was lepidocrocite (γ-FeO(OH)), while maghemite (γ-Fe_2O_3) and goethite (α-FeO(OH) were found in traces. Those results are in agreement with the severe corrosion attack detected in geopolymer mortars by the electrochemical tests and in agreement with the previous obtained results during partial immersion conditions [52].

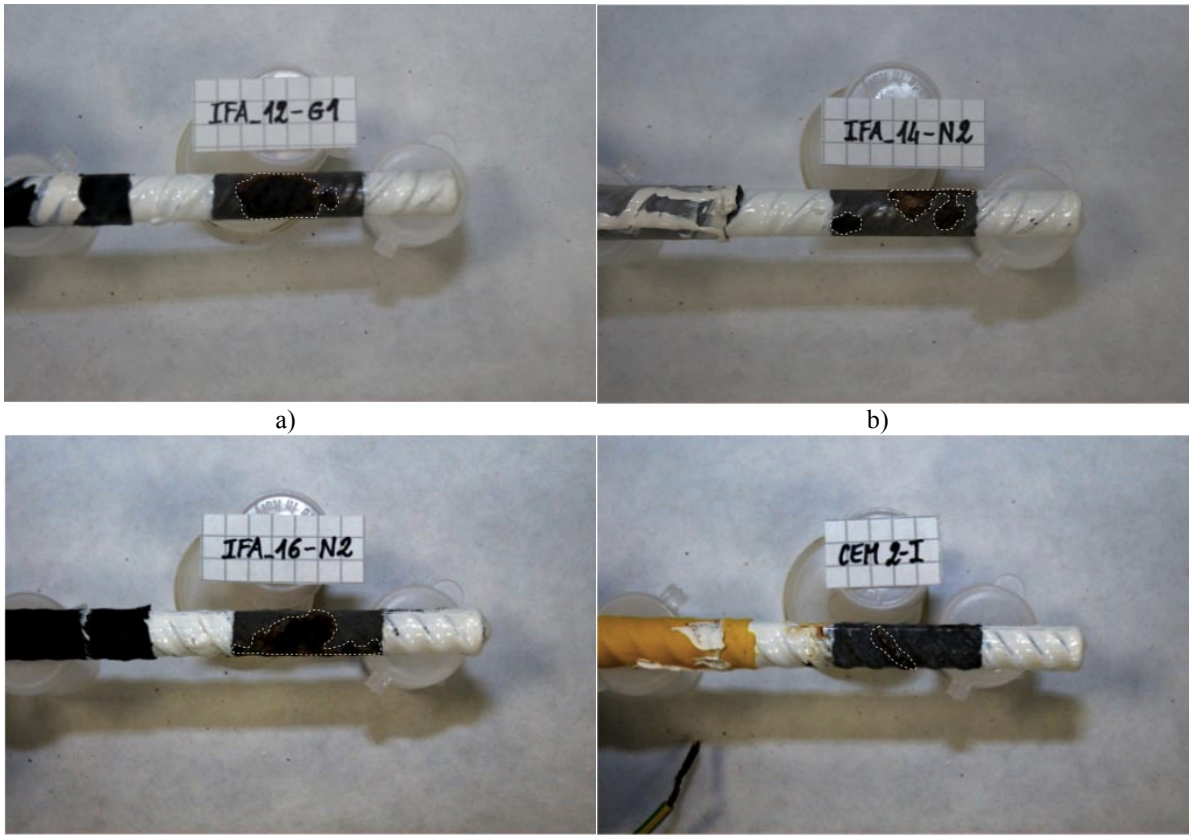

a) b)

c) d)

Figure. 6.20 Extent of corrosion attack on steel bars extracted from samples at the end of electrochemical tests: M3_IFA12 (a); M3_IFA14 (b); M3_IFA16 (c); CEM (d).

Sample	Lepidocrocite	Maghemite	Akaganeite	Goethite	δ-FeOOH
M3_IFA12	+/-		++		+/-
M3_IFA14		+/- (amorphous)	+ (amorphous)	+/- (amorphous)	
M3_IFA16		+ (amorphous)	++		
CEM	+	+/-		+/-	

Table. 6.12 Raman quantitative analysis for corrosion products formed on rebars in reinforced cylinders at the end of the w/d cycles (+/- = traces; + = small amounts detected; ++ = high amounts detected) [150].

6.3.4 Main remarks

In this section, the corrosion behaviour of rebars embedded in RT cured geopolymer mortars based on IFA was assessed during w/d exposure to 0.1 M NaCl solution and compared to that shown by rebars in a traditional cement-based mortar under the same aggressive conditions. The differences detected were interpreted in the light of chemical, physical and microstructural differences between the two systems. In particular, it was found that:

- the main difference in terms of physical-mechanical properties between CEM and

geopolymer mortars is due to a different microstructure leading to a much higher porosity and, consequently, transport properties for the latter system;

- under w/d exposure conditions, all geopolymers suffered a quick mortar carbonation reaching a common pH value of the pore solution around 10.5 - 10.8, which induced a fast rebar depassivation, in spite of the low chloride concentration accumulated around the rebars while CEM have been observed to offer a more protective environment. In the latter system, rebars depassivation occurred at the end of the test when a critical chloride content for corrosion onset in non-carbonated traditional mortars was achieved. All those information were supported by electrochemical tests.

The collected results suggested that, especially in w/d conditions, the microstructure of geopolymers plays a crucial role in enhancing the corrosion process of reinforcement caused by a fast carbonation and consequent rebar depassivation, in spite of a limited chloride accumulation inside these mortars. CEM mortar was much less susceptible to carbonation and rebar corrosion started when a sufficiently high chloride concentration was built up [150].

7 CONCLUSIONS

In this research the potential of fly ash based geopolymers activated at room temperature as innovative sustainable binders has been demostrated in many field of the civil sector, in view of a reduction of costs, environmental impact and carbon footprint produced by traditional building materials.

Different types of fly ash as geopolymer precursors have been tested and their efficience in developing a performant product has been assessed through several characterization techniques. The Na_2O/SiO_2 molar ratio in the activating solution (ranging form 0.12 to 0.20) has been chosen as the main parameter governing the geopolymerization process and different formulation have been tested with the aim to optimize the performances. Some extra experiments have been performed on different curing regimes. Geopolymers have been testes both as paste and mortar samples and a cement-based mortar was used as reference sample. Special attention was focused on durability issues such as high temperature and corrosion resistance of the embedded rebars in aggressive environments (carbonation and chlorides).

Experimental results show that this new FA-based system can be successfully used as a valid alternative to cement-based matrix compounds for non-structural applications, exhibiting a similar behaviour in terms of physical and mechanical properities.

Regarding thermal properties, geopolymers have been found to be very promising for high temperature applications and, when mild-cured in oven for the first 24 hours, the

obtained properties are similar to traditional semi-refractory/refractory ceramics.

Besides that, regarding reinforced systems, FA-based samples were found to undergo a fast carbonation, so that depassivation of the rebars occurred concurrently, resulting in a fast rebar corrosion compared to cement-based systems. This result has been interpreted in the light of a different microstructure between the two systems, which is responsible in different transport properties of external aggressive agents.

The potential of this novel system is so clear, but further steps are needed in order to develop tailor-made geopolymer products and an optimization of the obtained results is desirable primarly for reinforced systems applications, with future work to include analysis of the evolution of FA atomic structure during geopolymerization and, consequently, the control of the microstructure. The challenge of this thesis and of the research efforts worldwide is therefore to create a knowledge base that can be accessed in order to produce, in the next years, market-ready geopolymer products derived from waste materials for specific industrial applications, and on a cost-competitive basis.

8 REFERENCES

[1] Provis JL, van Deventer JSV, Alkali-activated materials: State-of-the-art report, RILEM TC 224-AAM, Dorderecht: Springer/RILEM, 2014.

[2] Singh B, Ishwarya G, Gupta M, Bhattacharyya SK, Geopolymer concrete: A review of some recent developments, Constr Build Mater 85 (2015) 78-90.

[3] van Deventer JSJ, Provis JL, Duxson P, Brice DG, Chemical research and climate change as drivers in the commercial adoption of alkali-activated materials, Waste Biomass Valor 1 (2010) 145-55.

[4] Davidovits J, Geopolymer: inorganic polymeric new materials, J Therm An 37 (1991) 1633-1656.

[5] Shi C, Krivenko PV, Roy D, Alkali-activated materials, Taylor and Francis, 2006.

[6] Davidovits J, 30 Years of successes and failures in geopolymer applications, market trends and potential breakthrough, Melbourne, Australia, 28-29/10/2002.

[7] Shi C, Fernández Jiménez A, Palomo A, New cements for the 21st century: The pursuit of an alternative to Portland cement, Cem Concr Res 41 (2011) 750-763.

[8] Roy DM, Alkali-activated cements Opportunities and challenges, Cem Concr Res 29 (1999) 249-254.

[9] Pacheco-Torgal F, Castro-Gomes J, Jalali S, Alkali-activated Binders: A review.

Part 1. Historical background, terminology, reaction mechanism and hydration products, Constr Build Mater 22 (2008) 1305-1314.

[10] Leonelli C, Romagnoli M, Geopolimeri: Polimeri inorganici chimicamente attivati, I.Cer.S., 2011.

[11] Al-Otabi S, Investigating some durability related properties of alkali-activated slag concrete, Kuwait Institute for Scientific Research, Kuwait, Proceedings of the 28th Conference on Our World in Concrete Structures, 25-26 August, 2004, Singapore.

[12] van Deventer JSJ, Provis JL, Duxson P, Technical and commercial progress in the adoption of geopolymer cement, Miner Eng 29 (2012) 89-104.

[13] Palomo A, Grutzeck MW, Blanc MT, Alkali-activated fly ashes: A cement for the future, Cem Concr Res 29 (1999) 1323-1329.

[14] Ryu GS, Lee YB, Koh KT, Chung YS, The mechanical properties of fly-ash based geopolymer concrete with alkaline activators, Constr Build Mater 47 (2013) 409-418.

[15] http://www.zeobond.com/products-e-crete.html, 12/18/2015.

[16] Davidovits J, Paper presented at IUPAC Symposium on Long-term properties of polymers and polymeric materials, Stockholm, 1976, Topic III; Applied Polymer Symposia.

[17] Komnitsas K, Zaharaki D, Geopolymerisation: A review and prospects for the minerals industry, Miner Eng 20 (2007) 1261-1277.

[18] Duxson P, Fernandez-Jimenez A, Provis JL, Lukey GC, Palomo A, van Deventer JSJ, Geopolymer technology: the current state of the art, J Mater Sci 42 (2007) 2917-2933.

[19] Provis JL, van Deventer JSJ, Geopolymerisation kinetics. 2. Reaction kinetic modeling, Chem Eng Sci 62 (2007) 2318-2329.

[20] White CE, Atomic structure evolution in amorphous geopolymer precursors and gel, Ph.D Thesis, Department of Chemical and Biomolecular Engineering, The University

of Melbourne, Australia, 2010.

[21] Pacheco-Torgal F, Castro-Gomes J, Jalali S, Alkali-activated binders: A Review. Part 2. About materials and binders manufacture, Constr Build Mater 22 (2008) 1315-1322.

[22] Fernández-Jiménez A, Palomo A, Characterization of fly ashes. Potential reactivity as alkaline cements, Fuel 82 (2003) 2259-2265.

[23] Chancey RT, Stutzman P, Juenger MCG, Fowler DW, Comprehensive phase characterization of crystalline and amorphous phases of Class F fly ash, Cem Conr Res 40 (2010) 146-56.

[24] Aughenbaugh KL, Stutzman P, Juenger MCG, Assesment of the glassy phase reactivity in fly ash used for geopolymer cement, ASTM Special Technical Publication 1566 (2013) 11-20.

[25] Keyte L, What's wrong with Tarong? The importance of coal fly ash glass chemistry in inorganic polymer synthesis, Ph.D. Thesis, Department of Chemical & Biomolecular Engineering, University of Melbourne, Australia, 2008.

[26] Oh JE, Jun Y, Jeong Y, Characterization of geopolymers from compositionally and physically different Class F fly ashes, Cem Concr Res 50 (2014) 16-26.

[27] Oh JE, Jun Y, Jeong Y, Monteiro PJM, The importance of network-modifying element content in fly ash as simple measure to predict its strength potential for alkali-activation, Cem Concr Res 57 (2015) 44-54.

[28] Nikolić V, Komljenović M, Baščarević Z, Marjanović N, Miladinović Z, Petrović R, The influence of fly ash characteristics and reaction conditions on strength and structure of geopolymers, Constr Build Mater 94 (2015) 361-70.

[29] Duxson P, Provis JL, Lukey GC, Mallicoat SW, Kriven WM, van Deventer JSJ, Understanding the relationship between geopolymer composition, microstructure and mechanical properties, Coll Surf A 269 (2005) 47-58.

[30] Rashad AM, Metakaolin as cementitious material: History, scours, production and composition - A comprehensive overview, Constr Build Mater 43 (2013) 303-318.

[31] Kakali G, Perraki T, Tsivilis S, Badogiannis E, Thermal treatment of kaolin: the effect of mineralogy on the pozzolanic activity, Appl Clay Sci 20 (2001) 73-80.

[32] Bellotto M, Gualtieri A, Artioli A, Clark SM, Kinetic study of the kaolinite-mullite reaction sequence, Phys Chem Minerals 22 (1995) 207-217.

[33] Fernandez R, Martirena F, Scrivener KL, The origin of the pozzolanic activity of clay minerals: A comparison between kaolinite, illite and montmorillonite, Cem Concr Res 41 (2011) 113-122.

[34] Siddique R**,** Khan MI, Supplementary Cementing Materials, Volume 37 of the series Engineering Materials, 2011, pp. 175-230.

[35] Snellings R, Mertens G, Elsen J, Supplementary cementitious materials, Reviews in Mineralogy and Geochemistry, 74 (2012) 211-278.

[36] Paolomo A, Glasser FP, Chemically-bonded cementitious materials based on metakaolin, British ceramic transactions and journal, 91 (1992) 107-112.

[37] http://www.sustainableaggregates.com, 7/01/2016.

[38] Fernández-Jiménez A, Puertas F, Sobrados I, Sanz J, Structure of calcium silicate hydrates formed in alkali-activated slag: Ingfluence of the type of activator, J Amer Cer Soc 86 (2003) 1389-1394.

[39] Gruskovnjak A, Lothenbach B, Holzer L, Figi R, Winnefeld F, Hydration of alkali-activated slag: comparison with Ordinary Portland Cement, Advances Cem Res 18 (2006) 119-128.

[40] Xu H, Provis JL, van Deventer JSJ, Krivenko PV, Characterization of aged slag concrete, ACI Mater J, 105 (2008) 131-139.

[41] http://www.great-wall.co, 7/01/2016.

[42] ASTM C618. Standard specification for coal fly ash and raw or calcined natural pozzolan for use in concrete. 2008.

[43] Gunasekara C, Law DW, Setunge S, Sanjayan JG, Zeta potential, gel formation

and compressive strength of low calcium fly ash geopolymers, Constr Build Mater 95 (2015) 592-599.

[44] Bignozzi MC, Manzi S, Natali ME, Richard WDA, van Riessen A, Room temperature alkali-activation of fly-ash: The effect of Na_2O/SiO_2 ratio, Constr Build Mater 69 (2014) 262-270.

[45] Fernández-Jiménez A, Palomo A, Composition and microstructure of alkali-activated fly ash binder: Effect of the activator, Cem Concr Res 35 (2005) 1984-1992.

[46] Chi M, Effects of modulus ratio and dosage of alkali-activated solution of the properties and micro-structural characteristics of alkali-activated fly ash mortars, Constr Build Mater 99 (2015) 128-136.

[47] Criado M, Palomo A, Fernández-Jiménez A, Alkali-activation of fly ashes. Part 1: effect of curing conditions on the carbonation of the reaction products, Fuel 84 (2005) 2048-1054.

[48] Winnefeld F, Leemann A, Lucuk M, Svoboda P, Neuroth M, Assesment of phase formation in alkali-activated low and high calcium fly ashes in building materials, Constr Build Mater 24 (2010) 1086-1093.

[49] Bakharev T, Thermal behaviour of geopolymers prepared using class F fly ash and elevated temperature curing, Cem Concr Res 36 (2006) 1134-1147.

[50] Pacheco-Torgal F, Abdollahnejad Z, Camões AF, Jamshidi M, Ding Y, Durability of alkali-activated binders: A clear advantage over Portland cement or an unproven issue?, Constr Build Mater 30 (2012) 400-405.

[51] Monticelli C, Criado M, Fajardo S, Bastidas JM, Abbottoni M, Balbo A, Corrosion behaviour of a low Ni austenitic stainless steel in carbonated chloride-polluted alkali-activated fly ash mortars, Cem Concr Res 55 (2014) 49-58.

[52] Monticelli C, Natali ME, Balbo A, Chiavari C, Zanotto F, Manzi S, Bignozzi MC, Corrosion behaviour of steel in alkali-activated fly ash mortars in the light of their microstructural, mechanical and chemical characterization, Cem Concr Res 80 (2016) 60-68.

[53] Blisset RS, Rowson NA, A review on the multi-component utilization of coal fly ash, Fuel 97 (2012) 1-23.

[54] Sow M, Hot J, Tribout C, Cyr M, Characterization of Spreader Stoker Coal Fly Ashes (SSCFA) for their use in cement based applications, Fuel 162 (2015) 224-233.

[55] Yao TZ, Ji XS, Sarker PK, Tang JH, Ge LQ, Xia MS, et al., A comprehensive review on the applications of coal fly ash, Earth Sci Rev 141 (2015) 105-121.

[56] http://www.ect.coop/emerging-technologies/r-d/crn-looks-at-future-of-fly-ash/57581, 7/01/2015.

[57] Bernal SA, Provis JL, Walkley B, San Nicolas R, Gehman JD, Brice DG, et al., Gel nanostructure in alkali-activated binders based on slag and fly ash, and effects of accelerated carbonation, Cem Concr Res 53 (2013) 127-144.

[58] Hemmings RT, Berry EE, Speciation in size and density fractionated fly ash. Materials Research Society Symposia Proceedings: V. 65. Fly Ash and Coal Conversion By-Products: Characterization, Utilization, and Disposal II. Boston, Massachusetts, USA, McCarthy, Glasser, Roy, 1985, pp. 91-104.

[59] Arjuan P, Silbee MR, Roy DM, Quantitative determination of the crystalline and amorphous phases in low calcium fly ashes. Proceeding of the 10th International Congress of the Chemistry of Cement, Gothenburg, Sweden, 1997, pp. 2-6.

[60] McCusker LB, Von Dreele RB, Cox DE, Louer D, Scardi P, Rietveld refinement guidelines, J Appl Cryst 32 (1998) 36-50.

[61] Pektov V, Nanostructure by high-energy X-ray diffraction, Mater Today 11 (11) (2008) 28-38.

[62] Provis JL, Hajimohammadi A, White CE, Bernal SA, Myers RJ, Winarski RP, et al., Nanostructural characterization of geopolymer by advanced beamline techniques, Cem Concr Comp 36 (2013) 56-64.

[63] Skinner LB, Chae AR, Benmore JC, Wenk HR, Monteiro PJM, Nanostructure of calcium silicate hydrates in cements, Phys Rev Let 104 (2010) 195502-195504.

[64] White CE, Daemen LL, Hartl M, Page K, Intrinsic differences in atomic ordering of calcium (alumino) silicate hydrates in conventional and alkali-activated cements, Cem Concr Res 67 (2015) 66-73.

[65] Morandeau AE, White CE, In situ X-ray pair distribution function analysis of accelerated carbonation of a syntetic calcium-silicate hydrate gel, J Mater Chem A 3 (2015) 8597-8605.

[66] Bell JL, Sarin P, Driemeyer PE, Heggerty RP, Chupas PJ, Kriven WM, X-ray pair distribution function analysis of metakaolin based, $KAlSi_2O_6{\cdot}5.5H_2O$ inorganic polymer (geopolymer), J Mater Chem 18 (2008) 5974-5981.

[67] Provis JL, Duxson P, van Deventer JSJ, Luckey GC, The role of mathematical modeling and gel chemistry in advancing geopolymer technology, Chem Eng Res Des 83 (2005) 853-860.

[68] Meral C, Benmore CJ, Monteiro PJM, The study of disorder and nanocrystallinity in C-S-H, supplementary cementituous materials and geopolymers using pair distribution function analysis, Cem Concr Res 41 (2011) 696-710.

[69] White CE, Page K, Henson NJ, Provis JL, In situ synchrotron X-ray pair distribution function analysis of the early stages of gel formation in metakaolin based geopolymers, Appl Clay Sci 73 (2013) 17-25.

[70] White CE, Provis JL, Poffen T, van Deventer JSJ, The effect of temperature on the local structure of metakaolin based geopolymer binder: a neutron pair distribution function investigation, J Amer Cer Soc 93 (2010) 3486-3492.

[71] White CE, Provis JL, Llobet A, Poffen T, van Deventer JSJ, Evolution of local structure in geopolymer gels: an in-situ neutron pair distribution function analysis, J Amer Cer Soc 94 (2011) 3532-3539.

[72] Morandeau AE, White CE, Role of magnesium-stabilized amorphous calcium carbonate in mitigating the extent of carbonation in alkali-activated slag, Chem Mater 27 (19) (2015) 6625-6634.

[73] Oh JE, Moon J, Mancio M, Clark SM, Manteiro PJM, Bulk modulus of basic

sodalite $Na_8[AlSiO_4]_6(OH)_2 \cdot 2H_2O$, a possible zeolite precursor in coal-fly-ash based geopolymers, Cem Concr Res 41 (2011)107-112.

[74] Natali ME, White CE, Bignozzi MC, Elucidating the atomic structures of different sources of fly ash using X-ray and neutron PDF analysis, Fuel 177 (2016) 148-156.

[75] Provis JL, Palomo A, Shi C, Advances in understanding alkali-activated materials, Cem Concr Res 78 (2015) 110-125.

[76] Silva de Vargas A, Dal Molin DCC, Masuero AB, Vilela ACF, Castro-Gomes J, de Gutierrez RM, Strength development of alkali-activated fly ash produced with combined NaOH and $Ca(OH)_2$ activators, Cem Concr Comp 53 (2014) 341-349.

[77] Garcia-Lodeiro I, Palomo A, Fernández-Jiménez A, Macphee DE, Compatibility studies between N-A-S-H and C-A-S-H gels. Study in the ternary diagram Na_2O-CaO-Al_2O_3-SiO_2-H_2O, Cem Concr Res 41 (2011) 923-932.

[78] Temuujin J, van Riessen A, MacKezie KJD, Preparation and characterisation of fly ash based geopolymer mortars, Con Build Mater 24 (2007) 1906-1910.

[79] Rattanasak U, Chindaprasirt P, Influence of NaOH solution on the synthetis of fly ash geopolymer, Miner Eng 22 (2009) 1073-1078.

[80] Wang H, Li H, Yan F, Synthesis and mechanical properties of metakaolinite based geopolymer, Coll Surf A: Physicochem Eng Aspects 268 (2005) 1-6.

[81] Rashad AM, Zeedan SR, Hassan AA, Influence of the activator concentration of sodium silicate on the thermal properties of alkali-activated slag pastes, Constr Build Mater 102 (2016) 811-820.

[82] Neto AA, Cincotto MA, Wellington R, Drying and autogenous shrinkage of pastes and mortars with activated slag cement, Cem Concr Res 38 (2008) 565-574.

[83] Allahverdi A, Shaverdi B, Najafi Kani E, Influence of sodium oxide on properties of fresh and hardened paste of alkali-activated blast-furnace slag, Int J Civil Eng 8 (4) (2010) 304-314.

[84] Chi M, Effects of dosage of alkali-activated solution and curing conditions on the properties and durability of alkali-activated slag concrete, Constr Build Mater 35 (2012) 240-245.

[85] Acevedo-Martinez E, Gomez-Zamorano LY, Escalante-Garcia JI, Portland cement-blast furnace slag mortars activated using waterglass: Part 1: Effect of slag replacement and alkali concentration, Constr Build Mater 37 (2012) 462-469.

[86] Yang K-H, Song J-K, Ashour AF, Lee E-T, Properties of cementless mortars activated by sodium silicate, Constr Build Mater 22 (2008) 1981-1989.

[87] Cincotto MA, Melo AA, Repette WL, Effect of different activators type and dosages and relation to autogenous shrinkage of activated blast furnace slag cement, in: Proceedings of the 11th International Congress on the Chemistry of Cement (ICCC), Cement's Contribution to the Development in the 21st Century, Hosted by: The Cement and Concrete Institute of South Africa, 11-16 May 2003, pp. 1878–1886.

[88] http://www.geopolymer.org/applications/, 7/01/2015.

[89] Izquierdo M, Querol X, Phillipart C, Antenucci D, Towler M, The role of open and closed curing conditons on the leaching properties of fly ash-slag based geopolymers, J Hazard Mater 176 (2010) 623-628.

[90] Wallah SE, Rangan BV, Low-calcium fly ash based geopolymer concrete, Research report GC2 Faculty of Engineering, Curtin University of Technology, Perth, Australia (2006).

[91] Atiş CD, Görür EB, Karahan O, Bilim C, Ilkentapar S, E. Luga, Very high strength (120 MPa) class F geopolymer mortar activated at different NaOH amount, heat curing temperature and heat curing duration, Constr Build Mater 96 (2015) 673-678.

[92] Adam AA, Horianto, The effect of temperature and duration of curing on the strength of fly ash based geopolymer mortar, Proc Eng 95 (2014) 410-414.

[93] Silva de Vargas A, Dal Molin DCC, Vilela ACF, da Silva FJ, Pavão B, Veit H, The effects of Na_2O/SiO_2 molar ratio, curing temperature and age on compressive strength, morphology and microstructure of alkali-activated fly ash based geopolymers,

Cem Concr Comp 33 (6) (2011) 653-660.

[94] Tchakoute HK, Elimbi A, Yanne E, Djangang CN, Utilization of volcanic ashes for the production of geopolymers cured at ambient temperature, Cem Concr Comp 38 (2013) 75-81.

[95] Zhang Z, Provis JL, Wang H, Bullen F, Reid A, Quantitative kinetic and structural analysis of geopolymers. Part 2. Thermodynamics of sodium silicate activation of metakaolin, Thermochim Acta 565 (2013) 163-171.

[96] Lee WKW, van Deventer JSJ, Structural reorganisation of class F fly ash in alkaline silicate solutions, Coll Surf A 211 (2002) 49-66.

[97] Lee NK, Lee HK, Setting and mechanical properties of alkali-activated fly ash/slag concrete manufactured at room temperature, Constr Build Mater 47 (2013) 1201-1209.

[98] Ismail I, Bernal SA, Provis JL, San Nicolas R, Brice DG, Kilcullen AR, et al., Influence of fly ash on the water and chloride permeability of alkali-activated slag mortars and concrete, Constr Build Mater 48 (2013) 1187-1201.

[99] Duxson P, Provis JL, Lukey GC, van Deventer JSJ, The role of inorganic polymer technology in the development of 'green concrete', Cem Concr Res 37 (2007) 1590-1597.

[100] Lloyd RR, Provis JL, van Deventer JSJ, Acid resistance of inorganic polymer binders. 1. Corrosion rate, Mater Struct 45 (2012) 1-14.

[101] Shi C, Stegemann JA, Acid corrosion resistance of different cementing materials, Cem Concr Res 30 (2000) 803-808.

[102] Fernández-Jiménez A, García-Lodeiro I, Palomo A, Durability of alkali-activated fly ash cementitious materials, J Mater Sci 42 (2007) 3055-3065.

[103] Bakharev T, Durability of geopolymer materials in sodium and magnesium sulfate solutions, Cem Concr Res 35 (2005) 1233-1246.

[104] Ismail I, Bernal SA, Provis JL, Hamdan S, van Deventer JSJ, Microstructural

changes in alkali-activated fly ash/slag geopolymers with sulfate exposure, Mater Struct 46 (2013) 361-373.

[105] Krivenko PV, Gelevera A, Fedorenko V, The effect of alkali on destructive and constructive processes during alkali-aggregate reaction, First International Conference on Advances in Chemically-Activated Materials, Jinan, China, RILEM/Springer 2010, pp. 140-147.

[106] Bakharev T, Sanjayan JG, Cheng YB, Resistance of alkali-activated slag to alkali-aggregate reaction, Cem Concr Res 31 (2001) 331-334.

[107] Skvara F, Alkali-activated Material - Geopolymer, Proceedings of 2007 International Conference on Alkali-Activated Materials, Research Production and Utilization, Prague, Czech Republic, 2007, pp. 661-676, ISBN 978-80-86742-19-9.

[108] Yunsheng Z, Wei S, Fly ash based geopolymer concrete, Indian Concr J 80 (2006) 20-24.

[109] Bortnovosky O, Dvorakova K, Roubieck P, Pousek J, Prudkova Z, Baxa P, Development, property and production of geopolymers based on secondary raw materials, In: Alkali-Activated Materials: Research, Production and Utilization 3rd Conference, Prague, Czech Repulic, 2007, pp. 83-96.

[110] Puertas F, Amat T, Fernandez-Jimenez A, Vazquez T, Mechanical and durable behaviour of alkaline cement mortars reinforced with polypropylene fibers, Cem Concr Res 33 (2003) 2031-2036.

[111] Kriven WM, Bell J, Effect of alkali choice on geopolymers porperties, Cer Eng Sci Proceedings 25 (2004) 999-1004.

[112] Rickard WDA, van Riessen A, Thermal Character of Geopolymers Synthesized from Class F Fly Ash Containing High Concentrations of Iron and α-Quartz, Appl Cer Tech 7 (2010) 81-88.

[113] Kong DLY, Sanjayan JG, Effect of elevated temperatures on geopolymer paste, mortar and concrete, Cem Concr Res 40 (2010) 334-339.

[114] Krivenko P, Guziy S, Fire resistant alkaline Portland cements. In: Alkali-

Activated Materials: Research, Production and Utilization 3rd Conference, Prague, Czech Repulic, 2007, pp. 333-347.

[115] Pernà I, Hanzlicek T, Straka P, Steinerova M, Utilization of fluidized bed ashes in thermal resistance applications. In: Alkali-Activated Materials: Research, Production and Utilization 3rd Conference, Prague, Czech Repulic, 2007, pp. 527-537.

[116] Zhao R, Sanjayan JG, Geopolymer and Portland cemens concrete in simulated fire, Mag Concr Res 6 (3) (2011) 163-173.

[117] Temuujin J, Van Riessen A, Williams R, Influence of calcium compounds on the mechanical properties of fly ash geopolymer pastes, J Hazard Mater 167 (2009) 82-88.

[118] Lloyd RR, Provis JL, van Deventer JSJ, Pore solution composition and alkali diffusion in inorganic polymer cement, Cem Concr Res 40 (9) (2010) 1386-1392.

[119] van Deventer JSJ, Feng D, Duxson P, Dry mix cement composition, methods and systems involving same, US Patent 7691,198 B2; 2010.

[120] Szklorzová H, Bílek V, Influence of alkali ions in the activator on the performance of alkali-activated mortars. In: Bílek V, Keršner Z, editors. 3rd International Symposium on Non-Traditional Cement and Concrete, Czech Republic, Brno, 2008, pp. 777-784.

[121] Škvára F, Pavlasová S, Kopecky L, Myšková L, Alberovská L, High temperature properties of fly ash based geopolymers. In: Bílek V, Keršner Z, editors. 3rd International symposium on non-traditional cement and concrete, Czech Republic: Brno; 2008, pp. 741-750.

[122] Kani E, Allahverdi A, Provis J, Efflorescence control in geopolymer binders based on natural pozzolan, Cem Concr Compos 34 (2011) 25-33.

[123] Bernal S, de Gutiérrez R, Pedraza A, Provis J, Rodriguez E, Delvasto S, Effect of binder content on the performance of alkali-activated slag concretes, Cem Concr Res 41 (2011) 1-8.

[124] Bernal S, de Gutiérrez R, Pedraza A, Provis J, Rose V, Effect of silicate

modulus and metakaolin incorporation on the carbonation of alkali silicate-activated slags, Cem Concr Res 40 (2010) 898-907.

[125] Bernal SA, Provis JL, Mejía de Gutiérrez R, van Deventer JSJ, Accelerated carbonation testing of alkali-activated slag/metakaolin blended concretes: effect of exposure conditions, Mater Struct 48 (2015) 653-669.

[126] Bernal SA, Mejía de Gutiérrez R, Provis JL, Engineering and durability properties of concretes based on alkali-activated granulated blast furnace slag/metakaolin blends, Constr Build Mater 33 (2012) 99-108.

[127] Angst U, Elsener B, Larsen CK, Luckey GC, Vennesland Ø, Critical chloride content in reinforced concrete - A review, Cem Concr Res 39 (2009) 1122-1138.

[128] Neville A, Chloride attack of reinfonced concrete: an overview, Mater Struct 28 (1995) 63-70.

[129] Ustabas I, The effect of capillarity on chloride transport and prediction of the accumulation region of chloride in concretes with reinforcement corrosion, Constr Build Mater 28 (2012) 640-647.

[130] Pacheco-Torgal F, Miraldo S, Labrincha JA, De Brito J, An overview on concrete carbonation in the context of eco-efficient construction: Evaluation, use of SCMs and/or RAC, Constr Build Mater 36 (2012) 141-150.

[131] Bastidas DM, Fernández-Jiménez A, Palomo A, González JA, A study on the passive state stability of steel embedded in activated fly ash mortars, Corr Sci 50 (2008) 1058-1065.

[132] Criado M, Monticelli C, Fajardo S, Gelli D, Grassi V, Bastidas JM, Organic corrosion inhibitor mixtures for reinforcing steel embedded in carbonated alkali-activated FA mortar, Constr Build Mater 35 (2012) 30-37.

[133] Roy DM, Jiang W, Silsbee MR, Chloride diffusion in ordinary blended and alkali-activated cement pastes, Cem Concr Res 30 (2000) 1879-1884.

[134] Saraswathy V, Muralidharan S, Thangavel K, Srinivasan S, Influence of activated fly ash on corrosion resistance and strength of concrete, Cem Concr Res 25

(2003) 673-680.

[135] Miranda JM, Fernandez-Jimenez A, Gonzalez A, Palomo A, Corrosion resistance in activated fly ash mortars, Cem Concr Res 35 (2005) 1210-1217.

[136] Aperador W, de Gutiérrez R, Bastidas D, Steel corrosion behaviour in carbonated alkali-activated slag concrete, Corros Sci 51 (2009) 2027-2033.

[137] Badar MS, Kupwade-Patil K, Bernal SA, Provis JL, Allouche EN, Corrosion of steel bars induced by accelerated carbonation in low and high calcium fly ash geopolymer concretes, Constr Build Mater 61 (2014) 79-89.

[138] Criado M, Fernández Jiménez A, De La Torre AG, Aranda MAG, Palomo A, An XRD study of the effect of the SiO_2/Na_2O ratio on the alkali-activation of fly ash, Cem Concr Res 37 (2007) 671-679.

[139] Criado M, Martínez-Ramirez S, Fajardo S, Gómez PP, Bastidas JM, Corrosion rate and corrosion product characterisation using Raman spectroscopy for steel embedded in chloride polluted fly ash mortar, Mater Corros 64 (2013) 372-380.

[140] Fernández-Jiménez A, Miranda JM, González JA, Palomo A, Steel passive state stability in activated fly ash mortars, Mater Construc 60 (300) (2010) 51-65.

[141] Imbabi MS, Carrigan C, McKenna S, Trends and developments in green cement and concrete technology, Int J Sust Built Env 1 (2012) 194-216.

[142] Habert G, d'Espinose de Lacaillerie JB, Roussel N, An environmental evaluation of geopolymer based concrete production: reviewing current research trends, J Clean Prouct 19 (2011) 1229-1238.

[143] Turner LK, Collins FG, Carbon dioxide equivalent (CO_2-e) emissions: A comparison between geopolymer and OPC cement concrete, Costr Build Mater 43 (2012) 125-130.

[144] Heath A, Paine K, McManus M, Minimising the global warming potential of clay based geopolymers, J Clean Product (2014) 75-83.

[145] Jamieson E, McLellan B, van Riessen A, Nikraz H, Comparison of embodied

energies of Ordinary Portland Cement with Bayer-derived geopolymer products, J Clean Product 99 (2015) 112-118.

[146] UNI EN 450-1. Fly ash for concrete - Part 1 - Definition, specifications and conformity criteria. 2012.

[147] EN 197-1. Cement - Part 1 - Composition, specifications and conformity criteria for common cements. 2000.

[148] EN 196-1. Methods of testing cement - Part 1 - Determination of strength. 2005.

[149] Natali ME, Bignozzi MC, Influence of curing conditions on fly ash based geopolymer for high temperature applications, Constr Build Mater, article under publication.

[150] Monticelli C, Natali ME, Balbo A, Chiavari C, Zanotto F, Manzi S, Bignozzi MC, Corrosion behavior of reinforced alkali-activated fly ash mortars under wet and dry exposures to chloride solutions, Cem Concr Res, article under revision.

[151] ASTM C1556. Standard test method for determinig the apparent chloride diffusion coefficient of cementitious mixtures by bulk diffusion. 2003.

[152] http://www.malvern.com/en/products/technology/laser-diffraction/, 25/01/2016.

[153] Qiang F, Wenbo S, Mie theory for light scattering by a spherical particle in an absorbing medium, Appl Optics 40 (9) (2001) 1354-1361.

[154] http://serc.carleton.edu/research_education/geochemsheets/techniques/SEM.html, 25/01/2016.

[155] http://wings.buffalo.edu/faculty/research/scic/sem-eds.html, 25/01/2016.

[156] Chupas PJ, Chapman KW, Lee PL, Applications of an amorphous silicon based area detector for high-resolution, high-sensitivity and fast time-resolved pair distribution function measurements, J Appl Cryst 40 (3) (2007) 463-470.

[157] Hammersley AP, Svensson SO, Hanfield M, Fitch AM, Hausermann D, Two-dimensional detector software: from real detector to idealised image or two-theta scan, High Press Res 14 (1996) 235-248.

[158] Qui X, Thompson JW, Billinge SJL, PDFgetX2: a GUI-driven program to obtain the pair distribution function from X-ray powder diffraction data, J Appl Cryst 37 (4) (2004) 678.

[159] Farrow CL, Juhas P, Liu JW, Bryndin D, Bozin ES, Bloch J, et al., PDFfit2 and PDFgui: computer programs for studying nanostructure in crystals, J Phys Condens Mat 19 (2007) 335219.

[160] Neuefeind J, Feygenson M, Carruth J, Hoffmann R, Chipley KK, The Nanoscale Ordered MAterials Diffractometer NOMAD at the Spallation Neutron Source SNS, Nucl Instrum Methods Phys Res B 287 (2012) 68-75.

[161] Cullity BD, Stock SR, Elements of X-ray diffraction (3rd edition), Prentice Hall, 2001.

[162] Egami T, Billinge SJL, Underneath the Bragg peaks: structural analysis of complex materials, Pergamon Press, Elsevier Science, Oxford, 2003.

[163] https://www1.aps.anl.gov/Structural-Science, 01/18/2016.

[164] https://neutrons.ornl.gov/nomad, 27/01/2016.

[165] UNI EN 1015-3. Methods of test for mortar for masonry - Part 3 - Determination of consistence of fresh mortar (by flow table). 2007.

[166] UNI EN 7699. Determination of water absorption at atmospheric pressure. 2005.

[167] UNI EN 1015-18. Methods of test for mortar for masonry - Determination of water absorption coefficient due to capillary action of hardened mortar. 2002.

[168] UNI EN 15801. Conservation of cultural property - Test methods - Determination of water absorption by capillarity. 2010.

[169] DIN 66133. Determination of pore volume distribution and specific surface area of solids by mercury intrusion. 1993.

[170]http://www.micromeritics.com/Repository/Files/Mercury_Porosemitry_Theory_poster_.pdf, 26/01/2016.

[171] EN 12617-4. Products and systems for the protection and repair of concrete structures - Test methods - Determination of shrinkage and expansion. 2003.

[172] Coats AW, Redfern JP, Thermogravimetric Analysis: A Review, Analyst 88 (1963) 906-924.

[173] http://www.durhamgeo.com/testing/concrete/mortar-testing.html, 26/01/2016.

[174] https://en.wikipedia.org/wiki/Optical_dilatometer, 26/01/2106.

[175] EN 13925. Products and systems for the protection and repair of concrete structures - Test methods - Determination of resistance to carbonation. 2004.

[176] Räsänen V, Penttala V, The pH measurement of concrete and smoothing mortar using a concrete powder suspension, Cem Concr Res 34 (2004) 813-820.

[177] Gardiner DJ, Practical Raman spectroscopy. Springer-Verlag. ISBN 978-0-387-50254-0, 1989.

[178] ASTM C1152/C1152M. Standard test method for acid-soluble chloride in mortar and concrete. 2004.

[179] ASTM C114. Standard test methods for chemical analysis of hydraulic cement. 2011.

[180]http://www.ecochemie.nl/download/Applicationnotes/Autolab_Application_Note_COR03.pdf, 26/01/2016.

[181] https://www.gamry.com/application-notes/EIS/basics-of-electrochemical-impedance-spectroscopy/, 26/01/2016.

[182] Rickard WD, Temuujin J, van Riessen A, Thermal analysis of geopolymer pastes synthesised from five fly ashes of variable composition, J Non-Crys Solids 358

(2012) 1830-1839.

[183] Gualtieri AF, Accuracy of XRPD QPA using the combined Rietveld-RIR method, J of Appl Cryst 33 (2000) 267-78.

[184] Ďurovič S, Refinement of the crystal structure of mullite, Chem Zvesti 23 (1969) 113-128.

[185] Shmakov AN, Kryukova GN, Tsybulya SV, Chuvilin AL, Solovyeva LP, Vacancy ordering in γ-Fe_2O_3: Synchrotron X-ray powder diffraction and high-resolution electron microscopy studies, J Appl Cryst 28 (1995) 141-145.

[186] Iizumi M, Koetzle TF, Shirane G, Chikazumi S, Matsui M, Todo S, Structure of magnetite Fe_3O_4 below the Verwey transition temperature, Acta Cryst B 38 (1982) 2121-2133.

[187] van Hoang V, Composition dependence of static and dynamic heterogenities in simulated liquid aluminum silicates, Phis Rev B 75 (2007) 174-202.

[188] Winkler A, Horbach J, Kob W, Binder K, Structure and diffusion in amorphous aluminum silicate: a molecular dynamics computer simulation, J Chem Phys 120 (2004) 384-393.

[189] Anderson PR, Swartz WE, X-ray photoelectron spectroscopy of some aluminosilicates, Inorg Chem 13 (9) (1974) 2293-2294.

[190] Petkov V, Billinge SJL, Shastri SD, Himmel B, Polyhedral units and network connectivity in calcium aluminosilicate glasses from high-energy X-ray diffraction, Phys Rev Lett 85 (16) (2000) 3436-3439.

[191] Cimasu AC, Michel FM, Tcaciuc AP, Brown Jr GE, Properties of impurity-bearing ferrihydrite III. Effects of Si on the structure of 2-line ferrihydrite, Geochim Cosmochim Acta 1333 (2014) 168-185.

[192] Babay S, Mhiri T, Toumi M. Synthesis, structural and spectroscopic characterizations of maghemite γ-Fe_2O_3 prepared by one-step coprecipitation route, J Mol Struct 1085 (2015) 286-293.

[193] King G, Ramezanipour F, Llobet A, Greedan JE, Local structures of Sr_2FeMnO_{5+y} (Y=0, 0.5) and $Sr_2Fe_{1.5}Cr_{0.5}O_5$ from reverse Monte Carlo modeling of pair distribution function data and implications for magnetic order, J Solid State Chem 98 (2013) 407-415.

[194] Weigel C, Cormier L, Calas G, Galoisy L, Bowron DT, Intermediate-range order in the silicate network glasses $NaFe_xAl_1{-}xSi_2O_6$ (x=0,0.5,0.8,1): A neutron diffraction and empirical potential structure refinement modeling investigation, Phys Rev B 78 (6) (2008) 064202.

[195] Fisher RX, Schneider H, Schmücker M, Crystal structure of Al-rich mullite. Am Miner 79 (1994) 983-990.

[196] Loewenstein W, The distribution of aluminum in the tetrahedra of silicates and aluminates, Am Mineral 39 (1-2) (1954) 92-96.

[197] Lloyd R, Provis JL, van Deventer JSJ, Microscopy and microanalysis of inorganic polymer cements.1: remnant fly ash particles, J Mater Sci 44 (2009) 608-619.

[198] Jacques SDM, Di Michiel M, Kimber SAJ, Yang X, Cernik RJ, Beale AM, et al., Pair distribution function computed tomography, Nat Commun 4 (2013) 2536.

[199] White CE, Effect of temperature on the atomic structure of synthetic calcium-silicate-detyerate gels: A neutron pair distribution function investigation, Cem Concr Res 79 (2015) 93-100.

[200] Brown TE, LeMay H, Bursten H, Chemistry The Central Science, Upper Saddle River, NJ: Simon & Schuster, 1997 (227), pp. 412-3.

[201] Trucano P, Chen R, Structure of graphite by neutron diffration, Nature, 258 (1975) 136-137.

[202] Yip CK, Luckey GC, van Deventer JSJ, The coexistence of geopolymeric gel and calcium silicate hydrate at the early stage of alkaline activation, Cem Concr Res 35 (2005) 688-697.

[203] Yip CK, Luckey GC, Provis JL, van Deventer JSJ, Effect of calcium silicate sources on geopolymerization, Cem Concr Res 38 (2008) 554-564.

[204] Bignozzi MC, Manzi S, Lancellotti I, Kamseu E, Barbieri L, Leonelli C, Mix-design and characterization of alkali-activated materials based on metakaolin and ladle slag, Appl Clay Sci 73 (2013) 78-85.

[205] Natali Murri A, Rickard WDA, Bignozzi MC, van Riessen A, High temperature behaviour of ambient cured alkali-activated materials based on ladle slag, Cem Concr Res 43 (2013) 51-61.

[206] Kong DLY, Sanjayan JG, Sagoe-Crentsil K, Comparative performance of geopolymers made with metakaolin and fly ash after exposture to elevate temperatures, Cem Concr Res 37 (2007) 1538-1589.

[207] Duxson P, Lukey GC, van Deventer JSJ, Physical evolution of Na-geopolymer derived from metakaolin up to 1000 °C, J Mater Sci 6 (2007) 3044-3054.

[208] Anovitz LM, Blencoe JG, Dry melting of high albite, Am Miner 84 (1999) 1830-1842.

[209] Temuujin J, Minjigmaa A, Rickard WDA, Lee M, Fly ash based geopolymer thin coatings on metal substrates and its thermal evaluation, J Hazard Mater 180 (2010) 748-752.

[210] Pastorino D, Canal C, Ginebra MP, Multiple characterization study on porosity and pore structure of calcium phosphate cements, A Biomater 28 (2015) 205-214.

[211] Bernal SA, Provis JL, Brice DG, Kilcullen A, Duxson P, van Deventer JSJ, Accelerated carbonation testing of alkali-activated binders significally understimates service life: the role of pore solution chemistry, Cem Concr Res 42 (2012) 1317-1326.

[212] Haq EU, Padmanabhan SK, Licciulli A, *In-situ* carbonation of alkali-activated fly ash geopolymer, Constr Build Mater 66 (2014) 781-786.

[213] Ho DWS, Lewis RK, Carbonation of concrete and its prediction, Cem Concr Res 17 (3) (1987) 489-504.

[214] Zhu H, Zhang Z, Zhu Y, Tian L, Durability of alkali-activated fly ash concrete: Chloride penetration in pastes and mortars, Constr Build Mater 65 (2014) 51-59.

[215] Metha PK, Manmohan D, Pore size distribution and permeability of hardened cement paste, 7th International Symposium of the Chemestry of Cement, Paris, 1980, pp. 1-5.

[216] Rilem report 12, In: Kropp J, Hilsdorf HK, editors, Performance criteria for concrete durability, 1995.

[217] Kumar R, Bhattacharjee B, Porosity, pore size distribution and in situ strength of concrete, Cem Concr Res 33 (2003) 155-164.

[218] Zhang JX, Fujiwara T, Resistance to frost damage of concrete with various mix proportions under salty condition, frost resistance of concrete, RILEM proceedings PRO, Cachan Cedex, France: RILEM Publications Carl, 2002, pp. 367-74.

[219] ASTM C876. Standard test method for half-cell potentials of uncoated reinforcing steel in concrete. 2009.

[220] Andrade C, Alonso MC, González JA, An initial effort to use the corrosion rate measurements for estimation rebar durability, in: Berke NS, Chaker V, Whiting D, (eds.), Corrosion rates of steel in concrete ASTM STP 1065, American Society for Testing and Materials, Philadelphia, 1990, pp. 29-37.

[221] Ma K-L, Xie Y-J, Long G-G, Wu K-G, Invading track of chloride ions in cemented based materials, J Cent South Univ Technol 17 (2010) 263-268.

[222] Refait P, Genin JMR, The mechanisms of oxidation of ferrous hydroxychloride β-$Fe_2(OH)_3Cl$ in aqueous solution: The formation of akaganeite *vs* goethite, Corros Sci 33 (1993) 539-553.

[223] Volpi E, Olietti A, Stefanoni M, Trasatti SP, Electrochemical characterization of mild steel in alkaline solutions simulating concrete environment, J Electroanal Chem 736 (2015) 38-46.

[224] Amaral ST, Müller IL, Passivation of pure iron in alkaline solution containing silicate and sulphate-galvanostatic and potentiostatic studies, Corros Sci 41 (1999) 747-758.

[225] Amaral ST, Müller IL, A RRDE study of the electrochemical behaviour of iron

in solutions containing silicate and sulphate at pH 10-13, Corros Sci 41 (1999) 759-771.

[226] Xie T, Ozbakkaloglu T, Behaviour of low-calcium fly and bottom ash based geopolymer concrete cured at ambient temperature, Cer Int (2015) //dx.doi.org/10.1016/j.ceramint.2015.01.031.

[227] Collins F, Sanjayan GJ, Effect of pore size distribution on drying shrinkage of alkali-activated slag concrete, Cem Concr Res 30 (2000) 1401-1406.

[228] Ma Y, Hu J, Ye G, The pore structure and permeability of alkali-activated fly ash, Fuel 104 (2013) 771-780.

[229] Lloyd RR, Provis JL, Smeaton KJ, van Deventer JSJ, Spatial distribution of pores in fly ash based inorganic polymer gels visualized by Wood's metal intrusion, Micorpor Mesopor Mater 126 (2009) 32-39.

[230] Fernandez Bertos M, Simons SJR, Hills CD, Carey PJ, A review of accelerated carbonation technology in the treatment of cement based materials and sequestration of CO_2, J Hazard Mater B112 (2004) 193-205.

[231] Ismail M, Ohtsu M, Corrosion rate of ordinary and high-performance concrete subjected to chloride attack by AC impedance spectroscopy, Constr Build Mater 20 (2006) 458-469.

[232] Serdar M, Valek Žulj L, Bjegović D, Long-term corrosion behaviour of stainless reinforcing steel in mortar exposed to chloride environment, Corros Sci 69 (2013) 149-157.

[233] Montemor MF, Simoes MP, Salta MM, Ferreira MGS, The assessment of the electrochemical behaviour of fly ash-containing concrete by impedance spectroscopy, Corros Sci 35 (1993) 1571-1578.

[234] Keddam M, Takenouti H, Nóvoa XR, Andrade C, C. Alonso C, Impedance measurements on cement paste, Cem Concr Res 27 (1997) 1191-1201.

[235] Feliu V, Gonzalez JA, Andrade C, Feliu S, Equivalent circuit for modelling the steel-concrete interface. I. Experimental evidence and theoretical predictions, Corros Sci 40 (1998) 975-993.

[236] Gu P, Elliot S, Beaudoin JJ, Arsenault B, Corrosion resistance of stainless steel in chloride contaminated concrete, Cem Concr Res 26 (1996) 1151-1156.

[237] Yohai L, Valcarce MB, Vázquez M, Testing phosphate ions as corrosion inhibitors for construction steel in mortars, Electrochim Acta (2016), http://dx.doi.org/10.1016/j.electacta.2015.12.124.

[238] Sagoe-Crentsil KK, Glasser FP, Irvine JTS, Electrochemical characteristics of reinforced concrete corrosion as determined by impedance spectroscopy, Br Corros J 27 (1992) 113-118.

[239] Trabanelli G, Monticelli C, Grassi V, Frignani A, Electrochemical study on inhibitors of rebar corrosion in carbonated concrete, Cem Concr Res 35 (2005) 1804-1813.

[240] Moreno JD, Bonilla M, Adam JM, Borrachero MV, Soriano L, Determining corrosion levels in the reinforcement rebars of buildings in costal areas. A case study in the Mediterranean coastline, Constr Build Mater 100 (2015) 11-21.